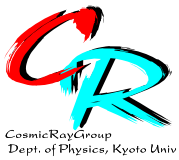

November 2006

Stereoscopic Observations of TeV Gamma-Rays from the Supernova Remnant RX J0852.0−4622 with the CANGAROO-III Imaging Air Čerenkov Telescopes

Watanabe Shio

Department of Physics, Graduate School of Science, Kyoto University,
Kitashirakawa-Oiwake-cho, Sakyo, Kyoto 606-8502, Japan

Submitted to the Department of Physics, Graduate School of Science, Kyoto University in partial fulfillment of the requirements for the degree of Doctor of Philosophy (Science)

Abstract

We carried out stereoscopic observations of the supernova remnant RX J0852.0−4622 with the CANGAROO-III imaging air Čerenkov telescopes (IACTs) in south Australia early in 2005 January and February. We detected 829 ± 113 gamma-ray photons in the range of 860 GeV to 5 TeV with the significance of 7.3 σ with data of 19 hours of live time by the CANGAROO-III standard analysis. The spectrum in this energy range is well described by a power law with a photon index of $\Gamma = 2.4 \pm 0.3$. The differential flux at 1 TeV is

$$\frac{dF}{dE} = (3.9 \pm 0.6_{\rm stat.}) \times 10^{-11} {\rm cm}^{-2} {\rm s}^{-1} {\rm TeV}^{-1}. \quad (1)$$

In addition, we improved the analysis and get a spectrum for a broader energy band up to ∼10 TeV. The best fit with a power-law assumption is

$$\frac{dF}{dE} = (4.1 \pm 0.6_{\rm stat.}{}^{-1.7_{\rm syst.}}_{+0.5_{\rm syst.}}) \times 10^{-11} \times \left(\frac{E}{1{\rm TeV}}\right)^{-(2.7 \pm 0.2_{\rm stat.} - 0.5_{\rm syst.})} {\rm cm}^{-2} {\rm s}^{-1} {\rm TeV}^{-1}. \quad (2)$$

The morphology in the energy range above 860 GeV shows the shell structure which is brighter to the west. Then we discussed the emission mechanism by the broadband spectrum from radio to TeV gamma-ray and the morphology of the X-ray emission. The filamentary structure of the X-ray emission, which indicates a magnetic field of hundreds of microgauss in the remnant, makes the leptonic scenario less favorable. On the other hand, the hadronic scenario explains the TeV flux much better. For a firmer conclusion, deeper observations are expected.

Contents

Chapter1

Supernova Remnants as an Origin of Cosmic Rays

§ 1 Origin of Cosmic Rays

Cosmic rays were discovered by Hess long ago in 1912 (Hess 1912). However, much of their nature remains mysterious. They are observed in a wide range of energies, from 10^6 eV to more than 10^{20} eV. The fluxes of the primary cosmic rays are detected by balloon experiments below 10^{14} eV and shower arrays above 10^{14} eV. The integral flux of cosmic rays is $\sim$1 cm^{-2}sec^{-1}str^{-1} above 1 GeV on the ground. Figure 1.1 shows the differential energy spectrum of the cosmic rays. It is well represented by a power-law in the energy range above 1 GeV. The spectral index is -2.7 below 10^{15} eV and changes to -3.0 at $\sim 10^{15}$ eV (knee). Note that the highest energy of the cosmic rays ever detected is $\sim 10^{20}$ eV (Hayashida et al. 1994). Cosmic rays up to $\sim 10^{15}$ eV are the main component in terms of numbers and are confined in our Galaxy due to their Larmor radius smaller than the disk thickness. Their energy distribution does not obey Maxwellian, but it behaves as thermal particles. They have an energy density of $\sim$1 eV cm^{-3} which is comparable to that contained in the galactic magnetic field or in the cosmic microwave background radiation. From the point of view of the energetics, it is a serious and interesting problem where and how such a large amount of energy is produced in the galaxy.

The investigation of the composition of the cosmic rays is an alternative way to understand their origin. Roughly speaking, 99 % of the particles are nuclei while 1 % are electrons. Among the nuclei, 90% are protons, 9 % are α particles, and 1 % are other elements. Figure 1.2 shows the relative abundances of the cosmic rays at Earth's orbit to those of the solar system. The abundance of elements in cosmic rays is similar to the typical solar abundance. Some of the differences privide some clues to the origin and the acceleration mechanisms of the cosmic rays. The

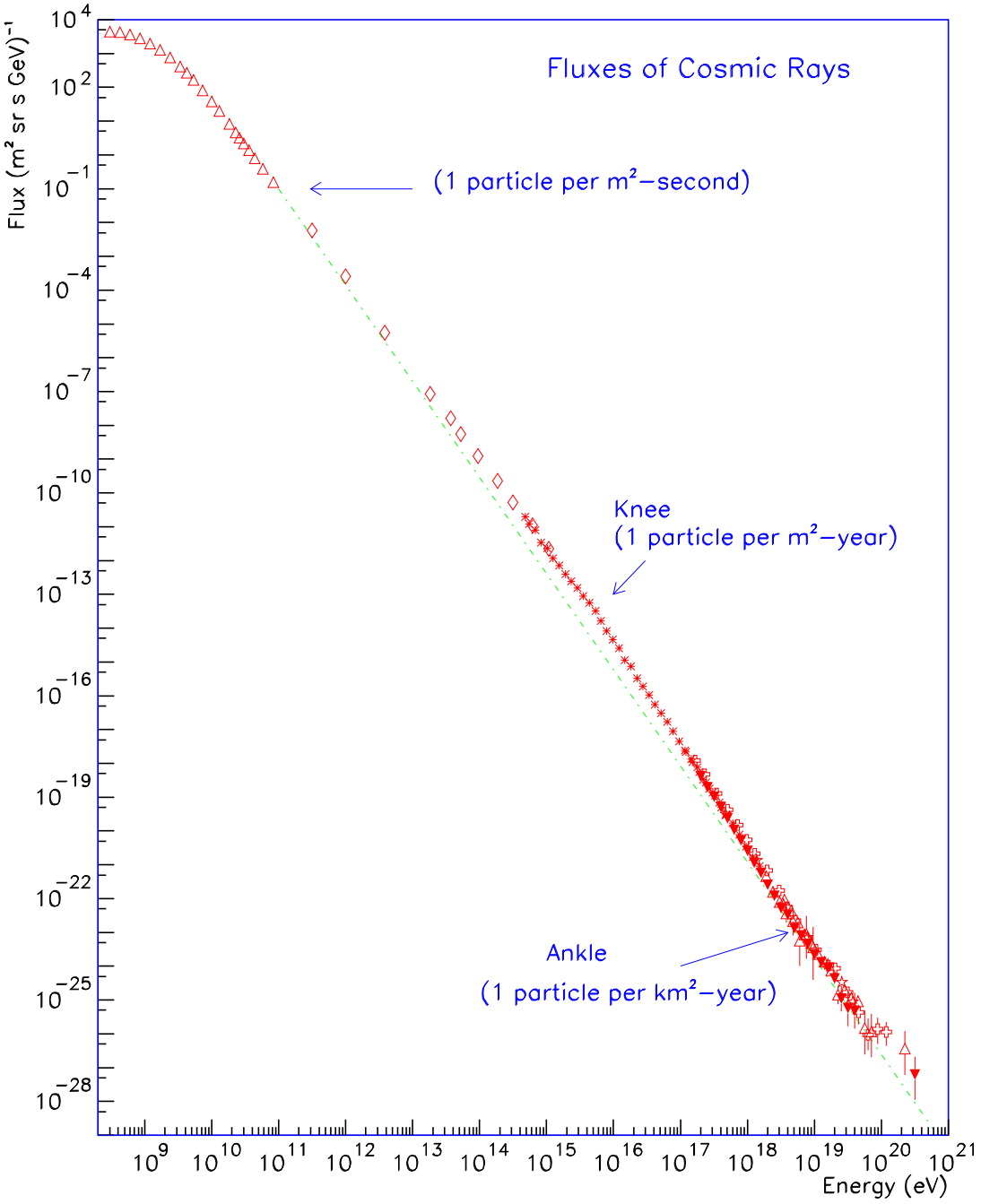

Figure 1.1: Energy spectrum of the cosmic rays (The Pierre Auger Observatory Design Report 1997).

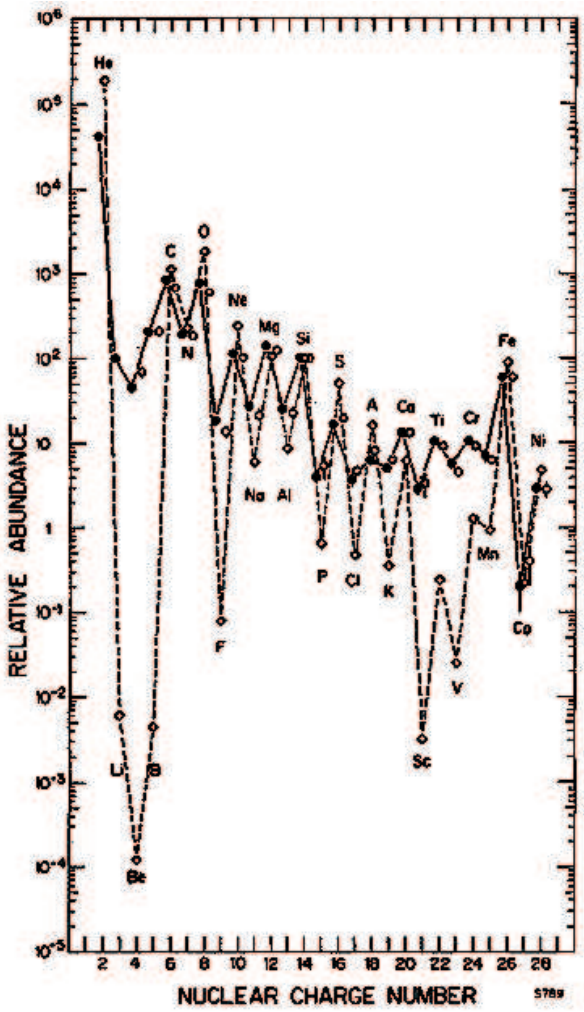

Figure 1.2: Cosmic ray elemental abundances (He-Ni) measured at Earth compared to the solar system abundances, all relative to silicon: (solid circles) low energy data, 70 to 280 MeV n(nucleon)$^{-1}$; (open circles) compilation of high energy measurements, 1000 to 2000 MeV n^{-1}; (diamonds) solar system. (Simpson 1983).

light elements such as lithium, beryllium, and boron, are grossly over-abundant in the cosmic rays. These elements are difficult to be produced by the nucleosynthesis either in the big bang or inside of the stars.

The high-energy nuclei in the cosmic ray such as carbon, nitrogen, and oxygen interact with the interstellar matters (mainly protons) during the propagation. This spallation process produces lighter nuclei and increases their abundance. The spallation produces the secondary light elements by the following processes.

$$^{12}_{6}\mathrm{C} + \mathrm{p} \rightarrow \ ^{6}_{3}\mathrm{Li} + \ ^{4}_{2}\mathrm{He} + \mathrm{p} + \mathrm{p} + \mathrm{n} + \cdots \tag{1.1}$$

$$^{12}_{6}\mathrm{C} + \mathrm{p} \rightarrow \ ^{9}_{4}\mathrm{Be} + \mathrm{p} + \mathrm{p} + \mathrm{p} + \mathrm{n} + \cdots \tag{1.2}$$

The lifetime of the cosmic rays is a key to understand the energetics of the cosmic rays in Galaxy. The ratio between the number of primary particles and those of secondary particles by the above interactions can be used to determine the lifetime. Here we consider the spallation of carbons (C). The ratio between the boron (B)-producing cross section and the total inelastic cross section is given as

$$\frac{\sigma_{\mathrm{B}}}{\sigma_{\mathrm{total}}} = 0.4. \tag{1.3}$$

Thus, the ratio of the number of boron to that of carbon in the cosmic rays (B/C ratio) is given as

$$\mathrm{C} = \mathrm{C_p} \exp\left(-\frac{x}{\lambda_{\mathrm{C}}}\right), \quad \mathrm{B} = \frac{\sigma_{\mathrm{B}}}{\sigma_{\mathrm{total}}}\mathrm{C_p}\left[1 - \exp\left(-\frac{x}{\lambda_{\mathrm{C}}}\right)\right], \tag{1.4}$$

$$\frac{\mathrm{B}}{\mathrm{C}} = 0.4\frac{1 - \exp\left(-\frac{x}{\lambda_{\mathrm{C}}}\right)}{\exp\left(-\frac{x}{\lambda_{\mathrm{C}}}\right)}, \tag{1.5}$$

where x, $\mathrm{C_p}$ and λ_{C} are the column density (g/cm^2) where carbon passed, the number of the primary carbons, and the mean free path of carbon (8.3g/cm^2), respectively. Figure 1.3 shows the B/C ratio versus the kinetic energy (Gupta & Webber 1989). Assigning B/C $\simeq 0.3$ from Fig.1.3 to Eq.(1.5), $x \simeq 5$g/cm^2 is obtained. The lifetime of the cosmic rays is given as $T = 5N/c = 3\times10^6$ yr, where N is Avogadro's number, and c is the light speed assuming the matter density of $\sim$1 H cm^{-3}. On the other hand, radioactive elements in the cosmic rays also give an additional constraint to the lifetime of the cosmic rays. ^{10}Be, of which lifetime is $\sim10^6$ yr, imposes a restriction on the cosmic-ray lifetime. Considering the discussion on the B/C ratio and the fact that this element is not positively detected yet in the cosmic ray, the lifetime (the galactic containment time) of the cosmic rays τ_{CR} is $\sim10^7$ yr.

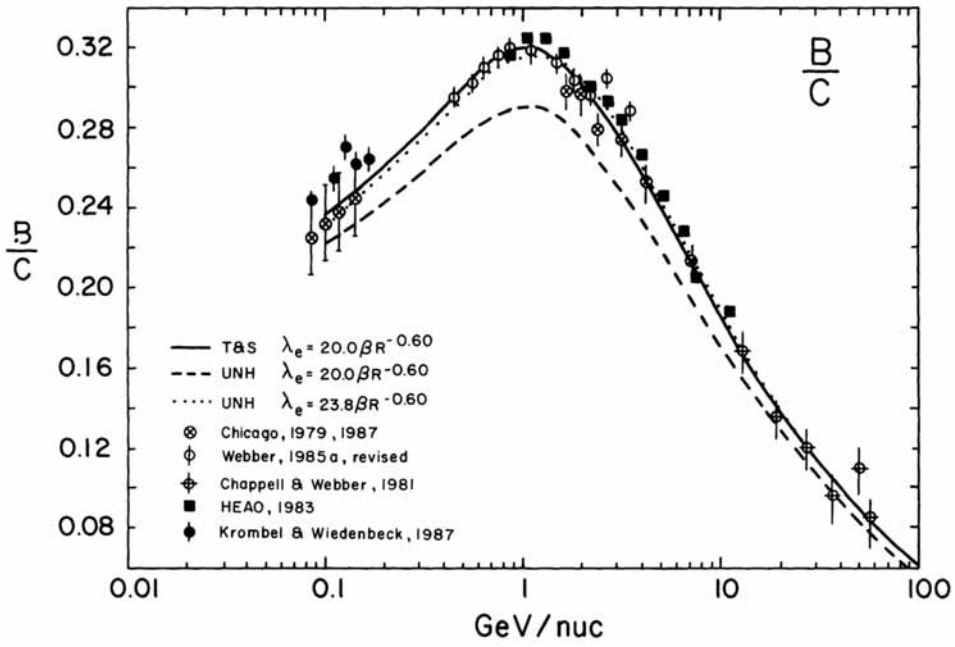

Figure 1.3: B/C ratio to the kinetic energy for various path length λ_e (Gupta & Webber 1989).

With the above arguments on the cosmic-ray lifetime, we discuss the cosmic ray origin in perspective of the energetics of the cosmic rays in our Galaxy. Assuming the region where the galactic cosmic rays are confined is a disk with a radius of 10 kpc and a thickness of 1 kpc, their total energy is given as

$$1 \text{ eV} \times \pi(10 \text{ kpc})^2 \times 1 \text{ kpc} \approx 10^{67} \text{ eV} \approx 10^{55} \text{ erg}. \tag{1.6}$$

Here we used the cited cosmic-ray energy density of 1 eV cm^{-3}. Using Eq.(1.6) and the galactic containment time of the cosmic rays, the required energy for the successive acceleration of the cosmic rays is given as

$$\frac{10^{55} \text{ erg}}{10^7 \text{ yr}} = 10^{48} \text{erg/yr} \simeq 10^{40} \text{ erg/sec}. \tag{1.7}$$

In 1932, Baade & Zwicky (1934) suggested that supernova remnants (SNRs) are the origin of the cosmic rays from this point of view, and Ginzburg and Hayakawa suggested again with more quantitative consideration (Ginzburg & Syrovatskii 1964; Hayakawa 1956). Assuming that the total kinetic energy of a supernova (SN) is 10^{51} erg, and the rate of SNe is once in every 30 years, then the total energy of SNe is given as

$$10^{52} \text{ erg/SN} \times \frac{1}{30} \text{ SNe/yr} \simeq \times 10^{42} \text{ erg/sec}. \tag{1.8}$$

A few percent of this energy is enough to explain the observed cosmic ray energy in the Galaxy. No other galactic object than SNe is ever thought to exist to give such a large amount of energy. The composition of the cosmic rays from SNR should be roughly the same as that by the nucleosynthesis inside stars. Thus, the SNR is believed as a favored acceleration site of the galactic cosmic rays.

§ 2 Acceleration Mechanisms of Cosmic Rays

2.1 Second-order Fermi Acceleration

Although SNRs have been thought as a possible source of the cosmic rays with the energy up to about 10^{15} eV, the acceleration mechanism is still unclear. The Fermi acceleration mechanism was first proposed by Fermi in 1949. Gas clouds in the interstellar matter have random velocities of $\sim$15 km/s superimposed on their regular motion around the galaxy. Cosmic rays gain energy on average when scattering off these magnetized clouds. A cosmic ray enters a cloud and scatters off irregularly in the magnetic field which is tied to the partly ionized cloud.

The cosmic ray scatters elastically with the cloud. The cosmic ray and the cloud have the velocity of nearly c (light speed) and v ($\ll c$), respectively. The cosmic ray is accelerated in the head-on collision and decelerated in the rear-end collision. The energy of the cosmic ray E in the laboratory frame is $E\gamma(1 \pm v/c)$ in the frame of the cloud ($+$ for head-on and $-$ for rear-end). Here the coordinate conversion is done by Lorentz transformation. $\gamma = (1 - (v/c)^2)^{-1/2}$ is the Lorentz factor, and it is about 1 in this case. In the cloud rest frame, the energy does not change in a collision. To go back to the laboratory frame, the energy after a collision $E\gamma(1 \pm v/c)$ is multiplied by $(1 \pm v/c)$ again. Then the energy of the cosmic ray shifts from E to $E \times (1 \pm v/c)^2 \sim 1 \pm 2v/c$ in a collision. Since the probability of collisions is proportional to the relative velocity between the cosmic ray and the cloud $(c \pm v)/(1 + v/c)$, the head-on collision is more frequent. The cosmic ray gains the energy by repeating collisions. The mean energy increment is aE, where $a = 2(v/c)^2$. This idea is called the second-order Fermi acceleration. In this process, the kinetic energy of the cloud accompanied by the magnetic field in the plasma and turbulence is converted to the energy of the cosmic ray. However, this process is inefficient and takes too much time to accelerate the cosmic rays to the observed energy.

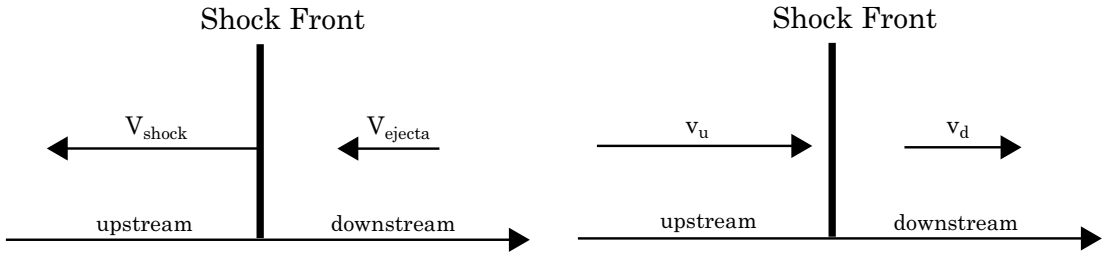

Figure 1.4: Schematic view of the shock front in the laboratory frame (left) and the shock's frame (right).

2.2 First-order Fermi Acceleration

It was about 30 years ago that the idea of the first-order Fermi acceleration in the SNR shock front appeared (Bell 1978; Blandford & Orstriker 1978). The first-order Fermi mechanism is the generally accepted model explaining the cosmic-ray acceleration. Suppose that there are two moving mediums with the different velocities of $v_{\rm d}$ and $v_{\rm u}$ ($v_{\rm u} > v_{\rm d}$). Such a situation is realized in the shock front of SNRs. Here the subscripts **u** and **d** denote the upstream and the downstream, respectively, as shown in Fig.1.4. The energy changes from E_0 into E_0' as

$$E_0' \simeq \gamma_{\rm d}^2 (1-\beta_{\rm d})^2 E_0, \tag{1.9}$$

where $\gamma_{\rm d} \equiv \sqrt{1-\beta_{\rm d}^2}$; $\beta_{\rm d} \equiv v_{\rm d}/c$ (c is the light speed). Conversely, the particle energy changes in the upstream by a scattering as

$$E_1 \simeq \gamma_{\rm u}^2 (1+\beta_{\rm u})^2 E_0' \simeq (1-2\beta_{\rm d})(1+2\beta_{\rm u}) E_0, \tag{1.10}$$

where we assume $\gamma_{\rm u} \simeq 1$, $\gamma_{\rm d} \simeq 1$, and $\beta_{\rm d} \ll 1$, $\beta_{\rm u} \ll 1$, which indicates that the shock speed is nonrelativistic. Since $\beta_{\rm u}$ is larger than $\beta_{\rm d}$, particles obtain the energy from the shock fluid during each round-trip between the two regions. The scattering occurs through the interactions between charged particles and the magnetic field, not through the Coulomb collisions. In the case of the three-dimensional treatments, particles are scattered in various directions, and then Eq.(1.10) should be somewhat modified. The mean energy of the particle after n round-trips is given as (Bell 1978)

$$E_n = E_0 \cdot \exp\left(\frac{4}{3} n(\beta_{\rm u} - \beta_{\rm d})\right). \tag{1.11}$$

Bell (1978) calculated the probability ($\equiv \eta_{\rm s}$) that a scattered particle escapes from

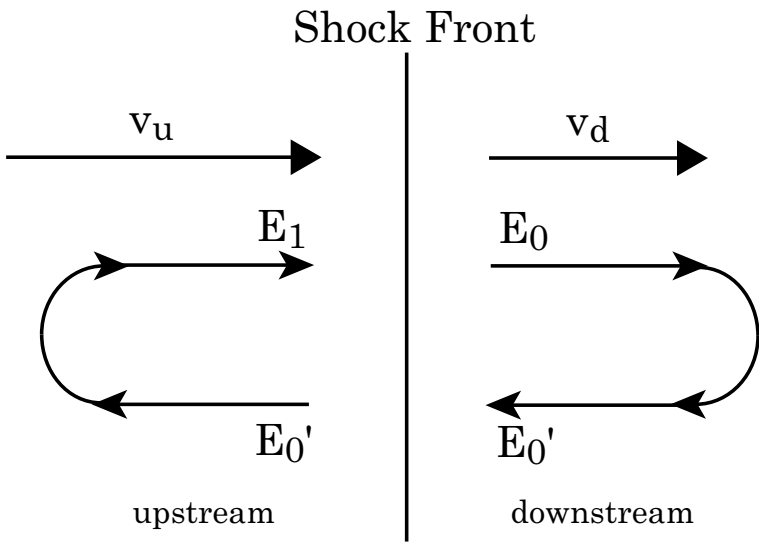

Figure 1.5: Schematic view of the Fermi acceleration.

the acceleration region for each round-trip as

$$\eta_{\rm s} = 4\,\frac{v_{\rm d}}{v_{\rm p}}, \tag{1.12}$$

where $v_{\rm p}$ is a particle velocity. Hence the probability that a particle makes n round-trips is given as

$$P_n = (1-\eta_{\rm s})^n = (1-4\beta_{\rm d})^n. \tag{1.13}$$

Here we assumed the particle is relativistic ($v_{\rm p} = c$). Using Eq.(1.13), the differential energy spectrum of accelerated particles is derived as

$$N(E) \propto \frac{dP_n}{dE_n} \propto E^{-\frac{\beta_{\rm u}+2\beta_{\rm d}}{\beta_{\rm u}-\beta_{\rm d}}}. \tag{1.14}$$

From the conservations of the mass, energy, and momentum, we can obtain the relation of $\beta_{\rm d} = \beta_{\rm u}/4$ for the ideal gas of monoatomic molecules in the strong shock wave, then,

$$N(E) \propto E^{-2}. \tag{1.15}$$

Equation (1.14) is important on the point that the energy index is independent of the shock speed, but depends only on the rate of the shock to pre-shock speeds.

§ 3 Emission Mechanisms of TeV Gamma-Rays from Supernova Remnants

3.1 π^0 decay

Nuclei with the energy higer than about 1 GeV sometimes collide with another nuclei, as

$$p + p \rightarrow \pi^{\pm} + \text{anything},$$

or

$$p + p \rightarrow \pi^0 + \text{anything } (\ \pi^0 \rightarrow 2\gamma\ ).$$

The produced π^0 mesons decay into two gamma-rays with a lifetime of $8.3 \times 10^{-16} \gamma_\pi$ sec, where γ_π is the Lorentz factor of the π^0 meson In the rest frame of the π^0 meson, each of the two gamma-rays takes the half of the rest energy of the π^0 ($\sim$134 MeV). Thus, in the laboratory frame, the distribution of the energy of the gamma-rays produced in the π^0 decay is symmetric with respect to the half energy of the rest energy of the π^0, $\sim$70 MeV. The symmetric point does not depend on the energy of the parent π^0 particle. The higher energy a parent π^0 has, the broader the energy distribution of the produced gamma-rays becomes.

In the astronomical phenomena, the nucleus which causes this interaction is mainly the proton, and the site is for example the molecular clouds, which is rich in the target protons.

3.2 Synchrotron Radiation

Charged particles running in the magnetic field are accelerated by the Lorentz force and then radiate. When the particles are extremely relativistic, the frequancy spectrum can extend to many times higher than the gyration frequency. This radiation is known as the synchrotron radiation.

The following is a simple estimation of the total emission power of the electron (Oda et al. 1989; Rybicki & Lightman 1979). The motion of a particle of mass m and charge e in a magnetic field $\boldsymbol{B}$ (without electric field, i.e., $\boldsymbol{E} = 0$) is described using the equations for relative particles as

$$\frac{d}{dt}(\gamma m \boldsymbol{v}) = \frac{e}{c}\boldsymbol{v} \times \boldsymbol{B} \tag{1.16}$$

$$\frac{d}{dt}(\gamma m c^2) = e\boldsymbol{v} \cdot \boldsymbol{B} = 0. \tag{1.17}$$

This last equation implies that γ = constant or that v = constant. Therefore, it follows

$$m\gamma\frac{d\boldsymbol{v}}{dt} = \frac{e}{c}\boldsymbol{v}\times\boldsymbol{B}. \tag{1.18}$$

Separating the velocity components along the field $v_{\|}$ and in a plane normal to the field $v_{\perp}$, we have

$$\frac{dv_{\|}}{dt} = 0 \tag{1.19}$$

$$\frac{dv_{\perp}}{dt} = \frac{e}{\gamma mc}v_{\perp}B. \tag{1.20}$$

Equation (1.19) indicates that $v_{\|}$ = constant. Since the total velocity v = constant, also $v_{\perp}$ = constant from Eq.(1.20). The solution to this equation is clearly uniform circular motion of the projected on the normal plane, since the acceleration in this plane is normal to the velocity and constant in magnitude. The combination of this circular motion and the uniform motion along the field is a helical motion of the particle. The frequency of the rotation, or gyration, is

$$\omega_B = \frac{qB}{\gamma mc}. \tag{1.21}$$

The acceleration is perpendicular to the velocity, with magnitude

$$a = a_{\perp} = \omega_B v_{\perp}, \tag{1.22}$$

so that the total emitted radiation in the laboratory frame $P_{\rm synch}$ is

$$\begin{aligned} P_{\rm synch} &= \frac{2e^2}{3c^3}(\gamma^2 a)^2 \\ &= \frac{2e^2}{3c^3}\gamma^4\left(\frac{eB}{\gamma mc}v_{\perp}\right)^2, \end{aligned} \tag{1.23}$$

or using $\beta_{\perp} = v_{\perp}/c$,

$$P_{\rm synch} = \frac{2}{3}\left(\frac{e}{mc^2}\right)^2 c\gamma^2\beta_{\perp}^2 B^2. \tag{1.24}$$

For an isotropic distribution of the velocities, it is necessary to average this formula over all angles for a given speedβ. Let α be the *pitch angle*, which is the angle between the magnetic field $\boldsymbol{B}$ and the velocity $\boldsymbol{v}$. Then we obtain

$$< \beta_{\perp} >= \frac{\beta^2}{4\pi}\int \sin^2\alpha d\Omega = \frac{2\beta^2}{3}, \tag{1.25}$$

and the result

$$P_{\rm synch} = \left(\frac{2}{3}\right)^2\left(\frac{e}{mc^2}\right)^2 c\gamma^2\beta^2 B^2, \tag{1.26}$$

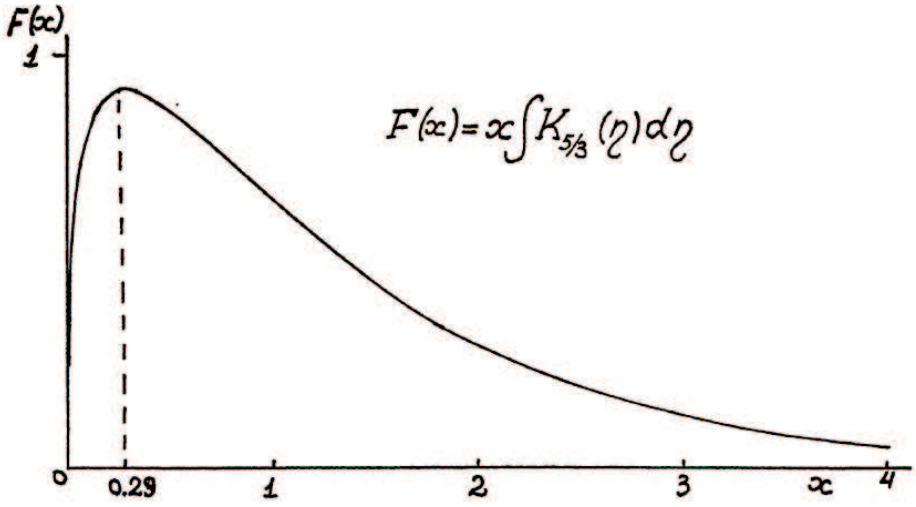

Figure 1.6: Spectral distrubution of the power of the total (over all directions) radiation from charged particles moving in a magnetic field (Ginzburg & Syrovatskii 1965). Here $x = \nu/\nu_c$ and $\nu_c = 3eB\gamma^2/4\pi mc$.

which may be written

$$P_{\rm synch} = \frac{4}{3}\sigma_{\rm T} c\gamma^2\beta^2 U_B. \tag{1.27}$$

Here $\sigma_{\rm T} = (8\pi/3)\cdot(e^2/mc^2)^2$ is the Thomson cross section, and $U_B = B^2/8\pi$ is the magnetic energy density.

Synchrotron radiation is important only for electrons because $P_{\rm synch}(\propto \sigma_{\rm T})$ is proportional to $1/m^2$ from Eq.(1.26). The frequency spectrum of the synchrotron radiation can extend to many times the gyration frequency. Figure 1.6 shows the spectral distribution of the power of the total (over all directions) radiation from charged particles moving through a magnetic field as a function of $x = \nu/\nu_c$ (Ginzburg & Syrovatskii 1965), where ν is the frequency of the emitted photons and $\nu_c = 3eB\gamma^2/4\pi mc$. The spectrum has a roughly monochromatic peak at $x \simeq 0.29$.

3.3 Inverse Compton Scattering

When relativistic electrons collide with photons, the photons are scattered, and the scattered photons take the energy form the electron via inverse Compton (IC) scattering.

The quantities with and without primed notation represent those in the laboratory frame and the electron's rest frame, respectively. We define ϵ and ϵ_1 as

the incident and scattered photon energy in the laboratory frame, respectively. We consider the relation of the two physical quantities, i.e., the photon phase space distribution $n(p)$ and the density of the protons having the energy in the range $d\epsilon$. We note that $n(p)$ is Lorentz invariant. v and n are related by

$$v d\epsilon = n d^3p. \tag{1.28}$$

d^3p transforms in the same way as energy under Lorentz transformations:

$$\epsilon = \gamma\epsilon' \tag{1.29}$$

$$d^3p = \gamma d^3p'. \tag{1.30}$$

Thus $vd\epsilon/\epsilon$ is a Lorentz invariant:

$$\frac{vd\epsilon}{\epsilon} = \frac{nd^3p}{\epsilon} = \frac{\gamma n d^3p'}{\gamma\epsilon'} = \frac{v'd\epsilon'}{\epsilon'}. \tag{1.31}$$

The total power emitted (i.e., scattered) in the electron's rest frame can be found from

$$\frac{dE_1'}{dt'} = c\sigma_{\rm T}\int \epsilon_1' v' d\epsilon', \tag{1.32}$$

where $v'd\epsilon'$ is the number density of incident photons. We now assume that the change in energy of the photon in the rest frame is negligible compared to the energy change in the laboratory frame, $\gamma^2 - 1 \gg \epsilon/mc^2$; thus we can equate $\epsilon_1' = \epsilon'$. We also know

$$\frac{dE_1}{dt} = \frac{\gamma dE_1'}{\gamma dt'} = \frac{dE_1'}{dt'}. \tag{1.33}$$

From Eqs.(1.32) and (1.33),

$$\frac{dE_1}{dt} = c\sigma_t \int \epsilon'^2 \frac{v'd\epsilon'}{\epsilon'}. \tag{1.34}$$

Thus we have the result using Eq.(1.31)

$$\frac{dE_1}{dt} = c\sigma_{\rm T}\int \epsilon'^2 \frac{vd\epsilon}{\epsilon}. \tag{1.35}$$

In Eqs.(1.33) and (1.35) we have again made the assumption that $\gamma\epsilon \ll mc^2$, so that the Thomson cross section is applicable.

Since we have $\epsilon' = \epsilon\gamma(1 - \beta\cos\theta)$ from the Doppler shift formula, Eq.(1.35) becomes

$$\frac{dE_1}{dt} = c\sigma_{\rm T}\gamma^2 \int (1 - \beta\cos\theta)^2 \epsilon v d\epsilon, \tag{1.36}$$

which now referes solely to the quantities in the laboratory frame. For an isotropic distribution of the photons we have

$$< (1 - \beta \cos\theta)^2 >= 1 + \frac{1}{3}\beta^2, \tag{1.37}$$

since $< \cos\theta >= 0$ and $< \cos^2\theta >= 1/3$. Thus we obtain

$$\frac{dE_1}{dt} = c\sigma_{\rm T}\gamma^2 \left(1 + \frac{1}{3}\beta^2\right) U_{\rm ph}. \tag{1.38}$$

Here $U_{\rm ph}$ is the initial photon energy density:

$$U_{\rm ph} \equiv \int \epsilon v d\epsilon. \tag{1.39}$$

The rate of the total initial photon energy is

$$\frac{dE_1}{dt} = -c\sigma_{\rm T} \int \epsilon v d\epsilon = -\sigma_{\rm T} c U_{\rm ph}. \tag{1.40}$$

Thus the net power lost by the electron, and thereby converted into increased radiation, is

$$\frac{dE_{\rm rad}}{dt} = c\sigma_{\rm T} U_{\rm ph} \left[\gamma^2 \left(1 + \frac{1}{3}\beta^2\right) - 1\right]. \tag{1.41}$$

Since $\gamma^2 - 1 = \gamma^2\beta^2$, we finally have

$$P_{\rm IC} = \frac{dE_{\rm rad}}{dt} = \frac{4}{3}\sigma_{\rm T} c \gamma^2 \beta^2 U_{\rm ph}. \tag{1.42}$$

3.4 Bremsstrahlung

When charged particles are passing through the Coulomb field of the nucleus, photons are emitted. This is called bremsstrahlung. As described in Chapter 3-1.1 in detail, the cross section and the emitted power of bremsstrahlung are same as those of synchrotron radiation, and then it is proportional to $1/m^2$, where m is the rest mass of the charged particle. Therefore bremsstrahlung is effective only for electrons and is negligible for nuclei.

§ 4 Evolution of Supernova Remnants

On the explosion of a supernova, a large fraction of the mass of the progenitor ($M_{\rm e}$) is ejected to the interstellar space with the large velocity ($V_{\rm e}$), which produces a shock wave. The shock wave expands and sweeps up the ambient interstellar

medium. The condition of the evolution is determined by the ratio between $M_{\rm e}$ and swept-up mass $M_{\rm b}$. Since the ejecta has a large momentum, it expands into the interstellar gas with constant momentum. This is the free expansion phase. Then as the swept-up mass increases, the ejecta mass becomes negligible compared with the total mass in the SNR. At this stage, the SNR consists of both the swept up mass and the ejecta mass, and therefore the shock wave is gradually decelerated. In this condition, the expansion is adiabatic until radiative cooling becomes effective. This period is called the adiabatic phase, or the Sedov phase since Sedov (1959) introduced a self similarity solution to describe the evolution of SNRs in this phase. He described the expansion speed $v_{\rm s}$ as

$$v_{\rm s} \equiv \frac{dR_{\rm s}}{dt} = \frac{2}{5}\frac{R_{\rm s}}{t}, \tag{1.43}$$

where $R_{\rm s}$ is the shock radius. After the shock velocity is decelerated down to about 200 km s^{-1}, the radiative cooling becomes sigmificant as shown in Fig.1.7. This effect has a large impact on the dynamics of the SNRs. The density behind the shock front is high, hence the time scale of the radiative cooling becomes small. Thus, a cool and dense shell is formed. In this phase, the significant fraction of the total energy has already been lost.

4.1 Shift from Free Expansion Phase to Adiabatic Phase

We define the radius $R_{\rm S}$ and the time $t_{\rm S}$ when the free expansion phase shifts to the adiabatic one. At this stage, the progenitor mass $M_{\rm e}$ and the swept-up mass $M_{\rm b}$ are written as

$$M_{\rm e} = M_{\rm b} = \frac{4\pi}{3} R_{\rm S}^3 \rho_0, \tag{1.44}$$

where ρ_0 is the interstellar density. While $R < R_{\rm S}$, the evolution is in the free expansion phase, and the expansion at the time t follows $R = V_{\rm e} t$ ($V_{\rm e}$ is the progenitor velocity). Then $t_{\rm S}$ is determined by

$$t_{\rm S} = \frac{R_{\rm S}}{V_{\rm e}}. \tag{1.45}$$

With the number density and the mass of H (n_0 and $m_{\rm H}$), and those of He ($n_{\rm He}$ and $m_{\rm He}$), the interstellar mass density ρ_0 is written approximately as

$$\begin{aligned} \rho_0 &= m_{\rm H} n_0 + m_{\rm He} n_{\rm He} \\ &= 1.4 m_{\rm H} n_0. \end{aligned} \tag{1.46}$$

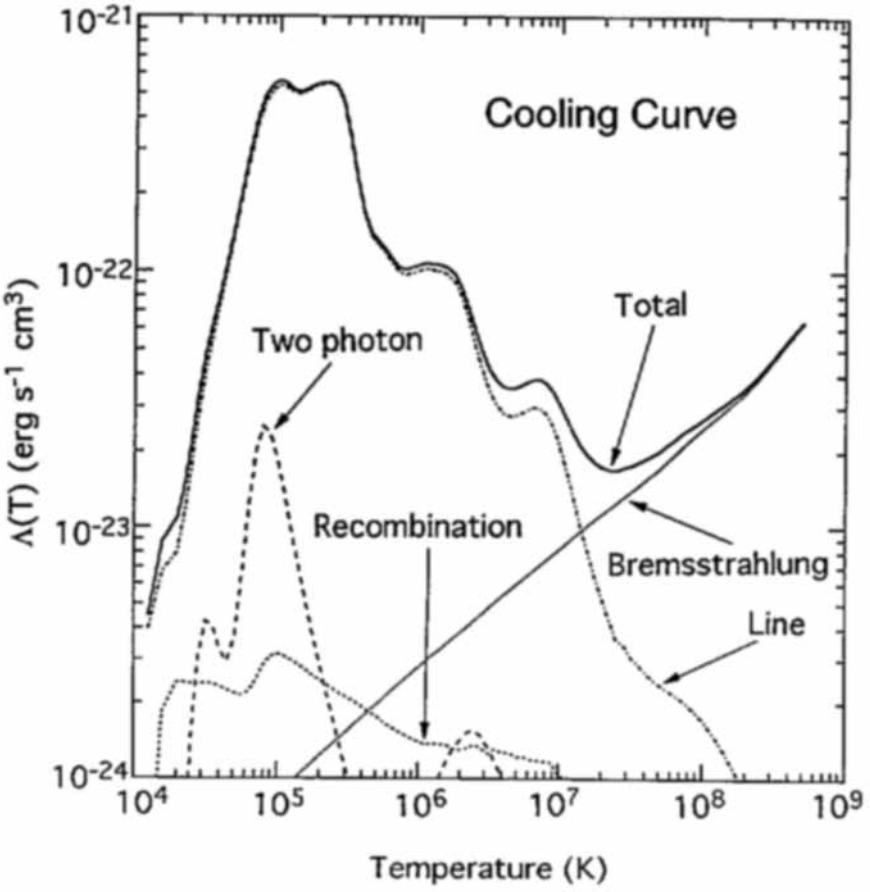

Figure 1.7: Temperature dependence of the cooling coefficient and its components for an optically thin plasma of cosmic abundance (Allen 1973; Gehrels & Williams 1993).

Here we assumed the typical value of $n_{\rm He}/n_0 = 0.1$. From Eqs.(1.44) and (1.45), $R_{\rm S}$ and $t_{\rm S}$ are derived to be

$$R_{\rm S}\ [{\rm pc}] = 1.9 \times \left(\frac{M_{\rm e}}{M_\odot}\right)^{1/3} (n_0\ [{\rm cm}^{-3}])^{-1/3} \tag{1.47}$$

$$t_{\rm S}\ [{\rm yr}] = 1.8 \times 10^6 \times (V_e\ [{\rm km\ s}^{-1}])^{-1} \left(\frac{M_{\rm e}}{M_\odot}\right)^{1/3} (n_0\ [{\rm cm}^{-3}])^{-1/3}. \tag{1.48}$$

4.2 Age and Maximum Acceleration Energy

The standard shock acceleration model is based on the first-order Fermi acceleration and the diffusion theory. The acceleration time in a shock front from a momentum $p_{\rm i}$ to $p_{\rm e}$ is

$$\tau_{\rm acc} = \frac{3}{v_{\rm u} - v_{\rm d}} \int_{p_{\rm i}}^{p_{\rm e}} \left(\frac{k_{\rm u}(p')}{v_{\rm u}} - \frac{k_{\rm d}(p')}{v_{\rm d}}\right) \frac{dp'}{p'}, \tag{1.49}$$

where k and v are the diffusion coefficient and the shock velocity, respectively (Drury 1983). The subscripts **u** and **d** respectively indicate the upstream and the downstream. We assume the mean free path $r_{\rm m}$ to be $\eta r_{\rm g}$, where $r_{\rm g} = E/eB$ is a larmor radius, and η is a parameter to be determined by the observations which is larger than unity (Reynolds & Stephen1998). Then the diffusion coefficient k is

$$k = \frac{r_{\rm m} c}{3} = \frac{\eta E c}{3eB}, \tag{1.50}$$

where E, e, c and B are the energy and charge of a particle, the light speed, and the magnetic field. Assuming a strong shock: $k_{\rm u} = k_{\rm d}$, $v_{\rm u} = 4v_{\rm d}$ of relativistic particles, Eq.(1.49) becomes

$$\tau_{\rm acc} = \frac{20\eta c}{3eBv_{\rm u}^2} E. \tag{1.51}$$

In the real SNRs, the shock speed $v_{\rm u}$ is not constant but time-dipendent. When the SNR is in the free expansion phase, the mass of swept-up matter is still less than the ejecta mass. Therefore the contribution of the mass swept up in the free expansion phase will be much smaller than that of ejecta. For an old SNR, even if the acceleration in the free expansion phase is included, the maximum energy would not be affected very much since the free expansion phase continues shorter than the Sedov phase. Therefore we neglect the acceleration in the free expansion phase. In the adiabatic phase, the shock speed is given in Eq.(1.43). The maximum energy of the accelerated particles at t is

$$E_{\rm max1} = \int_{t_0}^{t} \frac{3eBv_{\rm u}(t')}{20\eta c} dt'$$

$$= 15.4 \left(\frac{B_{-6}}{\eta}\right) \left(\frac{E_{51} v_9}{n_0}\right)^{1/3} \left(1 - \left(\frac{t}{t_{\rm tr}}\right)^{-1/5}\right) \quad [\rm TeV], \tag{1.52}$$

where t_{tr}, v_9, E_{51} and n_0 are the on-set time of the SNR adiabatic phase, the free expansion speed in units of 10^9 cm s^{-1}, kinetic energy of SN explosion in units of 10^{51} erg, and the ambient density in the unit of cm^{-3}, respectively. The unit of B_{-6} is μG. We derived $t_{\rm tr}$ as $t_{\rm S}$ in Eq.(1.47). It is rewritten as

$$t_{\rm tr} \equiv 65.5 \left(\frac{v_9}{10^9\ [\rm cm\ s^{-1}]}\right)^{-5/3} \left(\frac{E_{51}}{n_0}\right)^{1/3} \quad [\rm year]. \tag{1.53}$$

From Eq.(1.52), we can see the upper limit of the maximum energy is

$$E_{\rm limit} = 15.4 \left(\frac{B_{-6}}{\eta}\right) \left(\frac{E_{51} v_9}{n_0}\right)^{1/3} \quad [\rm TeV]. \tag{1.54}$$

As the SNR gets older, the synchrotron loss becomes more significant and indispensable. From Eq.(1.27), the time scale of the synchrotron energy loss of an electron is

$$\tau_{\rm sync} \equiv \frac{E_{\rm e}}{P} = \frac{3\pi m_{\rm e}^2 c^3}{\sigma_{\rm T} E_{\rm e} B^2} \tag{1.55}$$

$$= 6.3 \times 10^6 \left(\frac{B}{1\ [\mu\rm G]}\right)^{-2} \left(\frac{E_{\rm e}}{1\ [\rm TeV]}\right)^{-1} \quad [\rm year], \tag{1.56}$$

where $E_{\rm e}$ and $m_{\rm e}$ are the energy and the mass of an electron, respectively. When $B \sim 10\mu$G and $E_{\rm e} = 100$ TeV, the time scale is ~ 1000 year, which is smaller than the SNR age, and it is smaller for a higher B and $E_{\rm e}$. Therefore the maximum energy of the electron is determined by the synchrotron loss, either when the SNR is old or when the magnetic field is strong. The possible maximum energy of electron is obtained from Eqs.(1.51) and (1.56) as

$$E_{\rm max2} = 6.7 \times 10^3 (\eta B)^{-1/2} \left(\frac{E_0}{n_0}\right)^{1/5} t^{-1} \quad [\rm TeV], \tag{1.57}$$

where the unit of t is year. The real maximum energy should be the smaller one among $E_{\rm max1}$ and $E_{\rm max2}$. Figure 1.8 shows the time dependence of the maiximum energy for the electrons.

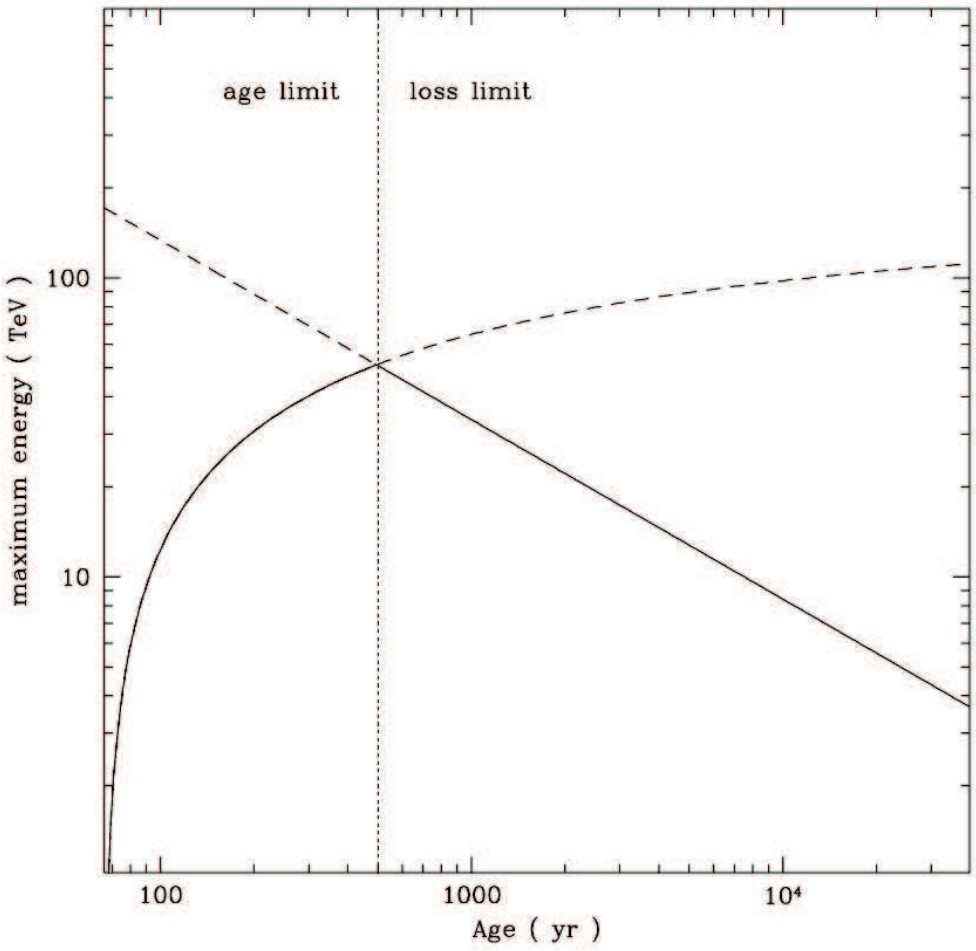

Figure 1.8: Time dependence of the maximum energy for electrons in the case of n=0.1, v_0=10^9 cm sec^{-1}, E_0=1, and η=1 (Tomida 2000). The curve shows Emax1, and the straight line shows $E_{\rm max2}$. The solid line indicate the effective one.

Chapter2

Supernova Remnant RX J0852.0−4622

§ 1 Discovery and Other Low Energy Observations

RX J0852.0−4622 (G266.2−1.2) is a young shell type supernova remnant (SNR) and it is one of a few SNR where the TeV-gamma-ray emissions were detected. RX J0852.0−4622 is located along the line sight to the southeast corner of the Vela SNR. It was discovered in the hard X-ray image by *ROSAT* all sky survey by Aschenbach (Aschenbach 1998), and the image is shown in Fig. 2.1. The observed X-ray emission of RX J0852.0−4622 extends over a roughly circular region with a diameter of 2° with brightening toward the north-western, western and southern part of the shell and toward the center. The CANGAROO-III (details in Chapter 3) telescopes' angular resolution of about 0°.15 and the field of view of 4° are suitable to unravel the gamma-ray morphology of extended sources like shell type SNRs.

The detection of the 1.157-MeV ^{44}Ti line was also reported with *COMPTEL* by Iyudin et al. (1998). The long-lived radioisotope ^{44}Ti is of considerable interest in astrophysics. ^{44}Ti decays to ^{44}Sc with the lifetime of ∼60 yr, emitting hard X-rays of 68 keV and 78 keV. ^{44}Sc subsequently decays to ^{44}Ca with a 3.9-h half-time, emitting a 1.157-MeV gamma-ray. Their schematic is shown in Fig.2.2. The 1.157 MeV line from this process is one of the probes of nucleosynthesis sites in the Galaxy, and it is probably the best indicator of young Galactic SNRs. ^{44}Ti is expected to be produced in each of the different types of supernovae (SNe), although with a large variance of abundances per type. The decay proceeds via electron capture, which means that its lifetime depends on the ionization stage, in particular on the degree of the population of the K shell. Hence ^{44}Ti's lifetime in SNRs could be larger, depending on the degree of the ionization of ^{44}Ti and its Lorentz factor (Iyudin

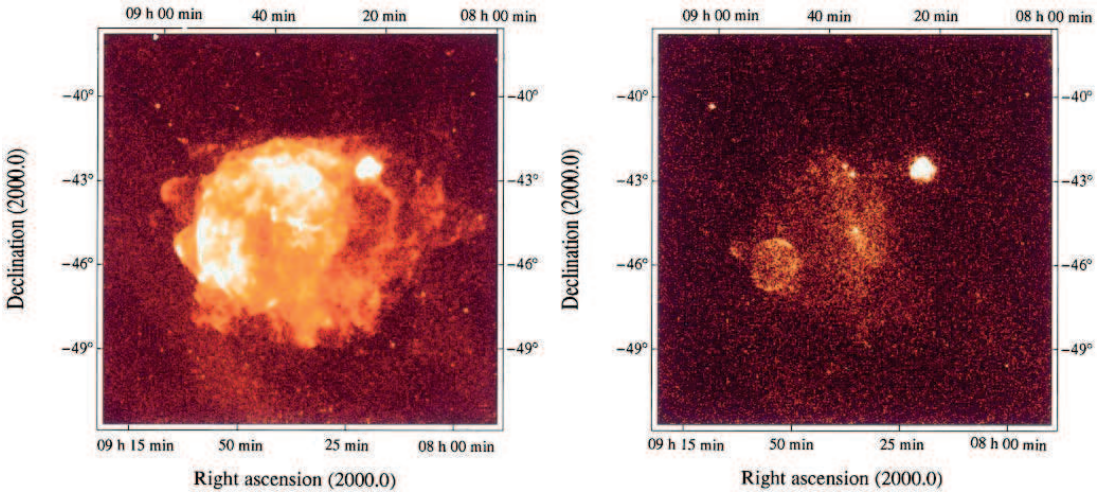

Figure 2.1: *ROSAT* all sky survey images of the Vela SNR and its surroundings. The left-hand image was taken for photon energies $0.1 < E < 2.4$ keV. The right-hand image is for photon energies > 1.3 keV. Most of the Vela SNR X-ray emission which dominates at low energies had disappeared. The very northwest (upper right) bright emission is from the Puppis-A SNR, which is seen in both images. The new shell type SNR RX J0852.0−4622 shows up in the lower left.

et al. 1998).

By combining the gamma-ray line flux and the X-ray diameter with the typical ^{44}Ti yield of $\sim 5 \times 10^{-5} M_{\odot}$ for supernovae of different types, and taking as a representative expansion velocity of ∼5000 km s^{-1} for the SN ejecta, the distance and age were estimated to be ∼200 pc and ∼680 yr, respectively (Iyudin et al. 1998). The question remains why it was not recorded historically in books despites this age of ∼680 yr. This SN explosion may have been seen in measurements of nitrate abundances in Antarctic ice cores (Burgess & Zuber 2000), since SNe can produce NO_3^- in the air of the earth when their radiations ionize the molecules in the atmosphere.

The X-ray emission line at 4.1± 0.2 keV, which was thought to come from highly ionized Ca, was detected by *ASCA* (Tsunemi et al. 2000) only in the northwestern shell of RX J0852.0−4622. Although the Ca isotopes cannot be distinguished, assuming that most of the Ca is ^{44}Ca, the age of RX J0852.0−4622 was estimated to be around 1000 yr by combining the amount of ^{44}Ca and the observed flux of the ^{44}Ti (Tsunemi et al. 2000). Aschenbach, Iyudin, and Schönfelder estimated the distance and age again (Aschenbach et al. 1999). They estimated the expansion velocity us-

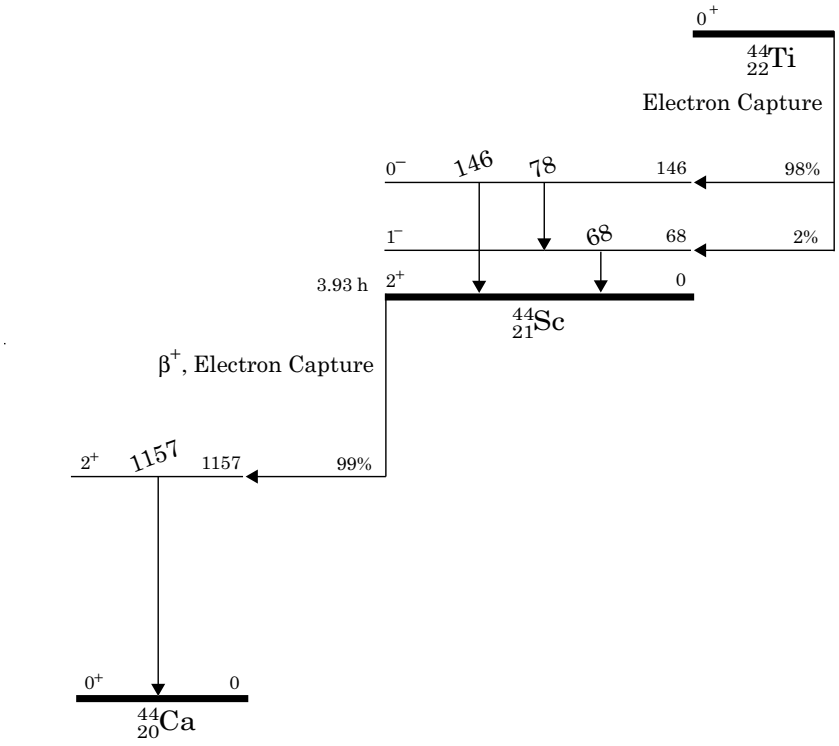

Figure 2.2: Relevant portion of the decay schemes of ^{44}Ti and ^{44}Sc. All energies are in keV. The 146-keV gamma-ray is very weak. Its intensity is approximately 0.1% of that of the 78-keV X-ray.

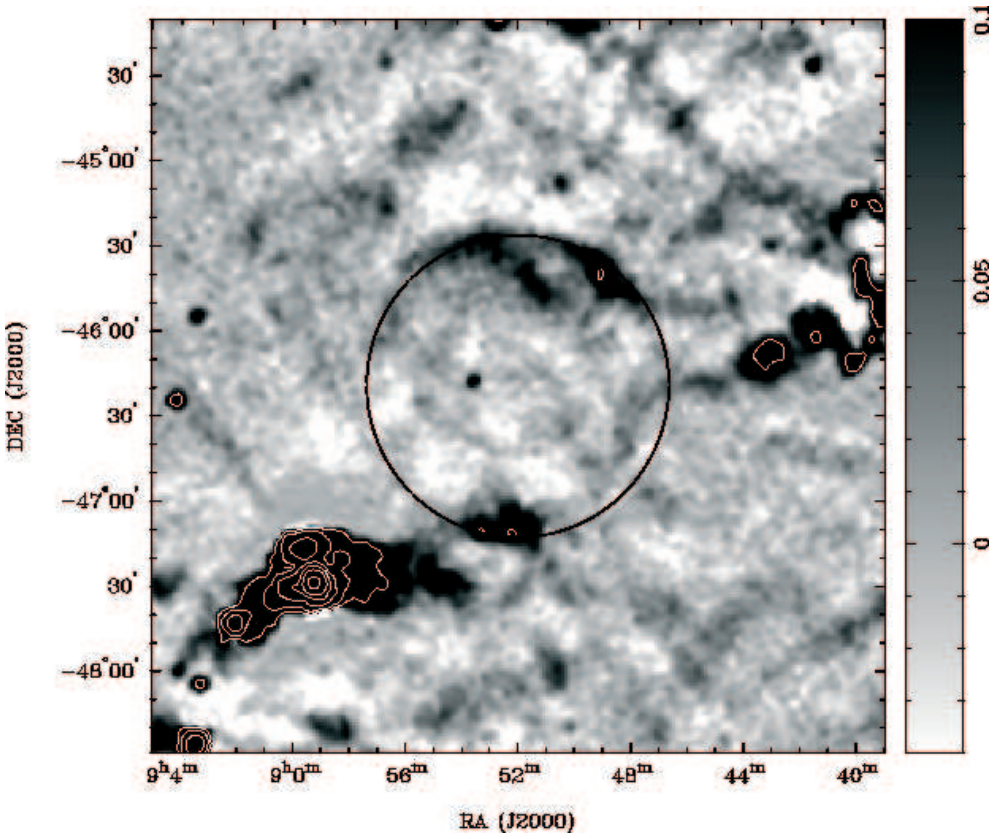

Figure 2.3: Image taken from the 4.85-GHz PMN survey, centered on the remnant RX J0852.0−4622. The angular resolution is $\simeq 5'$, and the rms noise is approximately 8 mJy beam-1. The gray-scale wedge is labeled in units of Jy beam-1. The white contours denote intensities of: 0.2, 0.8, 3.0, 10, 30 and 80 Jy beam-1. The black circle is centered on the X-ray coordinates of the source and is in angular diameter (Duncan & Green 2000).

ing X-ray spectra at the rim obtained by *ROSAT*. The minimal, best-estimate, and maximal velocities of expansion were 2000, 5000 and 10000 km s^{-1}, respectively. Model calculations provide a range for the mass yield of ^{44}Ti. Considering these uncertainties, the upper limit of the distance of RX J0852.0−4622 was estimated 500 pc and that of the age, 1100 yr. Chen & Gehrels (1999) have also used the X-ray temperature obtained from *ROSAT* data for the central region and derived a range of 2000-5000 km s^{-1}. If this is true, this SNR is currently expanding too slowly to consider it derived by a type-Ia-SN. However the estimate by Aschenbach, Iyudin and Schönfelder, allow it to be a type Ia SNR for the expansion speed.

Slane et al. (2001) found that the X-ray spectrum of this SNR is featureless and

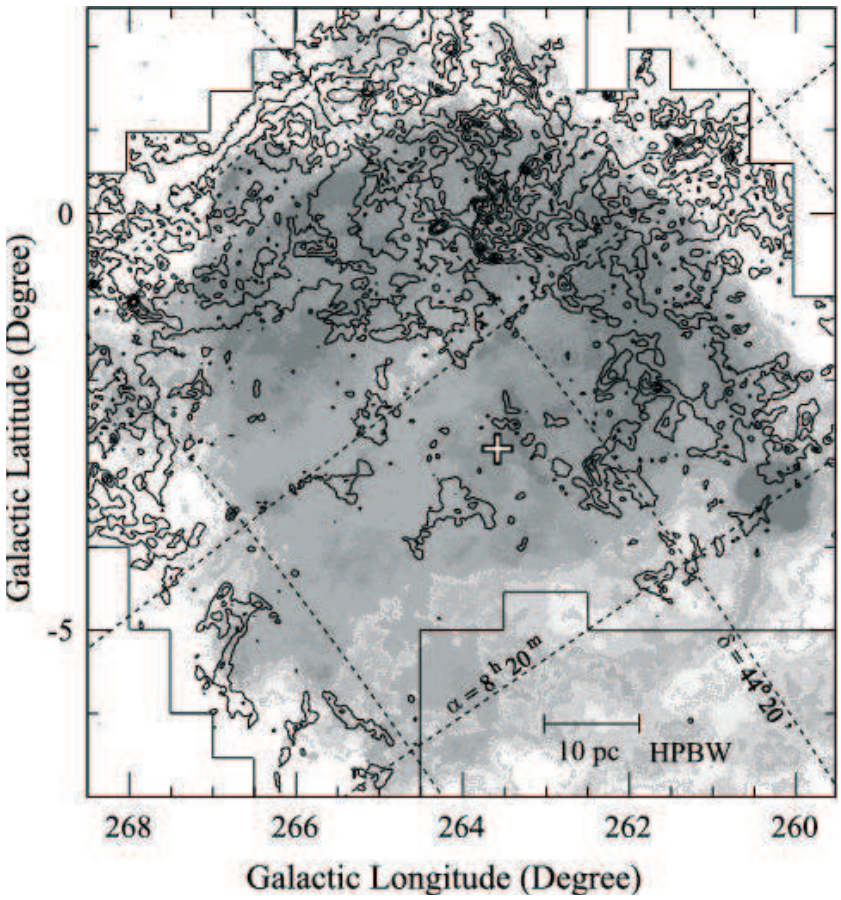

Figure 2.4: Integrated intensity map of CO obtained with *NANTEN* 4m millimeter radio telescope (contour) and the soft X-ray image by *ROSAT* (gray scale) (Moriguchi et al. 2001). The cross indicates the position of the Vela pulsar. The center of RX J0852.0−4622 is at $(266^{\circ}.2, -1^{\circ}.2)$ in the galactic coordinate. The equatorial coordinates are indicated by the dashed lines.

well described by a power law using *ASCA* data. The best-fit spectrum parameters for each observation region (the northwestern rim, the northeastern rim, the western rim, and the center diffuse emission) are summarized in Table 2.1.

Table 2.1: X-ray spectral parameters

Region	kT (keV)	$N_{\rm H}$ ($\times 10^{21}$ cm^{-2})	Γ (photon)	F_x (ergs cm^{-2} s^{-1})
Northwestern rim	$0.5^{+0.2}_{-0.3}$	4.0 ± 1.8	2.6 ± 0.2	4.2×10^{-11}
Northeastern rim	0.6 ± 0.1	$5.3^{+0.2}_{-0.9}$	2.6 ± 0.2	2.9×10^{-11}
Western rim	$0.5^{+0.1}_{-0.2}$	$1.4^{+2.8}_{-1.4}$	2.5 ± 0.2	2.1×10^{-11}
Center	0.7 ± 0.1	$11.5^{+14.3}_{-10.2}$	$2.0^{+0.6}_{-0.3}$	6.7×10^{-12}

The radio emission was found with the Parkes radio-telescope (Combi et al. 1999; Duncan & Green 2000). The fluxes at 2.42 and 1.40 GHz were 33 ± 6 Jy and 44 ± 10 Jy, respectively (Duncan & Green 2000). The spectral index were -0.40 ± 0.15 at the northern section of the shell (Duncan & Green 2000), and the 4.85 GHz radio image is shown in Fig. 2.3. A shell-like morphology can be seen, although the confusing structures from Vela SNR exist. CO observations showed the richness of large molecular clouds around RX J0852.0−4622 in the Vela Molecular ridge (May et al. 1988). The detailed morphology was mapped with the *NANTEN* 4m milli-meter radio telescope (Moriguchi et al. 2001). Figure 2.4 shows the CO map around the Vela SNR. CO observations has a better accuracy to determine the distance than 21 cm radio observations because of their narrow Doppler broadening. The correlation between RX J0852.0−4622 and the molecular clouds were not yet investigated. From above observations, the characteristics of RX J0852.0−4622 are similar to those of RX J1713.0−3946. Since molecular clouds can be targets of proton-nucleon collisions, if those which are seen around RX J0852.0−4622 is actually located adjacent to the SNR, TeV gamma-rays from π^0 decay produced by proton-nucleon collisions may be detected. On the other hand, considering that the existence of $\sim$100 TeV electrons are expected from the synchrotron radio and X-ray emission, TeV gamma-rays from inverse Compton scattering should be also produced. Whether they are detected or not depends on the magnitude of the ambient magnetic field.

§ 2 Age, Distance, and Origin

Various methods of the age and distance estimate for SNRs are known, and some of them are described in the previous section. However we do not yet have a conclusive answer of the age and the distance of RX J0852.0−4622. Moreover, since each estimate method is accompanied by some assumptions, the derived values have some uncertainty. Besides the above-mentioned example with the ^{44}Ti and/or Ca line, some authors tried to estimate the age and the distance of RX J0852.0−4622.

Bamba et al. (2005a) observed the edges of historical SNRs' shells with *Chandra* and studied the filamentary structures systematically. They derived a new method for the estimate of the age of an SNR. They introduced the empirical function, $\mathcal{B} = \nu_{\rm rolloff}/w_{\rm d}^2$, which decreases with the age of an SNR ($\mathcal{B}$-age relation). Here $w_{\rm d}$ is the scale width of the filamentary structure on the SNR's downstream side. $\nu_{\rm rolloff}$ is the best-fit rolloff frequency of the synchrotron X-rays. The rolloff frequency is related to the cutoff electron energy $E_{\rm max}$ via the relation

$$\nu_{\rm rolloff} \approx 0.5 \times 10^{16} \left(\frac{B}{10\ \mu G}\right) \left(\frac{E_{\rm max}}{10\ TeV}\right)^2. \tag{2.1}$$

They also observed the northwestern rim of RX J0852.0−4622 with *Chandra*, and found the filamentary structure of the nonthermal X-rays as shown in Fig. 2.7. Then they estimated the age and the distance from the $\mathcal{B}$-age relation as 660 (420-1400) yr and 330 (260-500) pc. They also derived the most preferable values $E_{\rm max} \sim 3$ TeV and $B_{\rm d} \sim 500\ \mu$G.

Slane et al. (2001) estimated via more simple and conventional way, the age with the assumption of a free-expansion phase or a Sedov phase, and the distance using the column density. They observed this SNR by *ASCA* GIS (Slane et al. 2001). The images clearly confirmed the shell-like structure as shown in Fig. 2.5. The hard X-ray spectrum was well fitted by a power law. The matter density of the X-ray intensity maximum was estimated to

$$2.9 \times 10^{-2} \frac{1}{d}^{-1/2} f^{-1/2} [{\rm H/cm^{-3}}], \tag{2.2}$$

where f is the filling factor of a sphere taken as the emitting volume in the region extracted. This means that the column density for this remnant is larger than that for Vela, which indicates that RX J0852.0−4622 is at a larger distance than Vela. The distance to the Vela SNR is estimated to be 250±30 pc using Ca II and Na I absorption line spectra toward the OB stars in the direction of Vela SNR

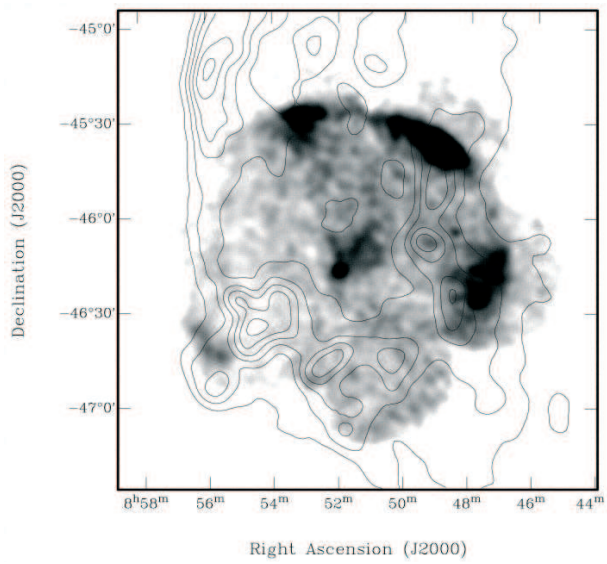

Figure 2.5: *ASCA* GIS image of RX J0852.0−4622 (E=0.7-10 keV). Contours represent the outline of the Vela SNR as seen in *ROSAT* survey data (Slane et al. 2001).

(Cha & Sembach 2000). The distances to the OB stars were well determined using trigonometric and spectroscopic parallaxes based on photometric colors and spectral types. They associated the origin of RX J0852.0−4622 with the star formation region located at a distance of 1-2 kpc. They developed this idea of the origin to the suggestion of a massive progenitor for RX J0853.0−4622, from which one could expect a relic neutron star.

In order to solve the problem on the origin, deep X-ray observations was made with the satellites of *ASCA*, *Chandra*, and *BeppoSAX*. They revealed a compact source in the central region of RX J0852.0−4622: AX J0851.9−4617.4 or CXOU J085201.4−461753. The spectram of the source and the absence of the optical counter part (a very high X-ray-to-optical flux ratio) suggest that it should be a neutron star. Some authors searched for pulsations but detected no obvious modulation of the flux. The association of this neutron star candidate with RX J0852.0−4622 supports that the progenitor of RX J0852.0−4622 is a core-collapse supernova.

However, by the *XMM-Newton* observations of RX J0852.0−4622, Iyudin et al. (2005) partially resolved the northwestern rim as shown in Fig. 2.6 and found the presence of an emission-line feature at 4.45±0.05 keV, which they suggest to be emission from Ti and Sc exited by atom/ion or ion/ion hi-velocity collisions. This discovery confirmed the existence and amount of Ti in the SNR claimed by

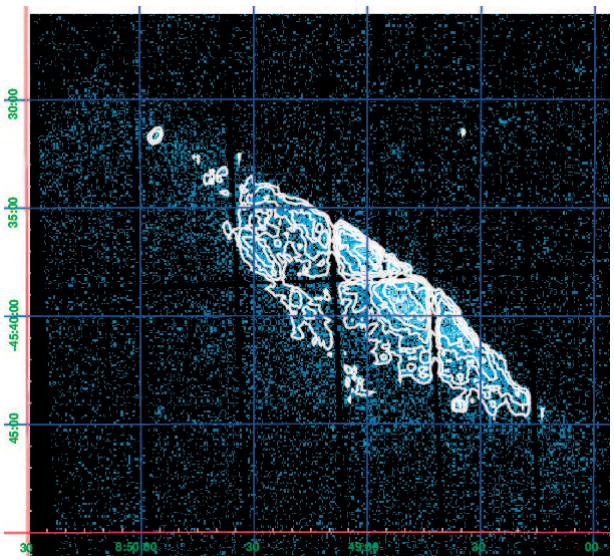

Figure 2.6: *XMM-Newton* image of the bright northwestern part of the RX J0852.0−4622 shell (Iyudin et al. 2005).

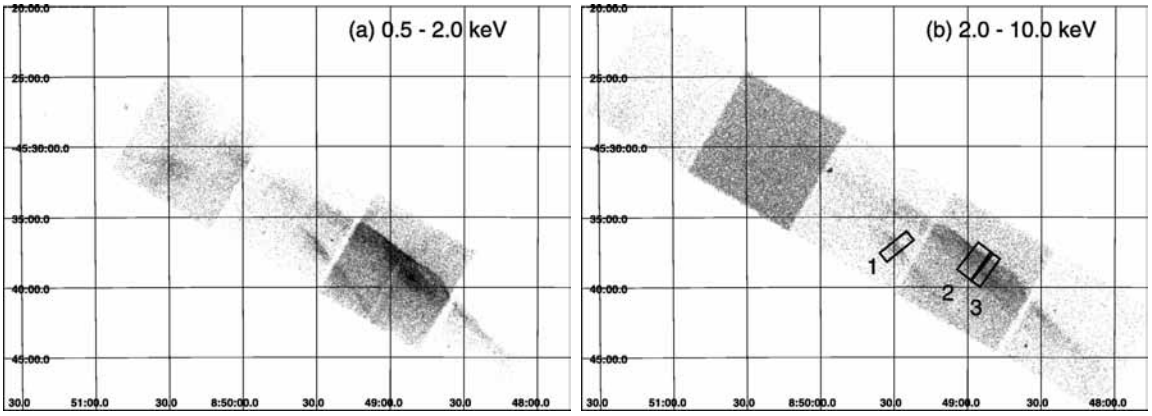

Figure 2.7: *Chandra* images of the northwest rim of RX J0852.0−4622 in (a) the 0.5-2.0-keV band and (b) the 2.0-10.0-keV band (Bamba et al. 2005b). Thin filament structures can be seen.

Iyudin et al. (1998). The high velocity is in agreement with the width of the 1.157 MeV gamma-ray line (Iyudin et al. 1998). Iyudin et al. suggested that this very-large broadening would indicate a large velocity of the emitting matter of $\sim$15000 km s^{-1}. Such high ejecta velocity for Ti is found only in explosion models of sub-Chandrasekhar type Ia SNe.

Now, the questions are still remaining what the nature and the origin of the central compact source CXOU J085201.4−461753 are and why the absorption column density apparently associated with RX J0852.0−4622 is much greater than the typical column for the Vela SNR.

Most recently, Reynoso et al. (Reynoso et al. 2006) observed the center of RX J0852.0−4622 with the Australia Telescope Compact Array at 13 and 20 cm. They searched the existence of a pulsar wind nebula (PWN) associated with the point X-ray source CXOU J085201.4−461753, which would strongly support the suggestion that CXOU J085201.4−461753 is a neutron star. However they found no evidence of the presence of a PWN, but found a radio source which could be explained as a planetary nebula. They concluded that CXOU J085201.4−461753 is more likely to be related to this radio source rather than to RX J0852.0−4622.

§ 3 Gamma-Ray Observations

Shell-type SNRs with nonthermal X-ray emission are prime candidates for the object accelerating cosmic rays up to the knee energies (Koyama et al. 1995; Koyama et al. 1997; Völk et al. 2005). Their detection in very high-energy (VHE) gamma-rays is expected to be possible with modern atmospheric Čerenkov telescopes, and to provide insight into the underlying acceleration mechanisms. Up till recently, only one of these SNRs, RX J1713.7−3946, was detected by two independent experiments (Muraishi et al. 2000; Enomoto et al. 2002a; Aharonian et al. 2004a) employing the imaging atmospheric Čerenkov technique. Last year in 2005, the detection of gamma-ray emission from the RX J0852.0−4622 SNR was reported by the CANGAROO (Katagiri, et al. 2005) and the HESS collaboration (Aharonian et al. 2005b).

First, the gamma-ray emission from the northwestern corner of RX J0852.0−4622 was discovered by the CANGAROO-II single telescope (Katagiri et al. 2005). The emission mechanism was discussed and the obtained spectrum was explained in terms of interactions of accelerated protons with the ambient gas (details on the

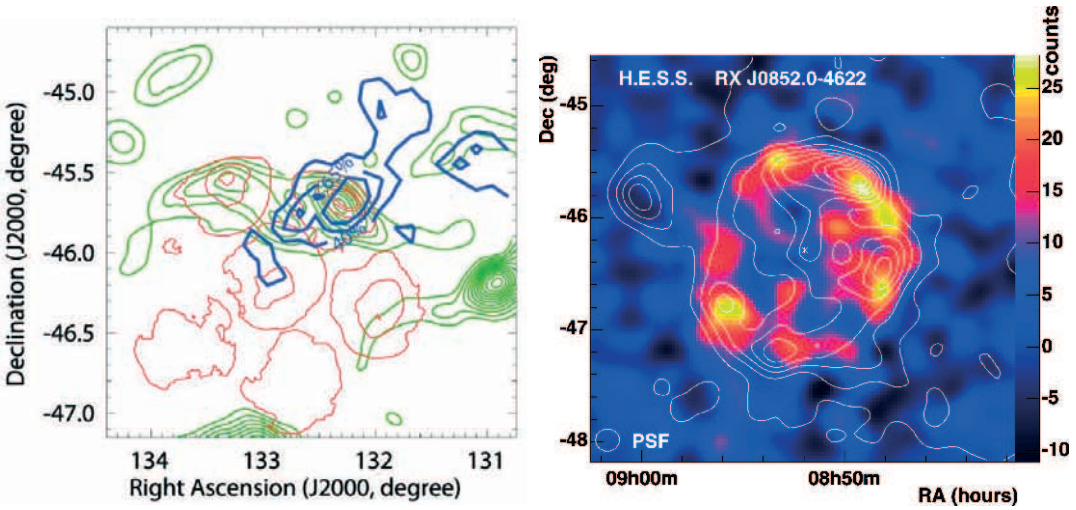

Figure 2.8: Results from two Čerenkov telescope groups. Left: Emission significance map of the NW rim of RX J0852.0−4622 by the CANGAROO-II single telescope observation (blue contours) with the X-ray data by *ASCA* GIS (red) and the 4.85 GHz radio data (green) (Katagiri et al. 2005). Right: Count map of gamma-rays from the direction of RX J0852.0−4622 reported by the HESS stereoscopic observation. The lines are the contours of X-ray data from the *ROSAT* all sky survey (above 1.3 keV) (Aharonian et al. 2005b).

emission mechanisms are in Chapter 1-§ 3). By the HESS group with their stereoscopic observations, it was spatially resolved at TeV energies for the whole shell with data of 3.2 h of livetime (Aharonian et al. 2005b). The spectrum in the energy range between 500 GeV and 15 TeV is well described by a power law. The detailed results are discussed in Chapter 8.

Chapter3

Imaging Air Čerenkov Technique

Our target particle is so-called "very high-energy (VHE)" gamma-rays, whose energies are from several hundreds GeV to several tens TeV. Because of their low flux, it is hardly possible to catch them using detectors on satellites or balloons which cannot have large effective detection areas, and thus, only ground-based detectors are feasible. These detectors are designed to catch secondary productions originated from the interaction between primary gamma-rays and atmospheric nuclei.

In this chapter, we mention about the both imaging air Čerenkov technique and the new observation method with a stereoscopic telescope system.

§ 1 Extensive Air Showers

An incident VHE particle interacts high up in the atmosphere with air molecules, and generates a huge number of secondary particles. These energetic secondaries also produce particles by collisions, and in repeating this process the number of particles increases rapidly like a cascade shower. Energies of the primary cosmic-rays are distributed to newly produced secondaries until the energy of the secondaries reaches the interaction's critical energy $E_{\rm c}$ (see below). Evolutions of the shower both in the longitudinal and transverse directions and species of secondary particles depend on the type of the primary particle.

1.1 Electromagnetic Showers

When the energy of the gamma-ray exceeds $2m_{\rm e}c^2$, the pair creation is the dominant process among the interactions between gamma-rays and atmospheric nuclei:

$$\gamma + Z \rightarrow e^+e^- + \text{anything}. \tag{3.1}$$

This process can be occurred when a gamma-ray gives a small fraction of momentum to an atomic nucleus, and it continues until a single gamma-ray cannot produce an

e^+e^- pair due to the conservation law of energy and momentum. The cross section for the pair creation $\sigma_{\rm pair}$ in the sufficiently high energy region ($h\nu/m_{\rm e}c^2 \gg 1/\alpha Z$) is approximately given as:

$$\sigma_{\rm pair} = \alpha r_{\rm e}^2 Z^2 \left[\frac{28}{9}\ln\left(\frac{183}{Z^{\frac{1}{3}}}\right) - \frac{2}{27}\right] {\rm m}^2 \ {\rm atom}^{-1} \quad (3.2)$$

$$\sim \sigma_{\rm T} \quad (3.3)$$

$$r_{\rm e}\text{: classical electron radius} \quad (3.4)$$

$$\alpha\text{: fine structure function} = 1/137 \quad (3.5)$$

$$Z\text{: charge number of the nucleus} \quad (3.6)$$

$$\sigma_{\rm T}\text{: Thomson scattering cross section; } \frac{8}{3}\pi r_{\rm e}^2. \quad (3.7)$$

Since, in this energy region, the cross section is almost independent of the energy of the primary gamma-ray, the first interaction point does not depend on the primary energy as for electromagnetic showers. Electrons and positrons produced by the pair creation emit gamma-rays by the bremsstrahlung process in the air, and then the gamma-rays create electron-positron pairs and repeatedly forms a electromagnetic shower.

Longitudinal evolution Radiation length of the bremsstrahlung process ($\xi_{\rm brems}$) for a relativistic particle is given as:

$$\xi_{\rm brems} = \frac{7160 M_{\rm A}}{Z(Z+1.3)[\ln(183Z^{-\frac{1}{3}}) + \frac{1}{8}]} \ {\rm kg\ m^{-2}}, \quad (3.8)$$

$$M_{\rm A}\text{: atomic mass.} \quad (3.9)$$

That of the air is 36.5 g/cm^2. The mean free path of the inverse Compton process($\xi_{\rm pair}$) is given as

$$\xi_{\rm pair} = \rho/M_{\rm A}\sigma_{\rm pair} \approx \frac{7}{9}\xi_{\rm brems}, \quad (3.10)$$

where ρ is the density of the target atmospheric nuclei. By this relation of $\xi_{\rm pair} \approx \xi_{\rm brems}$, the longitudinal evolution of an electromagnetic shower is well characterized with this single parameter (Fig.3.1). The wavefront of secondary particles is also well flat like a "pancake". According to the energy conservation law, gamma-rays give about half energies to each of the electron and the positron, and then the electron and the positron give their energy to gamma-rays in a radiation length. Thus, at the depth of $n\xi$, the number of the

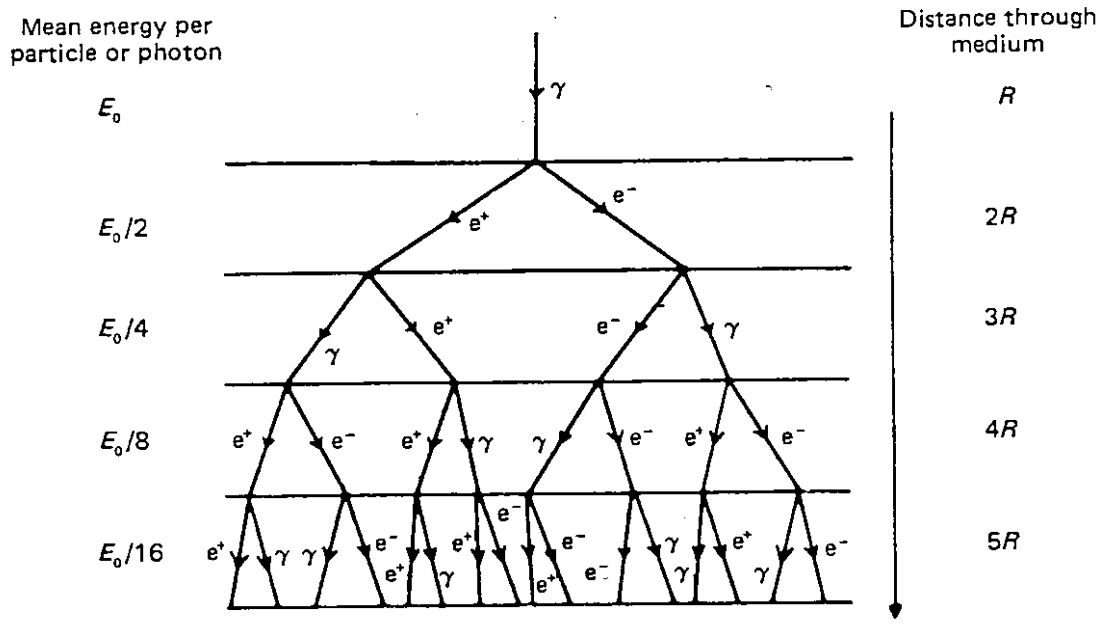

Figure 3.1: Schematic diagram of an electromagnetic cascade shower (Longair 1992).

produced particles increases to 2^n with the energy of $E_0/2^n$. About a third of them are gamma-rays and the rest is electrons and positrons. In repeating the energy division, the energy of electrons/positrons becomes lower than the critical energy E_c, where the cross section of the ionization loss exceeds that of bremsstrahlung, and the shower begins to decline. This critical energy E_C is given as

$$E_c \approx 800/(Z + 1.2) \text{ MeV}, \tag{3.11}$$

and is about 84 MeV for the air. Since the process mentioned above is also true for the primary cosmic-ray electrons, it is difficult to distinguish a gamma-ray primary or a cosmic-ray primary using the characteristics of its shower evolution.

1.2 Hadron Showers

Narrowly-defined "cosmic-rays" (high energy charged particles) also produce secondary-particle showers by the interaction with the atmospheric nuclei. Proton accounts for more than 90% of the atomic composition of cosmic-rays (Fig.1.2), and in a

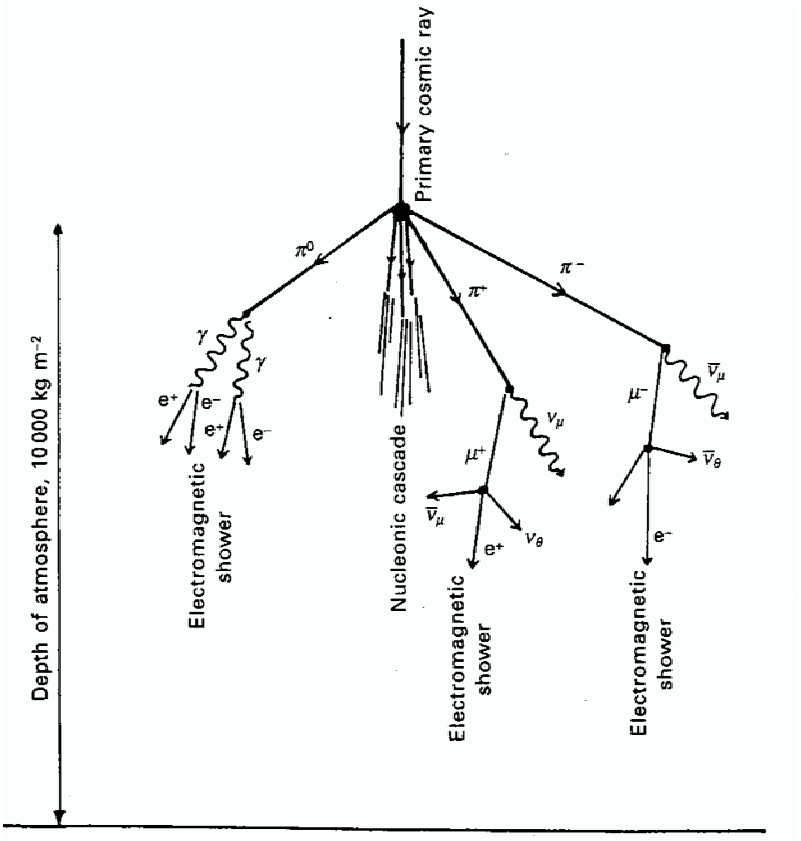

Figure 3.2: Schematic diagram of a nucleon cascade shower. (Longair 1992).

sufficiently high energy region, heavy atomic nuclei can be treated as a cluster of a single nucleon, therefore only proton is considered as a primary particle here.

The primary proton collides with atmospheric nuclei with the cross section approximately equal to the geometrical size, which gives the interaction length of $\sim$ 80 g/cm^2 in the air. The cross section of the pp collision is shown in Fig.3.3. It produces secondary particles such as nucleons(p, n), anti-nucleons($\overline{p}$, $\overline{n}$), neutral pions, charged pions and kaons. Secondary particles are continuously produced until their energies become less than the threshold energy of the pion production ("pionization" in nucleon cascade).

Longitudinal evolution Neutral pions are very short-lived, and immediately decay into two gamma-rays with the lifetime of $\tau = 8 \times 10^{-17}$ sec:

$$\pi^0 \rightarrow 2\gamma. \tag{3.12}$$

Those gamma-rays produce sub-electromagnetic showers. Charged pions also

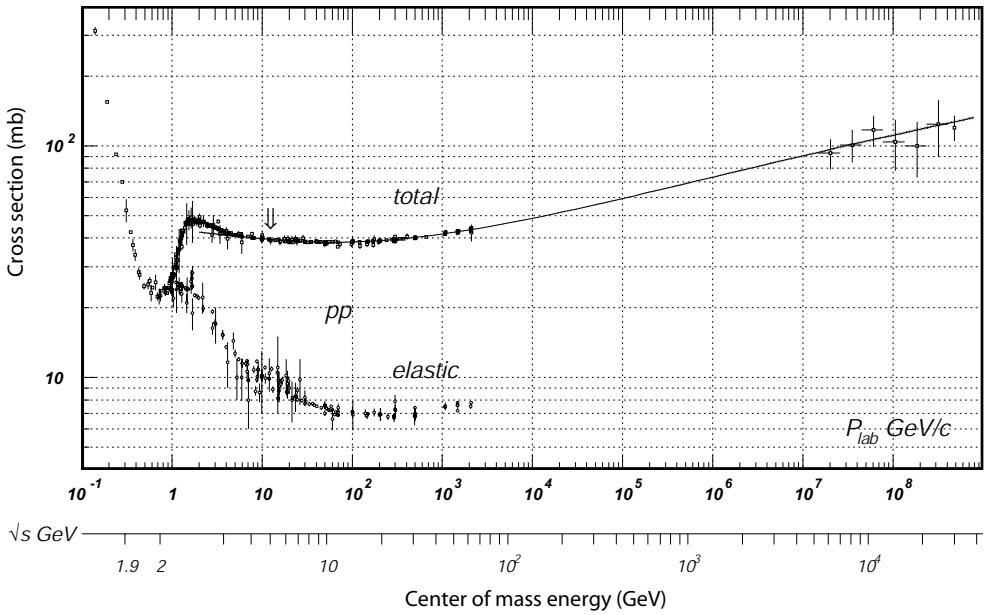

Figure 3.3: Total and elastic cross sections for pp collisions as a function of laboratory beam momentum and total center-of-mass energy (`http://pdg.lbl.gov/2006/hadronic-xsections/hadron.html`).

decay into muons and neutrinos in the hadron shower,

$$\pi^+ \to \mu^+ + \nu_\mu \tag{3.13}$$

$$\pi^- \to \mu^- + \overline{\nu}_\mu \tag{3.14}$$

with lifetime of $\tau = 2.5 \times 10^{-8}$ sec . Ratio of the number of the produced charged pions to the neutral is known to be about $2:1$. Muons also have a decay mode with the lifetime of $\tau = 2.2 \times 10^{-6}$ sec:

$$\mu^+ \to e^+ + \nu_e + \overline{\nu}_\mu \tag{3.15}$$

$$\mu^- \to e^- + \overline{\nu}_e + \nu_\mu. \tag{3.16}$$

However, since secondary muons do not experience strong interaction, many high energy muons ($\gamma > 20$) go to the ground with little energy loss due to ionization process before the decay.

A nucleon-primary shower consisting of many species of particles with various interaction length, and the longitudinal evolution is rather complicated (Fig.3.4).

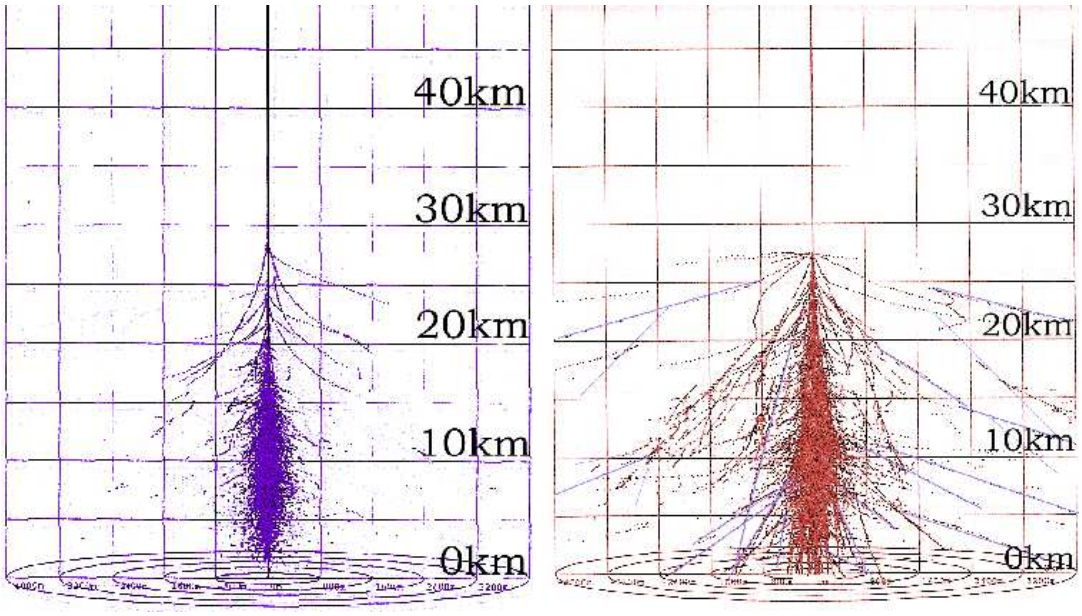

Figure 3.4: Development profiles of Monte Carlo simulated EASs from a 100 GeV gamma-ray (left) and 300 GeV proton (right).

§ 2 Čerenkov Radiation

Charged particles lose their energy in the form of photon when they travel faster than the light-speed in the medium, $c' = c/n$ (Čerenkov radiation). This phenomenon was explained as the polarization effect of the medium induced by the charged particles traveling in the medium.

When a charged particle of the velocity v emits photons, due to the conservation of their momentum and energy, the following relation should be satisfied:

$$\beta \cos\theta = \frac{1}{n,} \tag{3.17}$$

$$\beta = v/c, \tag{3.18}$$

$$n: \text{ atmospheric refraction index.} \tag{3.19}$$

Thus, Čerenkov photons are emitted in a certain angle $\theta = \cos^{-1}(1/n)$ from relativistic charged particles (Fig.3.5). This angle is called the Čerenkov angle and written as θ_c, hereafter. The atmospheric refraction index at the sea level is about n=1.000283, and the Čerenkov emission angle is 1°.36 for relativistic ($\beta \sim 1$) particles.

The number of the Čerenkov photons emitted while the particle travels a distance

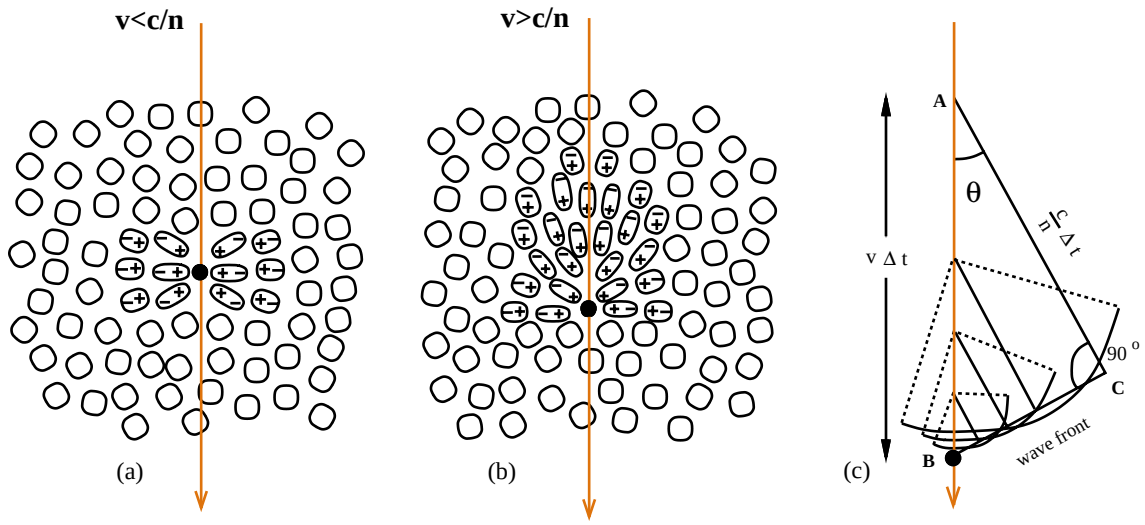

Figure 3.5: Polarization set up in a dielectric when a charged particle with (a)low energy, (b)high energy passes through, respectively. Huygens construction to illustrate coherence and to obtain the Čerenkov angle θ is shown in (c).

L in the medium is given as

$$dN = \frac{e^2}{\epsilon c^3 h}\left(1 - \frac{1}{n^2\beta^2}\right) L d\omega \propto \frac{1}{\lambda^2} d\lambda. \tag{3.20}$$

The amount of Čerenkov photons depends only on β, the velocity of the particle. Therefore the main emitter of the photons in the extensive air showers are light particles, i.e. electrons/positrons. Thus, the luminosity of the Čerenkov photons from the shower is well related to the production efficiency of electrons/positrons, and varies according to the mass of the primary particle. 1-TeV gamma-rays emit about three times as many Čerenkov photons as those emitted by protons of the same energy.

The distribution of the Čerenkov photons in an extensive air shower is determined by the particle shower profile, the atmospheric refraction index and the density distribution of Čerenkov photons at the ground. Most of the Čerenkov photons from an electromagnetic shower are distributed as a flat "light pool" with the radius r_c , and the photon density rapidly decreases out of this circle. Here, r_c is determined by the shower maximum height and the Čerenkov angle as

$$r_c = (\text{shower maximum height}) \times \theta_c. \tag{3.21}$$

The schematic is shown in Fig.3.6. r_c at the ground level is ∼200 m since the shower

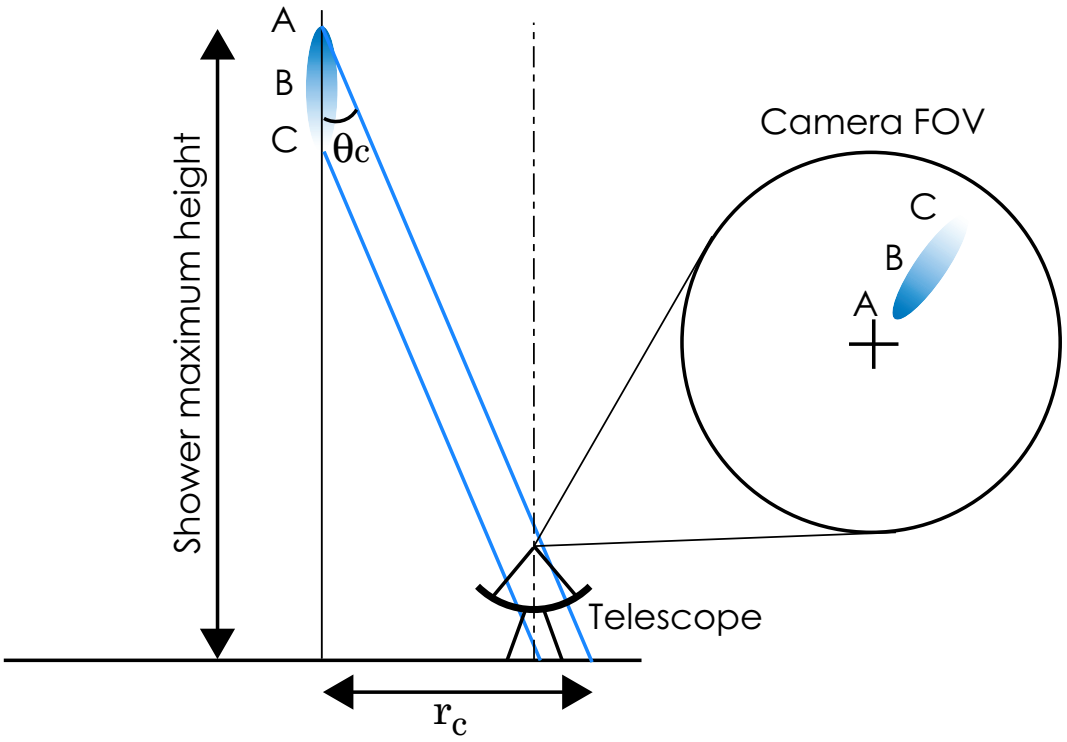

Figure 3.6: Geometrical relation of a shower and a Čerenkov telescope.

maximum for the shower induced by gamma-rays locates at the height of ∼10 km as seen in Fig.3.4. From the longitudinal flat distribution of the Čerenkov light photons in the shower, the arrival timings of the photons are also concentrated within the narrow timing of ∼10 ns. On the other hand, the distribution of the Čerenkov photons from nucleonic showers has a complicated structure induced by electromagnetic sub-showers and penetrating muons. Then arrival timing distribution of the photons becomes somewhat broader (∼20 ns). The most superior point of the atmospheric Čerenkov technique is that when a detector exists *anywhere* in this vast ($\sim 10^4$ m^2) light pool, it can detect a primary particle indirectly. Thus, we can obtain a large effective area of $\sim 10^4$ m^2 by a relatively small detector.

The angular cone of the Čerenkov radiation becomes smaller at higher altitudes, since the refraction index of the atmosphere is smaller. The ring on the ground where the Čerenkov photons fall is called a Čerenkov ring. Because of the Čerenkov angle variation, Čerenkov lights generated at the height between 7 km and 20 km above sea level would have similar size of Čerenkov ring if electrons do not undergo multiple scattering, which broadens the Čerenkov ring. The ring size is of 110 –

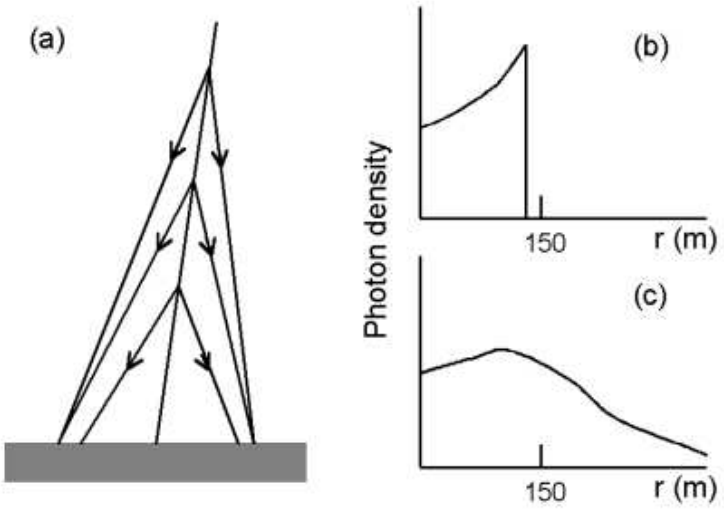

Figure 3.7: Longitudinal development of Čerenkov light. (a) Čerenkov light emission from an EAS at three different atmospheric heights, showing the effect of changing Čerenkov angle due to the variation of the atmospheric refraction index. (b), (c) Illustration of the resultant photon-density distribution at the ground level ignoring (b) and considering (c) the effect of electron multiple scattering, respectively.

145 m radius from the shower core. Figure 3.7 shows the schematic explanation and the lateral profiles of Čerenkov photons in the Čerenkov ring.

Profile of the Atmosphere

Since the atmosphere itself is used as a calorimeter in the VHE gamma-ray observations, the atmosphere structure should be well known. The structure of the mass density of the atmosphere can be written as a function of the height from the ground. The balance between the air pressure and the gravity for a derivative volume requires the following relation,

$$(p + \Delta p)S - pS = -\rho g S \Delta h \tag{3.22}$$

$$\frac{\Delta p}{\Delta h} = -\rho g. \tag{3.23}$$

From the equation of state for the ideal gas,

$$p = \rho R_{\rm d} T. \tag{3.24}$$

Here,

$$R_{\rm d} = \frac{10^3 R}{M_{\rm A}} \quad : \quad \text{gas constant of dry air}$$
$$M_{\rm A} = 28.8 \quad : \quad \text{mean molecular weight of the atmosphere.}$$

Thus, the density profile of the atmosphere is approximately given as

$$\rho(h) = \rho(0)\exp(-h/R_{\rm d}T) = \rho(0)\exp(-h/H) \tag{3.25}$$
$$H = R_{\rm d}T \ : \ \text{scale height of the air.}$$

This is a typical profile, and the condition of the atmosphere depends on many other parameters at the observation site. The atmospheric refraction index is also given as

$$n(h) = \sqrt{\epsilon/\epsilon_0} = \sqrt{1+\chi} \simeq 1 + \frac{\chi}{2} = 1 + 2\pi\alpha\rho(h) = \frac{2\pi\alpha p(h)}{kT} \tag{3.26}$$

$$= \frac{2\pi\alpha}{kT} p(0)\exp(-h/R_{\rm d}T) \tag{3.27}$$

$$\alpha \ : \ \text{polarization of the air,}$$

which indicates an exponential dependence on the height.

The threshold energy for the Čerenkov photon emission is 21 MeV for electrons and 4.4 GeV for muons.

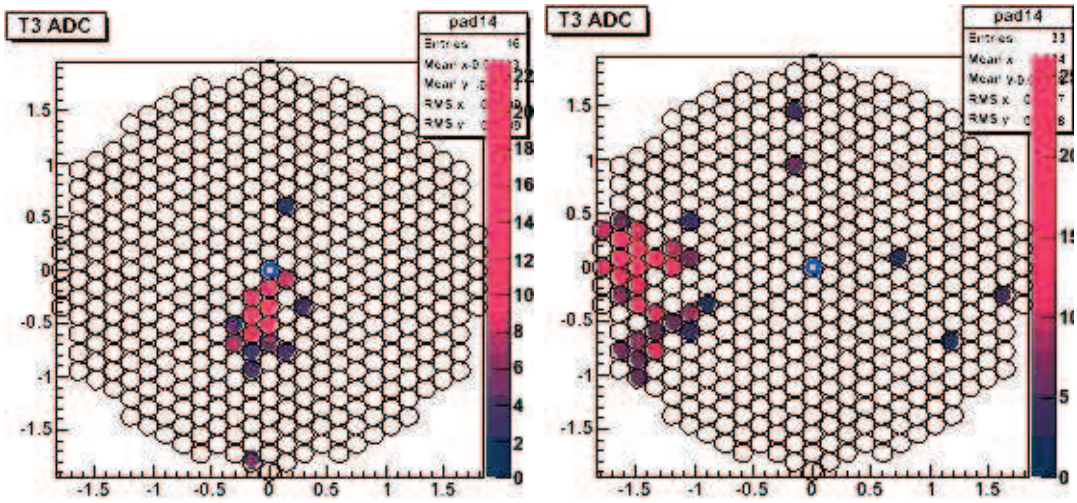

Figure 3.8: Shower images on the camera of T3 of CANGAROO-III. Left: a shower initiated by 1 TeV gamma-ray, Right: by 3 TeV proton. The lattices indicate pixel elements of the camera. The image by a gamma-ray event is relatively small and the axis of the elliptical image is oriented to the camera center. On the other hand, that by a proton is more extended and faces in a random direction. The isolated hits out of the cluster are considered as accidental hits by night sky lights (to be mentioned in § 5).

§ 3 Imaging Air Čerenkov Technique

3.1 Imaging Method

The huge flux of cosmic rays overwhelms the gamma-ray signals for all Čerenkov telescopes. Even the brightest TeV source, the Crab nebula, emits TeV gamma-ray with the integral flux of only $\sim 10^{-11}$ photons cm^{-2} sec^{-1}, whereas the background cosmic-ray proton flux is $\sim 10^{-6} \Delta\Omega$ photons cm^{-2} sec^{-1} ($\sim 10^{-9}$ photons cm^{-2} sec^{-1} for the 4° FOV of CANGAROO-III). Thus, the number of the detected protons is about 100 times larger than that of gamma-rays, which means that the efficiency of the gamma/hadron separation should be larger by orders of 100. To improve the sensitivity of IACTs, we must reject a significant fraction of the air showers initiated by cosmic ray primaries with keeping an adequate efficiency for those initiated by gamma-rays. Since species of the particles in the shower cannot be distinguished directly by the information obtained with atmospheric Čerenkov technique, the separation of gamma-rays' electromagnetic showers from hadron showers has been a difficult problem. To realize the high efficiency, we take advantage of differences in

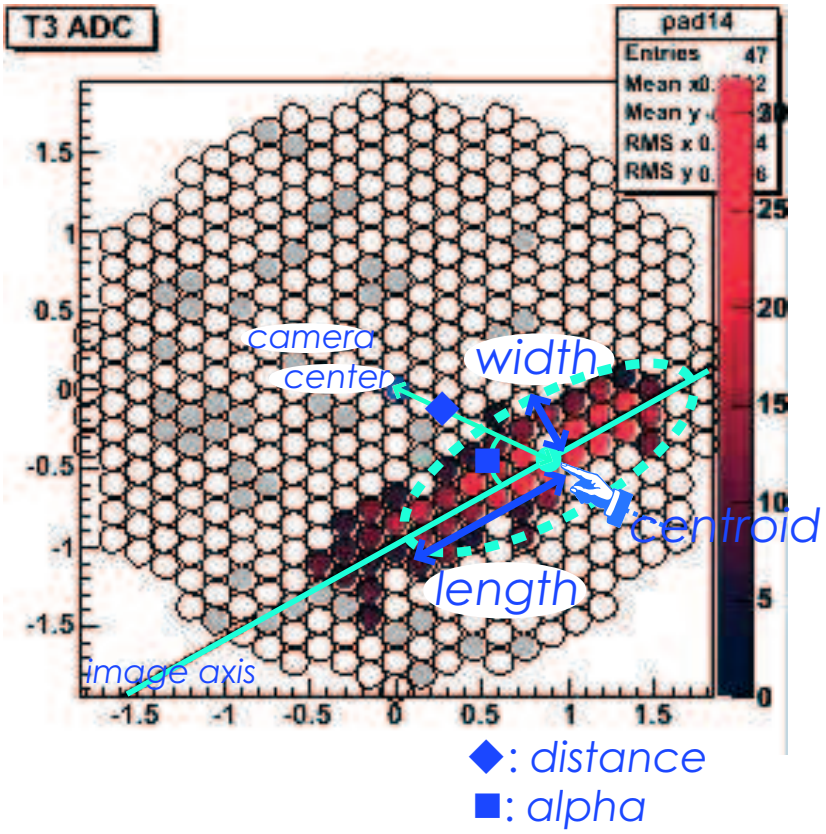

Figure 3.9: Definition of the image parameters. The small circles indicate the PMTs and the color bar represents the value of ADC count in each pixel. The pixels covered gray are "bad channels" (explained in Chapter 7).

the typical development of cosmic-ray and gamma-ray showers which results in the difference in the observed Čerenkov light on the ground. That is so-called imaging method introduced by Hillas in 1980s (Hillas 1982). In this method, Čerenkov photons are collected by a parabolic or spherical reflector, and the arrival direction of the photon is preserved at the focal plane. For a point source emitting gamma-rays, we also use the fact that cosmic rays arrive isotropically whereas gamma-rays arrive from the source direction.

Since the images recorded on the camera represent the shower development in the lateral and longitudinal dimensions, they hold the directional information contained in a shower. The shower images by gamma-rays on the camera are approximately elliptical with an orientation toward the source position, whereas the images by protons are irregular and oriented not in the source position but randomly in the camera plane (Fig.3.8). We fit the both images by ellipsoid, and characterize it by

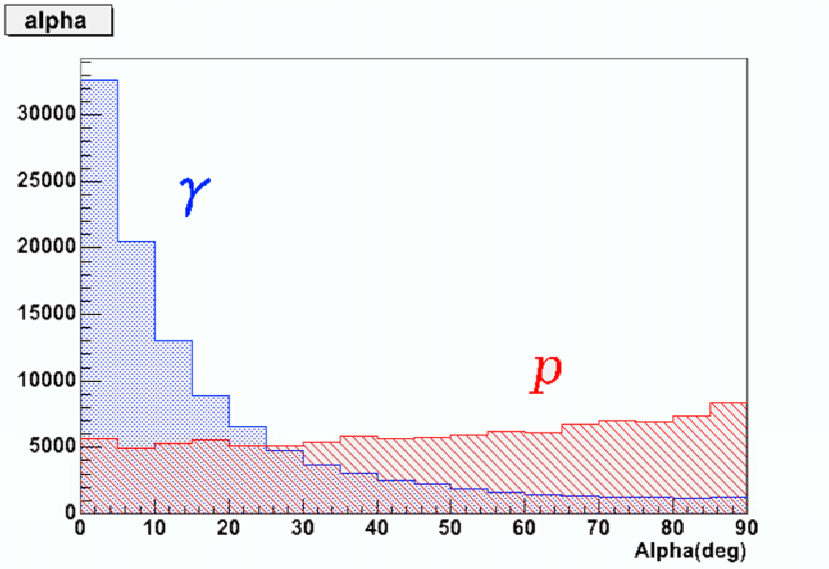

Figure 3.10: Distribution of one of the image parameters, ALPHA. They are based on the simulated data in the energy region of 100 GeV to 10 TeV with the law of $E^{-2.5}$ and 300 GeV -30 TeV with $E^{-2.7}$, for gamma-rays and protons, respectively.

following parameters (Fig.3.9):

WIDTH the minor axes of the projected ellipse (standard deviation),

LENGTH the major axes of the projected ellipse (standard deviation),

DISTANCE the distance from the centroid of the image to the center of the source position,

ALPHA the angle between the image major axis and the vector from the image centroid to the source position. For example, since the shower moving along the optic axis of the telescope produces an image concentrated at the center of the camera, it should ideally have the parameter of ALPHA=0. The distributions of ALPHA for shower images by gamma-rays and protons are shown in Fig.3.10.

ALPHA is an orientation parameter and was widely used to test the signal for the single telescope analysis. Although a single telescope does not allow the unique reconstruction of the arrival direction, the target should exist somewhere on the image major axis and the distribution of the excess from the gamma-ray source should make a peak at ALPHA=0.

§ 4 Stereoscopic Observations

CANGAROO-III is a stereoscopic telescope system, where multiple telescopes view the same air shower simultaneously.

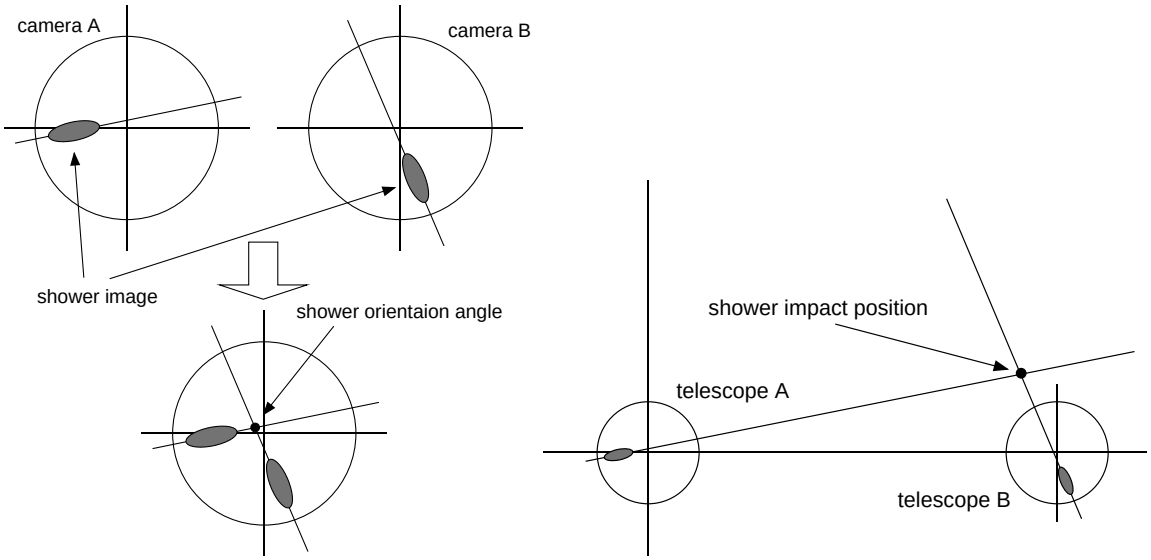

Figure 3.11: Definition of shower orientation angle (left) and impact position on the ground (right) by two telescopes.

In the stereoscopic observation, we can obtain more than one images for a shower event. It significantly improves the separation between gamma-ray events and hadron ones because we can set conditions for each image independently. Since a system of two or more telescopes provides multiple view points for the same shower, which give us additional information that cannot be achieved with a single telescope, it enables us to derive the arrival direction uniquely from the intersection of the major axes of the two superimposed images as shown in Fig.3.11. This intersection point corresponds to the arrival direction of the shower on the sky with an accuracy quantified by the angular resolution. Moreover, the stereoscopic view permits the three-dimensional reconstruction of the Čerenkov light distribution of air showers (Fig.3.12), and improves the imaging atmospheric Čerenkov technique in terms of the sensitivity, the gamma/hadron separation, the angular resolution, and the energy resolution. The sensitivity is improved by a better background suppression for the coincident events. The gamma/hadron separation and the angular resolution are directly linked to improve the sensitivity of multi-telescope systems. The accuracy of measuring air shower parameters such as the arrival direction and the energy of

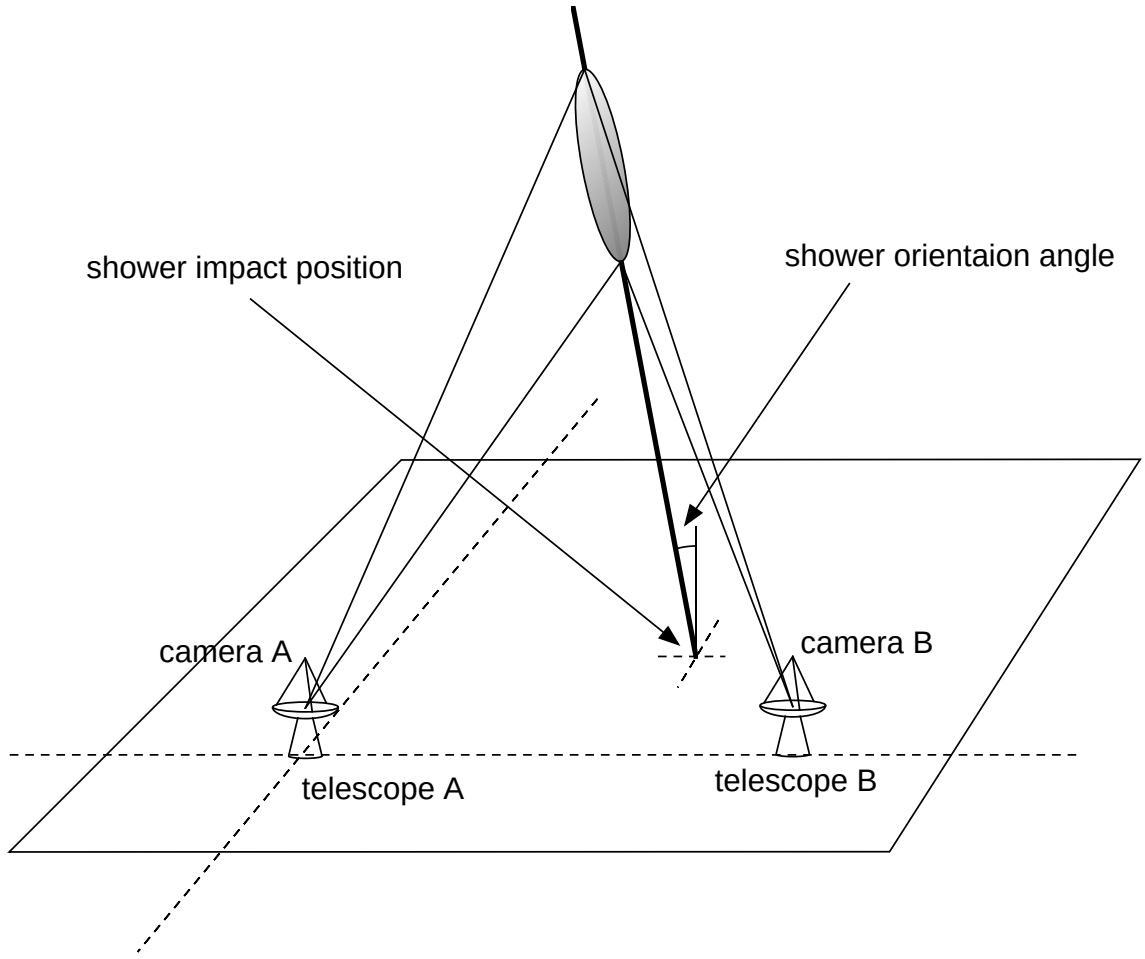

Figure 3.12: Schematic of stereoscopic observation and the three-dimensional reconstruction of a shower.

the primary photon improve the angular resolution and the energy resolution. In a two-telescope system observation at the zenith, the angular resolution is estimated to be $\sim 0.2^\circ$ at 200 GeV.

In addition, the stereoscopic view provides information of the shower-core impact point on the ground, which was missed in a single telescope observation (Fig.3.11). This information is crucial to improve the energy resolution. The details of the stereo analysis are described in the chapter § 6.

§ 5 Analytical Estimation of Telescope Performance

5.1 Estimation of Energy Threshold

Since the luminosity of the Čerenkov light, i.e. the number of the photons, from a gamma-ray shower is proportional to the primary energy E_γ, the number of photons obtained in each telescope can be written as

$$S = CE_\gamma A\epsilon, \tag{3.28}$$

where S, A, and C are the number of the detected photons, the collection area, and a constant number, and ϵ is the total efficiency including the product of the reflectivity of the mirror, the light collection efficiency of the light guide, and the quantum efficiency of the PMT. On the other hand, the noise component which is mainly Night Sky Background (NSB) is written as

$$N = \sqrt{BA\Omega t} \tag{3.29}$$

B : NSB flux, Ω : solid angle of a camera pixel,

t : trigger timing width.

Thus, signal-to-noise ratio (S/N) is given by

$$S/N = CE_\gamma \sqrt{A\epsilon/B\Omega t}. \tag{3.30}$$

Therefore, the detection energy threshold $E_{\rm th}$ follows

$$E_{\rm th} \propto \sqrt{B\Omega t/A\epsilon}. \tag{3.31}$$

This means that in order to obtain the lower energy threshold, the size of pixels should be smaller, and the surface area of the reflector should be larger.

5.2 Flux Sensitivity for a Point Source

If there were enough number of observed signals and background events, the detection significance N_σ is written by the Gaussian distribution

$$N_\sigma = \frac{\text{Signal}}{\sqrt{\text{Background}}}. \tag{3.32}$$

Assuming that the energy threshold for gamma-rays is $E_{\rm th}^{\gamma}$ and $E_{\rm th}^{\rm p}$ for protons, the number of the signal events are estimated as

$$S = F_\gamma(E_{\rm th}^{\gamma}) A_\gamma(E_{\rm th}^{\gamma}) T \tag{3.33}$$

$F_\gamma(E)$: gamma − ray integral flux above an energy E

$A_\gamma(E)$: effective area at an energy E

T : net observation time.

Also the cosmic-ray background rate is written as

$$N = F_{\rm p}(E_{\rm th}^{\rm p}) A_{\rm p}(E_{\rm th}^{\rm p}) \Omega T, \tag{3.34}$$

Ω : field of view used in trigger.

The effective areas for gamma-rays and for protons are defined respectively as

$$A_\gamma(E) = 2\pi \int_0^{\rm inf} \int P_\gamma(r) dr, \tag{3.35}$$

$$A_{\rm p}(E) = 2\pi \int_0^{\rm inf} \int_0^{\pi/2} P_{\rm p}(r,\theta) r \sin\theta dr d\theta, \tag{3.36}$$

$P_{\rm p}(r,\theta)$: trigger probability for an inclination angle of θ and core distance of r.

Here we assume that both gamma-rays and protons have a power-law energy spectrum:

$$F_\gamma(E) \equiv C_\gamma E^{\alpha_\gamma}, F_{\rm p}(E) \equiv C_{\rm p} E^{\alpha_{\rm p}}. \tag{3.37}$$

It is well known that the integral spectrum of the cosmic-ray proton near the Earth has an index of -1.7. Thus, the relation between the detection significance and the flux is derived as

$$N_\alpha \propto \frac{S}{\sqrt{N}} = \frac{C_\gamma}{\sqrt{C_{\rm p}}} E_{\rm th}^{-0.85-\alpha_\gamma} \frac{A_\gamma(E_{\rm th})}{\sqrt{A_{\rm p}(E_{\rm th})\Omega}} T^{1/2}, \tag{3.38}$$

and 5σ is favored as a criteria of the detection claim.

§ 6 Status of VHE Gamma-Ray Observation

At present four major projects which aim at VHE gamma-ray observations with imaging air Čerenkov telescopes are proceeding in the world. As the nature of the ground-based telescopes, observable areas in the celestial coordinate is limited by the location of the telescopes on the Earth. It follows that it is meaningful to have plural observatories at different latitude. Some features on the four projects are shown in Table 3.1, and their observation site is in Fig.3.13.

	Location	mirror shape	f	f/d	FOV	System
VERITAS	31.7N, 110.9W, 2300 m asl.	Davies-cotton	10 m	1.2	4°.0	array
HESS	23.3S, 16.5E, 1800 m asl.	Davies-cotton	15 m	1.2	5°.0	array
MAGIC	28.8N, 17.8W, 2225 m asl.	Parabola	17 m	1.0	3°.6	single
CANGAROO-III	31.1S, 136.8E, 160 m asl.	Parabola	8 m	0.8	4°.0	array

Table 3.1: Imaging atmospheric Čerenkov experiments in the world. f and f/d (a larger f/d decreases the aberration, see Chapter 4-§ 2) are the focal length and the ratio of focal length to reflector diameter, respectively. Explanation of the reflector mirror shape of CANGAROO-III is seen in Chapter 4.

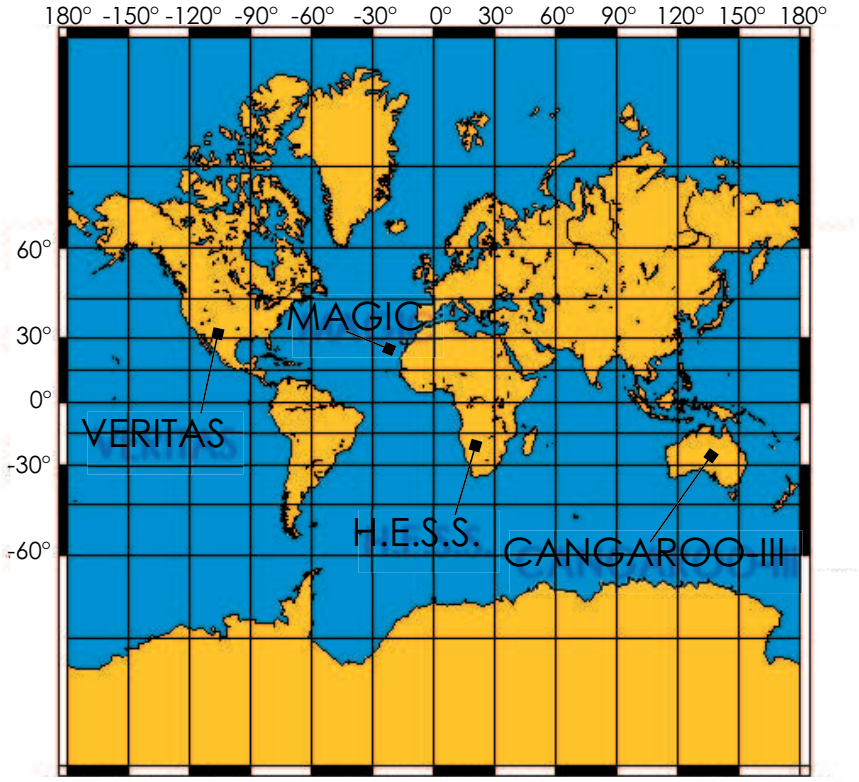

Figure 3.13: IACTs covering the world (Big 4).

Chapter4

The CANGAROO-III Telescopes

CANGAROO (Collaboration of Australia and Nippon for a GAmma-Ray Observatory in the Outback) is an international collaboration for the Gamma-Ray Astrophysics, aiming to study the existence and properties of very high energy gamma-rays from celestial objects in the southern sky by using imaging atmospheric Čerenkov telescopes at Woomera, Australia, shown in Fig.4.1. CANGAROO-III is a system of stereoscopic Imaging Atmospheric Čerenkov Telescopes in the energy range above 400 GeV. The system consists of four telescopes, and they are placed at the corners of a diamond with sides of about 100 m.

In this chapter, we introduce the specification of those telescopes, and how to make the common trigger for all the telescopes.

§ 1 History

In 2006, the CANGAROO project is now in the third phase (CANGAROO-III). The CANGAROO experiment started its observations in 1992 with a single telescope having a 3.8-m-diameter reflector mirror (hereafter "3.8 m telescope" etc.) with 250 photomultiplier tubes. In 1999, a new telescope was completed with a 7-m-diameter multi-mirror reflector and an imaging camera of 3°.0 field-of-view (CANGAROO-II). The reflector was upgraded to having a 10 m diameter a year later, and has detected some galactic objects. From 2002 to 2004, we added three more telescopes successively with making some improvements to new ones. Operations of the 2nd, 3rd and 4th telescope started in January 2003, July 2003, and March 2004, respectively.

Figure 4.1: Observation site of CANGAROO-III.

§ 2 Reflector

For cost reasons, the CANGAROO-III telescopes use — like all other large IACTs — a segmented reflector consisting of many individual mirror facets. A facet is manufactured as a spherical mirror of GFRP* (*cf.* CFRP† for T1). The possible options in the optics layout are concerned primarily with the arrangement of the mirror facets and the choice of the focal length for a given reflector size. In addition, there remains some freedom of the size and shape of mirror facets.

The mirror of the CANGAROO-III telescope is composed of 114 spherical facets with a radius of 39 cm. As the mirror arrangement, we adopted a parabolic layout. The other major design of the arrangement of large IACT reflectors is the Davies-Cotton layout, where identical spherical mirror facets are mounted on a spherical structure with a radius of curvature that is exactly half of the facets (Lewis 1990).

Both approaches provide an essentially point-like focus for rays parallel to the optical axis, while both suffer from significant aberrations for light incident at an angle to the optical axis. The aberration is produced to a slightly larger extent for parabolic layout than for the Davies-Cotton. Standard optics theory predicts that the aberrations should increase $\propto \theta(f/d)^{-2}$, where θ is the light's incident angle to the optical axis, and f/d is the focal length to the reflector diameter. However, the parabola shape has a great merit comparing with Davies-Cotton type in the mean of conservation of photon arrival timing. The maximum variation in the photon arrival times from different portions of a Davies-Cotton ($f/0.7$) 10 m reflector is 6 ns (Lewis 1990), while the paraboloid design provides an isochronous collection of photons. Even our tessellated paraboloid design with the diameter of 10 m has the variation in photon arrival times of less than 0.2 ns (Kawachi et al. 2001).

Telescope No.	Optical spot size (FWHM)
T1	0°.20
T2	0°.14
T3	0°.12
T4	0°.09

Table 4.1: Optical spot-size of all the four telescopes.

*grass fiber reinforced plastic

†carbon fiber reinforced plastic

§ 3 Imaging Camera

3.1 Design

Several attributes of the atmospheric Čerenkov radiation from the extensive gamma-ray shower greatly facilitate its detection and decides the camera design:

1. the Čerenkov pulse is within a very narrow time window (∼5 ns width),
2. the angular size of the Čerenkov beam on the ground is limited ($< 1°$), and
3. the spectrum of the Čerenkov light averagely peaks at the short wavelength (blue/UV) whereas the night sky light peaks at the long wavelength.

The imaging camera on the Čerenkov telescope for stereo observation is required to have a wide ($\sim 4°.0$) FOV with the modest pixel size ($\sim 0°.1$) and to equip with a high-speed (∼nano-sec) and high-gain (photon counting) photon sensor. Thus, an array of photo-multiplier tubes (PMTs) is the most suitable solution at present.

The wide FOV is needed to work out the observation of extended sources and surveys. The pixel size has to be small enough to resolve the details of a shower image, and for the suppression of backgrounds such as the light of the night sky, it must have a fast response.

The imaging cameras on the CANGAROO-III's newer telescopes (T2, T3, and T4) consist of 427 3/4-inch PMTs. All the PMTs are arranged on hexagonal close-packed. Light-collecting cones (light guides; the image is shown in Fig.4.3, right panel) were installed in front of the PMTs' photo-cathode surface as shown in Fig.4.2. The field of view is $4°.0$ (full angle) and the pixel size in angle is $0°.168$.

The camera apparatus, which weighs ∼120 kg, is fixed inside the camera-support cylinder. It is attached to the telescope focal ring supported by four steel stays. The 28-m signal cables from the camera were laid along the stay to the electronics hut at the telescopes' veranda. The parameters on the CANGAROO-III telescopes are summarized in 4.2.

3.2 Photomultiplier Tubes

HAMAMATSU R3479 3/4-inch PMT was selected for the CANGAROO-III imaging telescopes (Fig.4.3). To enhance the blue sensitivity, the UV glass was adopted. The quantum efficiency for R3479 photocathode is measured as shown in Fig.4.4.

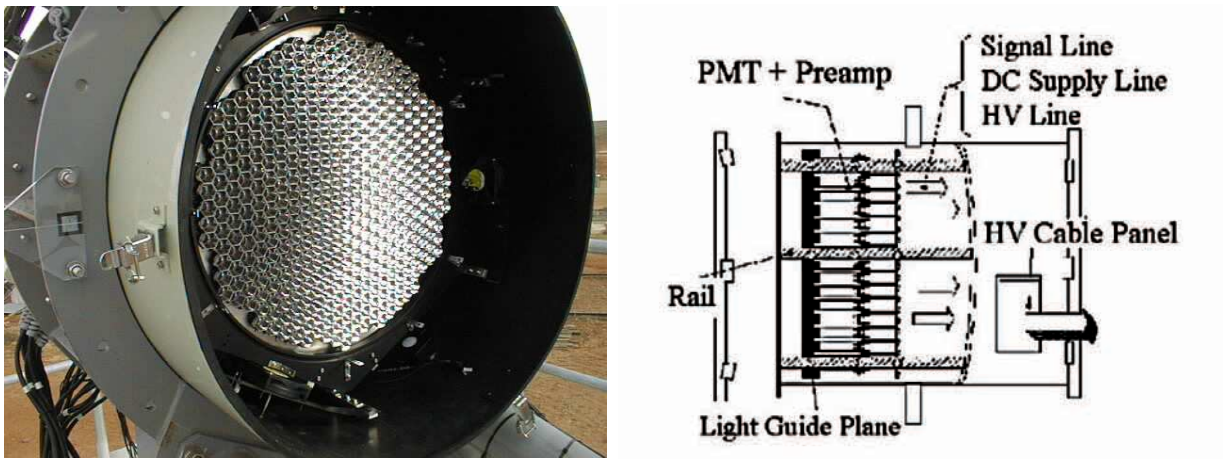

Figure 4.2: Left: Front view of the CANGAROO-III camera. Right: Schematic design of the camera (a side view).

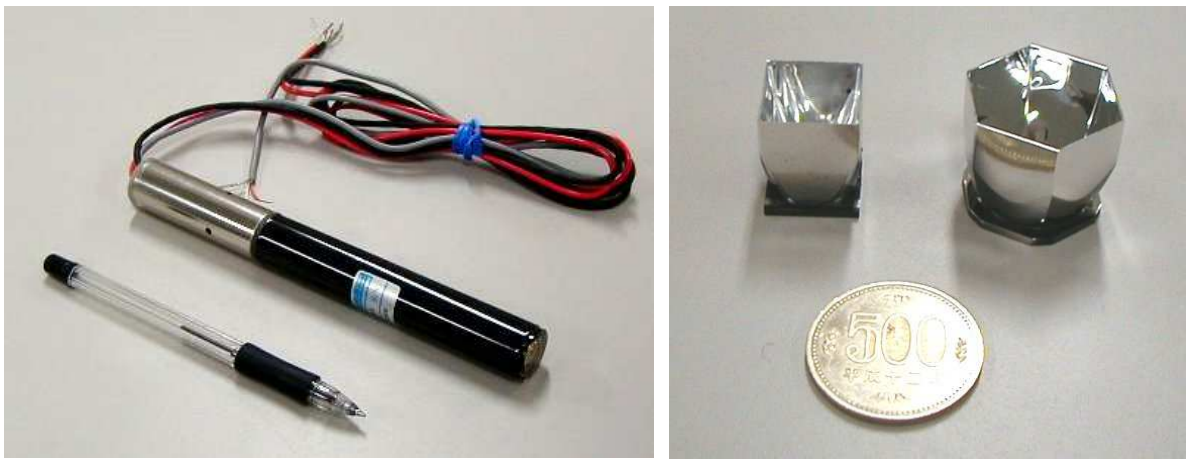

Figure 4.3: Left: HAMAMATSU R3479, Right: The right cone is the hexagonal light-collecting cone for T2, T3, and T4 of CANGAROO-III, and the left one is for T1.

	T1	T2/T3/T4
Focal length	8 m	8 m
Reflector mirror	57 m^2	53 m^2
Mirror material	CFRP	GFRP
Maximum tracking speed	0.5 deg/sec	1.0 deg/sec
Field of View	$3^o.0$	$2^o.0$
Number of pixels	552	427
Size of PMT	1/2 inch	3/4 inch

Table 4.2: Some hardware parameters of the CANGAROO-III telescopes.

A PMT, a bleeder circuit, and a preamplifier are assembled in a package for easy handling, and the PMT signal is directly amplified by a high-speed preamplifier (Maxim MAX4107) before 28-m transmission via the signal cable. The gains of all the PMT assemblies were absolutely calibrated in the laboratory before the shipment using 1-photon signal emitted from a fast blue LED. To achieve the uniformity of the gain all over the FOV, the high-voltage supply was set for each PMT depending on its measured gain, which resulted in the gain fluctuation in whole the camera of less than 1% in the laboratory.

A good linearity between the input photo-electron and the output is maintained up to 200 ph.-e., and the deviation at 250 ph.-e. is $\sim$10 %. The timing resolution of a pixcel is measured 0.94 ns at 30 ph.-e. In addition to the measurement in laboratory, the PMT gain distribution and timing characteristics are measured and corrected in software level in every observation (Chapter 7-§ 1). The light guide to compensate the dead space of the PMT alignment is a hexagonal-shaped Winston cone, which leads the photons with the incidence angle within 30° in half angle to the photo-cathode surface, and rejects larger incidence-angle photons from outer side of the FOV. Its light reflecting surface is coated by aluminum with a 90 % reflectivity at 400 nm.

3.3 High Voltage Supplier System

In the high voltage supplier system used in T2, T3, and T4, the high voltage (HV) level of each PMT can be adjusted from the high voltage modules CAEN SY527, A392. The polarity of the HV supply was set positive for T2, T3, and T4 in order

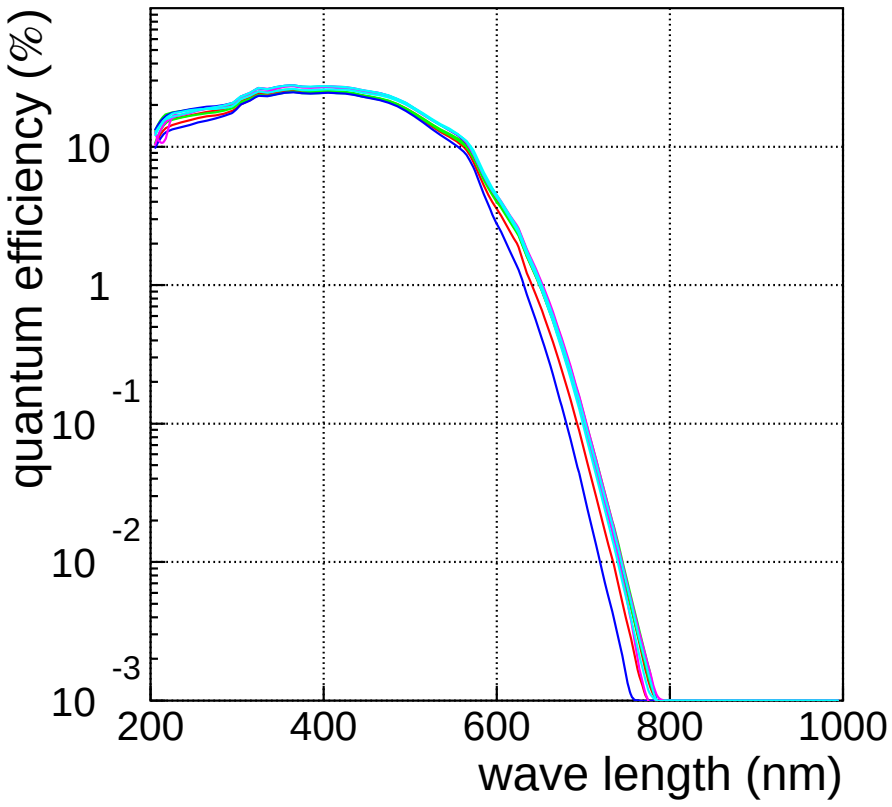

Figure 4.4: Quantum efficiency of HAMAMATSU R3479 as a function of the wavelength measured for 10 PMTs.

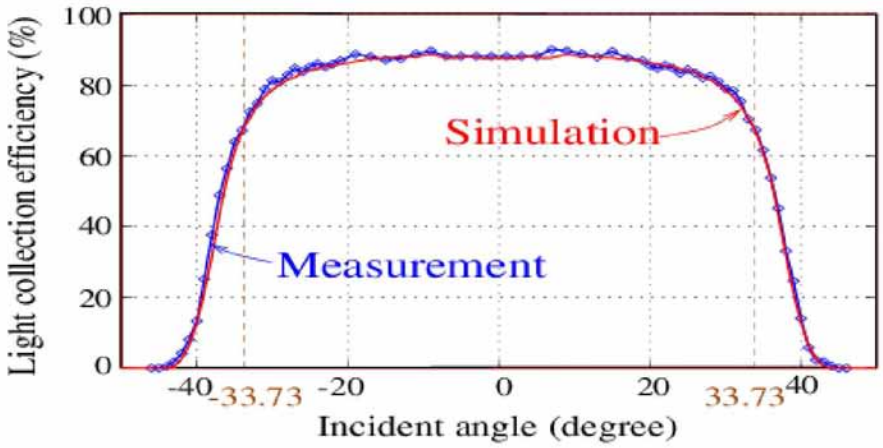

Figure 4.5: Comparison of light collection efficiency between a simulation and a measurement of the light guide.

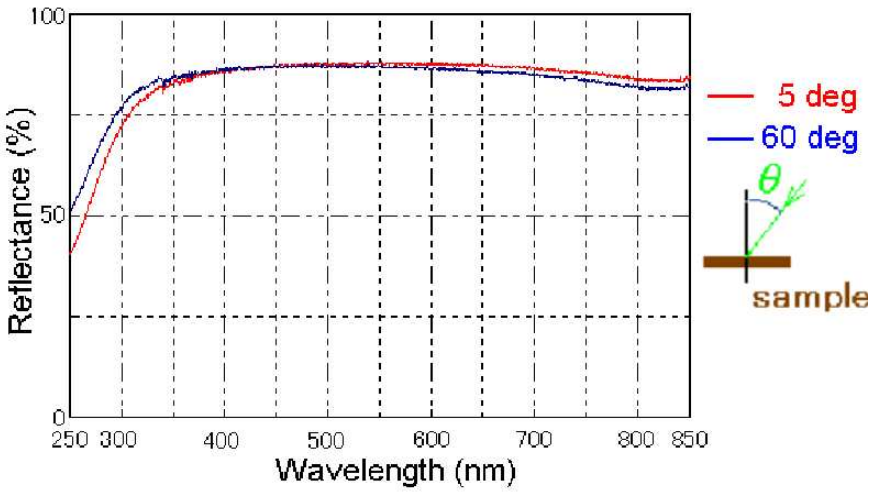

Figure 4.6: Measured reflectance of the light guide.

to avoid the discharge between the PMT photo-cathodes and the light-collecting cones. The voltage for each PMT is controlled individually via a CAENET VME-bus controller, CAEN V288. The HV control for each PMT helps to reduce the effect of bright stars in the FOV, where the positions of the stars in the camera are calculated every second by on-line computer, and the HV for the PMTs within a certain radius from the star position are turned off at on-line level.

§ 4 Electronics and Data Acquisition System

4.1 Electronics

The schematic view of the data acquisition (DAQ) system of the CANGAROO-III new telescopes is shown in Fig.4.7.

One of the important features required for the electronics of CANGAROO-III is that only VME modules are used to speed up the data transfer rate, while that of T1 used also a CAMAC bus and a TKO bus. The read-transfer speed of the CAMAC bus was at most 1 Mwords/s. On the other hand, the speed of the VME bus (VME32 type) used in the DAQ system for T2, T3, and T4 is 8 Mbytes/s. The signal from each PMT is fed to a Discriminator and Summing Module (HOSHIN 2548; hereafter DSM) on the VME bus shown in Fig.4.8. In the DSM, the signal is amplified with a fast shaping amplifier and divided into 4 outputs. One of the amplified signals

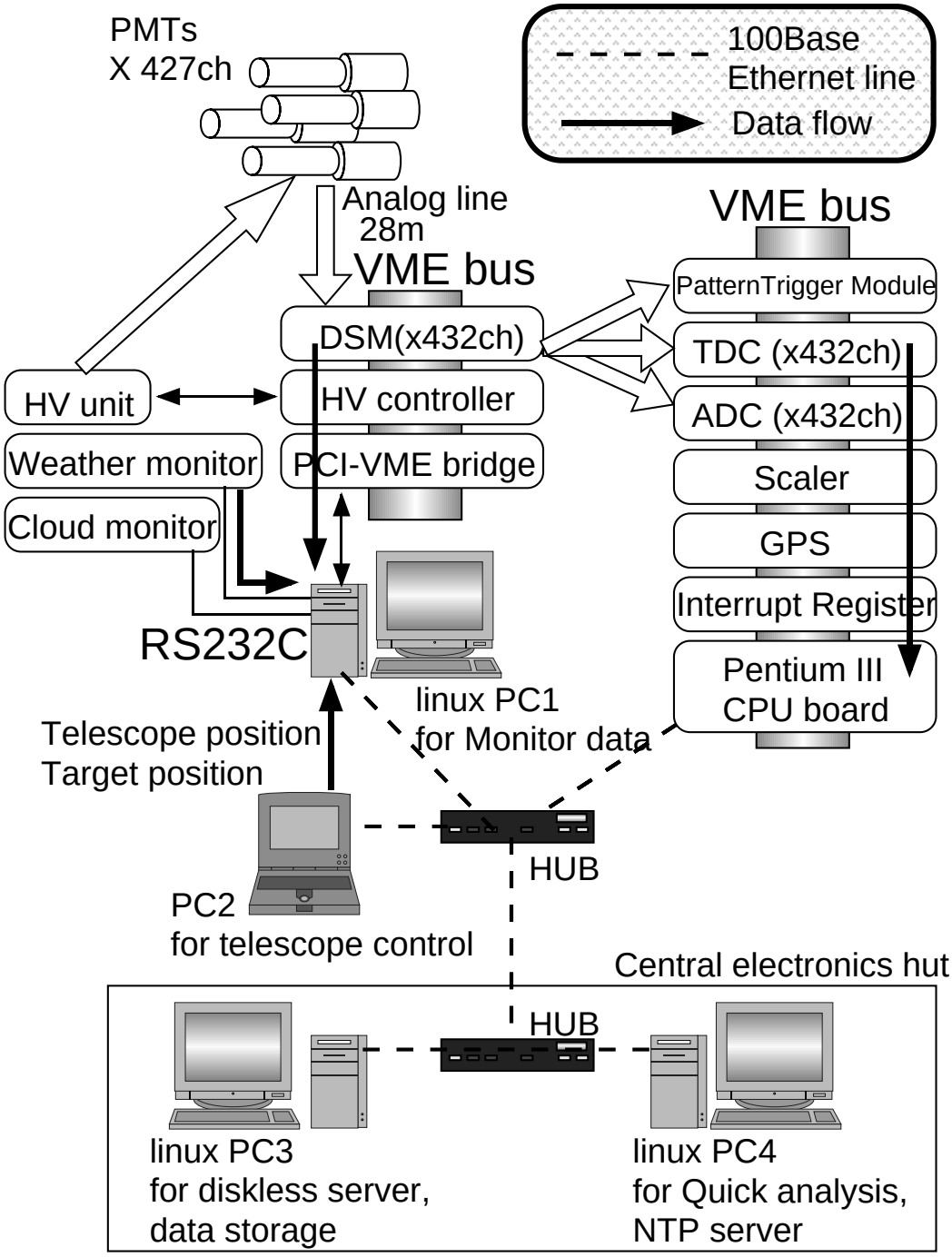

Figure 4.7: Overview of DAQ system of each telescope of CANGAROO-III (T2, T3, and T4).

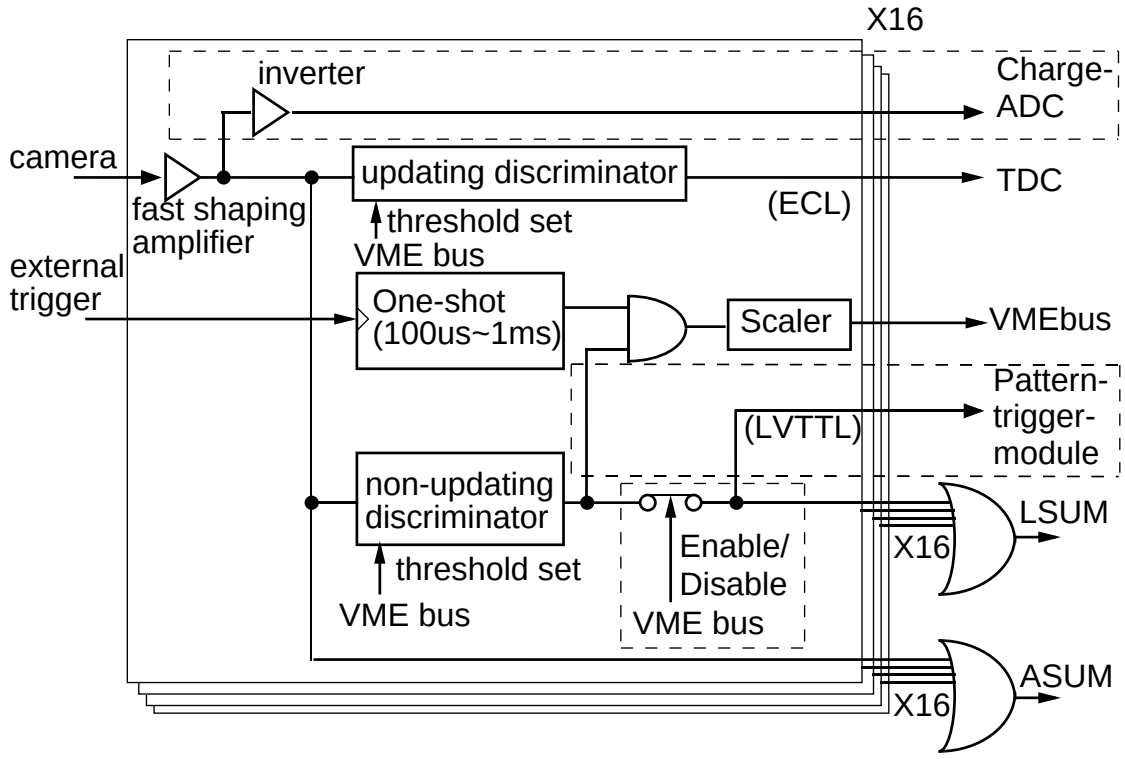

Figure 4.8: Block diagram of the DSM for the CANGAROO-III telescopes (T2, T3, and T4).

is inverted by adjusting the polarity of the following 32ch charge-integrating ADC[‡] module on a VME-9U bus (CAEN V430 type). The number of ADC chips on an ADC module was increased to 32 from 2 of T1 . One of other outputs is summed up over 16 PMTs (Analogue sum output; hereafter ASUM). Also the other two outputs are fed into two discriminators; one is for the measurement of the trigger timing by a TDC[§] with a 0.78 ns resolution, and the other is for counting the number of signals of which amplitude exceeds the preset threshold level during ∼1 ms. Both are useful to reduce the NSB in the off-line analysis. Since the reflector mirror is parabolic, the shower's time propagation can be reproduced by the timing information from the TDC with an accuracy of ∼1 ns. On the other hand, the counting rate is used to reject high counting PMTs hit by starlights or artificial lights. The thresholds of both discriminators are adjustable via the VME bus. The pulse of which height is proportional to the number of the PMTs hitting within the 20 ns gate time, is also generated for using the trigger decision (Logical sum; hereafter, LSUM).

§ 5 Trigger Condition

Figure4.10 shows the DAQ trigger system. LSUM signals from DSMs are summed and discriminated to determine the number of PMT hits within ∼20 ns in the camera. Here, the threshold is set to be 4 or 5 PMT-hits as shown in Fig4.9. On the other hand, the ASUM signal is discriminated to select the event with sufficient intensity of Čerenkov photon concentrated on some area in the FOV. Event triggers are generated from the coincidence of the outputs from these two discriminators. In order to check the DAQ system during the operation, a pulse per second from the GPS[¶] receiver is added to a DAQ trigger, and the event generated by this GPS trigger (empty event) is recorded every second.

The DAQ trigger promptly opens an ADC gate of and 100 ns width. ADC modules provide a 150 ns delay to the amplified signal from the DSM via the delay-line chip on it, and convert the signal to digital. The DAQ trigger also latches the time of the VME GPS receiver, and generates a common stop signal for the TDCs. The GPS receiver has a 1 μsec resolution, and the GPS data are read out with a

[‡]Analogue to Digital Converter

[§]Timing to Digital Converter

[¶]Global Positioning System; the satellite navigation system used for determining one's precise location and providing a highly accurate time reference.

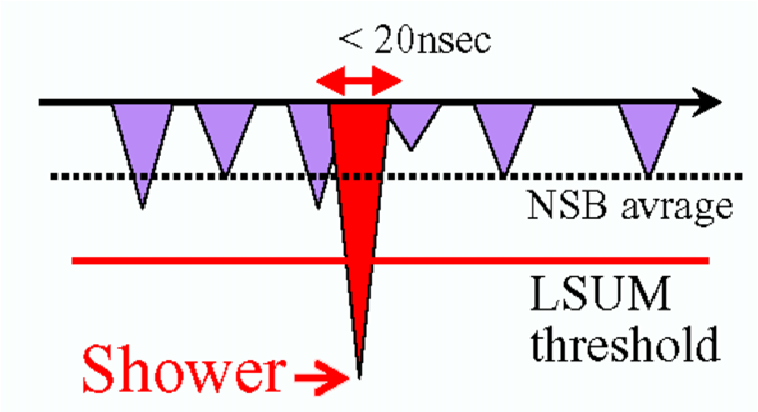

Figure 4.9: Pattern diagram of an LSUM signal and its discrimination. The discrimination of the hit PMT, which always exposed to the night sky light, takes advantage of the difference between the concentrated intensity of the NSB and that of showers.

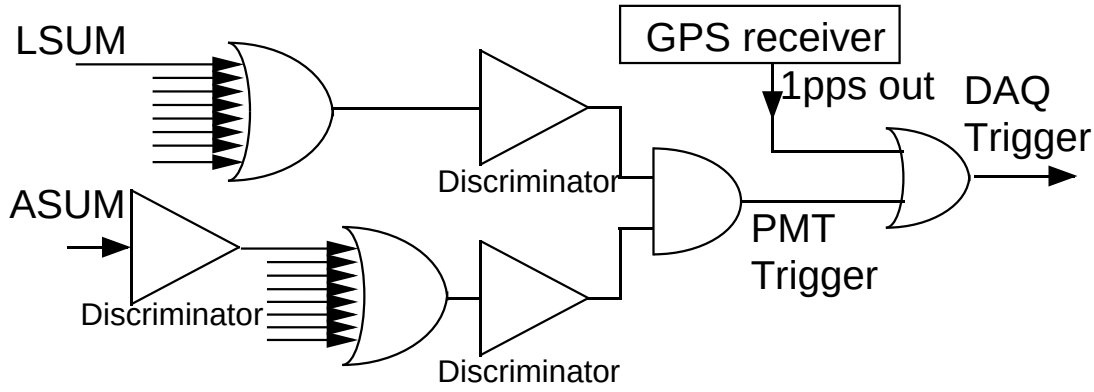

Figure 4.10: Trigger logic of the CANGAROO-III telescope.

100 μsec resolution. All the trigger signals shown in Fig.4.11 are counted by the VME scaler.

5.1 Data Acquisition

Types of data recorded in the CANGAROO-III system are summarized in Table 4.3.

Event data The VME-bus CPU board collects data from the ADCs, TDCs, and GPS. A reasonably portable modular DAQ system "UNIDAQ" was installed on the CPUs used in the DAQ for collecting and storing all data on a hard-disk under the Linux operating system. The total size of the data recorded in an event is $\sim$1.5 kbytes, which is variable depending on the data size of ADCs

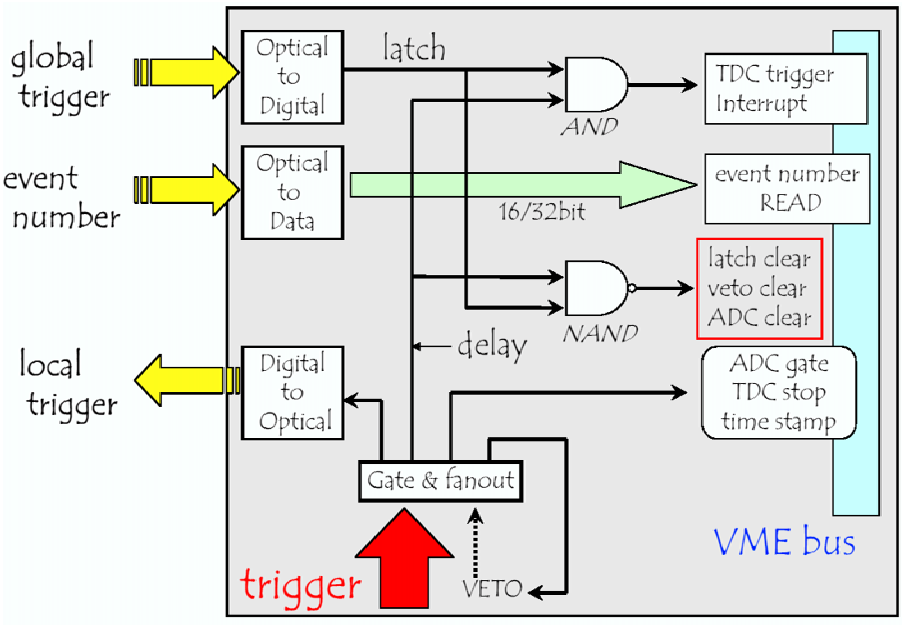

Figure 4.11: Trigger logic for each telescope. See text and Fig.4.12 for details.

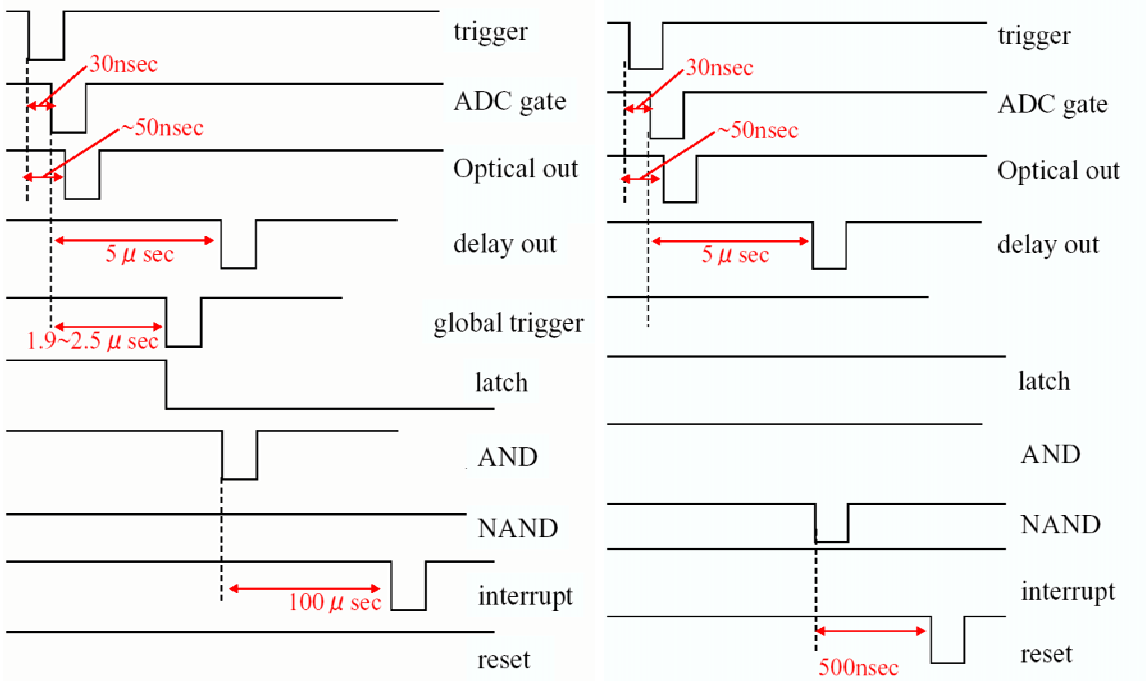

Figure 4.12: Time chart of the trigger logic in each telescope. For the case that a global trigger is generated and sent to this telescope, the interrupt signal for readout occurs as shown in the left panel. For the case that no global trigger is generated, a reset signal occurs as shown in the right.

Data name	Pathway	Data size	Data type
Header	-	24 bytes	event/monitor
ADC	VME bus	896 bytes	event
TDC	VME bus	4 bytes×(number of hits)	event
Interrupt register	VME bus	4 Bytes	event
Scaler	VME bus	96 bytes	event
DAQ mode	VME bus	4 bytes	event
Event number	VME bus	8 bytes	event/monitor
Tx trigger time	VME bus	32 bytes	event
GPS data	VME bus	12 bytes	event
System time	-	8 bytes	event/monitor
DSM scaler	VME bus	864 bytes	monitor
Telescope position data	Ethernet	56 bytes	monitor
Weather monitor data	RS232C	18 bytes	monitor
Cloud monitor data	RS232C	12 bytes	monitor

Table 4.3: Data types in CANGAROO-III system.

and TDCs recording only hit PMTs. The DAQ system can accept triggers at up to 350 Hz with a dead time of 20 % for this data size, as shown in Fig.4.13.

Monitor data Both weather and cloud monitors are connected to the Linux PC (PC1 in Fig.4.7) with an RS232C line, and are read every minute. The PC1 also collects the scaler counts of all PMTs in the DSMs via PCI-VME bridge every 10 seconds, and the real-time position of the telescope via a 100 Base-TX network from the PC (PC2 in Fig.4.7) which controls the operation of the telescope. In addition, the PC1 controls the HV controller described above.

§ 6 Stereoscopic Data Acquisition System

The stereo trigger is adopted to achieve the lower energy threshold by the efficient rejection of the contamination of muons and the NSB. The triggers from each telescope (local trigger) are sent to the central PC which judges if more than two telescopes' triggers are generated simultaneously (within 1 μsec) or not. Hereafter we call this

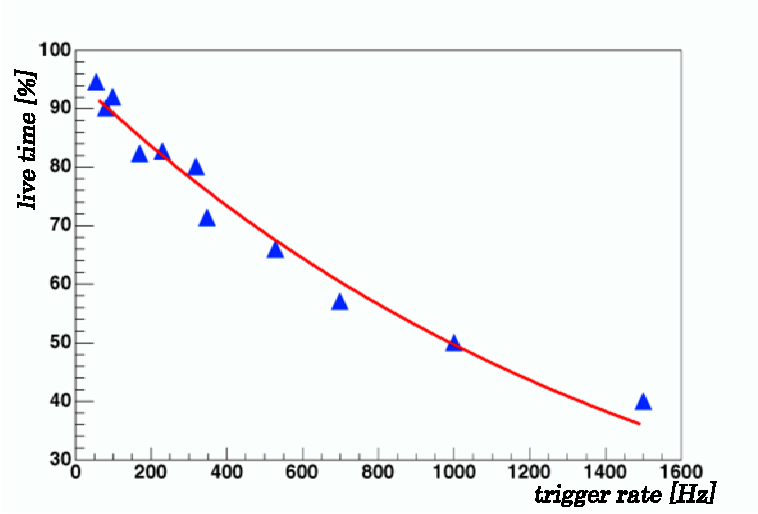

Figure 4.13: Live time of the DAQ. The triggers were generated randomly by shower events. An efficiency higher than 90% is expected for up to 100 Hz triggers.

PC the stereo trigger builder. When any two telescopes hit simultaneously, the stereo trigger builder post an accepted signal (i.e., the global trigger) to only the telescopes of which local trigger was generated, and considered as coincident with another, and then only the telescopes that received the global trigger start to record the event data. This communication is via optical fiber.

6.1 Logic of the Local Trigger in Each Telescope

In this global trigger system, the local trigger, which is generated by the single telescope according to the previous mentioned logic, is sent to the stereo trigger builder, and the telescope waits for the answer. The stereo trigger builder decides whether the data is read out or reset by hardware logic for saving the live time. The circuit assembly for this logic is shown in Fig. 4.10.

Once one or more telescopes are triggered and the local trigger is generated, the data of ADCs, TDCs and the GPS time are kept until the answer from the stereo trigger builder comes with a VETO signal for the next local trigger is generated. At the same time, it sends a message of local trigger to the stereo builder as an optical signal. Since the signal transportation to and from the stereo builder and the stereo-determination takes at most 2.5 μsec, the telescope makes a 5 μsec delay to the signal of "DAQ start" and waits for the stereo judgment. If the global trigger does not come back during this 5 μ sec, then ADC is reset, VETO signal is cleared,

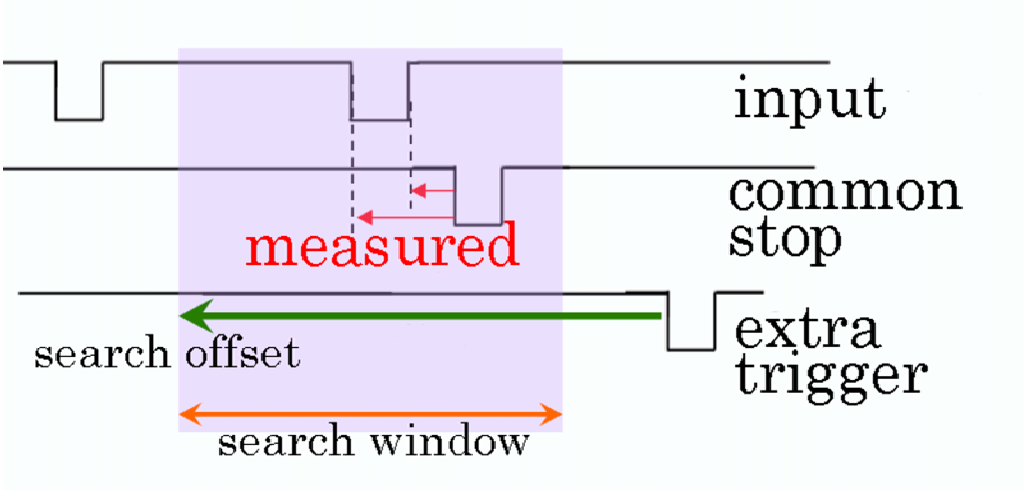

Figure 4.14: TDC behavior. The data read out occurs only when the common-stop signal is detected within the search window of 250 ns from 5.250-μsec search offset before the input of the extra trigger.

and the local trigger system is ready to wait for the next trigger again. Or, if the telescope received the global trigger, the reset signal to ADC is not generated, and the read-out trigger is sent to TDC, the interrupt signal to CPU for starting data read out as shown in Fig. 4.12.

The global trigger has to be received within 5 μsec after the local trigger was generated. This 5 μsec is set considering the exchange time between the telescope and the global trigger builder as introduced above. For the TDC read out, when there detected the common stop signal within the time window, in order to compensate this 5 μsec time gap, the CPU goes back 5.250 μsec from the extra global trigger and records the data in the time window of 250 nsec (Fig.4.14).

6.2 Stereo Trigger Mode

The overview of the stereo trigger system is shown in Fig. 4.15. As well as the telescope system, the DAQ system consists of the VME bus modules, and the data is collected by the onboard-CPU (DPC2, Pentium III 500 MHz).

This system receives the local triggers from each telescope in the form of optical signals, and records the timing in its own TDC. The local triggers are also sent to Gate & Delay module (CAEN V486), which can set the delay timing and the width to the output gates. The local triggers delayed through this module are used for

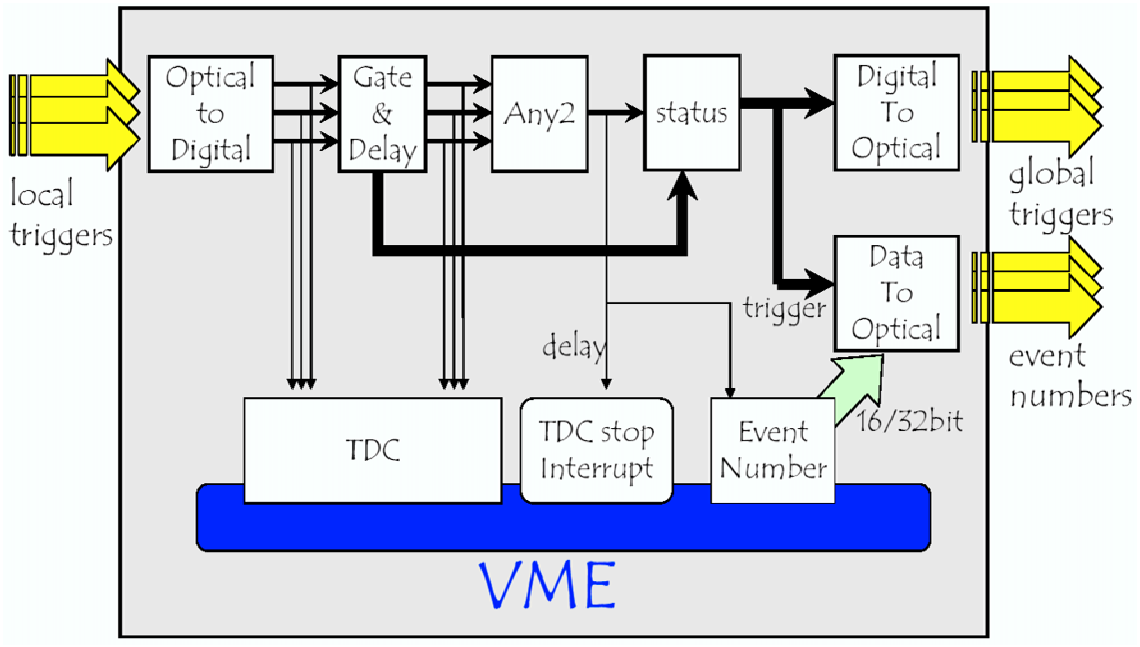

Figure 4.15: Stereo trigger system. The global triggers are sent only to the telescopes contributed to the trigger generation.

the coincidence determination the following module of "Majority logic" (Technoland N-RY011).

The Majority logic module generates a pulse (here, the global trigger) when the number of triggered telescopes during the duration set by the CPU exceeds the set value. We set the duration time window to 650 nsec, which is long enough to contain whole the possible time lag due to the telescopes' zenith angle (maximum lag for our telescopes is ∼500 nsec at a zenith of ∼ 30°). The number of the input local trigger signals for generating a global trigger is variable, and we set the threshold to any 2 out of 3 telescopes ("any-2").

Although the early-arrival two local triggers are enough to make a global trigger even in a 3-coincident event, in order not to miss the last triggered telescope, the system continues to accept the last trigger for ∼500 nsec after the global trigger is generated by precede two telescopes and then sent the global trigger also to the last-triggered telescope. After the global trigger is generated, the CPU of the global system starts reading out the system data. Although this system rejects the next local trigger during reading out the system data, we achieved ∼100% live time considering the typical global trigger rate of 20 ∼ 30 Hz. The data recorded in the global system are listed in Table 4.4.

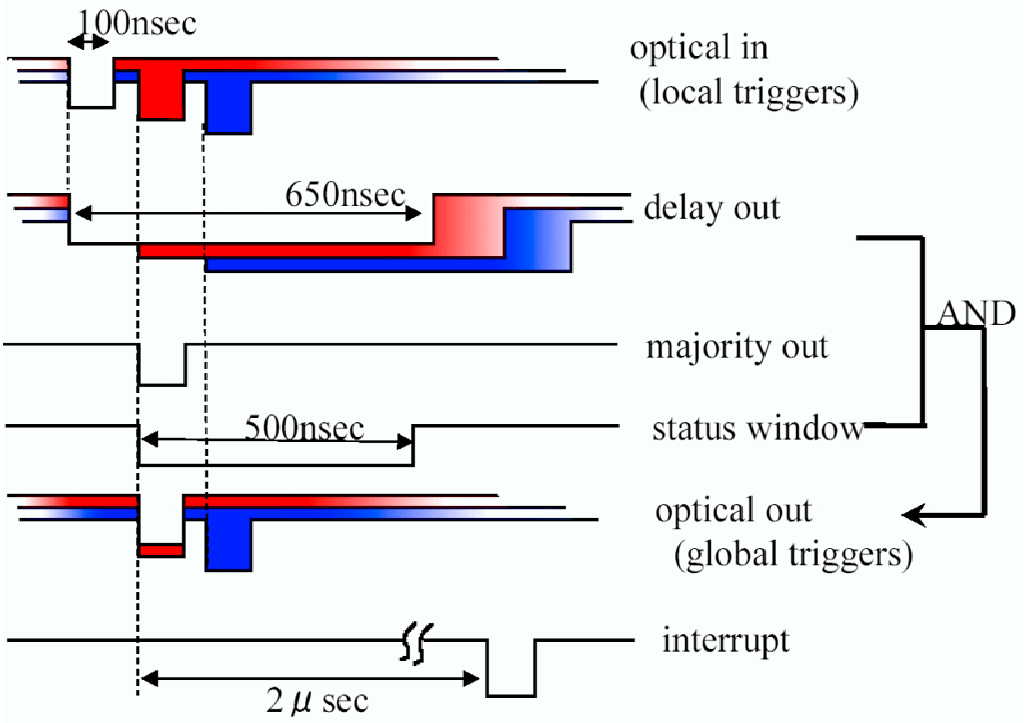

Figure 4.16: Time chart of the stereo judgment. The response to the triggers sent from three telescopes with time lags is shown.

Data name	Pathway	Data size
Header	-	24 bytes
System time	-	8 bytes
Scaler	VME bus	96 bytes
Event number	VME bus	16 bytes
TDC event	VME bus	4 bytes×(number of hits)

Table 4.4: Data of stereo trigger system.

6.3 Local Trigger Mode

In this local trigger mode, each telescope is operated individually for thee same object. The stereo events are reconstructed in the off-line analysis using the timing information of the event recorded by GPS signals.

In the global trigger mode, the rejection of the muon background events is strong and muon events are rejected in hard-ware level. However, we need the data of muons for the study of the telescope reflectivity. Therefore even after the global trigger system was installed, the local trigger mode is used in the observation for muon data.

Chapter5

Observations

Although the cosmic ray (background) events can be rejected to some extent by the imaging method, they still remain even after off-line analysis. Therefore we need the background observation for the estimation of the effect of the background events. We mainly have two observation modes of the "long ON/OFF" and the "wobble" mode.

In this chapter, we explain details of these observation modes, and show the observation data used in this thesis (the Crab Pulsar/Nebula and RX J0852.0−4622).

§ 1 Observation Mode

1.1 Long ON/OFF Mode

This mode is mainly used in single telescope observations. Observations pointing the target region (ON-source runs) are carried out typically for 1-5 hours over the culmination time of the target. Before and/or after the ON-source run, observations pointing the outside of the target region (OFF-source runs) are carried out in the same night. The offset in OFF-source runs is along the axis of Right Ascension to get the same tracking path in the sky as that of ON-source runs. Thus, the distribution of the elevation and the azimuthal angles are almost identical to the those of ON-source data. Although a half of the observation time should be used for OFF-source run, the background estimation is easy and reliable.

1.2 Wobble Mode

Recently, the stereoscopic observation with wide FOVs ($\geq 4^\circ$ diameter) enables us this "wobble mode", which is a main method in the stereo observation developed by HEGRA.

In this mode, the telescope tracking position is $\pm 0.^\circ 5$ away from the nominal

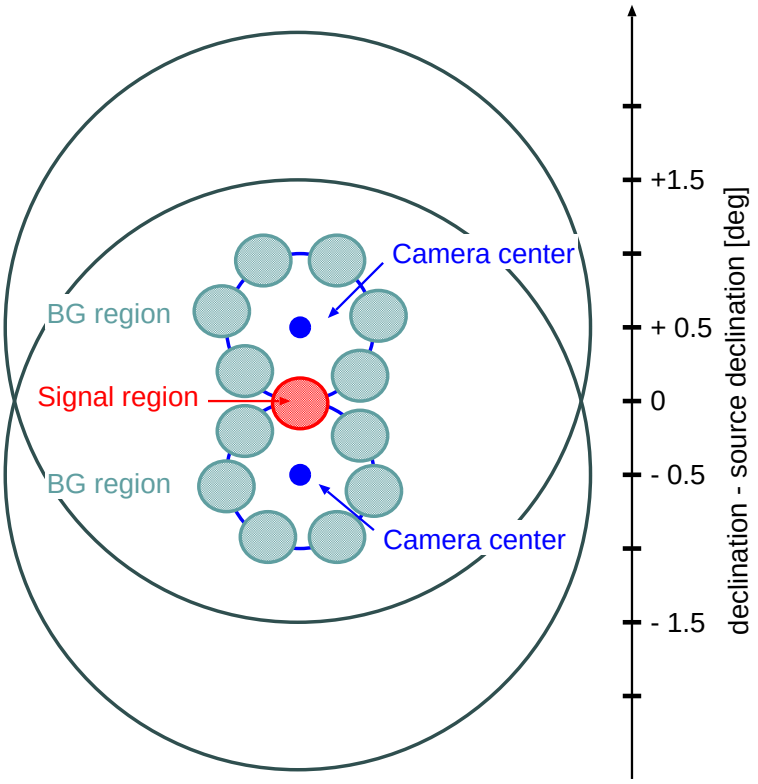

Figure 5.1: Setup of a wobble mode observation. The FOVs for two offset modes ($\pm 0°.5$) are sketched. The two blue points and large gray circles are the centers and the FOVs for each offset. The red circle is the target region, and the blue filled circles are background control regions.

position of the target, where the sign of the angular shift was alternated from one 20-minutes run to the next. We can get the OFF-source control regions in the ON-source FOV from the region outside of the target region as shown in Fig. 5.1. We typically use six non-overlapping control regions (blue circles in Fig. 5.1) centered on a circle with a radius of 0.°5 around the center of the FOV (blue points in Fig. 5.1) for the point source. In order to obtain the high statistics for the background, the number of the control regions is decided to get as many as possible under the condition that the target region's (a red circle in Fig. 5.1 and their ±0.°23 (PSF) radius circles are not overlapping. Wobbling gives the background data of the same declination as the target position as the average.

The wobble mode reduces the observation time about in half, but it is not suitable for extended sources because of the difficulties in selecting the OFF-source regions from the ON-source FOV. Then a hybrid approach of the long ON/OFF and the wobble mode is the best. The details are given in § 4.

§ 2 Trigger Mode

Using the "global trigger mode", which requires the simultaneous observation of an air shower at least two telescopes, we can reject muon-primary showers at the trigger level. However the muon data is used for the calibration of the performance of the telescopes (details in Chapter 6, § 2). Then we made an extra observation run for cosmic muons in the "local trigger mode".

§ 3 Observations of Crab Pulsar/Nebula

The Crab Pulsar/Nebula (R.A.=83°.223, Dec=22.°14, J2004) is known as one of the brightest TeV gamma-ray point sources, which has been confirmed by Whipple/HEGRA/CANGAROO-I groups. The gamma-ray emission is unpulsed and steady. Also, its spectrum was well observed from 100 GeV to 100 TeV. Its emission size is known to be compact enough taking into account the angular resolution of IACTs (∼0.1 degree). Then it is widely used as a standard candle for the new instruments to calibrate their flux sensitivity and angular resolution.

We also observed Crab Pulsar/Nebula in the global trigger mode in Decem-

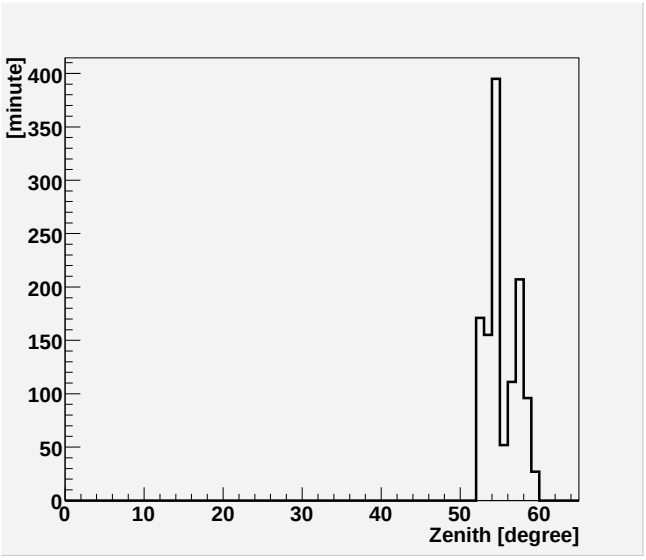

Figure 5.2: Distribution of the zenith angle for the Crab Pulsar/Nebula observation.

ber 2003 with the two telescopes of T2 and T3 to measure the performance the CANGAROO-III stereoscopic observation system. Since the Crab Pulsar/Nebula is a point source for Čerenkov telescopes, we observed it in the wobble mode. The total exposure time and the included telescopes are summarized in Table 5.1, and the distribution of the observation zenith angles for this observation period is shown in Fig .5.2.

Table 5.1: Observation log of the Crab Pulsar/Nebula in 2003.

Observation period	18 to 28 December 2003
Telescope	T2, T3
Total observation time	224 min.

§ 4 Observations of RX J0852.0−4622

RX J0852.0−4622 is known to have a shell-like structure of $\sim 1^\circ$ radius in X-ray observations. Its northwest rim, which is the maximum point of the X-ray emission, was observed several times by CANGAROO-II (a single telescope) and the first two telescopes of CANGAROO-III (Enomoto et al. 2006). To study not only the northwest rim, but also the whole shell, we pointed the center of the shell in 2005.

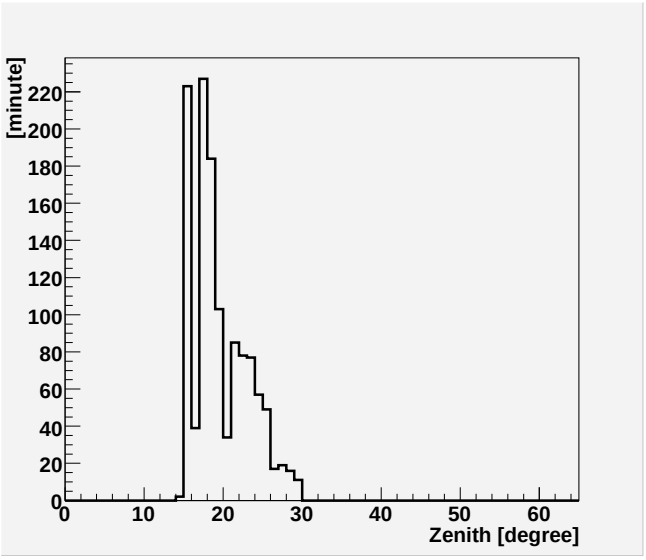

Figure 5.3: Distribution of the zenith angle for the RX J0852.0−4622 observation.

The wobble mode has another merit than saving the observation time. Generally the acceptance of IACT has a maximum at the center of the FOV, and it gradually decreases as getting away from the center of the camera. The simulation shows that the acceptance is the highest at the center of the FOV, and it drops about by half at a distance of 1°.0. When the target is at the center, there remains some possibility that a fake peak may be made at the target position. Then it is reasonable to wobble telescopes in observing an extended target in order to flatten the acceptance around the target. However, the extended structure of the target makes it difficult to select the appropriate OFF-source control region in the wobble-ON FOV. Therefore, we took an extra OFF-source run, which was also taken in the same wobble mode in order to set the pointing declination same as that in ON-source observation. The exposure times and the included telescopes are summarized in Table 5.2, and the observation zenith angles for this target is shown in Fig .5.3.

Table 5.2: Summary of observation data set of RX J0852.0−4622.

Observation period	2005, 16 to 18 January, 4 to 14 February
Telescope	T2, T3, T4
Observation time (ON-source)	1736 min.
Observation time (OFF-source)	1408 min.

Chapter6

Simulation

To investigate the features of the shower images, we simulate the process of shower images by IACT using Monte Carlo method.
In this chapter, we summarize the conditions for the simulations.

§ 1 Monte Carlo Simulation Code

The current Monte Carlo simulation used in the CANGAROO-III experiment is based on GEANT 3.21. GEANT is a system of detector descriptions and simulation tools for high-energy particle physics, which has been developed in CERN. The simulation code mainly consists of four components: the generators of primary particles and the medium description, the particle-interaction description, the Čerenkov-photon generation and the telescope response. In the medium description, the atmosphere is divided into 80 layers of an equal thickness of $\sim$12.9 g/cm^2, which is less than a half radiation length of the air. The dependence of the number of the generated Čerenkov photons in the air shower simulation was studied by changing the number of layers, and was confirmed to be less than 10 %. The geomagnetic field at the Woomera site (in South Australia) was also included (0.253 G in horizontal and 0.520 G in vertical directions, and 6°.8 off from the South; Enomoto et al. 2002b).

As for particle tracking, the lower energy threshold for a particle transport was set at 20 MeV, which is less than the Čerenkov radiation threshold of electrons at a normal temperature and pressure ($\sim$84 MeV). In order to save the CPU time, only particles whose direction is within a certain degree from the telescope optical axis were selected to be tracked to the ground, and Čerenkov photons are generated from only those particles. Alternatively, the number of generated Čerenkov photons is estimated from the Frank-Tamm formula describing the energy radiated per unit length and per unit frequency for the charge unbounded motion (Frank

1998). After generating photons, the number of photons is reduced as multiplying the following factors such as the atmospheric transmission, the quantum efficiency of PMTs and the mirror reflectivity in advance. Also photons are generated within the calculated Čerenkov angle. This photon-reducing method is generally used in another atmospheric Čerenkov simulator such as CORSIKA. As for the atmospheric transmittance, a simple Rayleigh-scattering length of 2970 (λ/400 nm) g/cm^2 was used in this simulation. Since the Rayleigh scattering angle is so large compared with the Čerenkov angle, all the scatterings are regarded as an extinction. The contribution of the Mie (Aerosol) scattering is thought to be at 10-20 % level, but not considered here. 21 sampling points between 189 nm to 672 nm are used for the quantum efficiency estimation, and 6 points between 200 nm and 800 nm for the reflectivity of the mirror are used to estimate the efficiency of the mirror.
For the survived photons, their reflection on the multi-mirror telescope is calculated assuming a perfectly accurate mirror surface since the reflectivity effect is already included as a point spread function. The photon distribution on the imaging camera is obtained by imposing Gaussian blur with a proper width obtained from the optical spot-size measurement. Every photon is accumulated in finite-size PMT pixels according its position. NSB photons are also added to the Čerenkov signals as a noise. The number of injected NSB photons is calculated from Jelley's value (Jelley 1958) (see Chapter 3). Then the response for the photons in each PMT is simulated for both PMTs and electronics modules. The hardware trigger condition described above is approximately realized in the simulation code, and the hardware trigger flag is tagged to the event. The output bunch of the Monte Carlo simulation code is matched with that of the calibrated real data, for example, the number of photoelectrons, photon arrival timing in ns, and so on. Therefore both of the simulation and the real data can be processed by the same program constructed.

§ 2 Reflectivity

We need to keep a careful watch on the reflectivity of the mirror because our telescopes are in a dessert and exposed to unfavorable circumstances, and then, their reflectivities are gradually but certainly decreasing.

The ideal image of the observed muon event has a ring shape or a part of that. The schematic is shown in Fig.6.1. The typical muon image on the CANGAROO-III camera is shown in Fig.6.2. The velocity of the muons observed by our telescopes

is 99.97%-light-speed or higher, and their Čerenkov angles are considered to be the same and constant along the track. In addition, their track length that the FOV of the camera views is almost the same among the muon events. In that case, the radius of the ring, which is corresponding to the Čerenkov angle, and the total photons emitted from a muon are approximately constant for all the muons coming to the same direction and incident angle. We defined the photoelectron density for the muon image as

$$Density = \frac{\text{Size [p.e.]}}{\text{Length [deg]}}, \tag{6.1}$$

where Size means the total number of photoelectron of the image, and Length is that of Hillas parameter (mentioned in Chapter 3). From above argument, *Density* should naturally be constant. The variation of the *Density* is considered due to the variation of the collecting efficiency. Therefore by monitoring *Density*, we always monitor the light-collecting efficiency of our telescopes, and use it in the Monte Carlo simulation (details in the master's thesis of Adachi (2005)).

The muon factor, which is the ratio of *Density* to that in the initial state of the T2 mirror, is computed for every observation term, and the variations are shown in Fig.6.3. The reflectivities using in the Monte Carlo simulation for the analysis in this thesis are summarized in Table 6.1. The deterioration of the mirror reflectivity was not negligible in 2005. We cleansed up the mirrors using water in September and October 2005 (some months after the observation of RX J0852.0−4622). The rising up of the muon factor around 2200 days seen in the Fig.6.3 is due to this cleaning work.

Target	T2	T3	T4
Crab Pulsar/Nebula (2003 Dec.)	0.70	0.70	–
RX J0852.0−4622 (2005 Jan. and Feb.)	0.45	0.58	0.73

Table 6.1: Muon factors input to the Monte Carlo simulations.

§ 3 Simulation Parameters

In order to estimate the differential flux, the acceptance and the effective area for the gamma-ray events were estimated with the simulation data. Here we assumed the spectral index of −2.1 for RX J0852.0−4622 following the HESS result (Aharonian

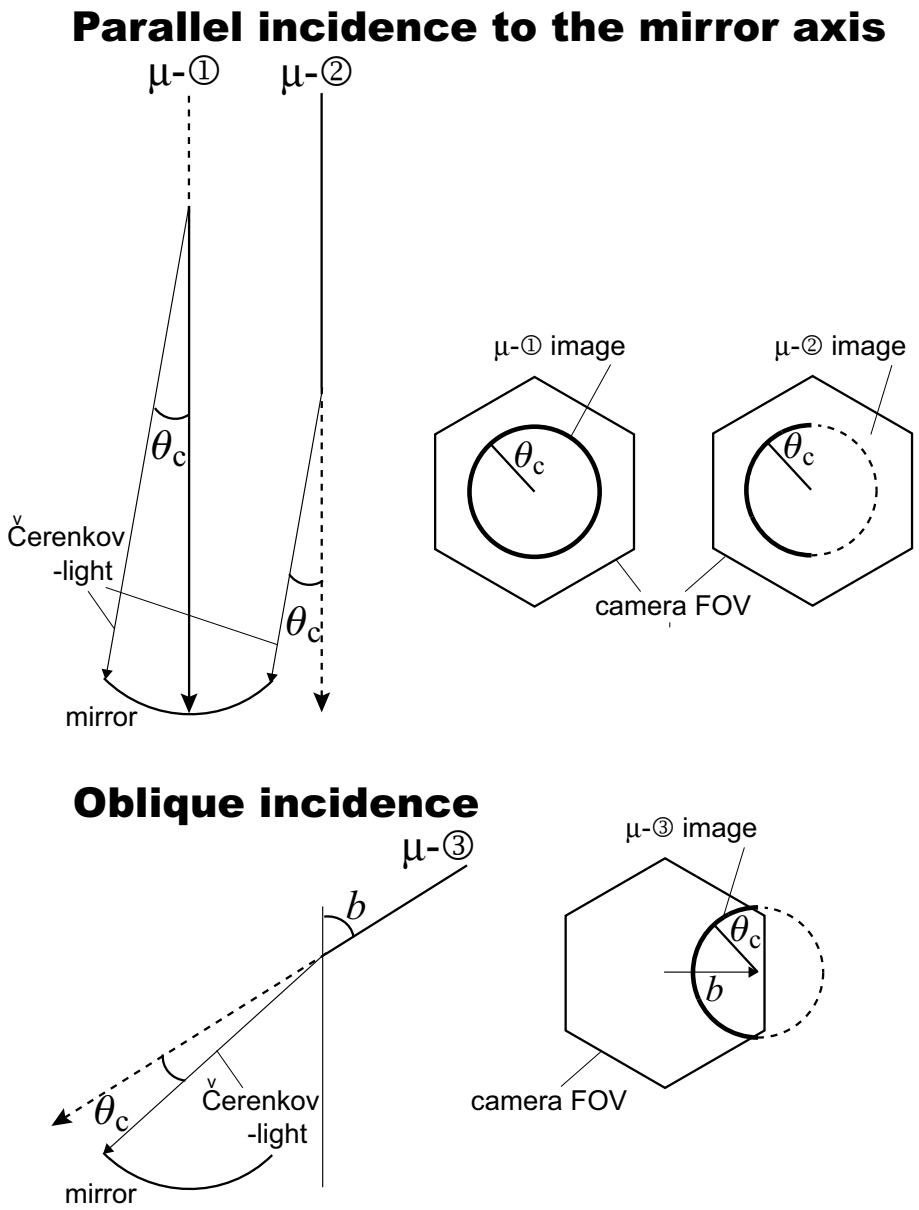

Figure 6.1: Schematic explanation of muon image. Upper: ***μ*-1** and ***μ*-2** are in parallel to the mirror axis. The event which incidents to the center of the mirror like ***μ*-1** makes a circle image, and the center of the circle is concentric with the camera center. If the shower axis is shifted from the center like ***μ*-2**, the image is an arc. Lower: ***μ*-3** incidents with an angle b to the mirror's normal vector. Its image on the camera is a circle of which center is shifted by b.

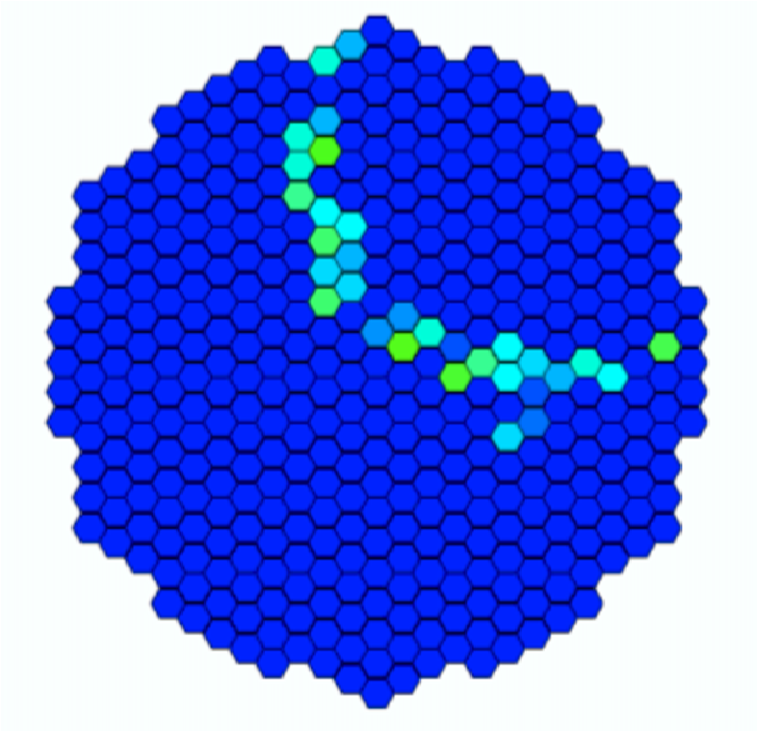

Figure 6.2: Typical muon ring image on the CANGAROO-III camera.

et al. 2005b). The zenith angles are altered to be distributed as same as that of the observation data (Fig.5.2 or Fig.5.3). The parameters for the simulation are summarized in Table 6.3.

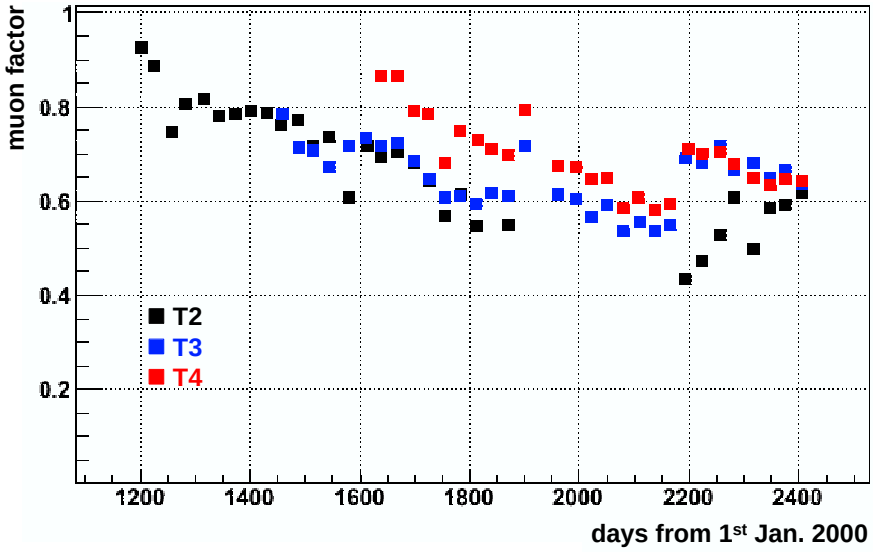

Figure 6.3: Muon factor transition. Horizontal axis shows the elapsed days since 1st January 2000. December 2003 when the Crab Pulsar/Nebula was observed is around 1450 day, and January 2005 when RX J0852.0−4622 was observed is around 1830 day.

Spattering area	250-m-radius circle
Zenith angle (averaged)	55°.26
Spectral index	−2.5
Energy lower limit	300 GeV
Energy upper limit	30 TeV
Edge cut	Outermost 1 layer cut*
Likelihood ratio cut	$LR > 0.1$

Table 6.2: Parameters for the Crab Monte Carlo simulation.
*Described in Chapter 7-8.1 and Chapter 8-§ 4.

Spattering area	250-m-radius circle
Zenith angle (averaged)	19°.07
Spectral index	-2.1
Energy lower limit	200 GeV
Energy upper limit	20 TeV
Edge cut	Outermost 1 layer cut
Likelihood ratio cut	$LR > 0.1$

Table 6.3: Parameters for the RX J0852.0−4622 Monte Carlo simulation.

Chapter7

Analyses

§ 1 Data sets

We have two types of the observation runs. One is the target observation run, and the other is the calibration run. The latter aims to monitor the performance of the telescope instruments. We carried out several kinds of calibration runs using LED flashers everyday before or after the target observation runs.

Calibration Runs

ADC LED run/pedestal run The number of the photoelectrons of a PMT is recorded as an ADC count. The number of primary photoelectrons emitted from a shower is calculated by multiplying ADC counts by the conversion factor (the ADC-to-photoelectron conversion factor). The absolute gains of PMTs, the amplifier, and the digitization constant of ADC were carefully measured before the construction. We also need the daily monitor for the variation of the conversion factor since hardware conditions may change by environmental factors day by day. In CANGAROO-III, a new calibration system of "Konan LED" system was introduced to measure the ADC-to-photoelectron conversion factor. The schematic view of this system is shown in Fig.7.1. The shading pattern which realizes the uniform exposure to blue LED light over the whole camera is printed to the sheets ("Patterned Screen" in Fig.7.1), and fixed to the internal side of the camera lids. We measured the ADC distribution and calculate the mean and RMS. These two parameters provides us with the absolute number of photoelectrons, since we know that the ADC distribution follows the Poisson statistics (details are described in Section 2.1)

TDC LED run/pedestal run For the correction of the time-walk (Fig.7.2, a blue LED attached to the reflector center is used to create a light flash of about

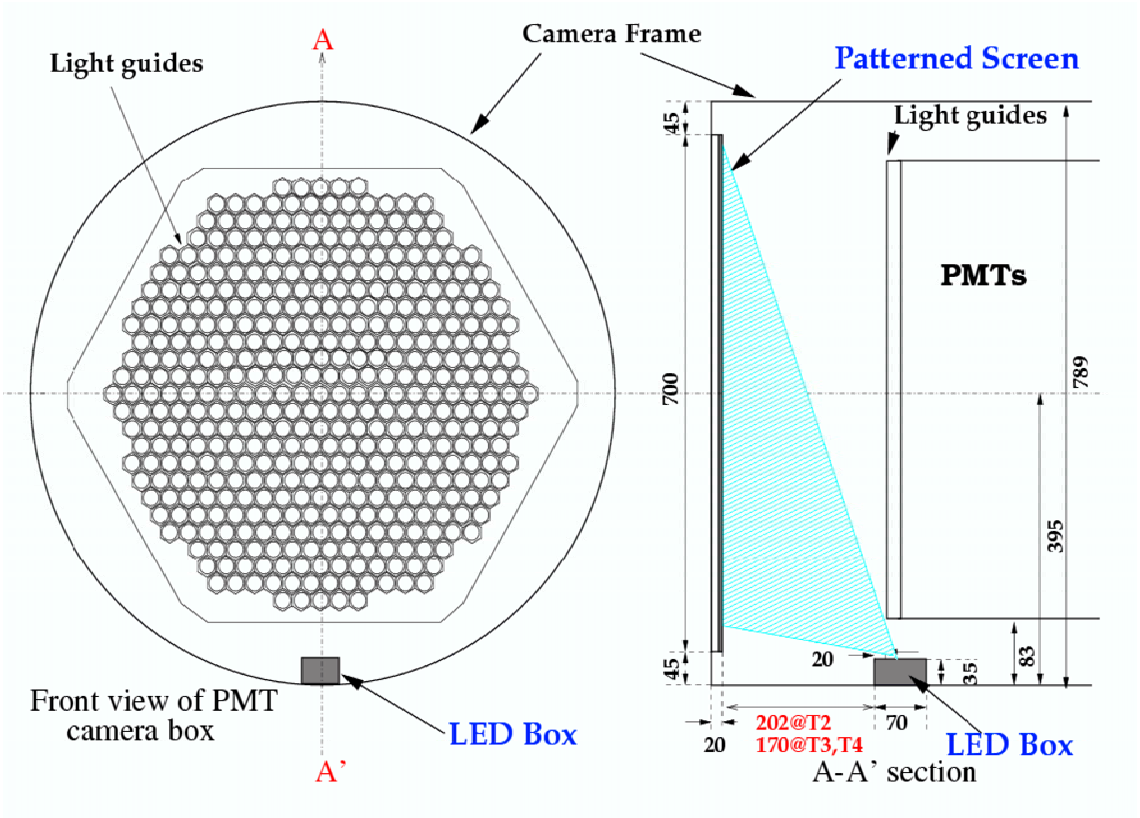

Figure 7.1: Set up of the "Konan LED" calibration run.

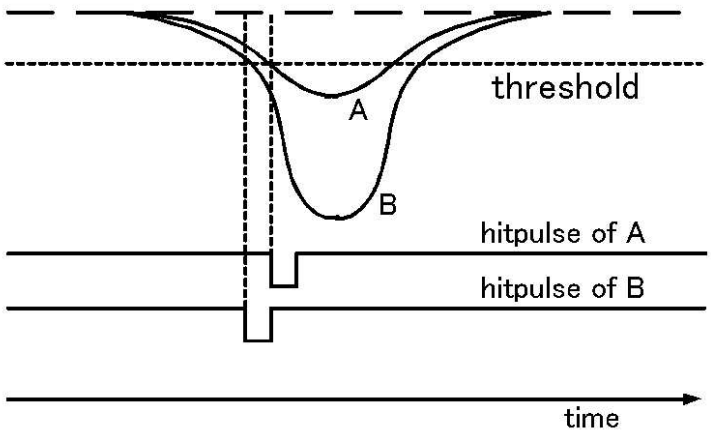

Figure 7.2: Schematic diagram of the time walk effect of hit pulses. The arrival timing of the discriminated pulse has offset depending on its pulse height.

10 ns. The relation between the arrival timing (TDC value) and the pulse height (ADC counts) was measured by changing the LED luminosity.

Target Observation Runs

ON-source run An ON-source run simply aims at the exposure of the target object. Sometimes the tracking position is deliberately displaced from the target positions depending on the observation mode or the circumstances of the target.

OFF-source run Even after the event selection with the imaging method, cosmic-ray background events still remain in ON-source run data. Therefore we need to know the background level to evaluate the significance of the gamma-ray signal. The background data for a compact source are taken simultaneously in ON-source run using wobble mode in a stereoscopic observation. On the other hand, we cannot take the background region from the ON-source view for broad sources. We then need extra OFF-source observation for these sources (see Chapter 5-1.2 for details).

The types of the runs are summarized in Table 7.1.

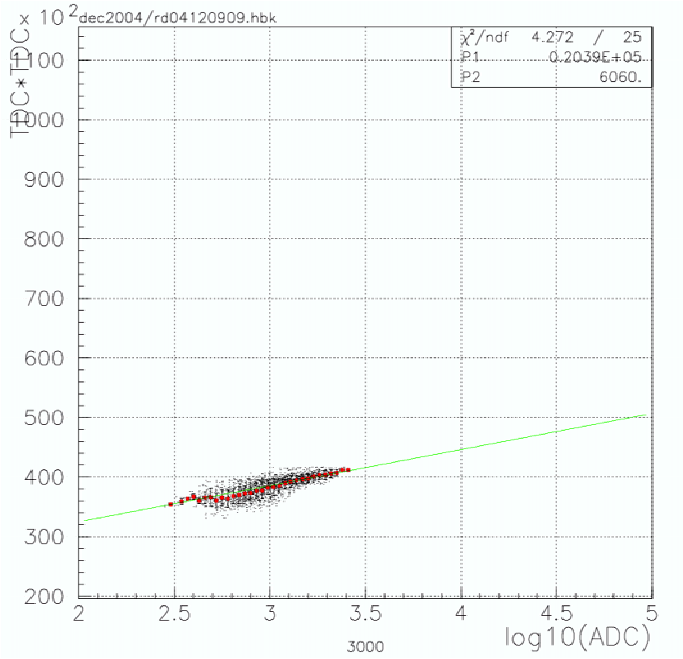

Figure 7.3: Correction of the time-walk. The x-axis is $\log_{10}$ ADC, and the y-axis is TDC^2

Table 7.1: Data sets in an observation night of the CANGAROO-III.

run name	trigger	purpose
ADC LED run	pulser	ADC to photoelectron conversion
ADC LED pedestal run	pulser	ADC to photoelectron conversion
TDC LED run	pulser	Time-walk correction
TDC LED pedestal run	pulser	Time-walk correction
ON-source run	shower	Target observation
OFF-source run	shower	Background measurement

§ 2 Data Calibration

2.1 Conversion from ADC Counts to the Number of Photoelectrons

ADC count is written using the number of photoelectrons ($n_{\text{ph.e.}}$, hereafter) in a PMT as

$$\begin{aligned} (\text{ADC count}) &= n_{\text{ph.e.}} \times (\text{PMT gain}) \times (\text{Amp. gain}) \times (\text{ADC constant}) \quad (7.1) \\ &\equiv n_{ph.e.} \times C_{ADC}. \quad (7.2) \end{aligned}$$

C_{ADC} is the ADC digitization constant. Assuming that the distribution of the photoelectrons obeys the Poisson statistics, the following relation is obtained:

$$\sigma_{\text{ph.e.}} = \sqrt{\mu_{\text{ph.e.}}} \quad (7.3)$$

μ: mean

σ: standard deviation.

From Eq.(7.2), ADC count is simply linked linearly with the number of photoelectrons by C_{ADC}, then we get the following relation.

$$\sigma_{\text{ADC}} = C_{\text{ADC}} \times \sigma_{\text{ph.e.}} = C_{\text{ADC}}\sqrt{\mu_{\text{ph.e.}}} = C_{\text{ADC}}\sqrt{\frac{\mu_{\text{ADC}}}{C_{\text{ADC}}}}. \quad (7.4)$$

Thus, C_{ADC} is simply determined from the observation data without any assumption as

$$C_{\text{ADC}} = \frac{\sigma^2_{\text{ADC}}}{\mu_{\text{ADC}}}. \quad (7.5)$$

The calibrated number of photoelectrons ($n_{\text{ph.e.}}$) is described as

$$n_{\text{ph.e.}} = \frac{\text{ADC} - \text{pedestal}}{C_{\text{ADC}}}. \quad (7.6)$$

This value is important for the energy determinations. It scales the energy of real data from Monte Carlo data. If the C_{ADC} is deviated by over 80 % from the averaged C_{ADC} for all 427 PMTs, that PMT is treated as the calibration failure PMT, and tagged as "bad channels" in the calibration. If C_{ADC} is 1/5 or less times as small as the average for the all channels, or 5 or more times as large, that channel is also marked as a bad channel. Such PMTs are not used in the analysis.

2.2 Time-Walk Correction

When the shape of the analogue signal from the PMT is assumed as Gaussian, the timing of the discriminated signal is approximately written as

$$T_c = \sqrt{P_1 \log(\mathrm{ADC}) + P_2}, \tag{7.7}$$

where P_1, P_2 are the constants obtained from the calibrated observation data. We make the plot of $(\mathrm{TDC})^2$ versus $\log(\mathrm{ADC})$ for each PMT, and fit it with a linear function (Fig.7.3). Thus, raw TDC count is corrected as

$$T_{\mathrm{start}} = 0.78 \times (T_{\mathrm{start\ raw}} - T_c)\ \mathrm{ns}. \tag{7.8}$$

Here, 0.78 is the TDC timing resolution.

§ 3 Reduction of Night Sky Background

3.1 Clustering

Generally, data of IACTs suffer from the night sky background (NSB) including star lights and artificial lights. Photons from the NSB scatter uniformly on the camera with random arrival timing, while those from gamma-ray or cosmic-ray shower make clear cluster images, and also the arrival timings of them are quite concentrated within about 10 ns. To minimize the effect of the NSB, we selected clustered images using the information of ADC count and TDC hit timing.

The ADC threshold was set for each PMT since the channels having small ADC count are considered as an accidental hit by the NSB. We set the threshold of 5 ph.-e. for each PMT to remove the NSB. Next requirement the cluster size of the image on the camera. Since a shower event should make a cluster of hit channels, we required at least 5-neighboring hits (Thresholded 5-adjacent; T5a). This requirement of 5 hits is large enough to obtain accurate axes of the clusters, which provide the shower direction.

3.2 TDC Distributions

In the IACTs observation, the arrival direction of the Čerenkov photons fluctuate, which might cause the inaccuracy of the trigger timing. We average the hit timings of the PMTs in order to correct the fluctuations. In order to correct this fluctuation

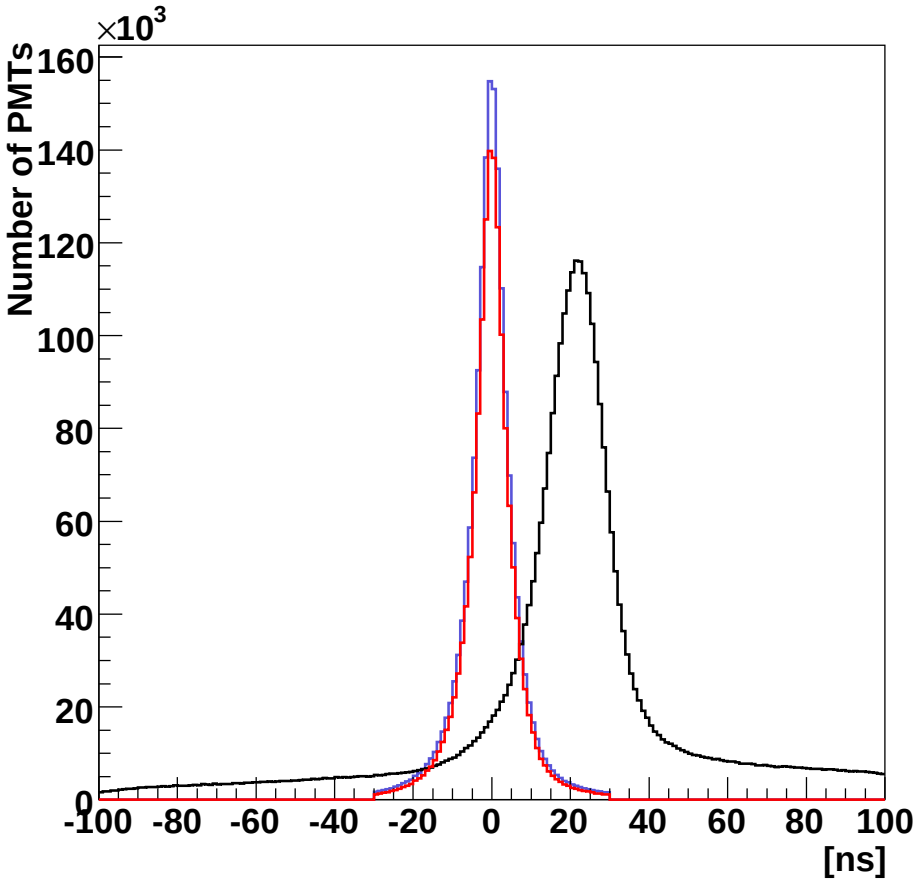

Figure 7.4: Distributions of TDC start time of all hit PMTs at 3 steps of data reduction in a typical run (Crab observations). Black: The distribution from calibrated raw data. Blue: The distribution after the average correction and set timing window of ±30 ns. Red: The distribution after the clustering cut.

of the trigger timing event by event, the average of the hit timings are calculated in each shower. This calculation is done for all PMTs which survived first clustering cut (details are described in the previous selection). The averaged timings of each event are adjusted to 0. The timing distributions before and after this correction are shown in Fig.7.4 as the black and the blue curves, respectively. The FWHM of the timing distribution was improved from $\sim$20 ns to $\sim$10 ns. We set the time window to the timing deviation from the average (TDC cut). The width of the time window is typically 27 ns. Although the shower expansion time is about 10 ns, the mean timing of small clusters are shifted to that extent. We apply T5a cut again to the images formed by the PMTs survived this TDC cut. The distribution after this second TDC cut is shown by the red curve in Fig.7.4.

§ 4 Cloud Cut and Elevation Cut

After the selections mentioned above, only the shower events generated by protons and gamma-rays remain. Therefore, the shower rate should be stable, and it can be used to monitor the conditions of the atmosphere. The data of which rate is significantly lower than the averaged event rate is classified in the data under cloudy weather. We set the criterion for the shower rate, and exclude the low-rate data from the analysis data (Cloud cut). The data at low elevations are also removed (Elevation cut). Since the path of Čerenkov lights is proportional to $1/\cos$(zenith angle), the observation of at a lower elevation has a lower detection acceptance for low-energy showers due to the absorption of the thicker atmosphere.

§ 5 Likelihood Method

We defined the image parameters as described in Chapter 3-3.1, Figure 7.6 shows the distributions of the image parameters as a function of energy for the shower events in the OFF source region and the Monte Carlo gamma-ray data. The distributions of the cosmic-ray showers by the Monte Carlo simulations are similar to those of the OFF source shower data. However there are slight differences due to the difficulty in generating hadronic showers by GEANT3.21 and some simplifications of the Monte Carlo simulations. Therefore we adopted the OFF source data as the background. As is seen in Fig.7.6, the distributions of the image parameters vary depending

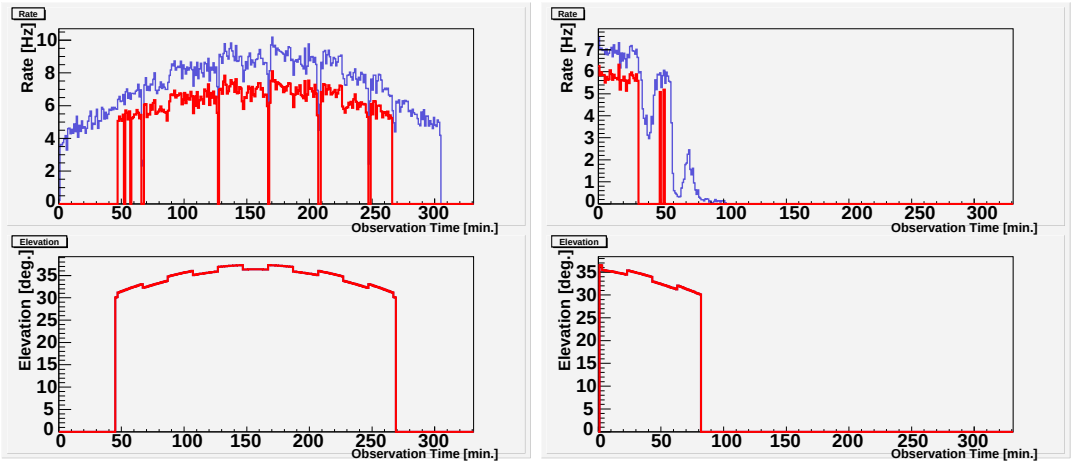

Figure 7.5: Upper: Event rate (blue lines) and shower rate after Cloud cut (red). Lower: Elevation distribution after Elevation cut. The tandem pairs are for the same runs. We showed them for the two runs taken under the good (left panels) and the bad (right panels) weather conditions.

on their sum-ADC value, namely the energy. Also, those distributions are different between for the gamma-rays and for the protons reflecting the shower developments. From those distributions, the probability density functions (PDFs) are obtained for both gamma-rays (PDF_γ) and cosmic rays (PDF_p) in each energy band. Figure 7.7 shows the PDFs for each of WIDTH and LENGTH normalized to unity. The PDF for an event is obtained as the product of the PDFs of WIDTH and LENGTH in Fig.7.7:

$$PDF_\gamma = PDF_\gamma(\mathrm{LENGTH}) \times PDF_\gamma(\mathrm{WIDTH}) \tag{7.9}$$

$$PDF_\mathrm{p} = PDF_\mathrm{p}(\mathrm{LENGTH}) \times PDF_\mathrm{p}(\mathrm{WIDTH}) \tag{7.10}$$

In order to obtain a likelihood parameter as an indicator of gamma-ray-like events, the likelihood ratio LR is defined as followings:

$$LR = \frac{PDF_\gamma}{PDF_\gamma + PDF_\mathrm{p}}. \tag{7.11}$$

In a stereoscopic observation data, LR is obtained for each telescope ($LR^{\mathrm{T}i}$; i =2,3,4), and LR for the stereo events is defined as

$$LR_\mathrm{stereo} = \prod_{\mathrm{Telescope}} LR^{\mathrm{T}i}. \tag{7.12}$$

Gamma-ray events should show a peak at 1, and background events should at 0 in the distribution of this parameter LR as shown in Fig.7.8.

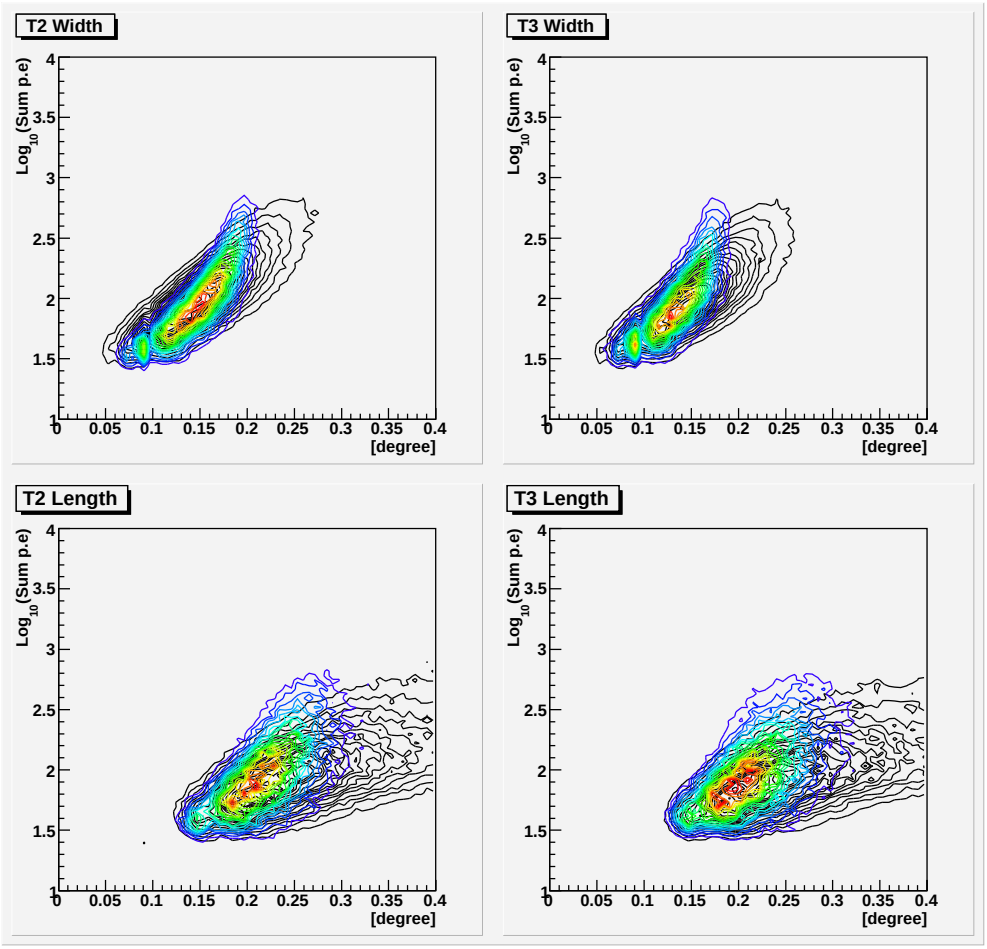

Figure 7.6: Distributions of WIDTH and LENGTH for each telescopes. The left and the right figures are for T2 and T3, respectively. The upper panels show those of WIDTH, the lower panels show those of LENGTH.

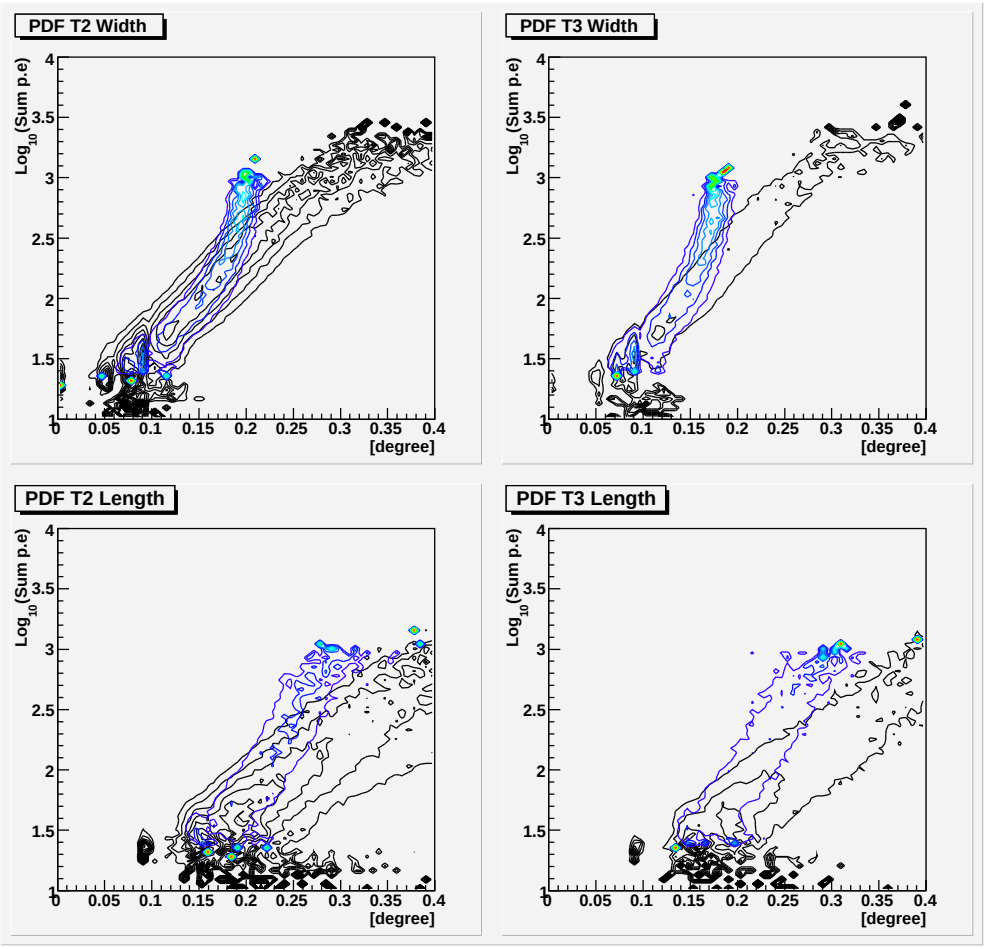

Figure 7.7: Probability density function (PDF) distributions for each of WIDTH and LENGTH. The left and the right figures are for T2 and T3, respectively, and the upper panels are those of WIDTH and the lower panels are those of LENGTH.

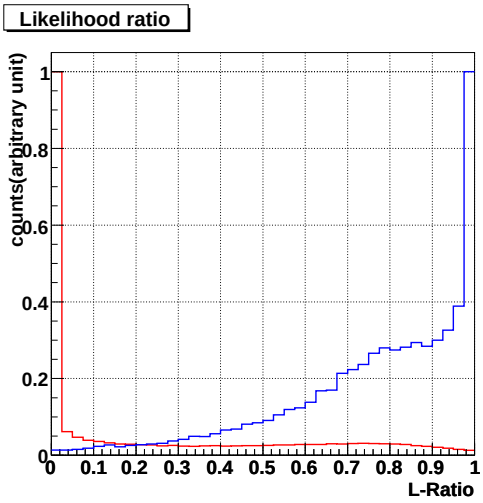

Figure 7.8: Likelihood ratio distributions for the simulated gamma-ray events (blue) and the OFF-source region events (red).

§ 6 Stereo Analysis

6.1 Stereo Coincident Event Combination

During the observation, the stereo builder (see Chapter 4-§ 6) tags the triggered events with the event serial number for stereo events, and records the triggered telescope ID in a stereo event and the serial trigger number in each telescope. In the off-line analysis, we can choose two or three telescopes as the combination of stereo events. For each stereo event number, we search the triggered telescope ID and their individual serial number, and combine the data of the telescopes contributing to the stereo event.

6.2 Arrival Direction

The arrival direction of the shower should be simply reconstructed by the calculation of the intersection point of the major axes of the shower images on the triggered telescopes (Fig.7.9). The determination accuracy of the intersection point of the major axes of two ellipses depends on the following factors. The equations of the major axes on the camera plane are written as linear functions

$$y = m_1(x - x_1) + y_1,\ \ y = m_2(x - x_2) + y_2$$

$$(x_i,\ y_i)\ :\ \text{Image centroid of telescope } i,$$

m_i : Inclination angle of their major axis,

where $(x,\ y)$ are the coordinates on the camera plane. The intersection-point coordinate (x_0, y_0) is simply derived as

$$x_0 = \frac{y_2 - y_1 + m_1 x_1 - m_2 x_2}{m_1 - m_2}, \quad y_0 = m_1(x_0 - x_1) + y_1. \tag{7.13}$$

Since x_0 and y_0 are measured in the unit of degree, they are often written in the terms of θx and θ_y. The errors of the inclination angles Δm_1 and Δm_2 cause the errors of the intersection position (in x direction) as

$$\Delta x = \frac{\Delta m_1(x_1 - x_0) + \Delta m_2(x_2 - x_0)}{m_1 - m2}. \tag{7.14}$$

Here x_0 is the intersection-point coordinate derived from Eq.(7.13). This means that the accuracy of the arrival-direction determination is inversely proportional to the difference in the inclination angle $(m_1 - m_2)$, that is the opening angle $\theta_{\rm open}$ in Fig.7.9. It causes a serious problem for the large zenith angle (z) observation. The light pools are elongated with the factor of $\cos 2z$, and the core distance tends to be large. Therefore, the opening angle becomes small, which results in a poor angular resolution ($\Delta x \propto (m_1 - m_2)^{-1}$ from Eq.(7.14)).

The reconstruction accuracy also depends on $x_1 - x_0$ from Eq.(7.14), which is the distance between the centroid of the image and the intersection point (this distance is denoted as "IP Distance" or "IPD", hereafter).

§ 7 Evaluation of Gamma-ray Events

7.1 θ^2 Distributions

In the stereoscopic IACT observation, we evaluate the existence of the signal with the θ^2 distribution. θ is the distance of the shower-arrival direction from the target position in the unit of degree. Once the intersection point $(\theta_x,\ \theta_y)$ is derived, it is simply calculated as

$$\theta^2 = \theta_x^2 + \theta_y^2. \tag{7.15}$$

The θ^2 of the background events should be approximately flat all over the FOV, while that of gamma-rays should concentrate to the source position.

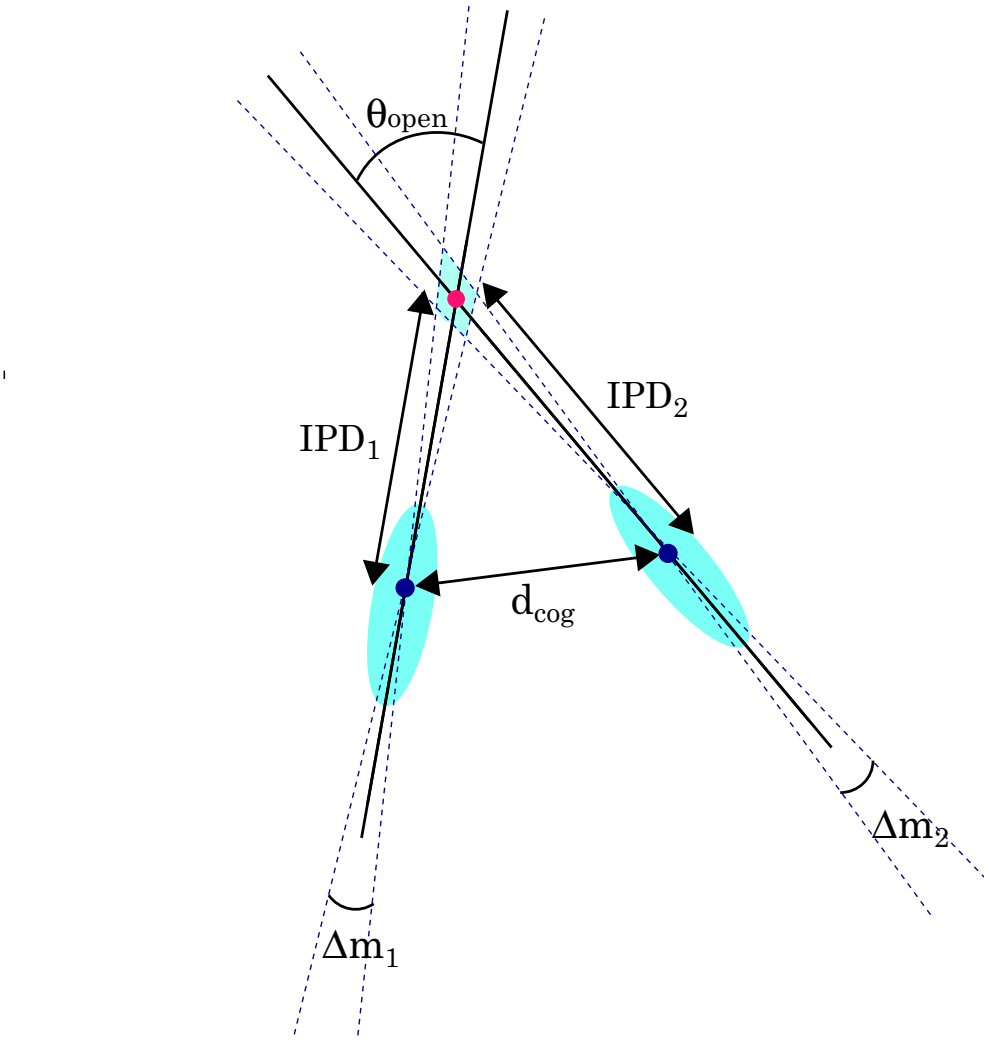

Figure 7.9: Determination of the shower arrival direction. For the accuracy of the axis direction δm_1 and δm_2, the intersection point fluctuates in the hatched box area.

7.2 Significance

In order to evaluate the reliability of the significance of the signal on the background, we adopted the statistical method proposed by Li & Ma (1983), which is generally used in cosmic-ray physics. We define the situation that the telescopes pointed in the direction of a source-suspected target for a certain time $t_{\rm on}$ and counted $N_{\rm on}$ events, and then they turned for background measurement for a time interval $t_{\rm off}$ and counted $N_{\rm off}$ events. The quantity α is the ratio of the ON-source time to the OFF-source time, $\alpha = t_{\rm on}/t_{\rm off}$. Then the number of background events included in the ON-source counts $N_{\rm on}$ is estimated as

$$\hat{N}_B = \alpha N_{\rm off}. \tag{7.16}$$

N_S, the probable number of gamma-ray events contributed by the source, is

$$N_S = N_{\rm on} - \hat{N}_B = N_{\rm on} - \alpha N_{\rm off}. \tag{7.17}$$

Since $N_{\rm on}$ and $N_{\rm off}$ are results of two independent measurements, the variance of the signal defined by Eq.(7.17) is calculated as

$$\sigma^2(N_S) = \sigma^2(N_{\rm on}) + \sigma^2(\alpha N_{\rm off}) = \sigma^2(N_{\rm on}) + \alpha^2\sigma^2(N_{\rm off}). \tag{7.18}$$

Then the estimate of the standard deviation of N_S is

$$\sigma(\hat{N}_S) = \sqrt{\hat{\sigma}^2(N_{\rm on}) + \alpha^2\hat{\sigma}^2(N_{\rm off})} = \sqrt{N_{\rm on} + \alpha^2 N_{\rm off}}. \tag{7.19}$$

Defining the significance S as the ratio of the excess counts above the background to its standard deviation, we have

$$S = \frac{N_S}{\hat{\sigma}(N_S)} = \frac{N_{\rm on} - \alpha N_{\rm off}}{\sqrt{N_{\rm on} + \alpha^2 N_{\rm off}}}. \tag{7.20}$$

The above formula is simply derived from the Poisson law of the counts $N_{\rm on}$ and $N_{\rm off}$. The discrepancy between the distribution calculated by Eq.(7.20) for Monte Carlo simulation samples and the expected normal distributions are considerable in the case $\alpha \neq 1$ (Fig.7.10). In the wobble mode observation, generally $\alpha > 1$, and it is necessary to improve further the estimate for the standard deviation of N_S.

Usually Eq.(7.16) is used to estimate the background. However, in the assumption that the gamma-ray events are quite few and the almost all the recorded events are due to the background, both ON-source and OFF-source counts follow a Poisson distribution. The expectations and the variance are $\langle N_B \rangle$ for ON-source, and

$\langle N_B\rangle/\alpha$ for OFF-source, where $\langle N_B\rangle$ is the expectation of the background counts in ON-source time $t_{\rm on}$. Then Eq.(7.18) is rewritten as

$$\sigma^2(N_S) = \sigma^2(N_{\rm on}) + \alpha^2\sigma^2(N_{\rm off}) = (1+\alpha)\langle N_B\rangle, \tag{7.21}$$

and the standard deviation of N_S,

$$\sigma(N_S) = \sqrt{(1+\alpha)\langle N_B\rangle}. \tag{7.22}$$

Now we got a more accurate estimate of $\langle N_B\rangle$, the expected number of the background events in $t_{\rm on}$, by using all the observed data ($N_{\rm on}$, $N_{\rm off}$):

$$\langle\hat{N}_B\rangle = \frac{N_{\rm on}+N_{\rm off}}{t_{\rm on}+t_{\rm off}}t_{\rm on} = \frac{\alpha}{1+\alpha}(N_{\rm on}+N_{\rm off}). \tag{7.23}$$

Then form Eq.(7.22) the estimate of the deviation of N_S is

$$\hat{\sigma}(N_S) = \sqrt{(1+\alpha)\langle\hat{N}_B\rangle} = \sqrt{\alpha(N_{\rm on}+N_{\rm off})}, \tag{7.24}$$

and the significance is

$$S = \frac{N_S}{\hat{\sigma}(N_S)} = \frac{N_{\rm on}-\alpha N_{\rm off}}{\sqrt{\alpha(N_{\rm on}+N_{\rm off})}}. \tag{7.25}$$

Li and Ma (1983) showed the distribution of significances evaluated by Eq.(7.25) is closer to a standard normal curve than those by Eq.(7.20) (see Fig.7.10).

Another way of estimating the significance is by use of the method of hypotheses test in the mathematical statistics. The theorem used here is used to solve a test problem of a composite hypothesis where just partial parameters are involved. In our case, the observed data are $N_{\rm on}$ and $N_{\rm off}$, with two unknown parameters: $\langle N_S\rangle$ and $\langle N_B\rangle$. "Null hypothesis" is $\langle N_S\rangle = 0$, and "alternative hypothesis" is $\langle N_S\rangle \neq 0$.

If the null hypothesis $\langle N_S\rangle$ is true, we can take the value of $\sqrt{-2\ln\lambda}$ as the significance of the observed result, where λ is the maximum likelihood ratio:

$$\lambda = \left[\frac{\alpha}{1+\alpha}\left(\frac{N_{\rm on}+N_{\rm off}}{N_{\rm on}}\right)\right]^{N_{\rm on}}\left[\frac{1}{1+\alpha}\left(\frac{N_{\rm on}+N_{\rm off}}{N_{\rm off}}\right)\right]^{N_{\rm off}}. \tag{7.26}$$

The significance S is written as

$$S = \sqrt{-2\ln\lambda} = \sqrt{2}\left\{N_{\rm on}\ln\left[\frac{1+\alpha}{\alpha}\left(\frac{N_{\rm on}}{N_{\rm on}+N_{\rm off}}\right)\right] + N_{\rm off}\ln\left[(1+\alpha)\left(\frac{N_{\rm off}}{N_{\rm on}+N_{\rm off}}\right)\right]\right\}^{1/2}. \tag{7.27}$$

For the purpose of checking the three methods of estimating statistical significance, Monte Carlo results are shown in Fig.7.10. The lines indicate the standard

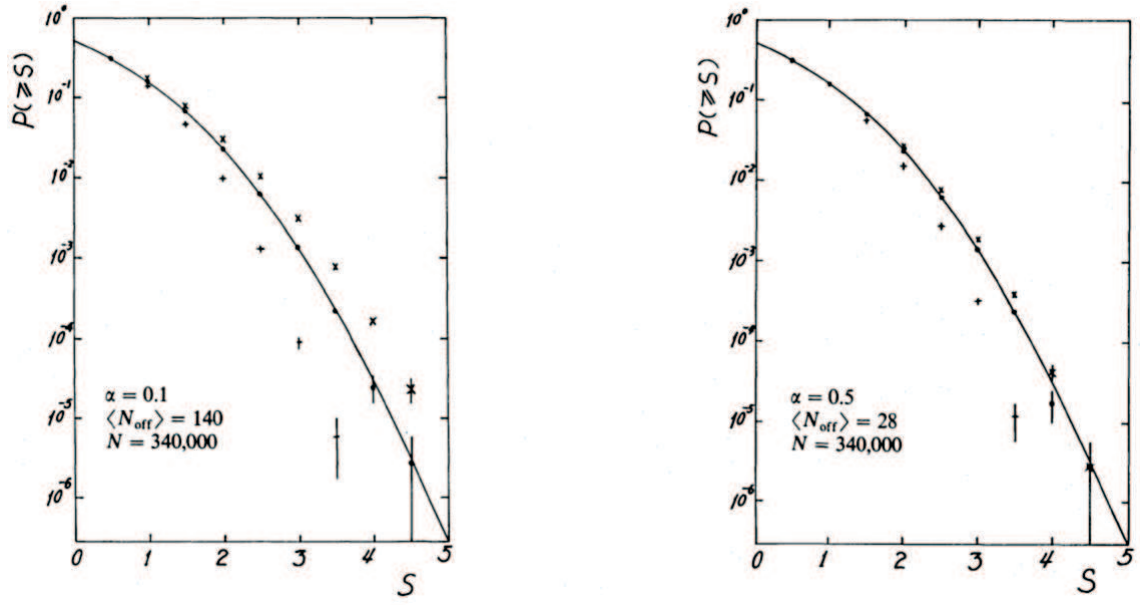

Figure 7.10: Integral frequency distributions of the significance of the Monte Carlo samples. Pluses, crosses, and filled circles are from Eq.(7.20), (7.25) and (7.27), respectively. N is the number of samples for the Monte Carlo procedure. The curves indicate the standard normal distribution.

normal distribution. Equation (7.25) systematically underestimates the significance for $\alpha < 1$ and overestimates for $\alpha > 1$. Equation (7.25) gives better significance than Eq.(7.20), but the distributions of the significances by Eq.(7.27) are generally most consistent with the expected Gaussian probabilities. Therefore we adopt the significance calculated by Eq.(7.27).

7.3 Differential Fluxes

In order to obtain the differential flux from the observed gamma-ray events, the binning of the energy is necessary. For the experimental data, the energy of the shower is obtained in the form of the ADC counts of the shower image (ADC-sum). For IACT experiments, the energy of the real data event is estimated only by the comparison with the simulation data. Therefore, the differential flux should be expressed as a function of ADC-sum. The mean energy $\overline{E}(x_{\rm l}, x_{\rm u})$ of the energy region of ADC-sum between $x_{\rm l}$ and $x_{\rm u}$ was estimated from the mean of each distribution.

By definition,

$$\int_{E_{\rm min}}^{E_{\rm max}} \left.\frac{dF}{dE}\right|_{\rm MC} dE = \frac{N_{\rm MC}^{\rm tot}}{S_0 T_{\rm MC}}, \tag{7.28}$$

where $E_{\rm max}$ and $E_{\rm min}$ are the maximum and minimum energy of the generated gamma-ray events in the Monte Carlo simulation, respectively, and $N_{\rm MC}^{\rm tot}$ is the number of the generated events in the simulation. S_0 is the area size at the ground where the gamma-rays are generated, which was converted considering the observation zenith angles. When events are spattered to an area of S' from the zenith angle of z, $S_0 = S' \cos^2 z$. Here we temporally introduced the hypothetical observation time $T_{\rm MC}$ for the simulation data. Simulation events were generated in the following power law spectrum.

$$\left.\frac{dF}{dE}\right|_{\rm MC} = C_0 E^{-\alpha}. \tag{7.29}$$

Here C_0, E, α are a constant, the energy of the gamma-rays, and the spectral index, respectively. For both the observed and simulated data, the differential fluxes are defined as

$$\int_{x_{\rm l}}^{x_{\rm u}} \frac{dF}{dE} dx = \frac{N_{\rm obs}(x_{\rm l}, x_{\rm u})}{S_{\rm eff}(x_{\rm l}, x_{\rm u}) T_{\rm ON}}, \tag{7.30}$$

and

$$\int_{x_{\rm l}}^{x_{\rm u}} \left.\frac{dF}{dE}\right|_{\rm MC} dx = \frac{N_{\rm MC}(x_{\rm l}, x_{\rm u})}{S_{\rm eff}(x_{\rm l}, x_{\rm u}) T_{\rm MC}}. \tag{7.31}$$

Equation (7.30) is the differential flux in the domain of the ADC-sum between $x_{\rm l}$ and $x_{\rm u}$ of the observed data, and Eq.(7.31) is that of the Monte Carlo data. By substituting Eq.(7.29) to Eq.(7.28) and carrying out the integration,

$$T_{\rm MC} = \frac{1-\alpha}{E_{\rm max}^{1-\alpha} - E_{\rm min}^{1-\alpha}} \frac{N_{\rm MC}^{\rm tot}}{C_0 S_0} \tag{7.32}$$

is obtained. The left side of Eq.(7.31) is approximated as $C_0 \overline{E}^{-\alpha}$ using Eq.(7.29). By dividing Eq.(7.30) by Eq.(7.31), we obtain the differential flux formula for the domain of the ADC-sum between $x_{\rm l}$ and $x_{\rm u}$:

$$\int_{x_{\rm l}}^{x_{\rm u}} \frac{dF}{dE} dx = \frac{(1-\alpha)\overline{E}^{-\alpha}}{E_{\rm max}^{1-\alpha} - E_{\rm min}^{1-\alpha}} \frac{N_{\rm MC}^{\rm tot}}{N_{\rm MC}(x_{\rm l}, x_{\rm u})} \frac{N_{\rm obs}(x_{\rm l}, x_{\rm u})}{S_0 T_{\rm ON}}. \tag{7.33}$$

§ 8 Crab Analysis

The Crab analysis with the CANGAROO-III telescopes is difficult because of the following two reasons. One is the observation at large zenith angle as shown in

Fig.5.2. The other is the star of the third magnitude in the Crab FOV. A third-magnitude star makes the HV supplies turned off for the PMTs within $\pm 0.^{\circ}3$ from the star, which causes the nonuniformity in the FOV.

The Crab Pulsar/Nebula was observed in "wobble mode" as is mentioned in § 3, and the background was estimated in the same FOV as the ON-source region. Normally six circles were sampled as the background control regions without overlapping.

8.1 Analysis Procedure and Resuls

The analysis was proceeded in the following steps, which are also adopted in the analysis of RX J0852.0−4622 in Chapter 8.

1. **Shower selection** Here we remove the data at elevations below 30° (Elevation cut) and selects the shower events that satisfy the criteria of T5a (details in § 3). The event rate after this selection is called "shower rate". We checked the shower rate by three telescope coincidence and excluded the data of which shower rate is below 5 Hz (Cloud cut). The shower rates of the Crab observation is shown in Fig.7.5 for the typical one and the excluded data. The total effective observation time selected here is 1367.3 min.
   Then we applied the following cuts to find the gamma-ray events. The criteria adopted here are summarized in Table 7.2.

2. **Outermost 1 layer cut** The images including the hit of the PMTs forming the outermost 1 layer are rejected, since these images are truncated by the edge of the camera and sometimes mimic a gamma-ray. Also, they possibly worsen the accuracy of the shower direction and the energy resolution. Details are in Chapter 8-§ 4.

3. **Likelihood ratio cut** The gamma-ray-like events are selected using their likelihood ratio.

   In the observation by N telesopes, the image axes are intersected for all pairs of telescopes resulting in $N(N-1)/2$ points. The schematic for $N = 3$ is shown in Fig.7.11. In the case of $N \geq 3$, we tried two different methods to define one intersection point with reflecting the determination accuracy of each point

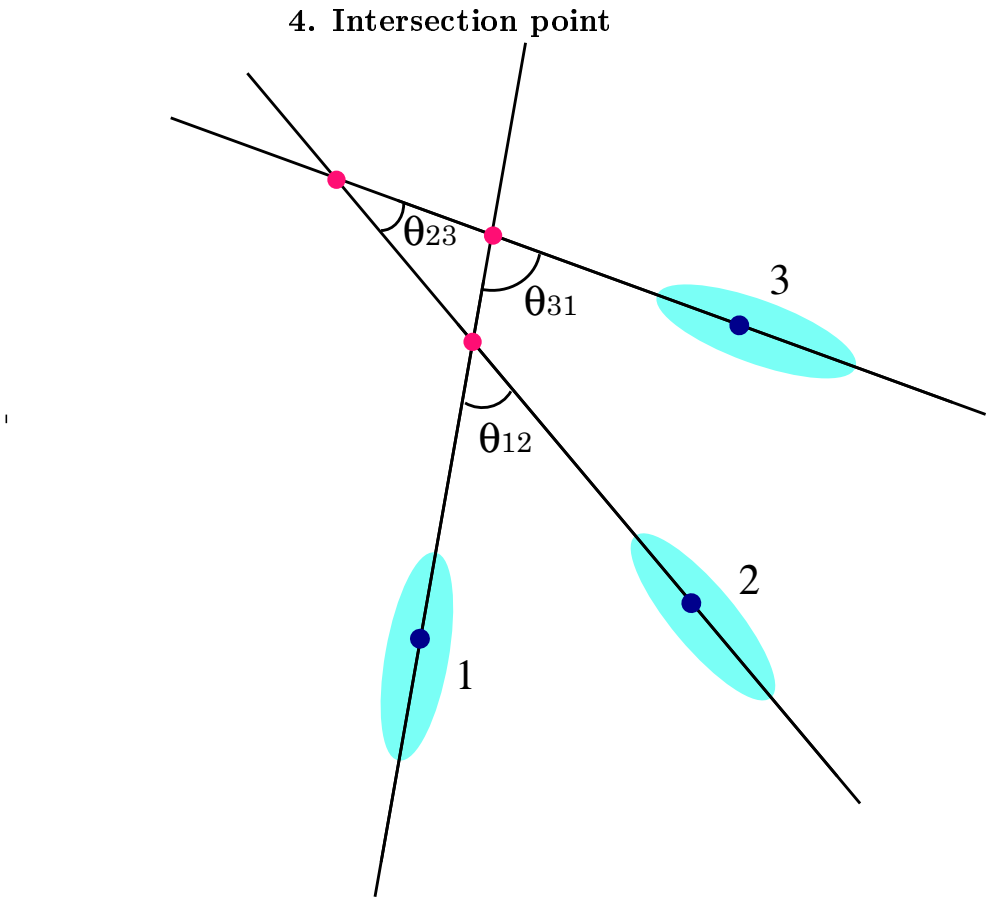

Figure 7.11: Intersection points by three telescope images. In order to define one, they are averaged weighted with the sine of the opening angle θ_{mn} in the sine-average method.

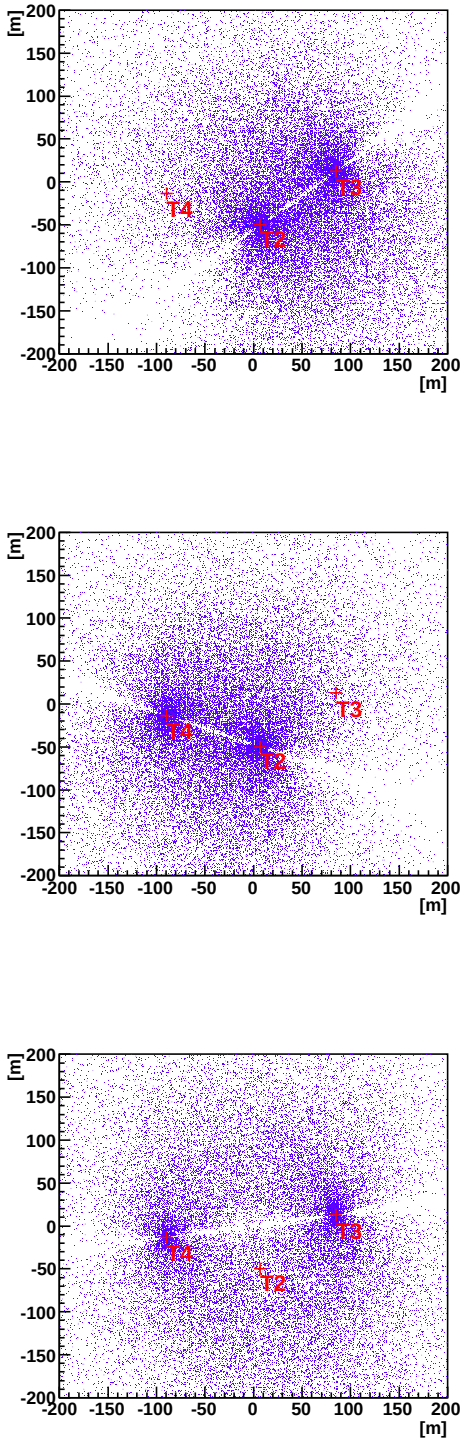

Figure 7.12: Reconstructed shower core locations for the observation data. The intersection points were calculated by any 2 telescopes. From top to bottom, T2–T3, T2–T4, and T3–T4. The locations of the telesopes are indicated by crosses.

Method-1: weighted with the opening angle. The resulting $N(N-1)/2$ intersection points (x_{mn}, y_{mn}) for a combination of T_m and T_n are averaged with being weighted with the sine of the angle between the image axes θ_{mn}, since the image pairs with a large stereo angle provide the most precise determination of the shower axis (Sec. 6.2). The intersection point $(x_{\rm IP}, y_{\rm IP})$ are written as folowings in this method.

$$x_{\rm IP} = \Sigma x_{mn} \sin\theta_{mn} \tag{7.34}$$

$$y_{\rm IP} = \Sigma y_{mn} \sin\theta_{mn} \tag{7.35}$$

Method-2: IP constraint fit. This fitting method is based on the facts on the ideal shower axis. First, the ideal shower axis, which overlaps with the LENGTH axis, should be vertical to the WIDTH axis, and therefore WIDTH, from its definition, is smallest when the shower axis is correct. Secondly, DISTANCE (the distance from the target position to the shower centroid) should be equal to IPD (see Section 6.2), and ideally its value depends only on the observation elevation angle, which is derived by simulation for each observation target. However, DISTANCE and IPD are not equal in the observation . Their distribution calculated by the Monte Carlo simulation is shown in Fig.7.13. The distribution should have a peak along the light blue line. Then we search the point which minimizes the folloing parameter of χ^2 by scanning the intersection point.

$$\chi^2 \equiv \sum_{{\rm Tel}_i} \left(\frac{{\rm WIDTH}^2}{\sigma_{\rm W}^2} + \frac{(\langle {\rm DISTANCE} \rangle - {\rm IPD})^2}{\sigma_{\rm D}^2} \right), \tag{7.36}$$

where $\sigma_{\rm W}$ and $\sigma_{\rm D}$ are the variance of WIDTH and DISTANCE, respectively, and $\langle$DISTANCE$\rangle$ is the mean of DISTANCE, which we assumed as the ideal expected value of DISTANCE. All the values are derived by simulation, and for the Crab observation, $\sigma_{\rm D} = 0.26$ and $\langle {\rm DISTANCE} \rangle = 0.74$. The divisions by $\sigma_{\rm W}$ and $\sigma_{\rm D}$ are introduced to control the contribution of each term according to how their determination accuracy is reliable.

For the Monte Carlo data of the Crab Pulsar/Nebula (a point source at the zenith angles of average $55^{\circ}.2$), the comparison of the θ^2-distributions obtained

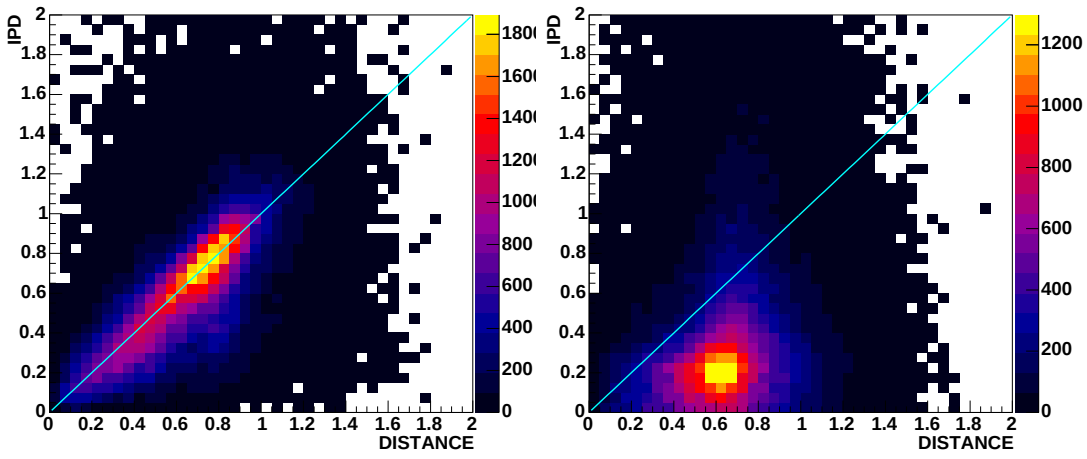

Figure 7.13: Relation between DISTANCE (lateral) and IPD (vertical) derived from the Monte Carlo data. Ideal gamma-ray events have the relation of DISTANCE=IPD, which is shown as the light blue lines. Left: A point source at moderately small zenith angles of average 19°.07. A beautiful correlation along the light blue line is seen. Right: A point source at zenith angles of average 55°.26 (a crab-like source). The peak of the distribution is not along the light blue line.

with Method-1 and Method-2 is shown in the right panel of Fig.7.14 as the blue and the red histogram. In the large zenith angle observation, since the opening angles tend to be small as described in Section 6.2, the result of Method-1 shows a poor resolution of the intersection point, and thus Method-2 should be adopted. Also, even in the two-telescope observation, where the intersection point can be calculated as exactly one particular point, the large zenith angle has the disadvantageous effect of a poor angular resolution as explained also in Section 6.2. the θ^2-distribution of simple intersection points was obtained with the simulation data as the blue histogram in the left panel of Fig.7.14, which has an unsharp peak toward $\theta^2 = 0$ deg^2. Then we calculated the intersection points with the fitting method (Method-2), and plotted the θ^2-distribution in the left panel of Fig.7.14 as the red histogram. These results show that Method-2 should be applied to such a case like our Crab observation in 2003. Hereafter, we adopt the method of IP constraint fit to the Crab analysis.

Figure 7.15 shows the radial distribution of the excess of gamma-rays from the Crab Pulsar/Nebula as a function of the reconstructed squared angular distance,

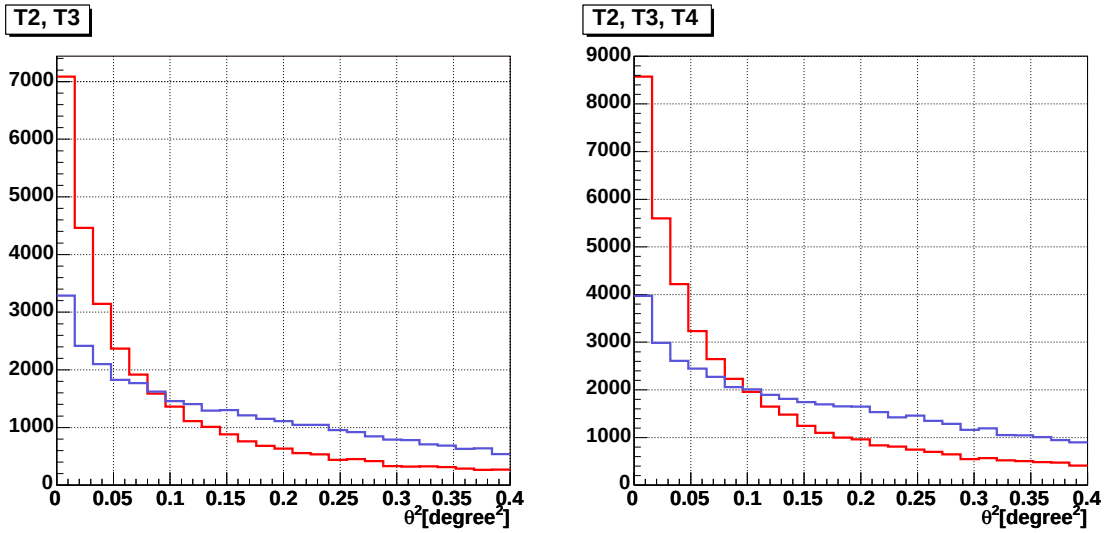

Figure 7.14: θ^2 distributions of the Monte Carlo data for Crab (a point source at zenith angles of average 55°.2) with two different methods. Left: For two-telescope observation (T2 and T3). The blue and the red line are with and without "IP constraint fit", respectively. Right: For three-telescope observation (T2, T3 and T4). The blue and the red line are by "weighted with sine" and by "IP constraint fit", respectively. They show that the method of IP constraint fit makes the peak sharper.

Table 7.2: Criteria for the Crab analysis.

Elevation cut	El $> 30°$
ADC (size) cut	$n_{\text{p.e.}} > 5$ ph.-e.
Cluster cut	T5a (CANGAROO-III standard)
TDC cut	$\lvert t - t_{\text{ave.}} \rvert < 30$ ns
Cloud cut	5 Hz
Edge Cut	Outermost 1 layer cut
Likelihood ratio cut	$LR > 0.1$

θ^2, from the nominal point of Crab. In the left figure, the distribution of the ON-source events is superimposed on that of the OFF-source events. The six background points were sampled as shown in Fig.5.1. The background data were normalized to the ON-source data with taking into account the area ratio of the sampling region of the signal region and the background region. Here, the background data were divided by 6. The distribution of excess in the right figure of Fig.7.15 was obtained by subtracting the normalized background data from the ON-source data. In the region $\theta^2 < 0.05$ deg^2, approximately corresponding to the point-spread function ($0^{\circ}.23$ in 1σ), an excess of 245.0 ± 48.0 events was found. The significance of the signal is 5.1σ, calculated with Eq.(7.27). For reference, we show the result derived with the $\sin^2\theta$ weighted method (Method-1) in Fig.7.16. We find the excess of gamma-ray events only in 2.4σ level with Method-1, which indicates the necessity of the IP fitting method.

The θ^2 distributions of each energy region are shown in Fig.7.17, and the mean energy, event counts, significance are summarized in Table 7.3. The differential flux of the gamma-ray emission from the Crab Pulsar/Nebula was calculated by Eq.(7.33). The parameters assigned to this formula were

$$\begin{aligned} S_0 &= 25000^2\pi/\cos^2(55^{\circ}.2) = 6.0 \times 10^9 [\mathrm{cm}^2] \\ \alpha &= 2.5 \\ N_{\mathrm{MC}}^{\mathrm{tot}} &= 2.41 \times 10^6 \\ E_{\mathrm{min}} &= 300 \text{ [GeV]} \\ E_{\mathrm{max}} &= 30000 \text{ [GeV]} \\ T_{\mathrm{ON}} &= 56739 \text{ [sec]}. \end{aligned} \tag{7.37}$$

The flux spectrum is shown in Fig.7.18. Our result shown as the red squares is consistent with the HESS result superimposed as the green squares.

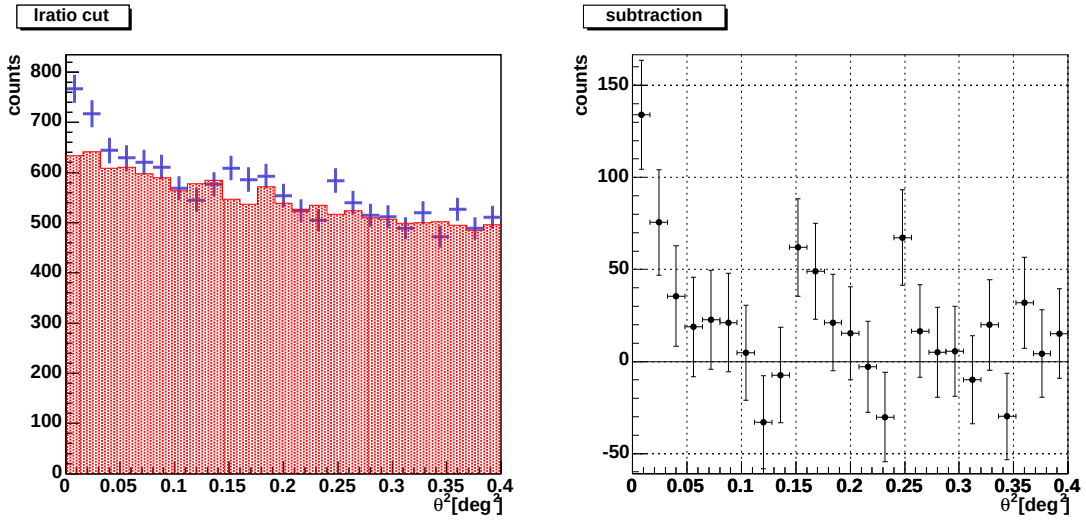

Figure 7.15: θ^2 distributions for the data of the Crab Pulsar/Nebula in 2003 with the likelihood method. The intersection points are obtained with fitting method. Left: The blue crosses are the distribution of the ON-source events with statistical errors, and the red hatched histogram is that of the background events. The event number of the background data is normalized to that of the ON-source data by the ratio of the effective observation time. Right: θ^2-plot of the excess of gamma-ray-like events. The excess events were 245.0 ± 48.0 events with the significance of 5.1 σ.

Table 7.3: Excess events of Crab in 2003 in each energy bin obtained with the likelihood method. The errors of excess number include only statistical ones.

SumADC[ph.-e.]	Mean energy[TeV]	Excess event	Statistical significance
50 to 100	2.6	91.8 ± 28.7	3.2
100 to 200	4.4	111.6 ± 32.7	3.4
200 to 400	7.0	39.3 ± 19.8	1.9
400 to 800	10.4	10.8 ± 8.0	1.4
800 to 1600	15.1	8.3 ± 2.2	3.7

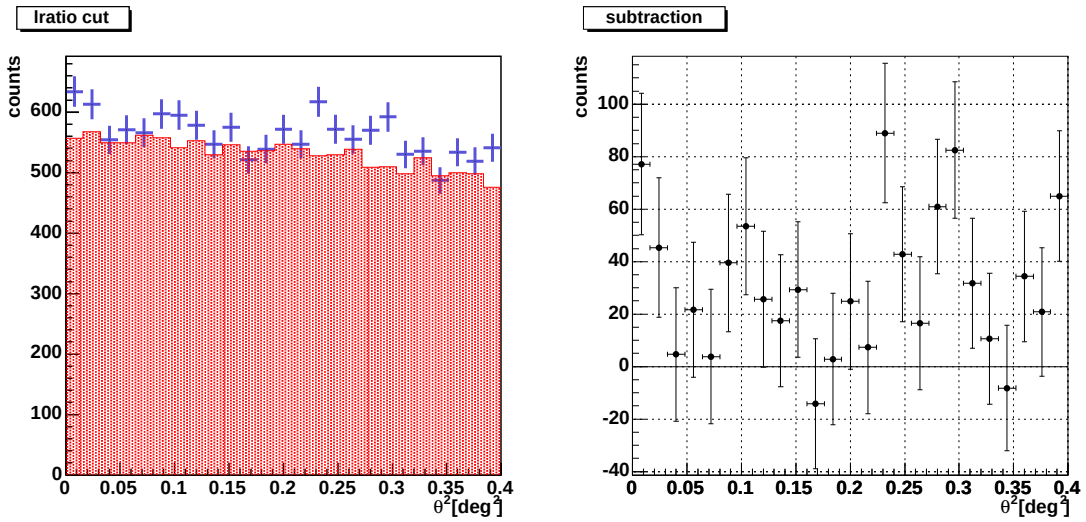

Figure 7.16: θ^2 distributions for the data of the Crab Pulsar/Nebula in 2003 with the likelihood method. The intersection points were derived without the fitting method. The significance of the excess of ON-source events is 2.4σ. Comparing with Fig.7.15, it is clear that the IP fitting method is necessary for this source. Left: The blue crosses are the distribution of the ON-source events with statistical errors, and the red hatched histogram is that of the background events. The event number of the background data is normalized to that of the ON-source data by the ratio of the effective observation time. Right: Subtraction of θ^2-plot of background data from that of ON-source data.

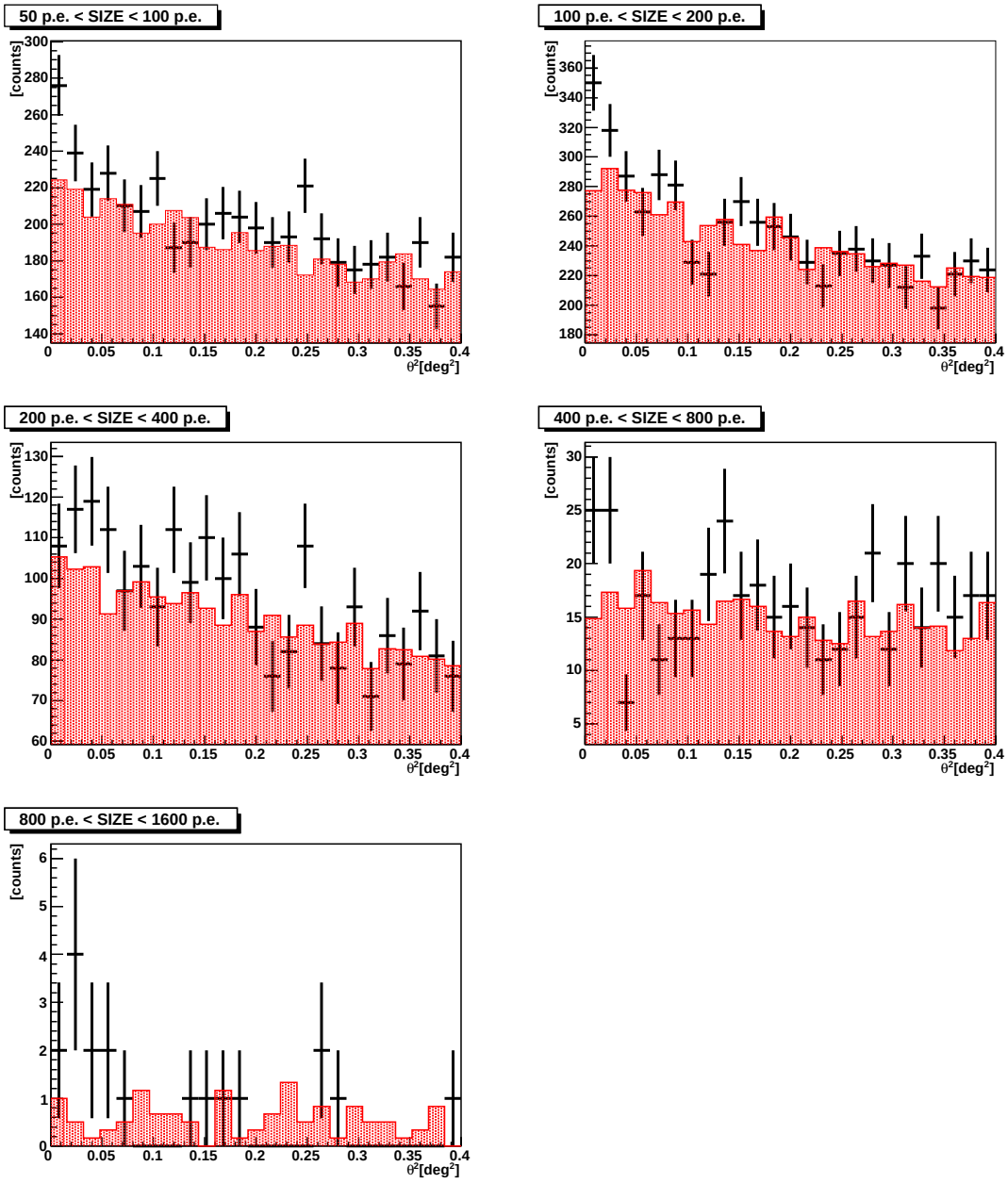

Figure 7.17: θ^2 distributions of the Crab Pulsar/Nebula in 2003 for each energy bin with the likelihood method. The crosses are from the ON-source data and the red hatched histograms are from background data. The size of the events in each histogram is indicated on the upper left and the corresponding energies are written in Table 7.3.

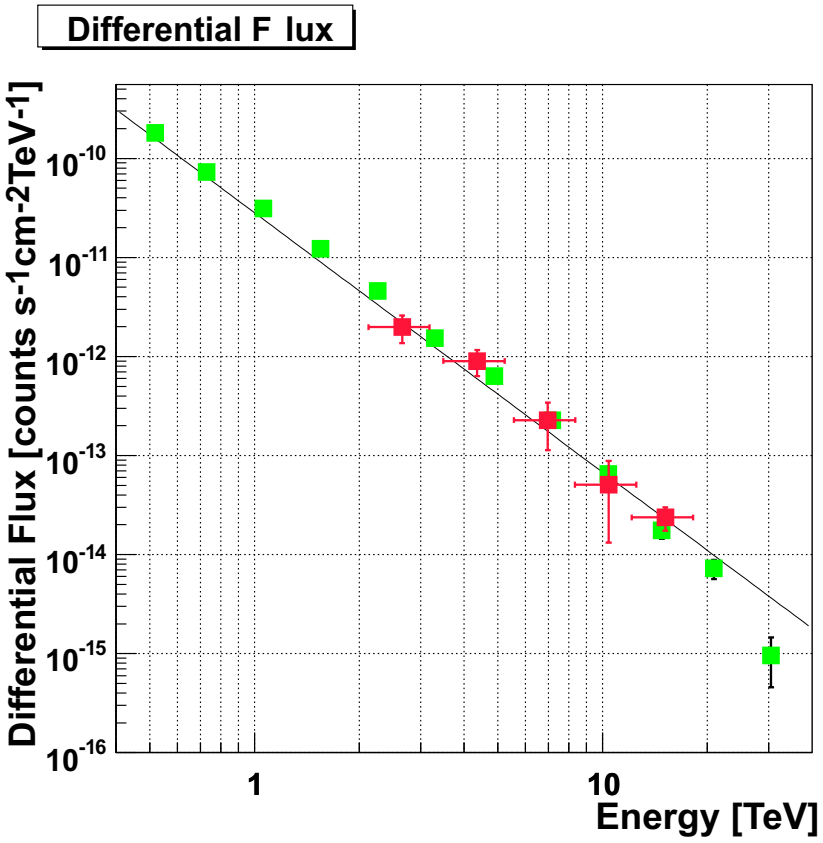

Figure 7.18: Differential flux obtained by the likelihood analysis of the Crab data in December 2003 (red boxes). The solid line is the best-fit of HEGRA results from Aharonian et al. (2004b): $d\Phi/dE = \Phi_0(E/\mathrm{TeV})^{\Gamma}$, where $\Phi_0 = (2.83 \pm 0.04_{\mathrm{stat}} \pm 0.6_{\mathrm{sys}}) \times 10^{-11}$ photons $\mathrm{cm}^{-2}\mathrm{s}^{-1}\mathrm{TeV}^{-1}$ and $\Gamma = -2.62 \pm 0.02_{\mathrm{stat}} \pm 0.05_{\mathrm{sys}}$. The green boxes are the HESS results from Aharonian et al (2006).

Chapter8

Analyses of RX J0852.0−4622

We showed our analysis procedure in Chapter 7 with its application to the Crab data. In this chapter, we applied the procedure to the data of RX J0852.0−4622.

§ 1 Background Reduction

First, we removed unfavorable data observed under bad weather or at low elevations. For the good data, the typical trigger rate and shower rate after the cluster cut were about 8 Hz and about 6 Hz, respectively. We settled the criteria for the shower rate to 5 Hz. The examples of the trigger rate and the shower rate with its observation elevation are shown in Fig. 8.1.

RX J0852.0−4622 was observed in the long ON/OFF mode with the wobbling telescope pointing, also called the wobble ON/OFF mode (details are described in Chapter 5-§ 4). The background events are estimated simply using the OFF source data. The criteria adopted to RX J0852.0−4622 are summarized in Table 8.1. The distributions of the likelihood ratio of the events which survived the elevation cut, the cluster cut, the cloud cut and the edge cut are shown in Fig. 8.2.

Table 8.1: Criteria for the analysis of RX J0852.0−4622.

Elevation cut	El $> 60^{o}$
ADC cut (Size cut)	$n_{\mathrm{p.e.}} \geq 5$ ph.-e.
Cluster cut	T5a
TDC cut	$\lvert t - t_{\mathrm{ave.}} \rvert < 30$ ns
Cloud cut	> 5 Hz
Edge Cut	Outermost 1 layer cut
Likelihood ratio cut	$LR > 0.1$

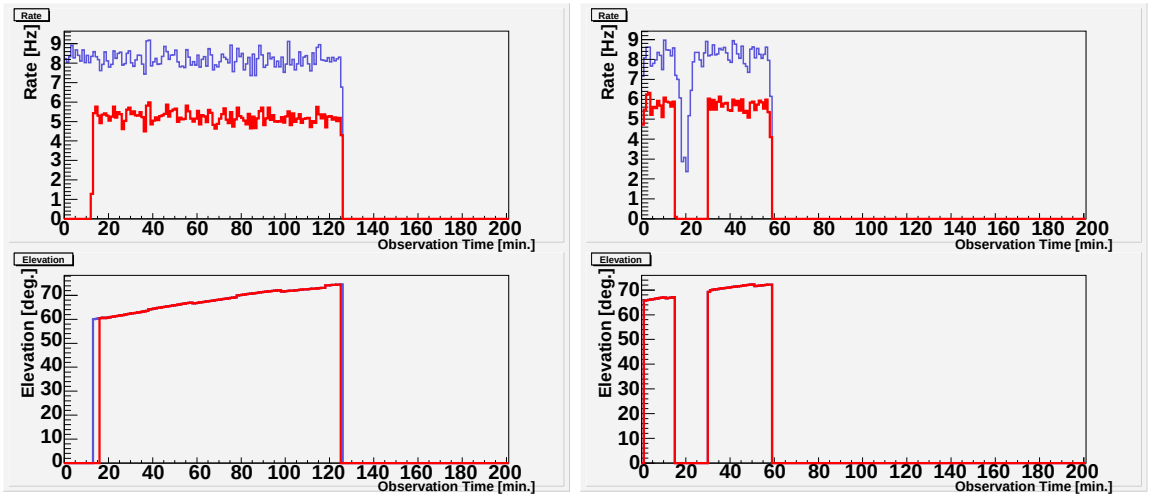

Figure 8.1: Upper left: Event rate (blue) and shower rate after the cloud cut (red) in one observation run under favorable weather conditions. The trigger rate is 0 Hz in the first 10 minutes because the elevation angle is lower than 60°. Lower left: Elevation distribution of this run. Upper right: Event rate (blue) and shower rate after the cloud cut (red) in one observation run including the cloudy period. The trigger rate is 0 Hz in 15 to 30 minutes because of the cloudy weather. Lower left: Elevation distribution of this run.

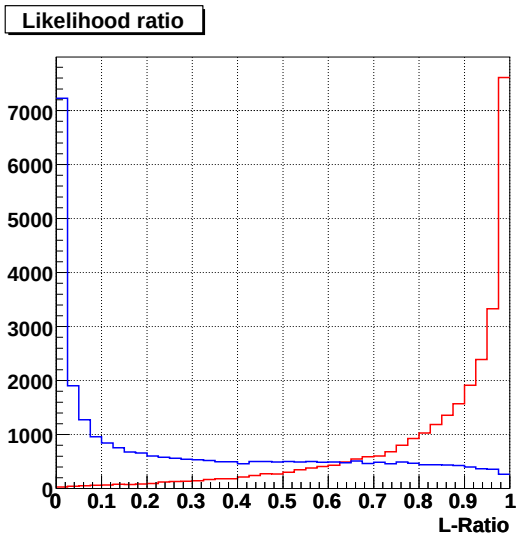

Figure 8.2: Distributions of the likelihood ratio of the observation data (i.e., proton events: blue) and the simulated gamma-ray events (red) for RX J0852.0−4622.

§ 2 Intersection Point

As discussed in Chapter 7-6.2, we need to use a fitting method to determine the intersection point (IP) for low-elevation sources. Although RX J0852.0−4622 is observed at favorable elevations above 60°, the fitting method is also necessary because of the following reason. RX J0852.0−4622 has a shell structure of the X-ray emission with a radius of ∼1°, and possibly its gamma-ray emission also has a similar shape. In order to simplify the simulation, we made the following approach. When we consider only the θ^2 distribution, the emission from a circle with a 1° radius is equivalent to that from a point source shifted by ∼1° from the camera center in appropriate directions. Therefore, we generated the Monte Carlo simulation data under this condition (the other parameters are all the same as the normal simulation for RX J0852.0−4622). The obtained θ^2 distributions using the two methods introduced in Chapter 7-6.2 are shown in Fig. 8.3. The blue histogram is by Method-1, which derives the sine-weighted IP, the green is by Method-2, fitting with WIDTH and DISTANCE constraints. The distribution with Method-1 is shifted to the camera center. The distribution with Method-2 has the same feature and the peak is shifted towards $\theta^2 = 0$ deg^2 from 1 deg^2. Then we examined the fitting method without DISTANCE constraint and obtained the θ^2 distribution (red histogram). It has a symmetric peak about the target point at 1° from the camera center. Therefore, we adopted the fitting method without DISTANCE constraint.

§ 3 Results

The θ^2 distribution for RX J0852.0−4622 after applying likelihood ratio cut (the analysis criteria are summarized in Table 8.1) is shown in Fig. 8.4, where θ^2 is calculated from the nominal center of the SNR. In the left figure, the distribution of the ON-source events is superimposed on that of the OFF-source events. Here, the background data were normalized to the ON-source data by the ratio of their live times. The normalizing factor was 1128min/1009min = 1.118. The distribution of the excess in the right figure of Fig.8.4 was obtained by subtracting the normalized background data from the ON-source data. This figure shows the good agreement between the ON-source and the OFF-source data in the range above 2 deg^2. The distributions are not flat outside of the signal region ($\theta^2 > 1.0$ deg^2) since the

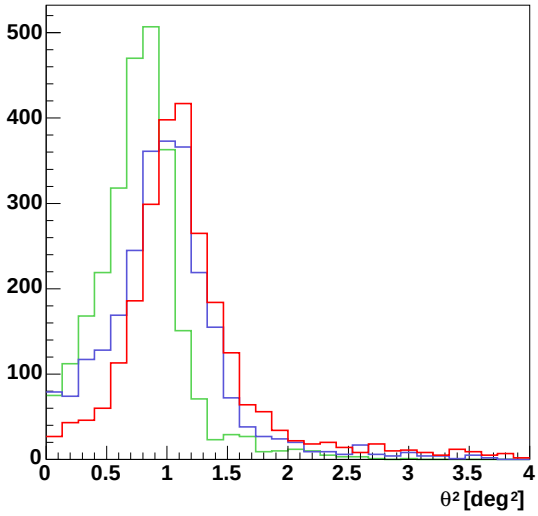

Figure 8.3: Comparison of the θ^2 distributions of the source shifted by 1° from the center of the FOV. Blue histogram is by the method of the IP weighted with sine (Method-1), and green and red are by the fitting with and without DISTANCE constraint, respectively.

instrument's acceptance drops off towards greater values of θ^2. A clear excess of 829.8 ± 113.1 was found in the region of in the region of $\theta^2 < 1.0$ deg^2. This radius roughly agrees with the X-ray radius of the SNR. The significance of the signal is 7.3σ, calculated by Eq.(7.27). The θ^2 distribution of the excess is much wider than that which was measured for the Crab Pulsar/Nebula, which is a point-like source (see Chapter 7-8.1). We see an unknown flat excess of gamma-ray like events outside of the SNR region. We will have some discussion on this excess in § 6.

The variation of the signal significance by changing the criterion of the likelihood ratio cut is shown in Fig.8.5. A tighter cut generally give a higher significance with a sufficient statistics. Figure 8.5 a different tendency. The significance decreases as we apply tighter cuts. For the reference, we showed the variation plot for the Crab 2003 analysis in Fig.8.6, which is also differnt from the ideal distribution. One of the possible reason is the fact that the number of the gamma-ray events we detect with the Čerenkov telescopes are very few and statistically poor. Figure 8.7 shows the number of surviving events for each cut criterion. This figures indicate that there can be a risk to exclude the gamma-ray events when we apply a tight cut. Meanwhile, a large number of the background events remain with the looser cut

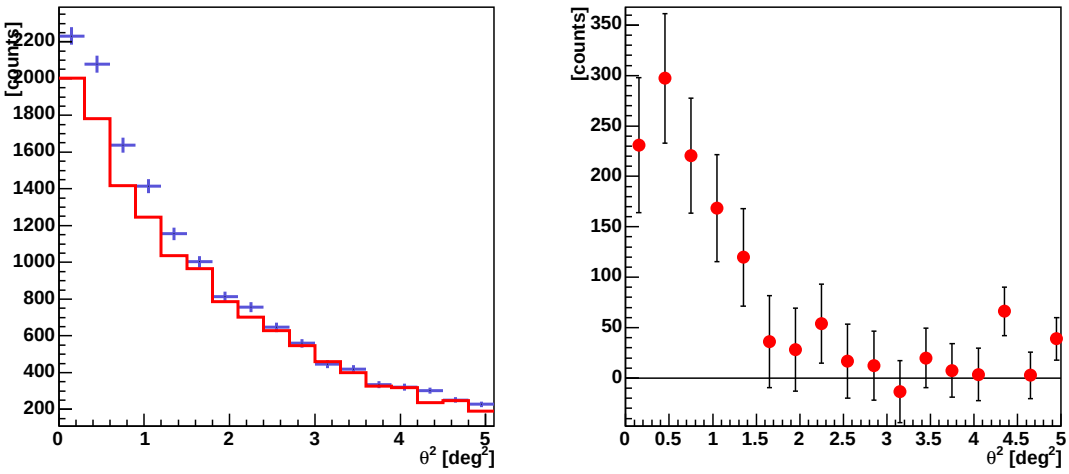

Figure 8.4: θ^2 distributions of RX J0852.0−4622. Left: Blue crosses are from ON-source data, and the red histogram shows OFF-source data. The number of the OFF-source events were normalized to that of the ON-source events by the ratio of their live time. Right: θ^2-plot of the excess of gamma-ray like events. The peak of the excess events extends beyond 1^o.

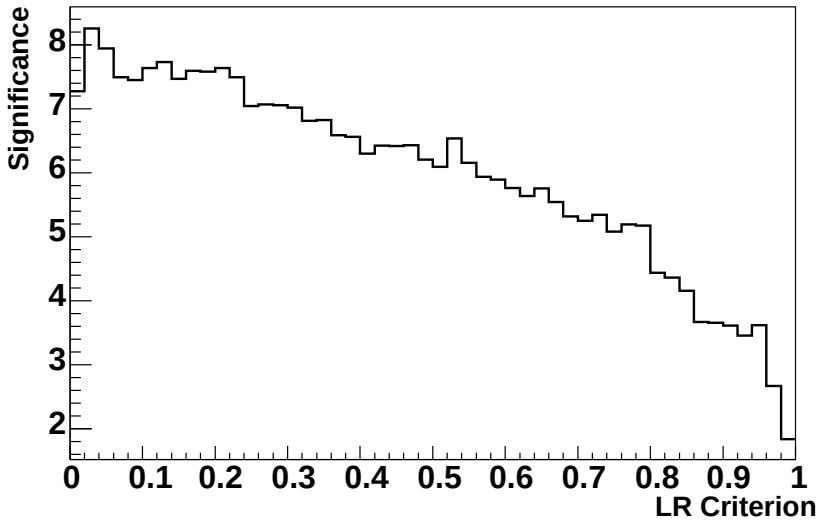

Figure 8.5: Statistical significance of the RX J0852.0−4622 excess versus LR cut value in the 2005 observation.

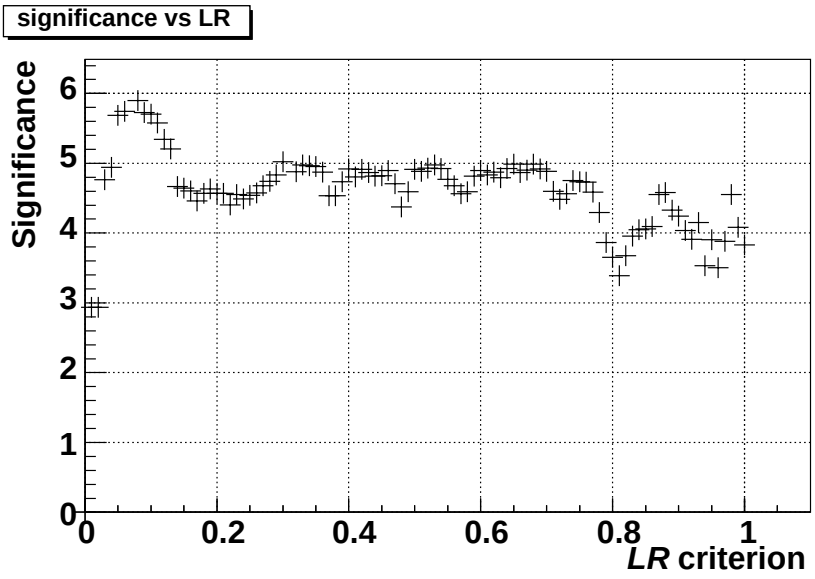

Figure 8.6: Statistical significance of the Crab Pulsar/Nebula excess versus LR cut value in the 2003 observation.

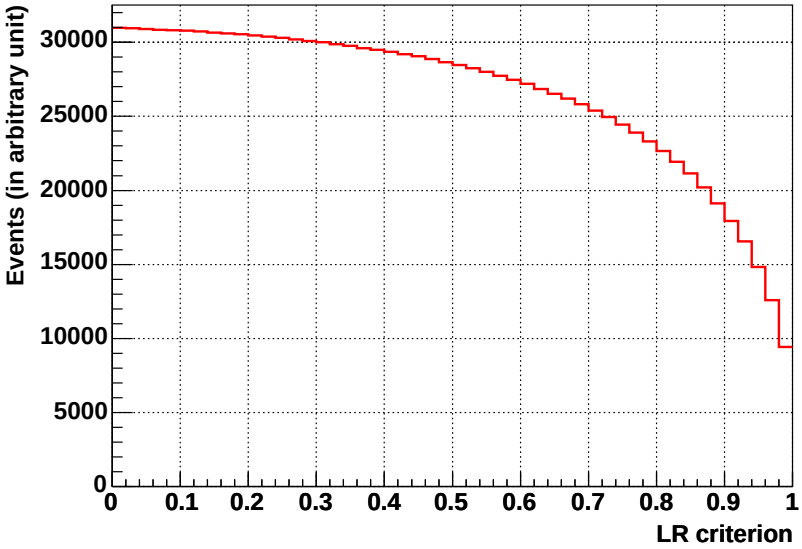

Figure 8.7: Surviving gamma-ray events for each LR cut criterion by the Monte Carlo simulation.

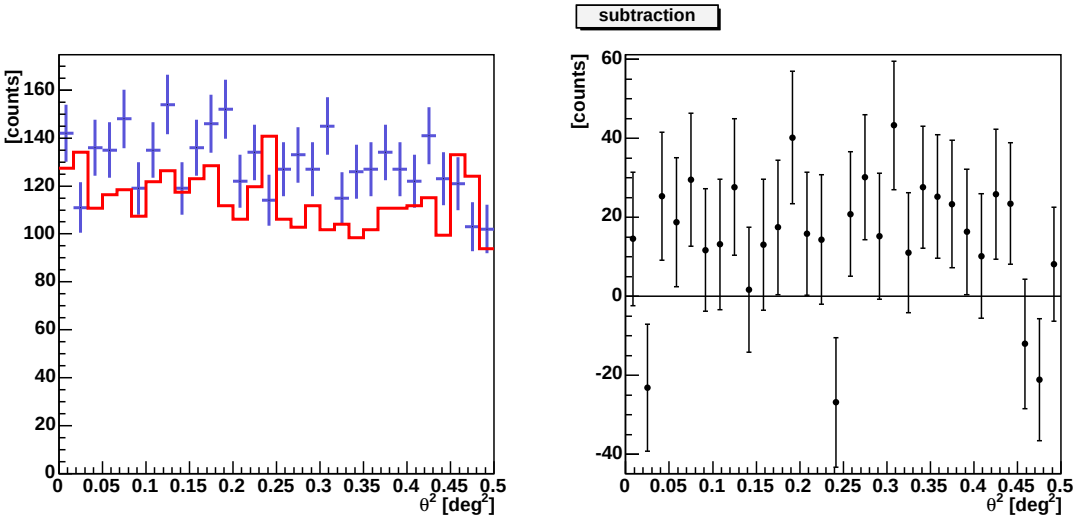

Figure 8.8: θ^2 distributions of RX J0852.0−4622 in the range of 0 deg^2 $< \theta^2 <$ 0.5 deg^2. Left: Blue crosses are from ON-source data, and red histogram is OFF-source data. The OFF-source events were normalized to that of the ON-source events by the ratio of their live time. Right: Subtraction of θ^2-plot of OFF-source data from that of ON-source data. No significant peak of excess events for a point source are found. Gamma-rays from a point source should make a peak towards 0 deg^2 from ∼0.05 deg^2.

than $LR > 0.1$ as indicated by Fig.8.2 (blue histogram). Considering this fact, we adopted the cut of $LR > 0.1$.

To treat the question of the emission from a compact central object, the central region of the SNR was tested for the presence of a point-like source by applying a point-source cut ($\theta^2 < 0.05$ deg^2). No significant excess as a point source was found as shown in Fig.8.8.

Then we obtained the differential flux of RX J0852.0−4622 following Eq.(7.33). First we obtained the numbers of the excess events in each energy bin. The θ^2 distributions in each energy bin are shown in Fig.8.9 for ON-source data (blue crosses) and OFF-source data normalized by the ratio of the live time (red histograms). Their subtractions (ON−normalized-OFF) are shown in Fig.8.10. The excess event numbers are summarized in Table 8.2. With the MC simulation data, we estimated the event acceptance after imposing all the cut conditions. The simulation parameters are shown in Table 6.3. The black histogram in Fig.8.11 is the distribution of the all generated events, and the red is that of the surviving events. The parameters

assigned to Eq.(7.33) were

$$\begin{aligned} S_0 &= 25000^2\pi/\cos^2(19^{\rm o}.7) = 2.2\times10^9[{\rm cm}^2] \\ \alpha &= 2.1 \\ N_{\rm MC}^{\rm tot} &= 2.41\times10^6 \\ E_{\rm min} &= 200\ [{\rm GeV}] \\ E_{\rm Max} &= 20000\ [{\rm GeV}] \\ T_{\rm ON} &= 67688\ [{\rm sec}]. \end{aligned} \tag{8.1}$$

Figure 8.12 shows the energy distributions for the events of the MC simulation surviving in each energy region. The number of the all events and the mean energy in each energy region are used as the surviving event number $N_{\rm MC}(x_{\rm l}, x_{\rm u})$ and the representative energy $\overline{E}$, respectively. Here $x_{\rm l}$ and $x_{\rm u}$ indicate the lower and the upper limits of SumADC in each region. The obtained result is plotted in Fig.8.13 with the best fit function (solid line). The best fit function is

$$(3.9\pm0.6)\times10^{-11}\times\left(\frac{E}{1{\rm TeV}}\right)^{-2.4\pm0.3}\ {\rm cm}^{-2}{\rm s}^{-1}{\rm TeV}^{-1}. \tag{8.2}$$

Table 8.2: Excess events in each energy bin. The OFF data was normalized by the ratio of the observation live time.

SumADC [ph.-e.]	Mean energy [TeV]	Excess event	Statistical significance	Flux [photons s^{-1} cm^{-2} TeV^{-1}]
25 to 100	0.86	184.2 ± 61.2	3.0	$4.15\pm1.38\times10^{-11}$
100 to 150	1.13	311.6 ± 68.2	4.6	$3.67\pm0.80\times10^{-11}$
150 to 300	1.68	302.1 ± 68.2	4.4	$1.29\pm0.29\times10^{-11}$
300 to 500	2.58	61.9 ± 29.5	2.1	$3.55\pm1.69\times10^{-12}$
500 to 1600	3.96	15.3 ± 12.3	1.2	$9.20\pm7.40\times10^{-13}$

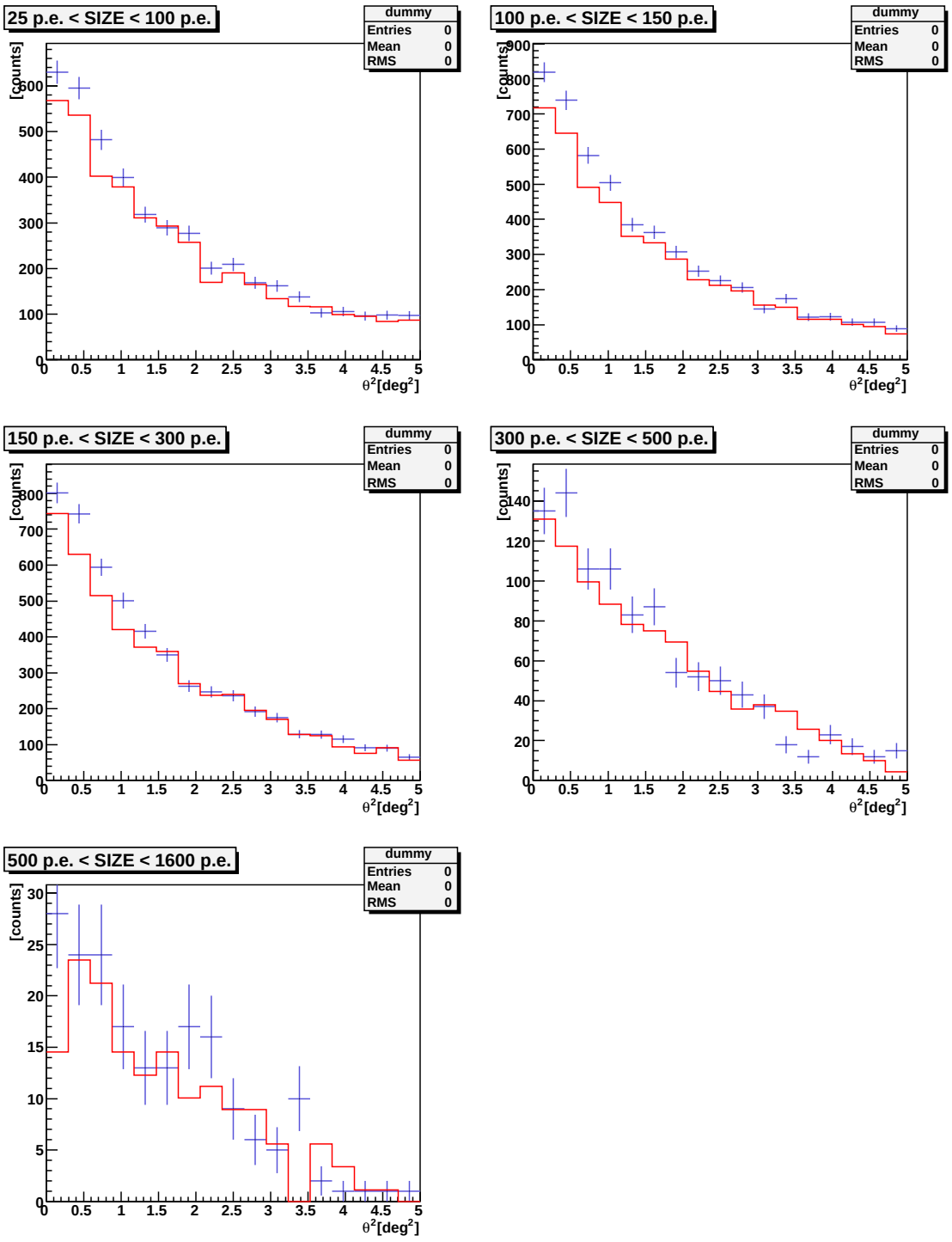

Figure 8.9: θ^2 distributions of RX J0852.0−4622 in 2005 for each energy bin with the likelihood method. The blue crosses indicate the events from the ON-source data, and the red histograms shows the OFF-source data normalized to the ON using their live time ratio. The error bars denote $\pm 1\sigma$ statistical errors.

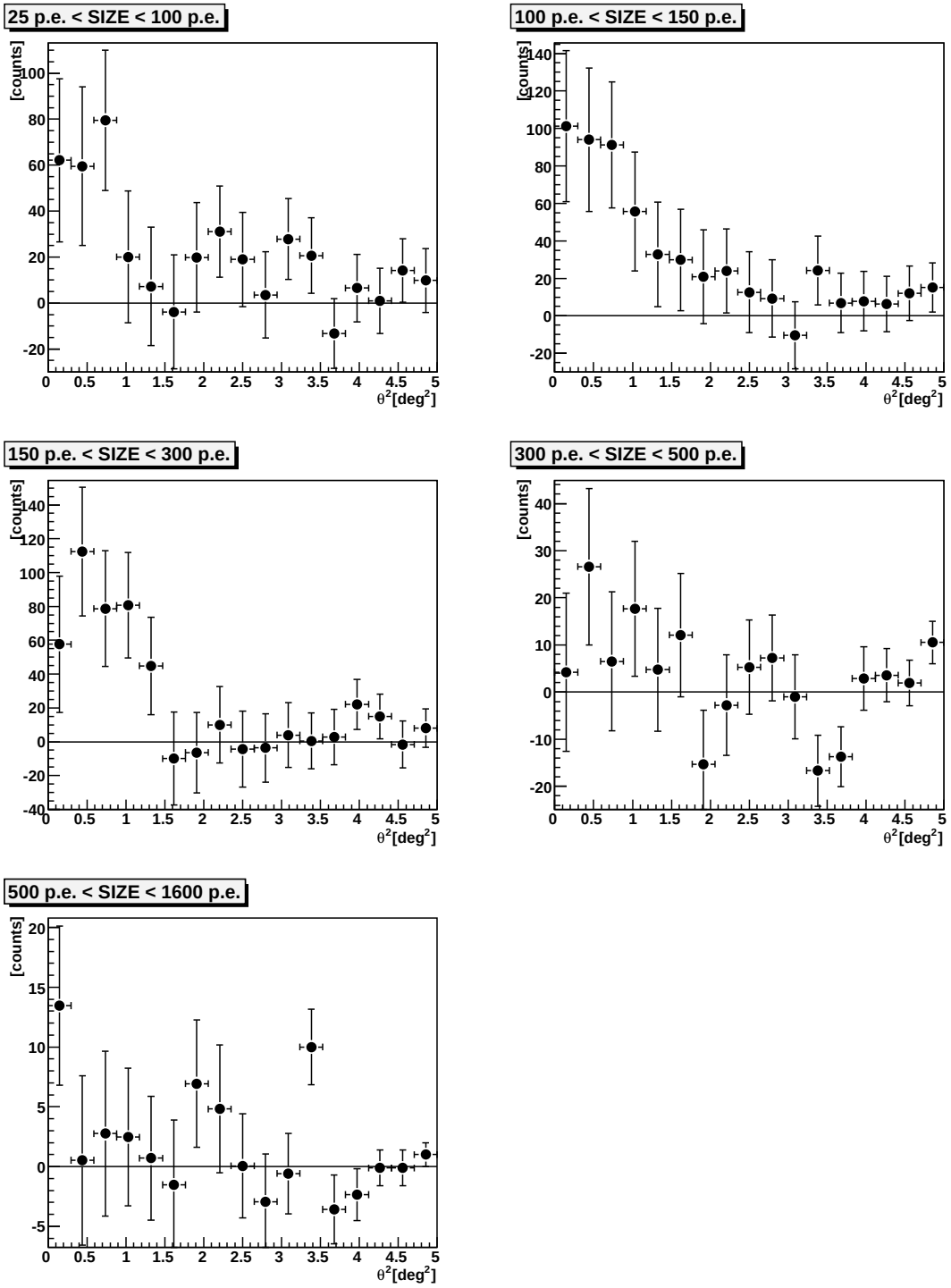

Figure 8.10: θ^2-plots of the excess of gamma-ray like events from RX J0852.0−4622 in each energy region. The error bars denote $\pm 1\sigma$ statistical errors.

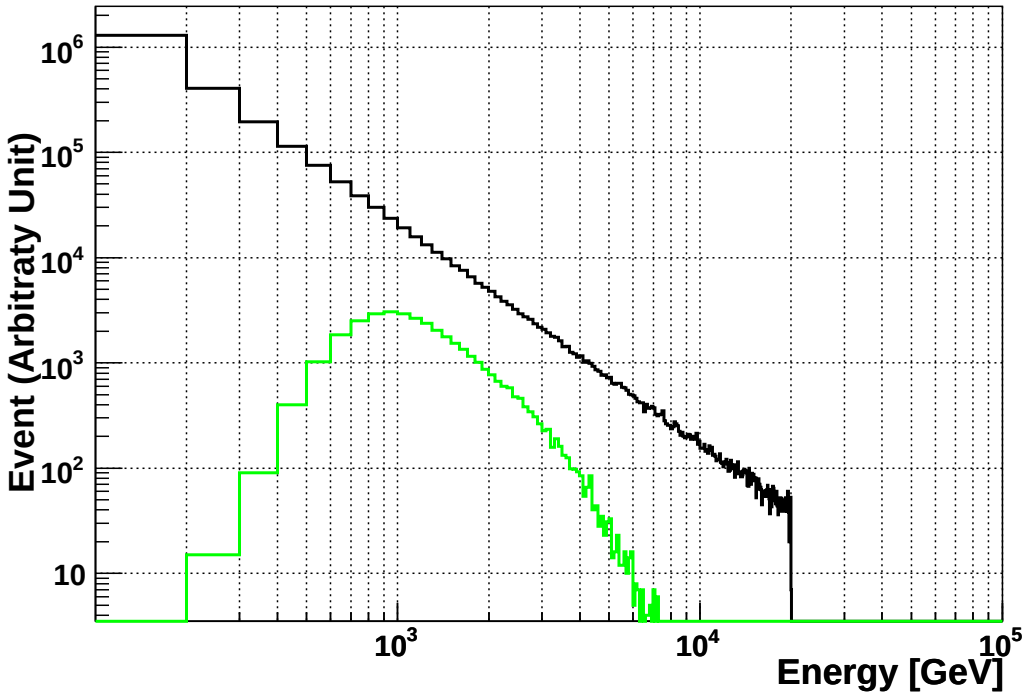

Figure 8.11: The black histogram is the energy distribution of the all generated gamma-ray events by the Monte Carlo simulation. The green is that of the events which survived all cuts including the edge cut.

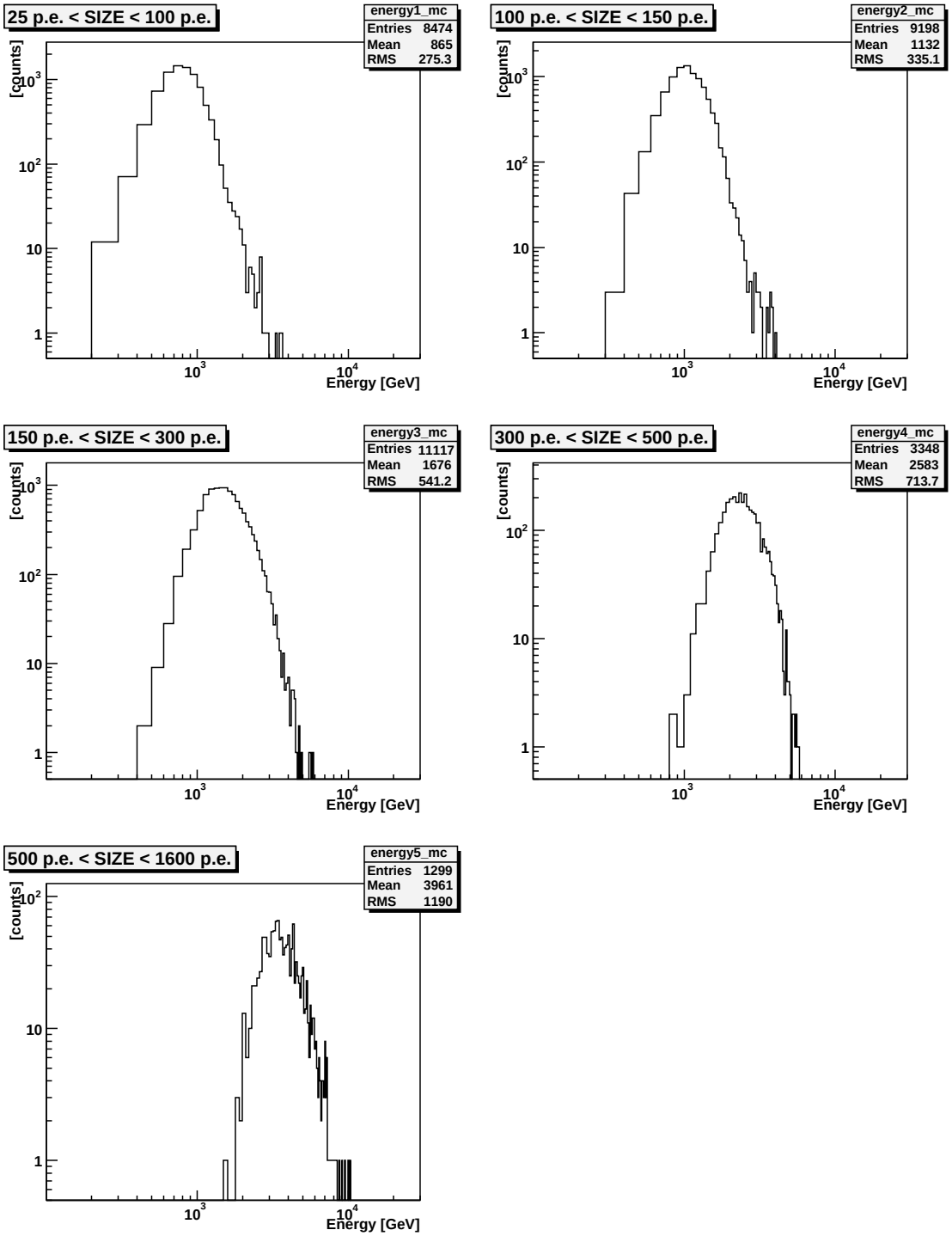

Figure 8.12: Energy distributions of the Monte Carlo gamma-ray events for each energy bin divided by the ADC value. The mean energies in each region are summarized in Table 8.2

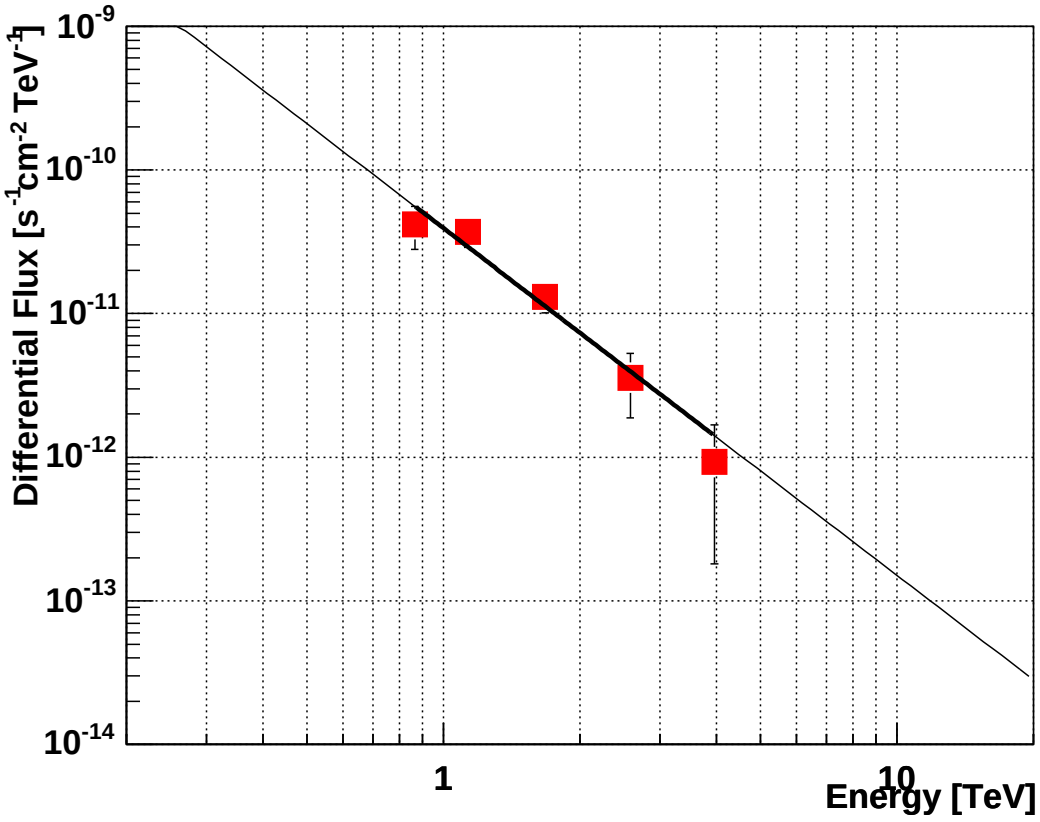

Figure 8.13: Differential photon flux spectrum of the gamma-rays detected by CANGAROO-III from the direction of the whole RX J0852.0−4622 with the conventional edge cut (red boxes). The solid line is the fitting result: $(3.9 \pm 0.6) \times 10^{-11}(E/1\mathrm{TeV})^{-(2.4\pm0.3)}$. The error bars denote $\pm 1\sigma$ statistical errors. The LR criterion is $LR > 0.1$, and the ON/OFF normalization is time-based.

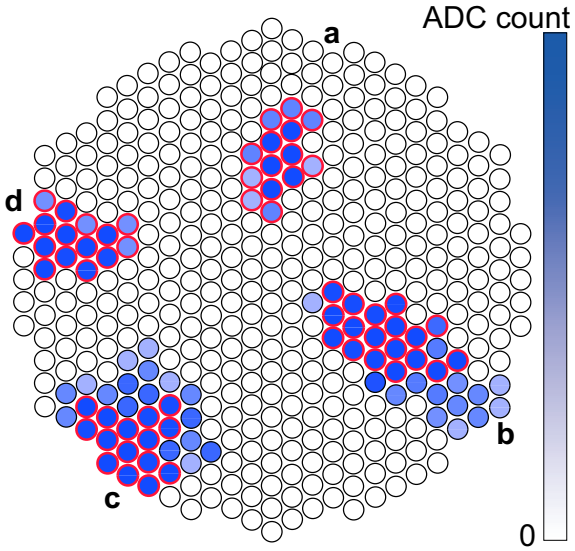

Figure 8.14: Diagram of the edge cut. The circles are the camera pixels, and the blue ones are hit pixels. In the conventional edge cut, the images **b**, **c**, and **d** are removed since they have hit PMTs on the edge. In the improved edge cut, only the 15 PMTs (the red-framed pixels in the figure), which have highest ADC count, are considered. Then the images **a** and **b** survive this edge cut.

§ 4 Improvement of Edge Cut

As indicated in Fig.8.11, the higher energy event has a lower acceptance, which is due to the edge cut. A high-energy event has a large shower image and tends to hit the PMTs on the outermost layer. If only the outer end of the shower image is just glancing the camera edge, the image is not deformed by the edge effect. We revised the edge cut by reducing the number of the PMTs sampled for the edge cut. The schematic explanation is shown in Fig.8.14. We extracted the 20 or 15 of the brightest PMTs in the cluster of the shower image for the edge cut. When the number of the hit PMTs is less than those numbers, all the hit PMTs are used for the conventional edge cut. The improvement of the acceptance by this modification is shown in Fig. 8.15. The red line parallel to the black line indicates that the decrease in the acceptance in the higher energy region can be recovered when we extract 15 PMTs and the blue shows that the condition of "20-PMT" is still too tight. Figure 8.16 shows that the determination accuracy of the intersection point is slightly better with the new edge cut with selected 15 PMTs than with normal one. Another reason of the edge cut is to avoid the underestimation of the energy. The

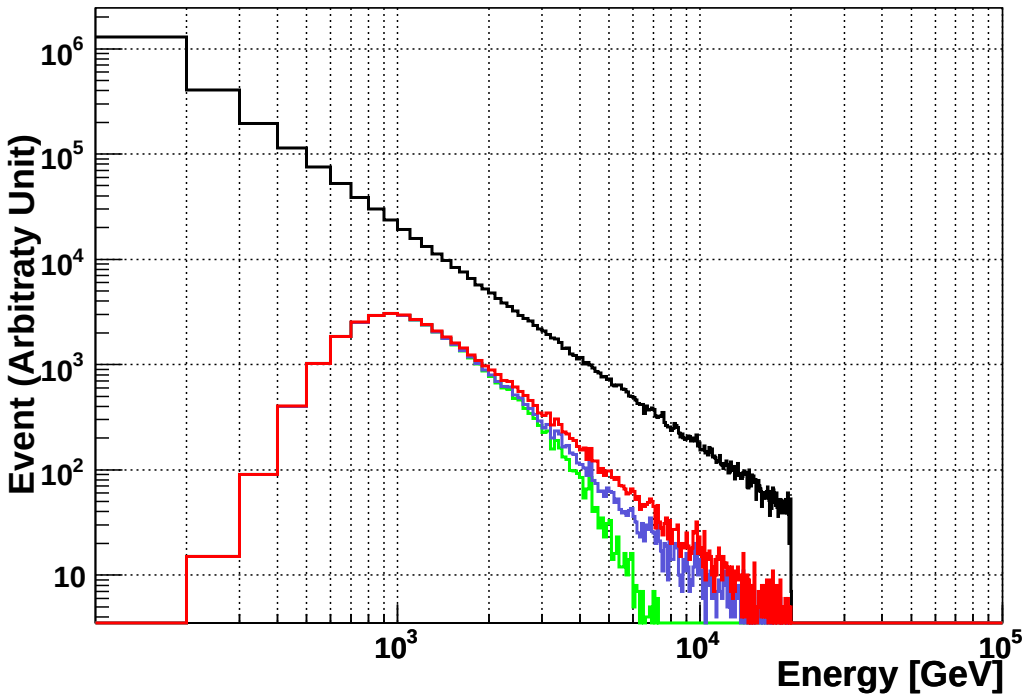

Figure 8.15: Increase of the survived events as loosening the condition of the edge cut. The black histogram is the energy distribution of the all generated events in the Monte Carlo simulation. The parameters for this simulation are summarized in Table 6.3. The green is that of the events which survived the normal edge cut. The blue and the red are the survived events in the improved edge cut with brightest 20 and 15 PMTs, respectively.

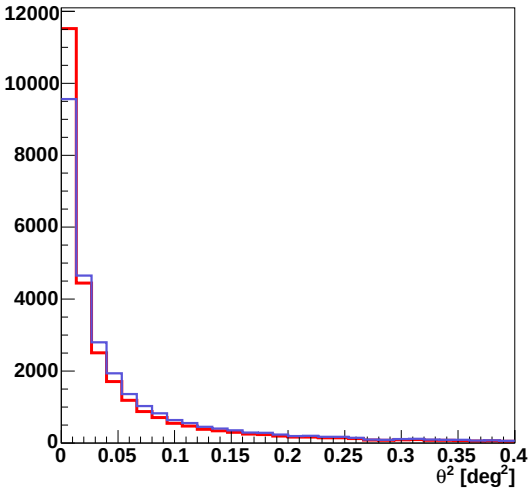

Figure 8.16: θ^2 distributions for the simulation data of a point source with the normal edge cut (blue) and the improved "15 PMTs" edge cut (red). θ^2 distribution is almost the same.

simulated energy resolutions for gamma-rays obtained with various edge treatments are shown in Fig.8.17. The red and the blue line show the better resolution in the higher energies. Although the normal edge cut gives the best one at 5 TeV (∼12%), the "15PMT edge cut" also gives acceptably good resolution (∼20% at 5 TeV). With considering the improvement of the acceptance, we decided to adopt the edge cut with 15-PMT selection.

The improved θ^2-plot in all energies is shown in Fig.8.18. In the region $\theta^2 < 1.0$ deg^2, the excess is 876.5 ± 116.7 events. The significance of the signal is 7.5σ, calculated with Eq.(7.27). The θ^2-plot and the distribution of the excess events in each energy region were obtained as Fig.8.19 and Fig.8.20, respectively. The number of the excess events in each energy region is summarized in Table 8.3. The revised differential flux was calculated again by Eq.(7.33) with the same parameters with Eq.(8.1), and plotted in Fig.8.22. A remarkable improvement was seen. The upper energy boundary of the analysis increased nearly to 10 TeV. That was about 4 TeV with a normal edge cut as shown in Fig.8.13. The solid line is the best fit function:

$$(4.1 \pm 0.6) \times 10^{-11} (E/1\mathrm{TeV})^{-(2.7 \pm 0.2)}. \tag{8.3}$$

The emission profile was obtained as Fig.8.23. The energy threshold here is approximately 860 GeV. The event counts of gamma-rays are plotted in colors in a

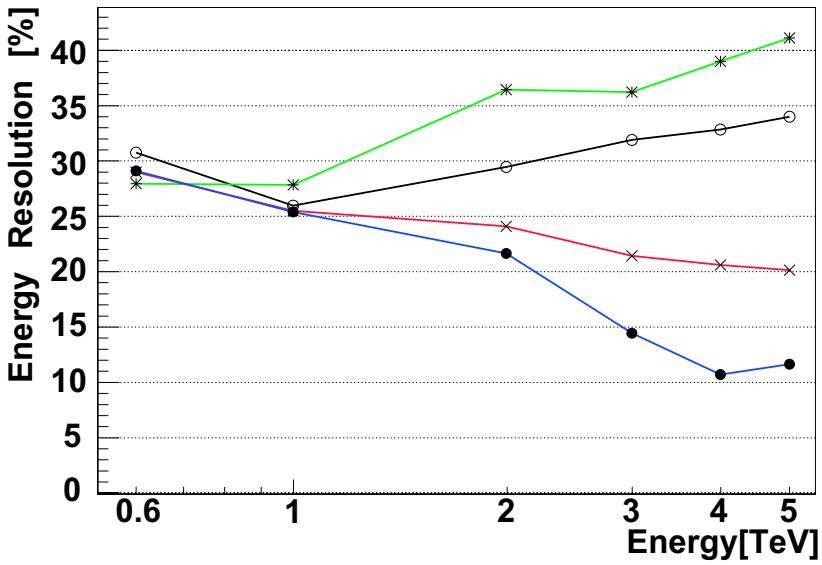

Figure 8.17: Simulated energy resolutions for gamma-rays with four different edge treatments. (From top) Green: Without any edge treatment. Black: Events of which distance between the nominal SNR center and the centroid of the shower image is less than 1.5 degrees (DIS0 < 1.5). Red: With the edge cut with "15 PMTs". Blue: With the normal edge cut. Upper two lines show worth energy resolution for the energy increase, and the lower two show the better one.

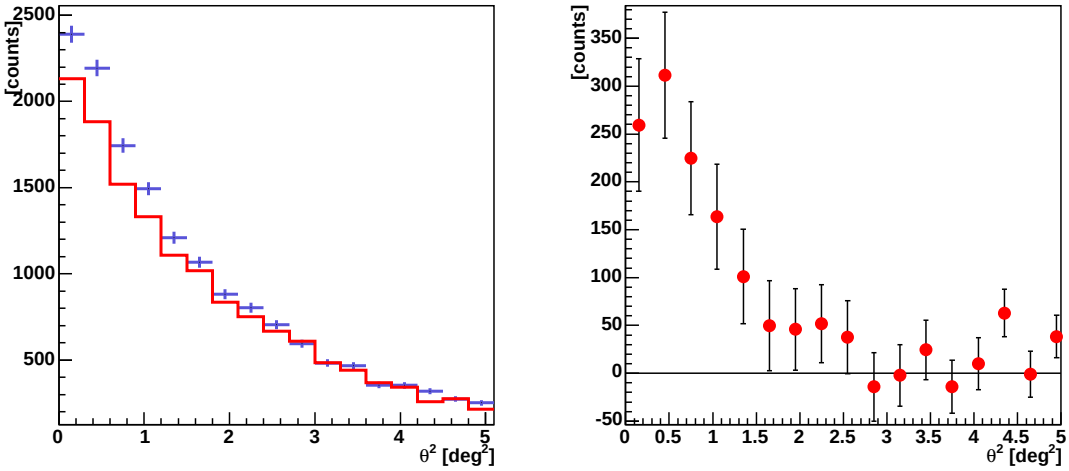

Figure 8.18: Revised θ^2 distributions of RX J0852.0−4622 using the improved edge cut. Here, only the brightest 15 PMTs are considered in the edge cut. Left: Blue crosses are from ON-source data, and red line represents OFF-source data. The number of the OFF-source events were normalized to that of the ON-source events by the ratio of their live-time. Right: θ^2-plot of the excess of gamma-ray like events. The peak of the excess events is extended beyond 1^o.

field of right ascension (lateral axis) vs. declination (vertical). The X-ray image by *ASCA* (Tsunemi et al. 2000; Slane et al. 2001) is superimposed by contours. The gamma-ray emission shows an open shell structure bright in the west side inside the circle (the dotted circle in the figure) of a ∼1 degree radius with the center at the nominal center of the SNR (the black cross in Fig.8.23). Considering the position resolution of the Čerenkov telescopes (indicated as a dashed circle at the lower left in Fig.8.23), it can be said that the emission structures of TeV gamma-rays and X-rays bear a slight resemblance.

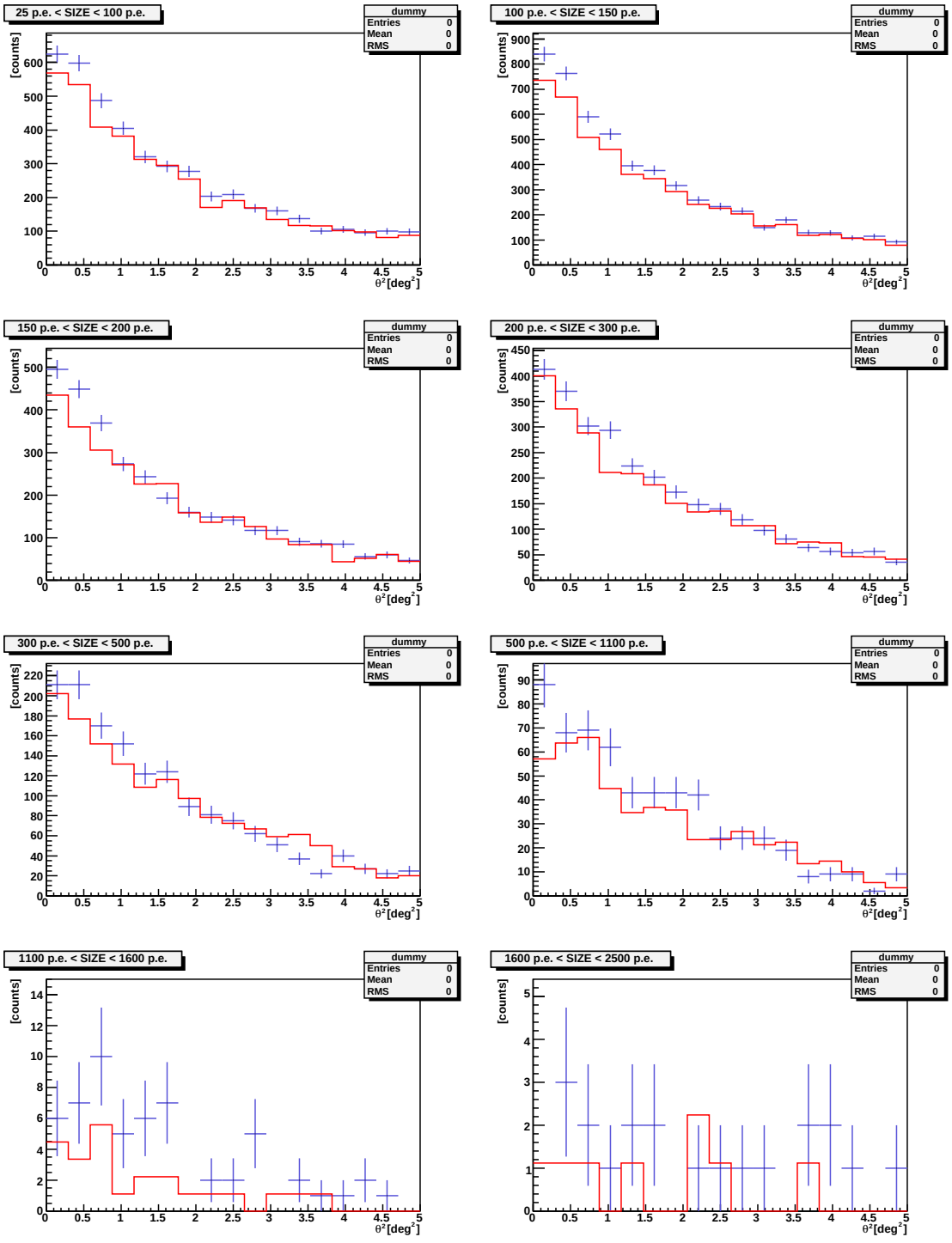

Figure 8.19: Revised differential θ^2-plots of RX J0852.0−4622 in 2005 for each energy bin with the improved edge cut. The blue crosses indicate the events from the ON-source data. The red histograms indicate the OFF-source data normalized to the ON using their live time ratio. The error bars denote $\pm 1\sigma$ statistical errors.

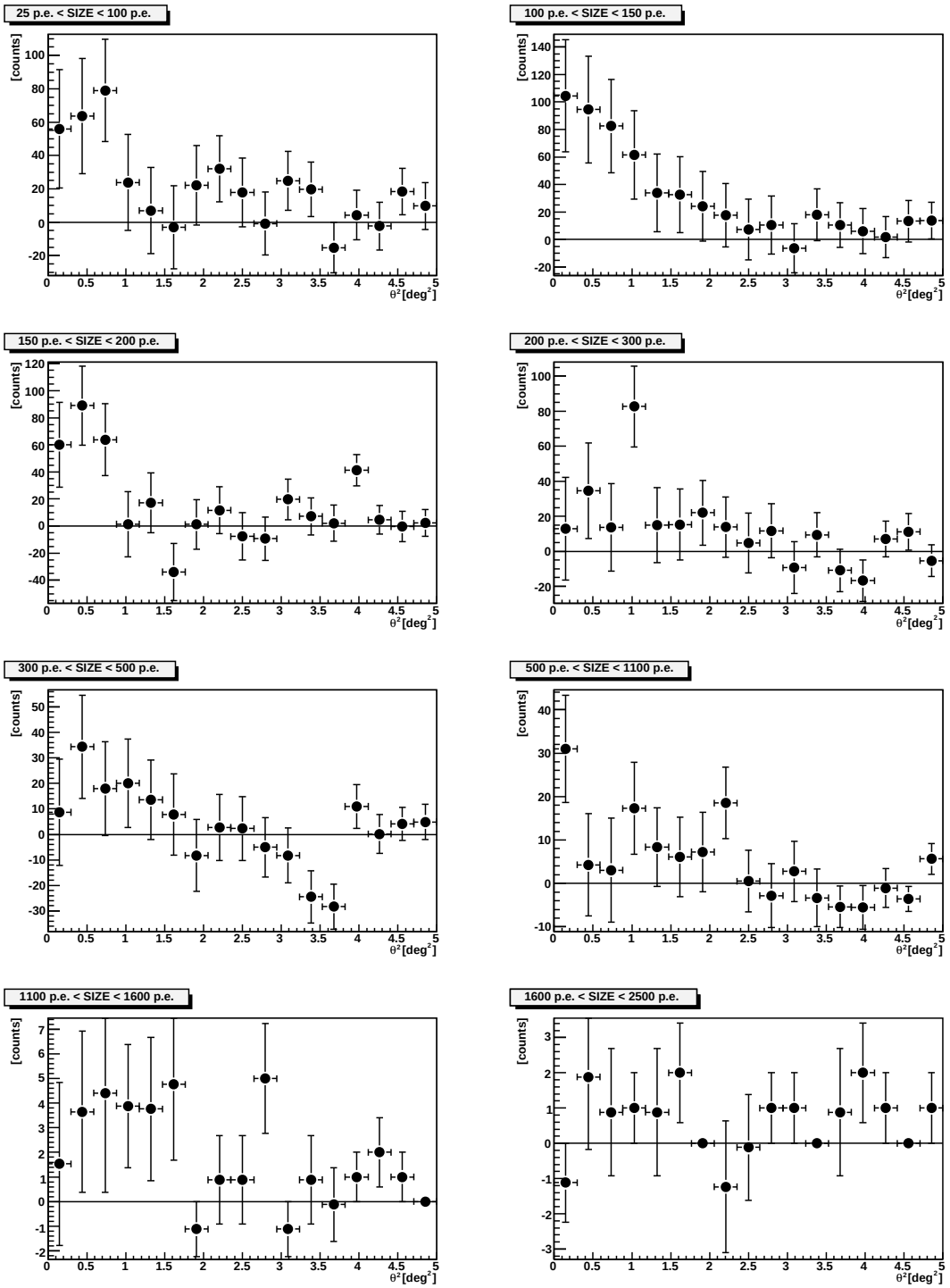

Figure 8.20: Revised θ^2-plots of the excess of gamma-ray like events from RX J0852.0−4622 in each energy region with the improved edge cut. The error bars denote $\pm 1\sigma$ statistical errors.

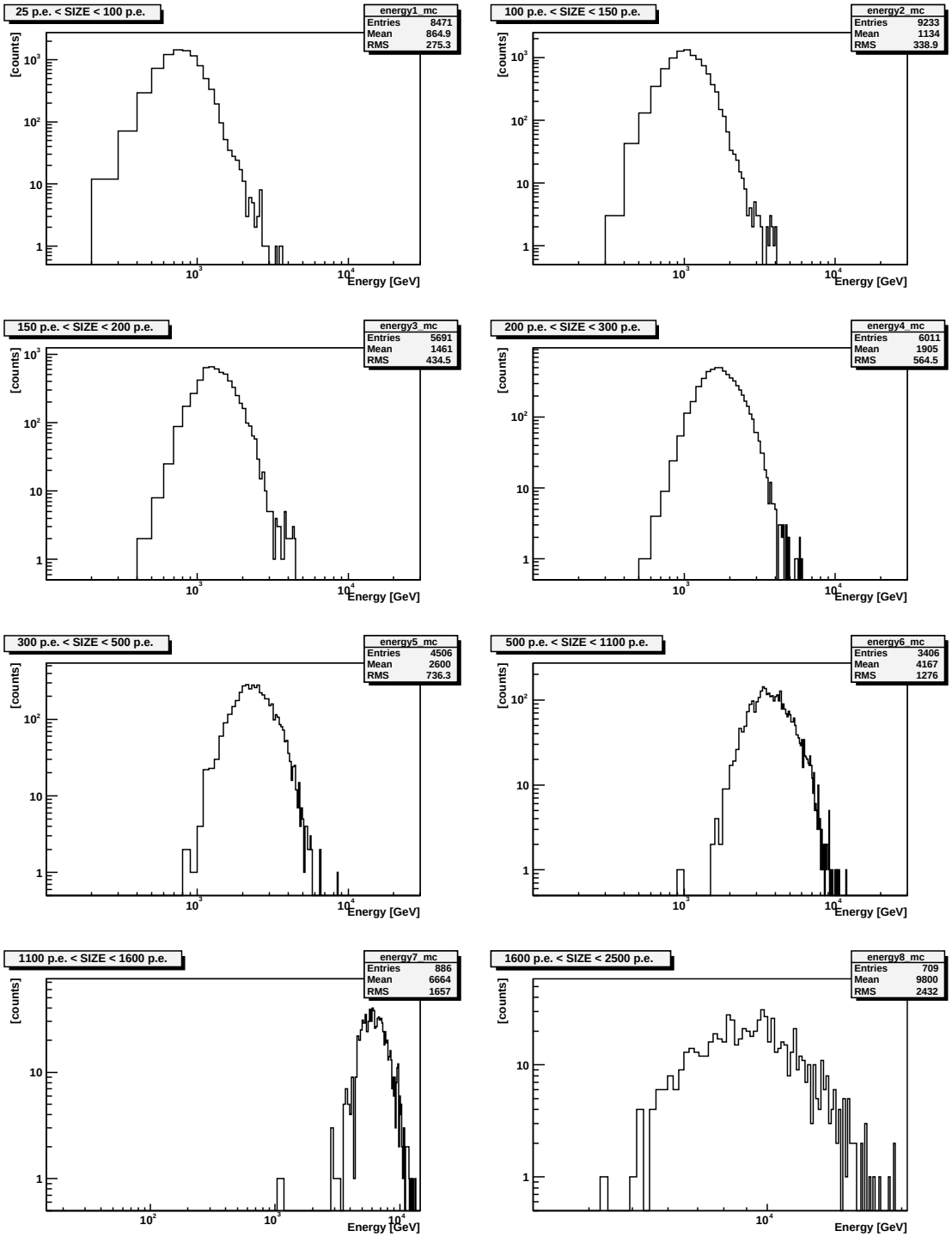

Figure 8.21: Revised energy distributions for each bin divided by the ADC value in the simulation after the improved edge cut. The mean energies in each region are summarized in Table 8.2

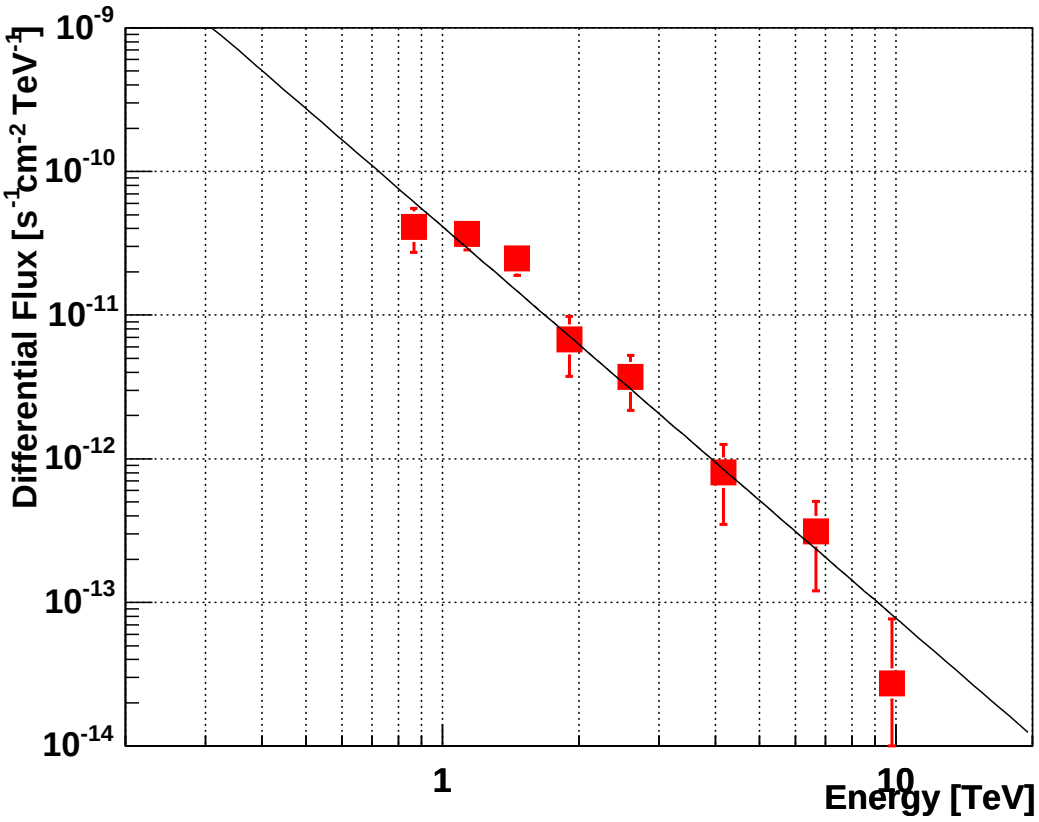

Figure 8.22: Differential photon flux spectrum of the gamma-rays detected by CANGAROO-III from the direction of the whole RX J0852.0−4622 (red boxes) after modified edge cut. The solid line is the fitting result: $(4.1 \pm 0.6) \times 10^{-11}(E/1\mathrm{TeV})^{-(2.7\pm0.2)}$. The error bars denote $\pm 1\sigma$ statistical errors. The ON/OFF normalization is time-based.

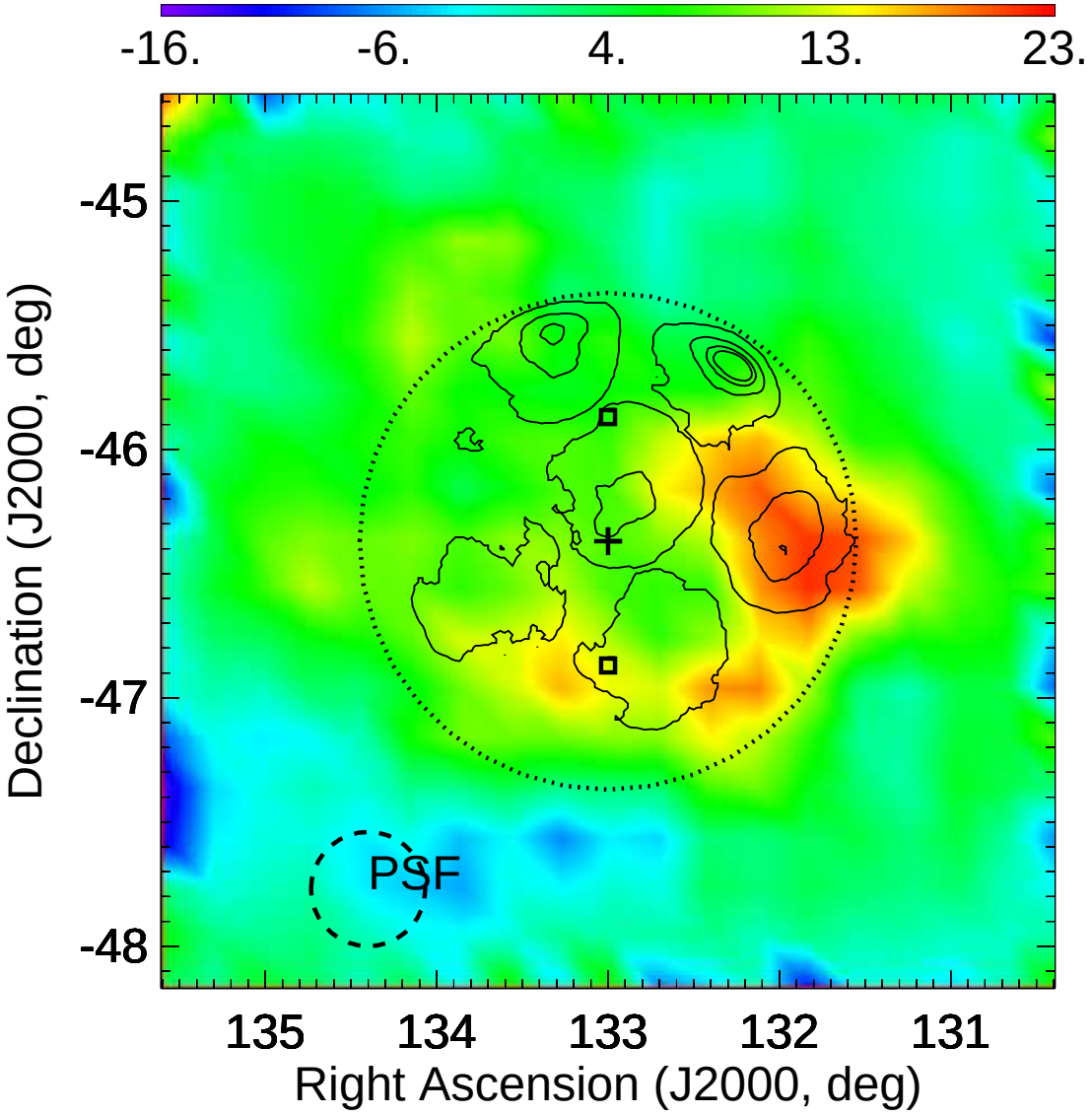

Figure 8.23: Morphology of the gamma-ray-like events obtained by the likelihood analysis. The smoothing was carried out using the average of the center and the neighboring 8 pixels, where the pixel size was 0.2×0.2 deg^2. The vertical scale (number of excess events) is indicated in the top bar. A dotted circle of 1^o from the SNR center is shown. The dashed circle of $0^o.23$ radius (plotted in lower left) is the (1σ) point-spread function, where 68% of events are contained. The cross indicates the averaged pointing position, i.e., the center of the remnant, and the squares the wobble pointing positions. The contours are the 20%, 45%, 65%, and 80% levels in the *ASCA* Gas Imaging Spectrometer X-ray map (Tsunemi et al. 2000; Slane et al. 2001).

Table 8.3: The number of the excess events in each energy bin with the improved edge cut. ON/OFF normalization was based on the ratio of background event counts.

SumADC [ph.-e.]	Mean energy [TeV]	Excess event	Statistical significance	Flux [photons s^{-1} cm^{-2} TeV^{-1}]
25 to 100	0.86	181.3 ± 61.3	3.0	$4.09\pm1.38 \times10^{-11}$
100 to 150	1.13	309.9 ± 69.2	4.5	$3.63\pm0.81 \times10^{-11}$
150 to 200	1.46	220.9 ± 52.8	4.2	$2.46\pm0.59 \times10^{-11}$
200 to 300	1.90	111.0 ± 49.5	2.2	$6.72\pm3.00 \times10^{-12}$
300 to 500	2.60	87.7 ± 36.4	2.4	$3.68\pm1.53 \times10^{-12}$
500 to 1100	4.16	38.5 ± 21.7	1.8	$7.96\pm4.48 \times10^{-13}$
1100 to 1600	6.66	10.5 ± 6.4	1.6	$3.10\pm1.90 \times10^{-13}$
1600 to 2500	9.79	1.6 ± 3.0	0.5	$2.71\pm4.89 \times10^{-14}$

§ 5 Unknown Flat Excess

We can see the unknown flat excess of gamma-ray like events.

The possible explanations are:

1. they are really from RX J0852.0−4622,
2. we cannot reject the background events yet in the FOV, or
3. there is other large gamma-ray source covering this SNR.

The third explanation is the most exciting and it can be true because there exists the large Vela supernova remnant over this SNR. Vela SNR is known to be near at ∼250 pc from us and, though it is estimated to be 10^4 years old and possibly in final phase of its evolution, an enough acceleration may be going on. We carried out a scanning observation crossing a part of the shell of Vela SNR in January to March 2006, and the analyses will take more time. Here, we simply tried to subtract by normalizing ON and OFF events using the event entries in outside $1^o.5$ circle. The results are in Fig.8.24. We obtained 563.2 excess events, and the significance is 5.0 σ.

The differential flux is shown in Fig.8.25. as comparison with the result of time-basis normalization. The best fit function is the dashed line:

$$(2.4 \pm 0.6) \times 10^{-11} (E/1\mathrm{TeV})^{-(2.6 \pm 0.3)} \ \mathrm{cm}^{-2}\mathrm{s}^{-1}\mathrm{TeV}^{-1}. \tag{8.4}$$

We can see our results are consistent regardless of the choice of the method of ON/OFF normalization (time based or count based). The dispersion of the best fit parameters should be considered as one of the systematic errors.

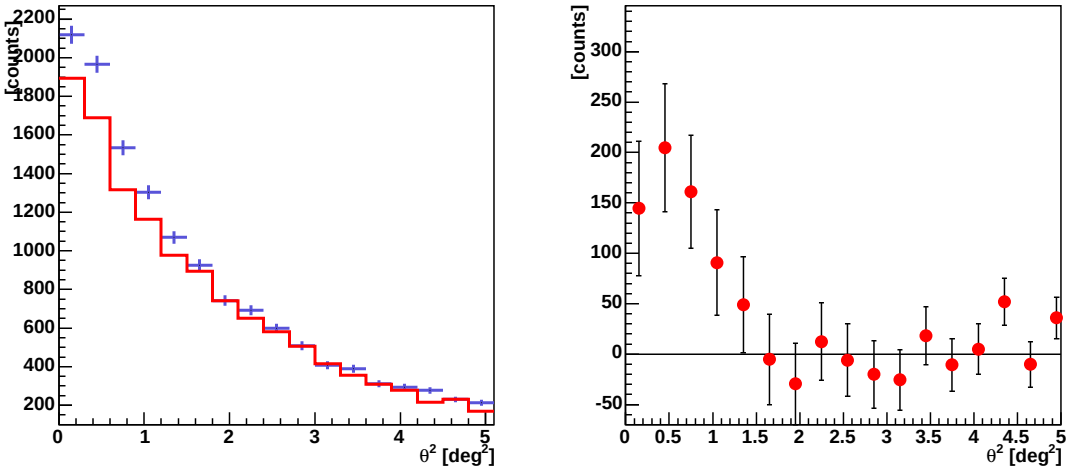

Figure 8.24: θ^2 distribution of RX J0852.0−4622. OFF-source data was normalized to ON-source by the count ratio in 1.5 to 5.0 deg^2. Left: The blue crosses are from ON-source data, and the red histogram is OFF-source data. Right: Excess of ON-source event.

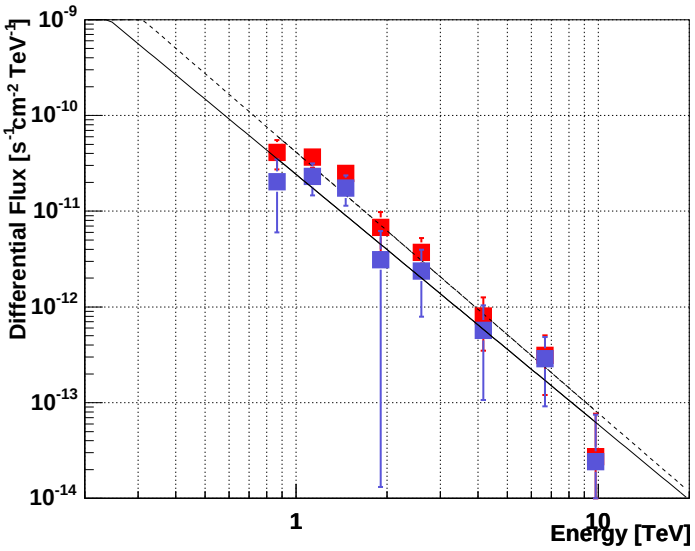

Figure 8.25: Differential photon flux spectra of the gamma-rays detected by CANGAROO-III from the direction of the whole RX J0852.0−4622 with two different event-normalizing methods on time basis (red) and event basis (blue). Their fitting lines are dashed: $(4.1 \pm 0.6) \times 10^{-11} \times (E/1\mathrm{TeV})^{-(2.7\pm0.2)}$, and the solid: $(2.4 \pm 0.6) \times 10^{-11} \times (E/1\mathrm{TeV})^{-(2.6\pm0.3)}$, respectively. The error bars denote $\pm 1\sigma$ statistical errors.

§ 6 Systematic Errors

Four factors are considered here in the estimation of the systematic errors.

1. Error in the likelihood ratio cut efficiency

The error in the likelihood analysis cut efficiency is estimated using the variation of the obtained flux level for the various likelihood ratio cut criteria. This variation reflects the image parameter uncertainty originated in such parameters as an atmospheric condition. The primary hardware uncertainty which affects the image parameter is the optical spot size of the reflector, and the measured spot size is included in the present Monte Carlo simulation. Figure 8.7 shows the variation of the number of the surviving Monte Carlo gamma-ray events by changing the criterion of the LR cut. Here, we considered the flux fluctuation in the range of criteria assuring about 80 % of the total gamma-rays surviving in the Monte Carlo simulation. Hence we took into account the criteria from LR>0.1 to LR>0.8. For some values of the criteria, we summarized the number of excess events, the significance and the flux as the ratio to that with LR>0.1. The power-law index Γ changes from 2.7 ($LR > 0.1$) to 2.2 ($LR > 0.6$).

Table 8.4: Statistical significance of the excess of RX J0852.0−4622 with various LR criteria (some points from the plot of Fig.8.5).

LR cut criterion	> 0.1	> 0.2	> 0.3	> 0.4	> 0.5	> 0.6	> 0.7	> 0.8
Excess event	876	724	635	553	501	404	353	269
Significance	7.5σ	6.7σ	6.3σ	5.8σ	5.7σ	5.1σ	5.0σ	4.5σ
Relative flux	1	0.83	0.74	0.66	0.62	0.53	0.5	0.43

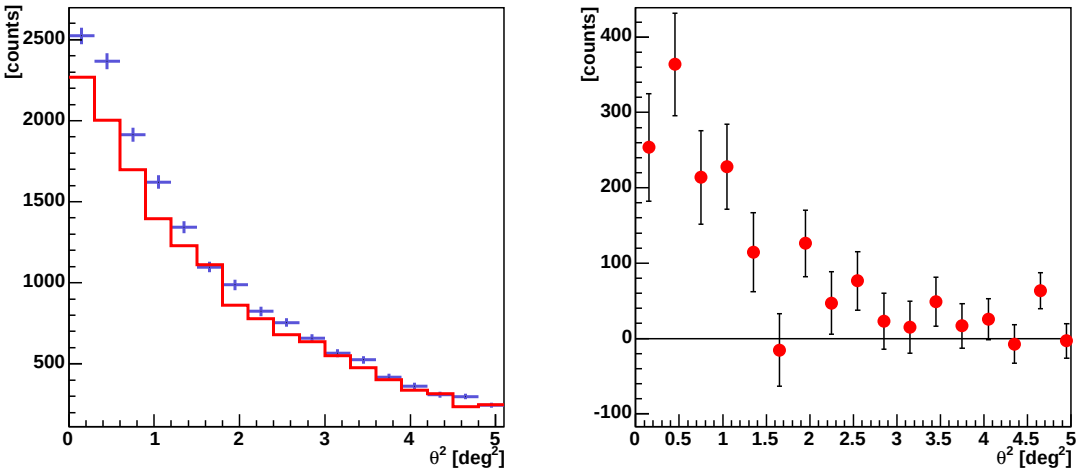

Figure 8.26: θ^2-plots of RX J0852.0−4622 obtained by CANGAROO-III with the shower selection of ADC>4ph.-e. and T4a. Here the LR criterion is $LR > 0.1$. Left: The blue crosses show the distribution of ON-source data with the statistical error bars, and red histogram show that of OFF-source data. Right: Distribution of ON-source excess events. The number of excess events in 0 deg^2 $< \theta^2 <$ 1.0 deg^2 is 924±121, with the significance of 7.6σ.

2. Error in the normalizing method

As described in § 5, the choice of the ON/OFF normalizing method effects on the result. The variation due to this factor is also shown in § 5.

3. Error in the shower selection

The error in the shower selection is also estimated. The standard ADC cut is ADC>5ph.-e. and the standard cluster cut is T5a. We examined the cut of ADC>4ph.-e. and T4a, and the obtained θ^2-plots and differential flux are shown in Fig.8.26 and Fig.8.27, respectively. The fitting result by a power law function is

$$(4.6 \pm 0.5) \times 10^{-11} \times \left(\frac{E}{1\mathrm{TeV}}\right)^{-2.7\pm0.2} \ \mathrm{cm}^{-2}\mathrm{s}^{-1}\mathrm{TeV}^{-1}. \qquad (8.5)$$

4. Shower rate fluctuation

The shower rate fluctuation is regarded here as an acceptance fluctuation in the flux conversion. We sampled all the data of which shower rate exceeds the rate threshold

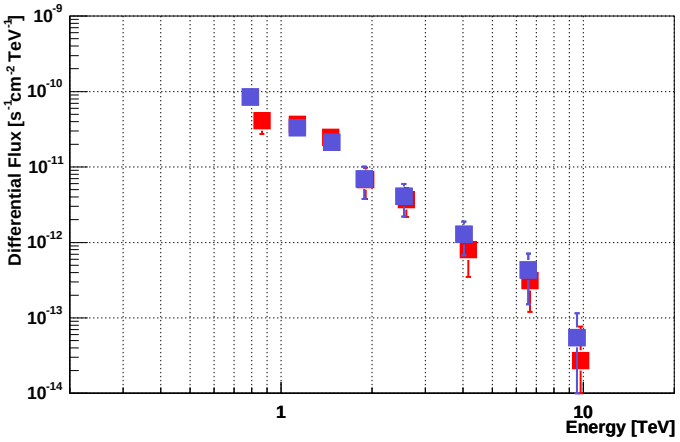

Figure 8.27: Blue: Differential photon flux spectra of RX J0852.0−4622 obtained by CANGAROO-III with the shower selection criteria of ADC>4ph.-e. and T4a. The LR criteria is $LR > 0.1$. The ON-OFF event normalization is based on the ratio of the observation time. Red: That with the shower selection criteria of ADC>5ph.-e. and T5a (the standard analysis). The errors are all statistical.

of 5 Hz from all the observation runs. Their rates are distributed in less than 7 Hz. Assuming that the average of the rates is 5 Hz, which is absolutely underestimated, the Poisson statistics predicts the fluctuation of 5 ± 2 Hz. Then, the fluctuation observed here is considered as statistic.

Considering above all, the fitting function of the flux including the systematic errors is

$$\frac{dF}{dE} = (4.1 \pm 0.6_{\mathrm{stat.}}{}^{-1.7_{\mathrm{syst.}}}_{+0.5_{\mathrm{syst.}}}) \times 10^{-11} \times \left(\frac{E}{1\mathrm{TeV}}\right)^{-(2.7\pm0.2_{\mathrm{stat.}}-0.5_{\mathrm{syst.}})} \mathrm{cm}^{-2}\mathrm{s}^{-1}\mathrm{TeV}^{-1}. \tag{8.6}$$

The subscripts stat. and syst. indicate the statistical error and systematic one, respectively. We analyzed the same data with another method of the fisher discriminant method (details in AppendixA). The edge cut applied here is the normal edge cut. The energy flux spectrum obtained there is described as

$$\frac{dF}{dE} = (2.5 \pm 0.6_{\mathrm{stat.}} \pm 0.6_{\mathrm{syst.}}) \times 10^{-11} \times \left(\frac{E}{1\mathrm{TeV}}\right)^{-(2.2\pm0.3_{\mathrm{stat.}}\pm0.3_{\mathrm{syst.}})} \mathrm{cm}^{-2}\mathrm{s}^{-1}\mathrm{TeV}^{-1}. \tag{8.7}$$

These two results are consistent within the statistic and the systematic errors.

Finally, we compared our results with the results of RX J0852.0−4622 by the

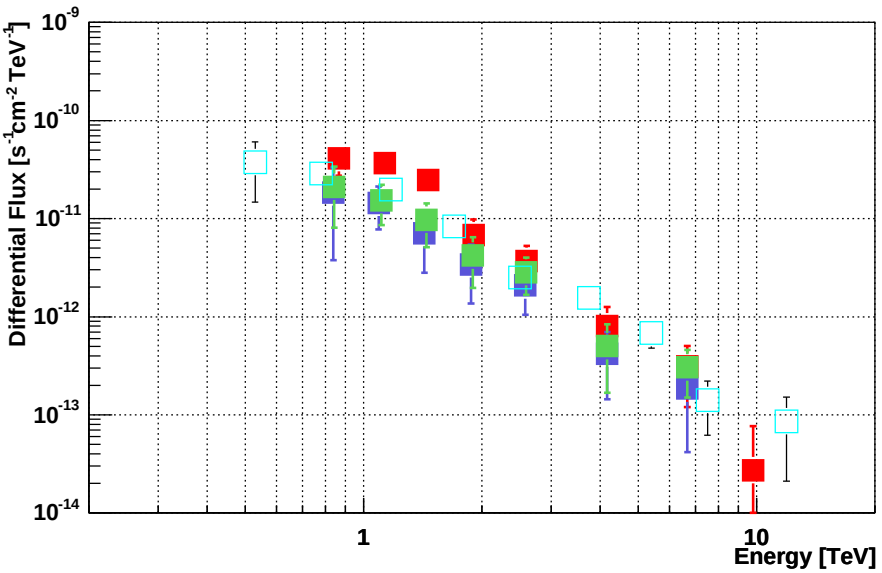

Figure 8.28: Differential flux spectra of RX J0852.0−4622 comparing the results of CANGAROO-III with the result of HESS. Red: The result of CANGAROO-III with $LR > 0.1$. Green: The result of CANGAROO-III with $LR > 0.6$. Blue: The result of CANGAROO-III with $LR > 0.8$. Blue blank: The HESS result,

HESS group (Aharonian et al. 2005b). Their best fit function of the gamma-ray flux is

$$\frac{dF}{dE} = (2.1 \pm 0.2_{\rm stat.} \pm 0.6_{\rm syst.}) \times 10^{-11} \times \left(\frac{E}{1{\rm TeV}}\right)^{-(2.1\pm0.1_{\rm stat.}\pm0.2_{\rm syst.})} {\rm cm}^{-2}{\rm s}^{-1}{\rm TeV}^{-1}. \quad (8.8)$$

The HESS result and the CANGAROO-III result are consistent within the statistic and the systematic errors. Their data points are shown in Fig.8.28 (blank light blue) with the CANGAROO-III results with the LR criteria of $LR > 0.1$ (red), $LR > 0.6$ (green), and $LR > 0.8$ (blue).

Chapter9

Discussion

§ 1 Emission Mechanisms

1.1 Total Emission

In Chapter1 we described three mechanisms of the gamma-ray emission, and hence, the total gamma-ray emission flux is given as

$$F_\gamma \propto nQ^{\pi^0}(E, \alpha_{\rm p}) + nR_eQ^{\rm brems}(E, \alpha_{\rm e}) + R_{\rm e}Q^{\rm IC}(E, \alpha_{\rm e}). \tag{9.1}$$

Here n is the nucleon number density in the region of the SNR, and $R_{\rm e}$ is the electron-to-proton (e/p) spectrum ratio above 1 GeV. $Q^{\pi^0}(E, \alpha_{\rm p})$, $Q^{\rm brems}(E, \alpha_{\rm e})$ and $Q^{\rm IC}(E, \alpha_{\rm e})$ are the radiation emissivities (in cm^{-3}s^{-1}GeV^{-1}) for the process of π^0 decay, bremsstrahlung, and inverse Compton (IC) scattering, respectively. Here, $n = 1$ cm^{-3} and $R_{\rm e} = 1$ are assumed, and E, $\alpha_{\rm p}$, $\alpha_{\rm e}$ are the energy of gamma-rays, the spectral index of protons, and that of electrons, respectively. They are plotted in Fig.9.1 multiplied by E^2 for $\alpha_{\rm p} = \alpha_{\rm e} = 2$. This formula was originally considered in a radiation field analogous to that of IC 443. IC 443 is the SNR from which sub-GeV gamma-ray signals were observed by the *EGRET* instrument (Esposito et al. 1996), and then its emission has been well studied. This emissivity spectrum seems universal for SNRs in the Galaxy except for the local infrared radiation field (the short-dashed line in Fig.9.1) because the Galactic infrared background varies as a function of the Galactocentric distance. However, the variance is negligible. In Fig.9.1, the contributions of various IC processes are clearly dominant for $R_{\rm e} = 1$ and $n = 1$, which is 3 to 4 orders of magnitude higher than that of π^0 decay around 1 TeV. Among them, the IC scattering on the cosmic microwave background (CMB) is the strongest. The actual ratio of the contribution of π^0 to that of IC scattering is $n/R_{\rm e}$. $R_{\rm e}$ can be assumned to be ~ 0.01 at the spot of the particle acceleration (Reynolds 1996; Kobayashi et al. 2004) and $n \sim 0.2$ at the shock wave of RX J0852.0−4622 as described later in Section 2.2. Using these values, the ratio of emission by π^0 to that

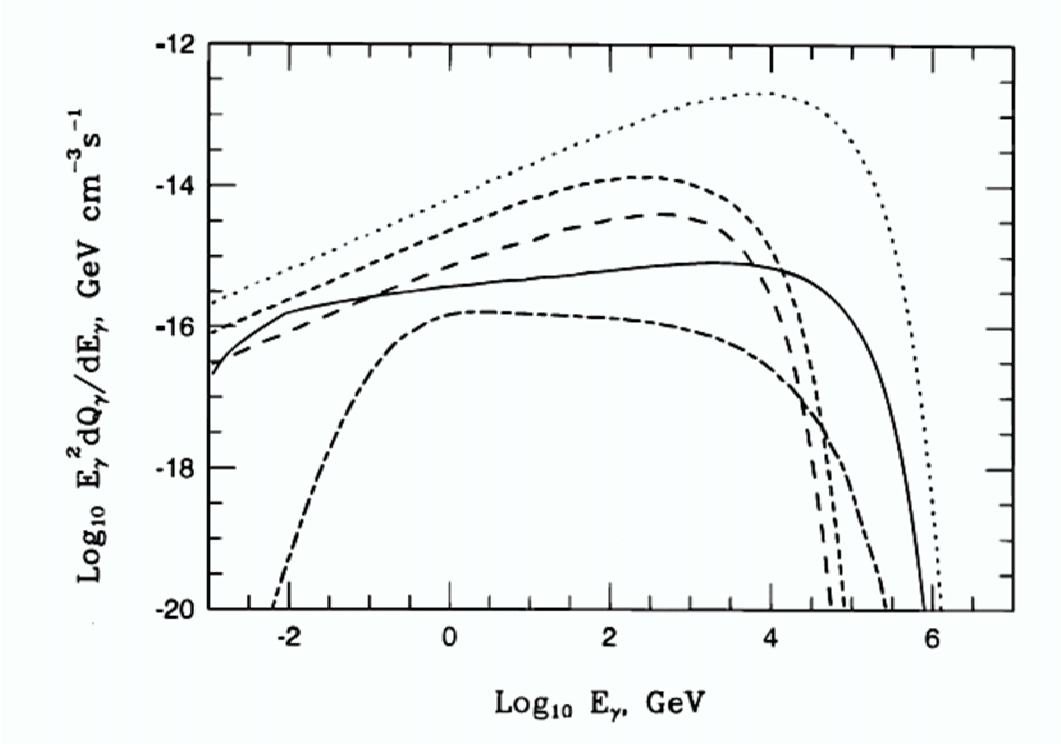

Figure 9.1: Gamma-ray emissivity at IC 443 produced by particles (electrons and protons) with a spectral index of -2, interacting with interstellar matter with nucleon number density 1 cm^{-2}, and with interstellar infrared optical (IR/O) and cosmic microwave radiation fields same with the circumstances of IC 443, respectively. Dot-dashed line: π^0 production, solid line: bremsstrahlung, long-dashed line: IC on interstellar IR/O, short-dashed line: IC on infrared radiation at IC443, dotted line: IC on microwave.

by bremsstrahlung is ~ 0.1 (as seen in Fig.9.1) $\times 1/R_{\rm e}$. From the above assumption, it is an order of magnitude higher than the bremsstrahlung emissivity. Therefore, we have to consider only two strongest emission mechanisms of IC scattering on the CMB and π^0 decay, and thus, we neglect the effects of the bremsstrahlung and the IC scattering on the other photons, hereafter.

1.2 Inverse Compton Scattering

The high-energy electrons emit photons via both synchrotron radiation and IC scattering with the CMB. The former is observed in the radio to the X-ray region, and the latter in the gamma-ray region. In order to evaluate the spectrum of the TeV emission from IC scattering, we assume the energy spectrum of the relativistic electrons as

$$Q(E_{\rm e}) = A\left(\frac{E_{\rm e}}{m_{\rm e}c^2}\right)^{-\alpha}\exp\left(-\frac{E_{\rm e}}{E_{\rm max}}\right), \tag{9.2}$$

where $E_{\rm e}$, $m_{\rm e}$, α and $E_{\rm max}$ are the electron energy, the mass of the electron, the spectral index, and the exponential cut-off energy of electrons, respectively. The differential flux of the electron is described as

$$\frac{dF(E)}{dE} = \frac{1}{4\pi d^2}\cdot VQ(E_{\rm e})dE_{\rm e}\cdot\frac{1}{\tau}\cdot\frac{1}{dE} = \frac{V}{4\pi d^2}Q(E_{\rm e})\frac{dE_{\rm e}}{dE}\frac{1}{\tau}, \tag{9.3}$$

where V, d and τ are the volume of the emission region, the distance from the Earth, and the average deceleration time in which one electron with the energy of $E_{\rm e}$ emits the photon of energy E. $E_{\rm e}$ is given as

$$E_{\rm e} = \gamma_{\rm e}m_{\rm e}c^2, \tag{9.4}$$

where $\gamma_{\rm e}$ is the Lorentz factor of the electron. Here we used δ-function approximation (Rybicki & Lightman 1979; Oda et al. 1989). In nonrelativistic IC process ($\gamma_{\rm e}h\nu \ll m_{\rm e}c^2$), E is given as

$$E = \gamma_{\rm e}^2\bar{E}_{\rm CMB}, \tag{9.5}$$

where the $\bar{E}_{\rm CMB}$ is the average energy of the CMB. τ is approximately estimated as

$$\frac{1}{\tau_{\rm IC}} \sim \frac{1}{E}\left[\frac{dE_{\rm e}}{dt}\right]_{\rm IC} = \frac{1}{E}\frac{4}{3}\sigma_T c\gamma_{\rm e}^2 U_{\rm CMB} = \frac{4}{3}\frac{\sigma_T c U_{\rm CMB}}{\bar{E}_{\rm CMB}}, \tag{9.6}$$

where the σ_T and $U_{\rm CMB}$ are the cross section of Thomson scattering and the energy density of CMB, respectively. Then, the differential flux of gamma-rays from IC

process is given as

$$\left[\frac{dF(E)}{dE}\right]_{\rm IC} = \frac{V}{4\pi d^2}\frac{2}{3}\frac{A}{m_{\rm e}c^2}\sigma_T c U_{\rm CMB}\left(\frac{\bar{E}_{\rm CMB}}{m_{\rm e}c^2}\right)^{\frac{\alpha-3}{2}}\left(\frac{E}{m_{\rm e}c^2}\right)^{-\frac{\alpha+1}{2}}\exp\left[-\frac{m_{\rm e}c^2}{E_{\rm max}}\left(\frac{E}{\bar{E}_{\rm CMB}}\right)^{\frac{1}{2}}\right]. \tag{9.7}$$

From Eq.(9.7), the power-law index of the gamma-ray spectrum should be 1.5 for $\alpha = 2$, which is predicted by the diffusive shock acceleration theory discussed in Chapter 1.

In order to obtain the differential flux of synchrotron radiation, the $U_{\rm CMB}$ can be replaced with

$$U_B = \frac{B^2}{8\pi}. \tag{9.8}$$

B and U_B are the ambient magnetic field and its energy density, respectively. $\bar{E}_{\rm CMB}$ can be also replaced with

$$\bar{E}_{\rm sync} = 0.29 h\nu_c\frac{\pi}{4}, \tag{9.9}$$

where $\bar{E}_{\rm sync}$ is the peak energy of the synchrotron radiation (again δ-function approximation). After these replacements, the differential flux is given as

$$\left[\frac{dF(E)}{dE}\right]_{\rm sync} = \frac{V_{\rm sync}}{4\pi d^2}\frac{2}{3}\frac{A}{m_{\rm e}c^2}\sigma_T c U_B\left(\frac{\bar{E}_{\rm sync}}{m_{\rm e}c^2}\right)^{\frac{\alpha-3}{2}}\left(\frac{E}{m_{\rm e}c^2}\right)^{-\frac{\alpha+1}{2}}\exp\left[-\frac{m_{\rm e}c^2}{E_{\rm max}}\left(\frac{E}{\bar{E}_{\rm sync}}\right)^{\frac{1}{2}}\right]. \tag{9.10}$$

The power-law index of the synchrotron spectrum is equal to that of IC scattering. When the particle is relativistic, the quantum effect on the cross section is not negligible. The differential cross section for the unpolarized radiation is shown in quantum electrodynamics (Heitler 1954), and given by the Klein-Nishina formula:

$$\frac{d\sigma}{d\Omega} = \frac{r_0^2}{2}\frac{\epsilon_1^2}{\epsilon^2}\left(\frac{\epsilon}{\epsilon_1} + \frac{\epsilon_1}{\epsilon} - \sin^2\theta\right). \tag{9.11}$$

Here ϵ and ϵ_1 are the incident and scattered photon energies, respectively, and θ is the recoil angle of the scattered photon. In the case of the above IC scattering, $\epsilon = E_{\rm e}$ and $\epsilon_1 = E$ ($E_{\rm e}$ and E are defined by Eq.(9.4) and Eq.(9.5), respectively). The dominant effect is to reduce the cross section from its classical value (limit of $\epsilon_1 \sim \epsilon$) as the photon energy becomes large. Thus, IC scattering becomes less efficient at higher energy. The total cross section can be shown to be

$$\sigma = \frac{3}{4}\cdot\sigma_T\left[\frac{1+x}{x^3}\left\{\frac{2x(1+x)}{1+2x} - \ln(1+2x)\right\} + \frac{1}{2x}\ln(1+2x) - \frac{1+3x}{(1+2x)^2}\right], \tag{9.12}$$

where $x \equiv \epsilon/mc^2$. We used this cross section instead of σ_T for Eq.(9.10).

1.3 π^0 Decay by Proton-Nucleon Collisions

In this section, all characters for the energy in equations are described in the unit of GeV unless otherwise noted.

π^0s are produced in collisions of accelerated protons with interstellar matter. Here, the model based on the isobaric model and the scaling model (Naito & Takahara 1994) was used. The spectrum of the gamma-rays produced from this process are calculated from its phase space as

$$F^{\gamma}(\epsilon_{\gamma}) = 2\int_{E_{\pi}^{\min}(\epsilon_{\gamma})}^{\infty} dE_{\pi}\frac{F^{\pi}(E_{\pi})}{\sqrt{E_{\pi}^2 - m_{\pi}^2}} \ \ [\text{photons cm}^{-3}\ \text{s}^{-1}\ \text{GeV}^{-1}], \tag{9.13}$$

where E_{π} is the π^0 energy, m_{π} is its rest mass in GeV c^{-2}, $F^{\pi}(E_{\pi})$ denotes the π^0 spectrum, ϵ_{γ} is the gamma-ray energy, and $E_{\pi}^{\min}(\epsilon_{\gamma})$ is the minimum energy of π^0s to create photons of energy ϵ_{γ}, respectively. $F^{\pi}(E_{\pi})$ is derived kinetically using the following relation:

$$F^{\pi}(E_{\pi}) = 4\pi n_0 \int_{E_{\rm p}^{\min}(E_{\pi})}^{E_{\rm p}^{\max}} dE_{\rm p} j_p(E_{\rm p})\frac{d\sigma_{\pi}(E_{\pi}, E_{\rm p})}{dE_{\pi}} \ \ [\text{pions cm}^{-3}\ \text{s}^{-1}\ \text{GeV}^{-1}]. \tag{9.14}$$

Here n_0 is the number density of protons where the interactions occur, $E_{\rm p}$ is the energy of cosmic ray protons, $E_{\rm p}^{\min}(E_{\pi})$ is the minimum cosmic-ray proton energy to produce π^0s of energy E_{π}, and $j_{\rm p}$ is the energy spectrum of cosmic ray protons, respectively. $d\sigma_{\pi}(E_{\pi}, E_{\rm p})/dE_{\pi}$ is the differential cross section. Now we assume

$$j_{\rm p}(E_{\rm p}) = \frac{K}{V}\left(\frac{E_0}{10^{50}\ \text{erg}}\right) E_{\rm p}^{-\alpha} \exp\left(-\frac{E_{\rm p}}{E_{\rm p}^{\max}}\right) \ \ [\text{protons (cm}^2\ \text{s GeV sr)}^{-1}], \tag{9.15}$$

where V is the volume of the SNR shell, E_0 is the total energy of the cosmic ray protons in the observed part of the SNR, and $E_{\rm p}^{\max}$ is the maximum accelerated energy of protons. The assumption of the exponential cut off is adopted because it fits better to the experimental data than a simple power law. (Gaisser et al. 1998). K is the normalization factor determined to satisfy the following equation.

$$\int_{m_{\rm p}c^2}^{\infty} \frac{4\pi}{c} j_{\rm p}(E_{\rm p}) E_{\rm p} dE_{\rm p} = \frac{E_0}{V}. \tag{9.16}$$

§ 2 Multiwavelength Spectrum

2.1 Synchrotron / Inverse Compton Model

In order to fit the observed spectrum with this model, we used the data of radio, X-ray, and gamma-ray in $\sim$ GeV to TeV. The radio data of Parkes are from Table 2 of

Duncan & Green (2000) and the X-ray data, which are taken by *ASCA* satellite, are based on Table 2.1 (Slane et al. 2001). Slane et al. (2001) only show the fluxes for the northwest, northeast, west, and central regions of the SNR. We combined them and calculated five data points from 0.5 to 10 keV. Since this observation does not covere the whole remnant, these fluxes are the lower limit. The flux from the central region might not be included here because its spectral index is significantly different from those of others, which can origin from the different emission mechanism. However the flux from the center is an order of magnitude less than those of other three points, then the result would be changed little. The only error we took into account is that for spectral indices, then the errors in Fig.9.2, 9.3, 9.5 are also underestimated. The GeV to TeV data are our 8 points and 9 points from HESS report (Aharonian et al. 2005b).

The total spectrum from radio to TeV was fitted with Eqs.(9.7) and (9.10), and we used Eq.(9.12) as the cross section. The input electron spectrum accountable for the multiwavelength emission is assumed to be proportional to $E^{-\gamma}e^{-E/E_{\rm max}}$. In these calculations, there are three free parameters, the magnetic field B, the power-law index of the electron spectrum γ, and the maximum accelerated energy of the electrons $E_{\rm max}$. The best fit parameters are $B = 3.8 \pm 0.1$ μG and $\gamma = 2.34 \pm 0.01$, and $E_{\rm max} = 40.6 \pm 2.8$ TeV. The best fit curve is shown in Fig.9.2.

The filamentary structure of nonthermal X-ray emission was observed by *Chandra* as shown in Fig 9.4. Using this filament, Bamba et al. (2005b) estimated a high magnetic field of 500 μG and low $E_{\rm max}$ of 3 TeV via the empirical function of $\mathcal{B}$-age relation (Bamba et al. 2005a). This energy $E_{\rm max} = 3$ TeV is too low to explain the observed relatively flat spectrum of TeV emissions via IC scattering or π^0 decay process. On the other hand, the filamentary structure indicates the existence of the strong magnetic field of order of 100 μG, and thus the above best fit result $B \sim 3$ μG is unacceptable. In order to describe the TeV emission, an order of magnitude higher cut-off energy is definitely necessary which favors a 2 orders of magnitude lower magnetic field, because the maximum energy of the synchrotron radiation is a function of $E_{\rm max}\sqrt{B}$.

As Bamba et al. (2005b) indicated, the filamentary structure is thought to be the result of synchrotron radiation with the bound by a strong magnetic field in the limited region as in case of other SNRs (Vink & Laming 2003; Berezhko et al. 2003; Berezhko & Völk 2004). Then we may need to introduce the magnetic field filling factor ($f_B < 1$) to explain the TeV gamma-ray emission by electron origin. f_B

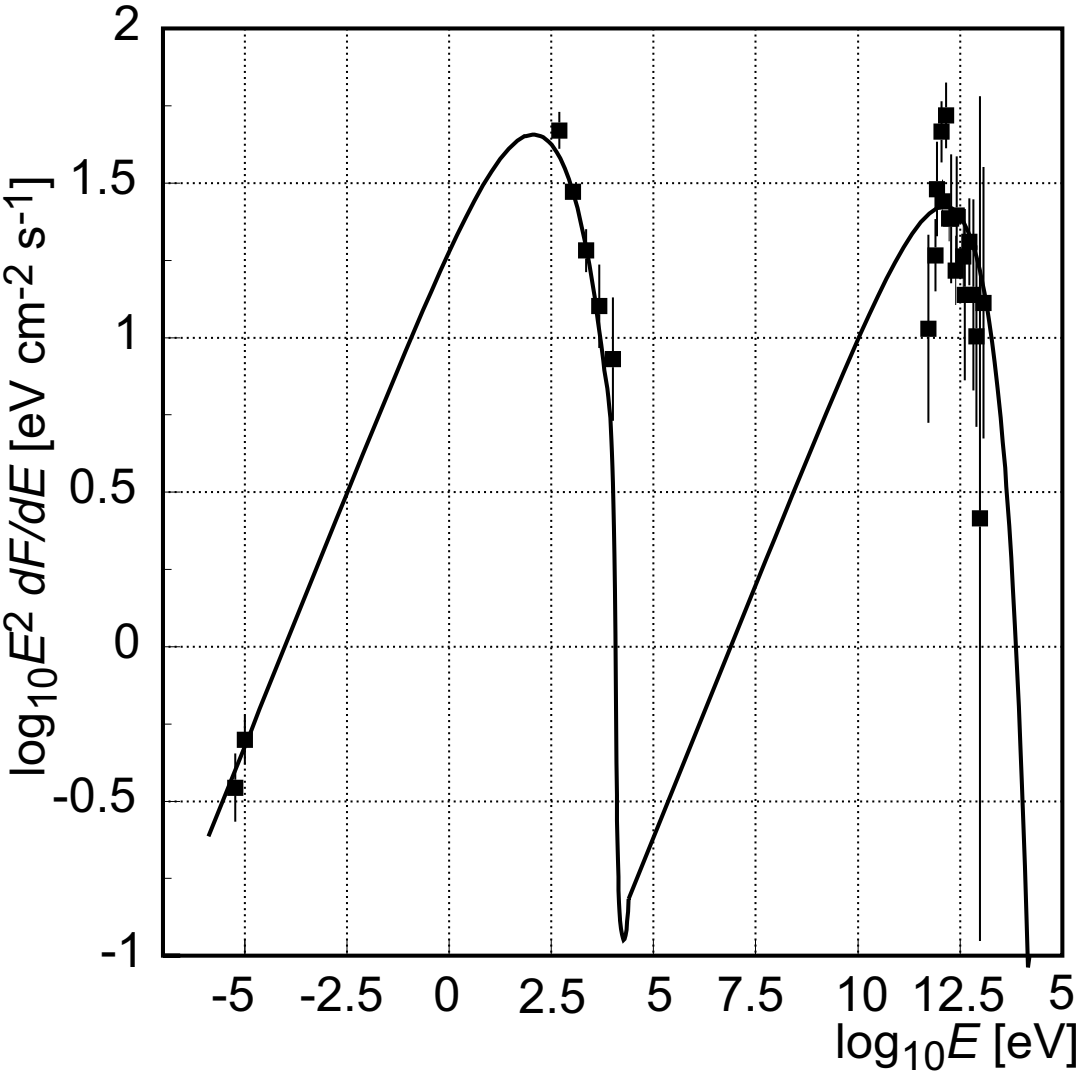

Figure 9.2: Fitting result under the assumption of $\gamma = 2.1$. The best fit parameters are $B = 3.8 \pm 0.1$ μG and $E_{\rm max} = 40.6 \pm 2.8$ TeV.

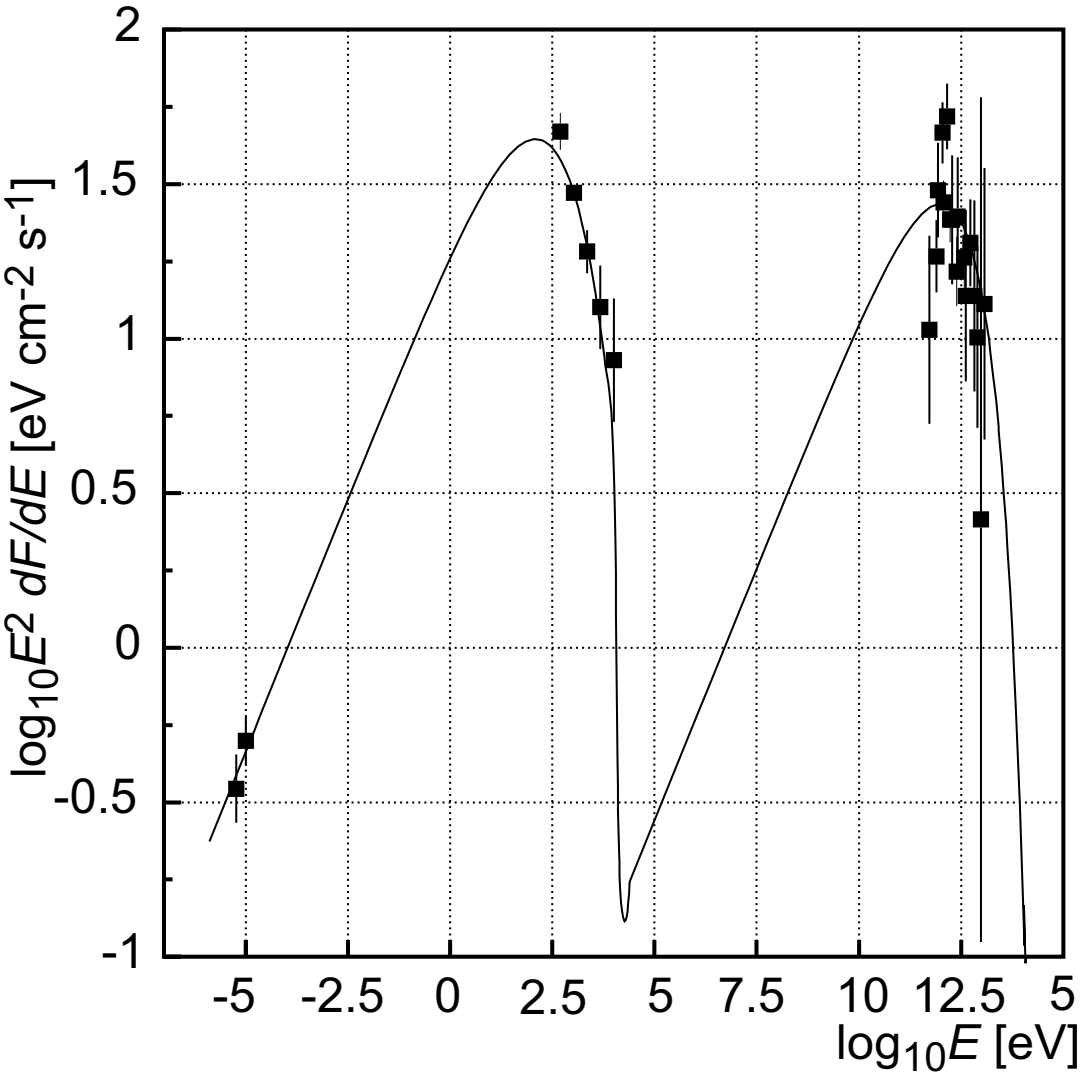

Figure 9.3: Fitting results with the magnetic field filling factor as one of the free parameters. The best fit results are $B = 5.9 \pm 0.7$ μG, $E_{\rm max} = 33 \pm 3$ TeV, $\gamma = 2.3 \pm 0.01$, and $f_B = 0.40 \pm 0.10$.

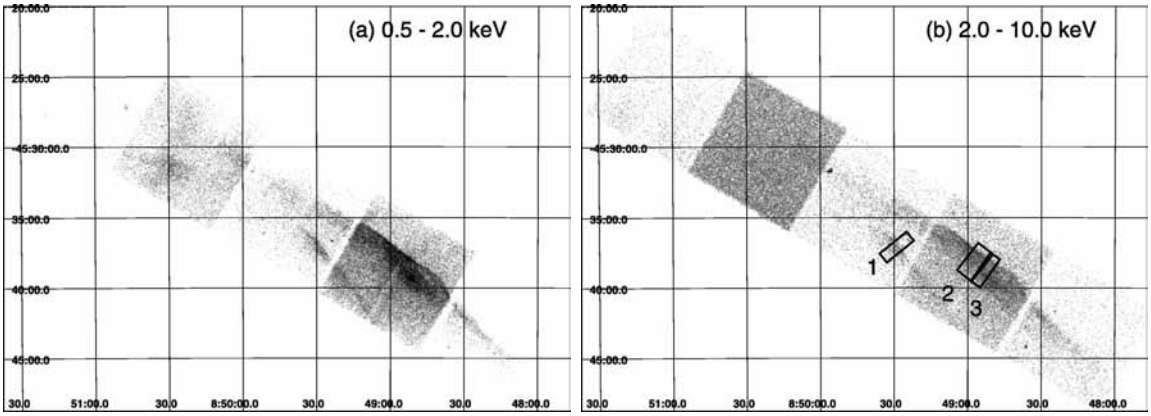

Figure 9.4: *Chandra* images of the northwest rim of RX J0852.0−4622 in (a) the 0.5-to-2.0-keV band and (b) the 2.0-to-10.0-keV band (Bamba et al. 2005b). Thin filament structures can be seen in the both panels.

corresponds approximately to the ratio of the region of the X-ray emission to that of the gamma-ray emission. The spectrum was fitted with the four free parameters, i.e., B, $E_{\rm max}$, γ, and f_B, and the best fit function is shown in Fig.9.3. The best fit parameters are $B = 5.9 \pm 0.7$ μG, $E_{\rm max} = 33 \pm 3$ TeV, $\gamma = 2.3 \pm 0.01$, and $f_B = 0.40 \pm 0.10$. $f_B = 0.40$ is equivalent to an uneven distributed magnetic field in the shell with the thickness of $0.2 \times (Radius\ of\ the\ SNR)$ at the shock wave. This result is too thick for the observed filament image. As a trial, we fixed f_B to 0.01, and get the best fit parameters as $B = 32.5 \pm 0.8$ μG, $\gamma = 2.38 \pm 0.01$ and $E_{\rm max} = 18.1 \pm 1.5$ TeV. The fitting curve is shown in Fig.9.5. Though this value B=32.5 μG is rather acceptable than before as the magnetic field in an SNR, it is not sufficiently high compared to an estimate of some hundreds μG. Therefore, the IC scattering solution seems difficult. This contradiction can be resolved by introducing a different energy spectrum between electrons and protons as is predicted by kinetic nonlinear acceleration theories where synchrotron cooling of electron is taken into account (see, for example, Berezhko et al. 2003). For a sufficiently high magnetic field, the kinetic energy of the electrons is restricted to significantly lower than that of the protons. Additionally, we consider the energetics of the SNR as an accelerator of the cosmic ray before we discuss the hadronic scenario. The total energy of the electrons is 3.7 $\times 10^{45}$ ergs at 200 pc from the Earth. If we assume the electron to proton ratio is 0.01 (a typical value), the electron energy of 10^{45} ergs is equivalent to 10^{47} ergs of the proton energy. Since the SNR genesis of the cosmic ray requests

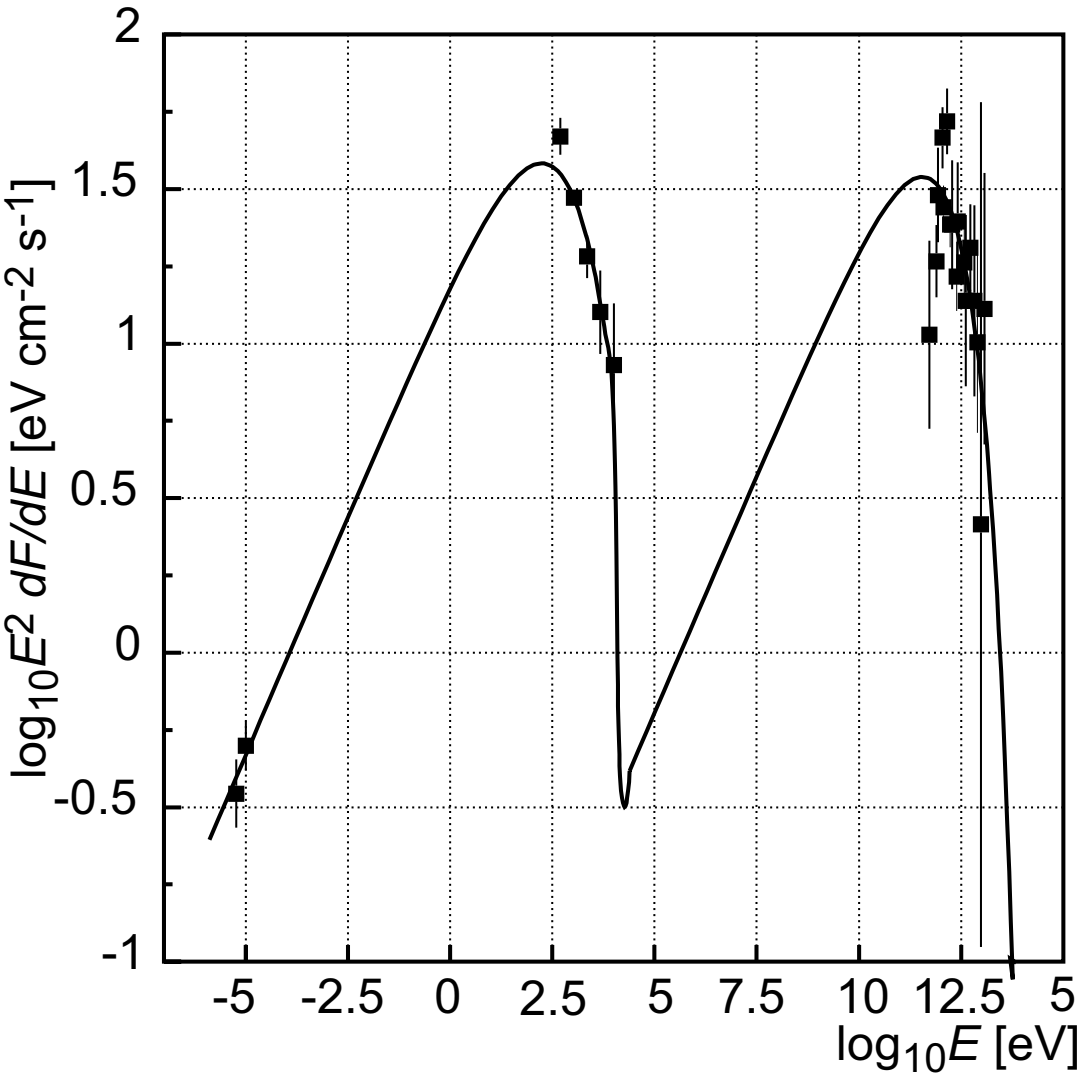

Figure 9.5: Fitting results with the fixed magnetic field filling factor to 0.01. The best fit results are obtained with $B = 32.5 \pm 0.8$ μG, $\gamma = 2.38 \pm 0.01$ and $E_{\rm max} = 18.1 \pm 1.5$ TeV.

10^{50} ergs as the particle kinetic energy in the SNR, it seems too low. Here, it should be noticed that the report by *ASCA* (Slane et al. 2001) refers only the restricted four regions and not the whole shell. When the emission from whole the shell is considered, the flux is probably larger. According to Hiraga (private comm.), the total emission is expected to be about 4 times as large as reported, and then the magnetic field should be twice as large as above result, However, even if this fact is taken into account, B is ~ 65 μG, which is still low.

2.2 π^0 Decay Model

Then we considered the protonic contributions to the TeV-gamma-ray flux. Hereafter, we assume that the magnitude of B is order of hundred microgauss, which is accompanied by the fact that electron-derived TeV gamma-rays cannot be observed, and we address only the proton genesis. The age, the shock velocity, and the origin of this SNR have some ambiguity as we mentioned in Chapter2. Here we adopt the age of 680 yr, the velocity of 5000 km s^{-1} and the type-Ia-SN origin theory. At this age, the SNR is considered to be at the stage of the free expansion or just shifting to the Sedov (adiabatic) phase. Then the mass is order of the ejecta mass, which is $\sim M_\odot$ for a type Ia SNR. Assuming the distance of 200 pc, which is consistent with the fact of the age 680 yr and the angular diameter $\sim 2^\circ$, the matter density is ~ 0.29 p/cc. We fitted our result and the HESS's TeV flux (Aharonian et al. 2005b) with two parameters, i.e., $E_{\rm max}$ and the total proton energy $E_{\rm p}$. The best fit was $E_{\rm max} = 155 \pm 116$ TeV, and the fitting curve is plotted in Fig.9.6.

We discussed the upper limit of the maximum energy in Chapter1-4.2, and described it as Eq.(1.52). Under the assumptions of

$$\begin{aligned} (B, \eta, E_0, v_0, n_0) &= (100\mu\mathrm{G}, 1, 1, 5000\mathrm{km/s}, 0.29) \\ \text{SNR age}: \ t &\sim 10^3 \text{ yr}, \end{aligned}$$

we obtained $E_{\rm max} \sim 400$ TeV. Here t is possibly overestimated, and therefore the actual $E_{\rm max}$ should be less. However, even considering this fact, $E_{\rm max} \sim 155$ TeV seems rather reasonable.

The protonic cosmic-ray energy at $d = 200$ pc is $E_{\rm p} = 0.98 \times 10^{50}$ ergs. This proton energy seems slightly too large because it means that as much as 10% of SN energy should be used to accelerate cosmic rays. If the target matter density is $\sim$1 p/cc, which is assuming that of interstellar matter, $E_{\rm p} = 0.19 \times 10^{50}$ ergs at

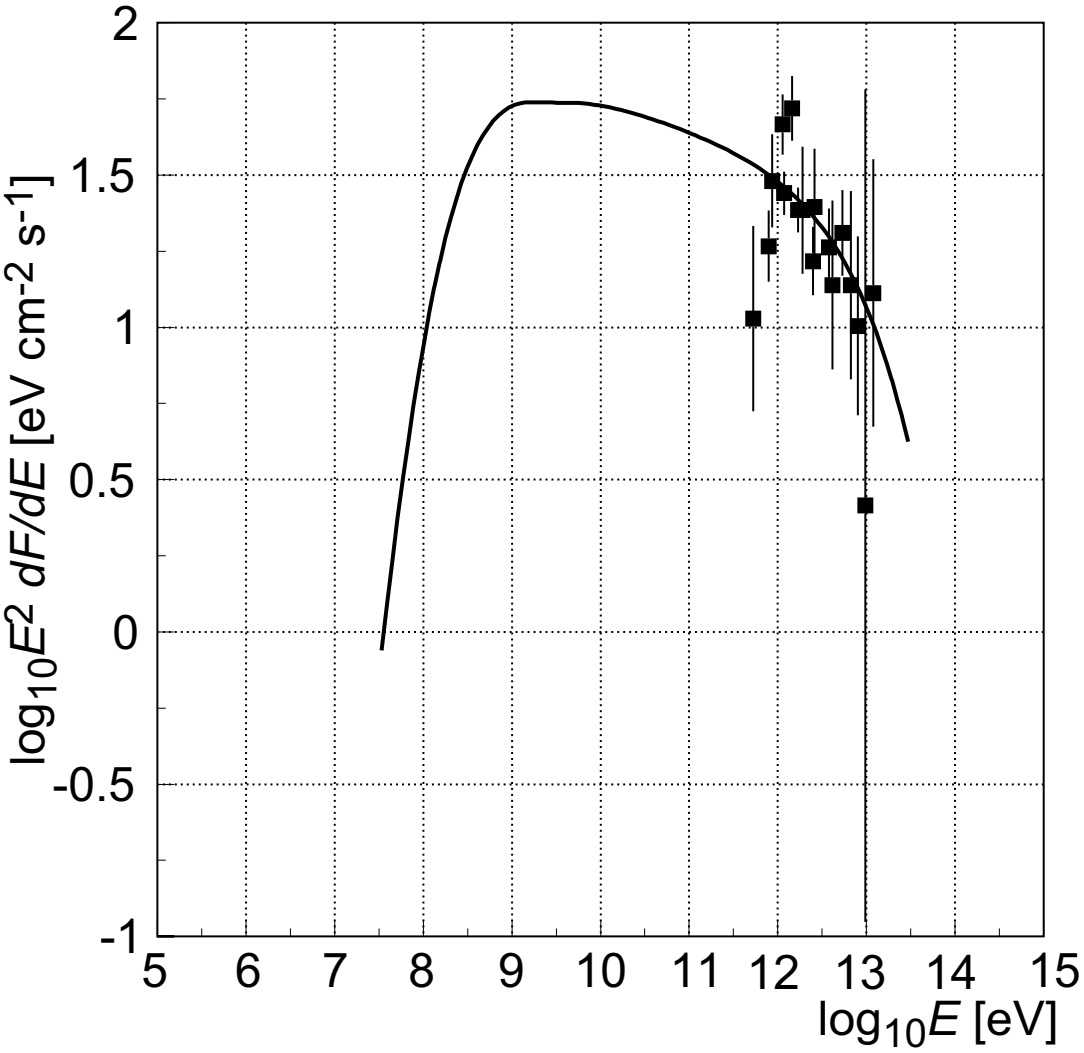

Figure 9.6: Fitting results with the π^0 decay model.

200 pc. This is acceptable for the SNR genesis of the galactic cosmic rays. From the above discussions, the proton scenario is more favorable.

We will show the various observations of anothoer TeV gamma-ray SNR, RX J1713.7−3946, and make some comparison with RX J0852.0−4622 in Appendix B.

AppendixA

Fisher Discriminant Method

We investigated an alternative approach for the comparison of observational and Monte Carlo data and to derive more efficient and reliable selection method for the gamma-ray showers: Fisher Discriminant (FD) Method (Fisher 1936). This method is based on a analytical method. When the multiparameter used here is

$$\boldsymbol{P} = (\text{Vector of Hillas moments for all telescopes}), \tag{A.1}$$

a linear combination F is defined as

$$F = \boldsymbol{\alpha} \cdot \boldsymbol{P}. \tag{A.2}$$

This value F is named Fisher discriminant. $\boldsymbol{\alpha}$ is the set of linear coefficients, which is determined to provide the best separation of the F distribution between the signal and the background. It is uniquely calculated mathematically as

$$\boldsymbol{\alpha} = \frac{\boldsymbol{\mu}_{\rm sig} - \boldsymbol{\mu}_{\rm BG}}{E_{\rm sig} + E_{\rm BG}}. \tag{A.3}$$

Here, the subscripts "sig" and "BG" denote gamma-ray signals and background events, respectively. $\boldsymbol{\mu}$ is a vector of the mean value of $\boldsymbol{P}$ for each sample, i.e., $\mu =< \boldsymbol{P} >$, and E is their error matrix, i.e., $E =< \boldsymbol{P}\boldsymbol{P}^T > - < \boldsymbol{P} >< \boldsymbol{P}^T >$. The values of $\boldsymbol{\mu}$ and E are calculated from the test sample of the Monte Carlo gamma-ray data and the observed background data for the signals and the background events, respectively. The purpose is to separate "sharp (gamma-ray-like) images" from "smeared (background) ones". This method has been regularly used in high-energy experiments such as B factory in order to separate the events with spherical topology form those with jetlike one (Abe et al. 2001). The separation efficiency strongly depends on which form of the linear combination we select. We cannot say this format of $\boldsymbol{\alpha} \cdot \boldsymbol{P}$ gives the best separation combination, but it is one of the better selection. Moreover, the separation efficiency also depends on which parameters we

chose. Here we used *width* and *length* for all the telescopes. They are both second-order cumulative moments of shower images, and thus their linear combination is a reasonable assumption.

In order to remove the offset ambiguity by the dependence of the parameters on the energy and the telescope, we made the following correction. The distributions of the parameter were fitted with a second-order polynomials for the Monte Carlo gamma-ray events:

$$\boldsymbol{P} = \boldsymbol{P}_{\rm raw} - \boldsymbol{a}_0 - \boldsymbol{a}_1 \log(\Sigma ADC) - \boldsymbol{a}_2 \log(\Sigma ADC)^2, \tag{A.4}$$

where $\boldsymbol{a}_i$s were determined from the two-dimensional plots of the Hillas parameters versus $\log(\Sigma ADC)$ using the Monte Carlo gamma-ray simulations, and $\boldsymbol{P}_{\rm raw}$ is a vector made of the values of Hillas parameters. The best-fit function was subtracted from the parameter distributions obtained from the observation events. Then the means of the corrected parameters are all set to zero for gamma-rays independently of the energy:

$$< \boldsymbol{P}_{\rm sig} >= 0. \tag{A.5}$$

This procedure also ensures that the linear combination F has the approximately Gaussian distribution with the mean of zero:

$$< \boldsymbol{F}_{\rm sig} >= 0. \tag{A.6}$$

The distribution of F for the Monte Carlo gamma-ray events is shown in Fig.A.1 as the blue line. On the other hand, the $F_{\rm BG}$ distribution is deviated to the x<0-side, which is shown as the red histogram in Fig.A.1 The advantage of this method is to remove the artificial cut-selection bias. F is understood as the hybrid parameter which is produced from the conventional parameters in consideration of the energy dependency and the linear difference among the different parameters.

Once the F distributions for Monte Carlo gamma-ray events and OFF-source events are obtained, they are assumed to be the signal and the background behaviors, respectively. Therefore, the F distribution of ON-source data is fitted as a linear combination of above emulated signal and background functions to derive the number of signal events without the selection criteria nor positional subtractions. This is a two-parameter ($F_{\rm sig}$ and $F_{\rm BG}$, in other words, $\boldsymbol{\alpha}_{\rm sig}$ and $\boldsymbol{\alpha}_{\rm BG}$) fitting. These coefficients can be exactly derived analytically, which removes any subjective bias in cut determination. First, we tried this method for the data of the Crab

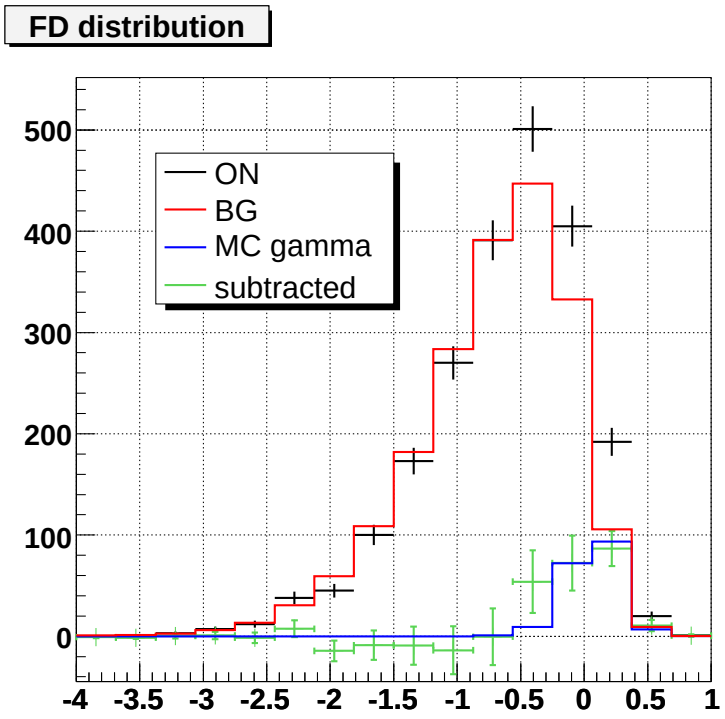

Figure A.1: F distributions for the data of the Crab Pulsar/Nebula in 2003. The horizontal axis and the vertical are F and the number of events in arbitrary units. The black crosses are those with statistical error for the events inside a $0^{o}.05$-radius-circle centered on the target. The red and blue histogram are for OFF-source and Monte Carlo gamma-ray data. The normalization of these histograms is determined by the fitting procedure described in the text. The green crosses show the background subtracted signals.

Pulsar/Nebula in 2003. The fitting result is shown in Fig.A.1. The red and the blue histogram are the best-fit Fs of background and signal, respectively, for the ON-source data shown as the black crosses. The background-subtracted signals are indicated by the green crosses. We can see the excess distribution of the gamma-ray candidate events (green crosses) and it is reasonably similar to that of Monte Carlo gamma-ray events (blue histogram). The θ^2 distribution of the excess events are plotted in Fig.A.2. The estimated gamma-ray signals are 182.8 events and their Li&Ma significance is 6.7σ.

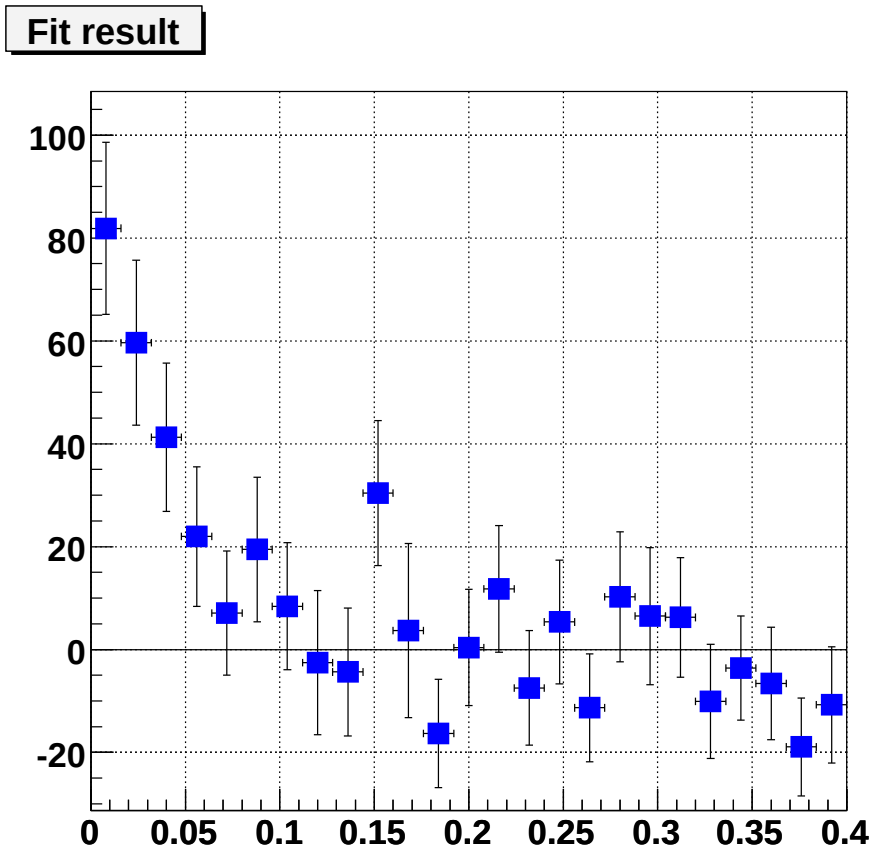

Figure A.2: θ^2-plot obtained for the Crab Pulsar/Nebula in 2003 by the Fisher discriminant method with fit.

We applied this method to the analysis of RX J0852.0−4622 with the conventional edge cut). The distribution of F and the obtained θ^2-plot are shown in Fig.A.3 and A.4, respectively. The number of excess events is 557 ± 77 (7.2σ). The gamma-ray fluxes within a 1° radius were derived by fitting the FD distributions within this area on an energy by energy basis. The blue boxes in Fig.A.5 are obtained by this FD-fitting method, and the red boxes are by the likelihood method. The light-blue squares are the HESS result. This figure shows that our results by the FD-fitting and the likelihood method are consistent with each other. The best fit with a power law assumption for this energy spectrum is

$$\frac{dF}{dE} = (2.5 \pm 0.6_{\rm stat.} \pm 0.6_{\rm syst.}) \times 10^{-11} \times \left(\frac{E}{1{\rm TeV}}\right)^{-(2.2\pm0.3_{\rm stat.}\pm0.3_{\rm syst.})} {\rm cm}^{-2}{\rm s}^{-1}{\rm TeV}^{-1}. \tag{A.7}$$

The numerical data are listed in Table A.1. The resulting morphology by the fitting method is shown in Fig.A.6. Although the brightest region has chanced from that of Fig.8.23, this difference can be considered to be within the level of fluctuations.

Table A.1: Differential flux within 1° from the SNR center.

Mean energy [TeV]	dF/dE [cm^{-2}s^{-1}TeV^{-1}]
1.02	$2.77 \pm 0.88 \times 10^{-11}$
1.24	$1.32 \pm 0.43 \times 10^{-11}$
1.51	$1.03 \pm 0.29 \times 10^{-11}$
1.77	$4.40 \pm 2.14 \times 10^{-12}$
2.24	$7.11 \pm 1.17 \times 10^{-12}$
2.98	$1.93 \pm 0.46 \times 10^{-12}$
4.72	$8.83 \pm 5.03 \times 10^{-13}$

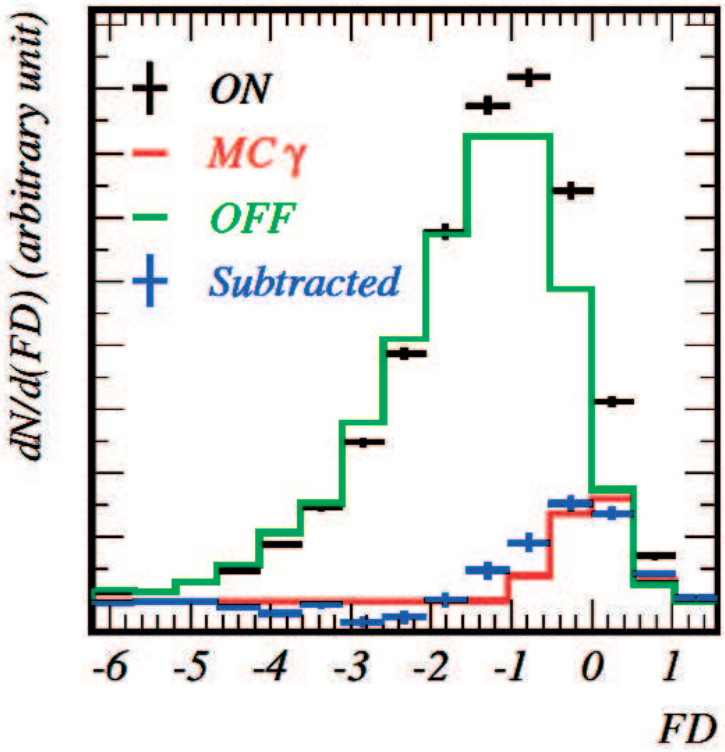

Figure A.3: F distributions for RX J0852.0−4622. The black crosses are those for events inside a 1°-radius circle centered on the SNR with statistical-1-σ errors. The green histogram is for OFF-source data, of which normalization was determined by the fitting procedure described in the text. The blue crosses show the background subtracted signals and the red histogram is the best fit for gamma-rays from Monte Carlo simulations.

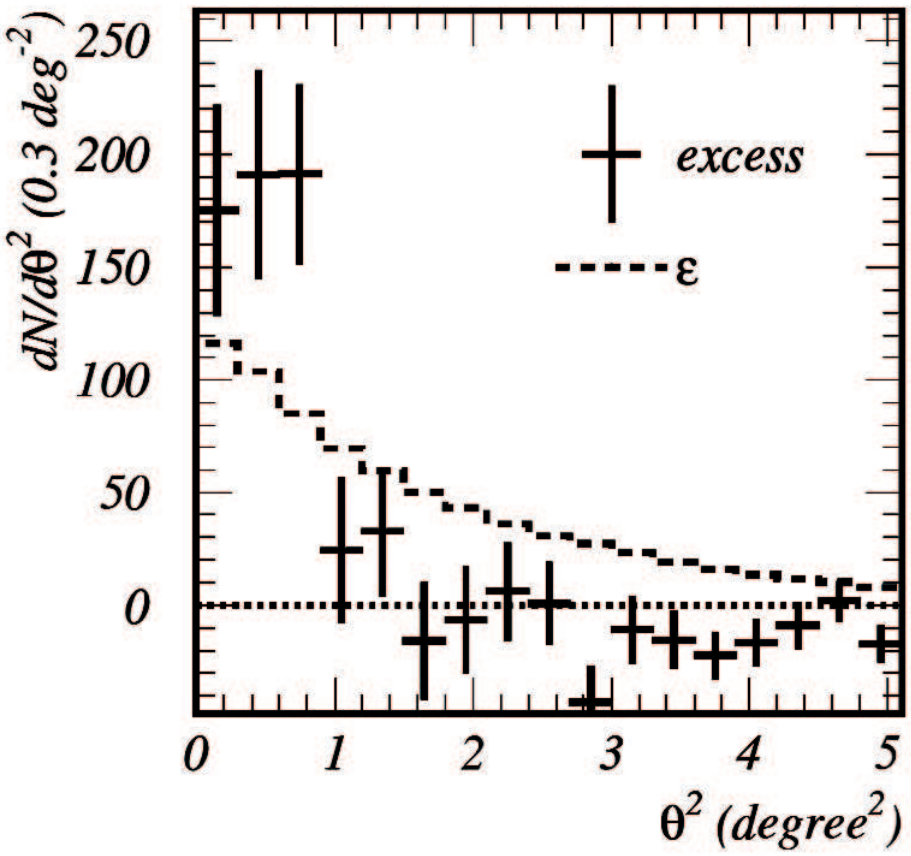

Figure A.4: θ^2-plot. The vertical scale is the number of excess events per 0.3 deg^2. The dashed histogram shows the acceptance (in arbitrary units).

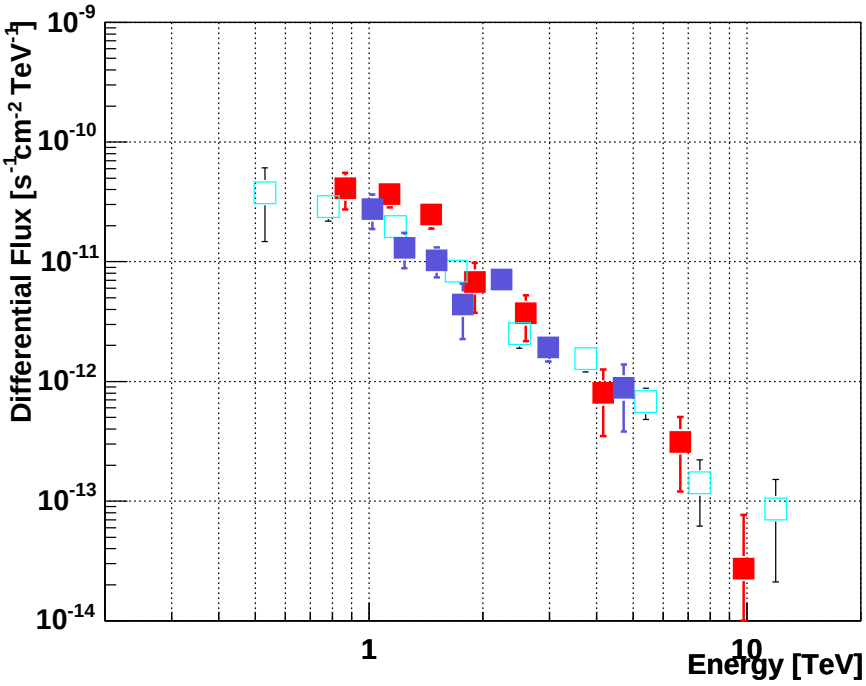

Figure A.5: Differential energy spectra for the whole remnant; the blue boxes by CANGAROO-III with the FD fitting method, the red boxes are also by CANGAROO-III with the LR method ($LR > 0.1$), the the light-blue squares by HESS. The error bars are all statistical.

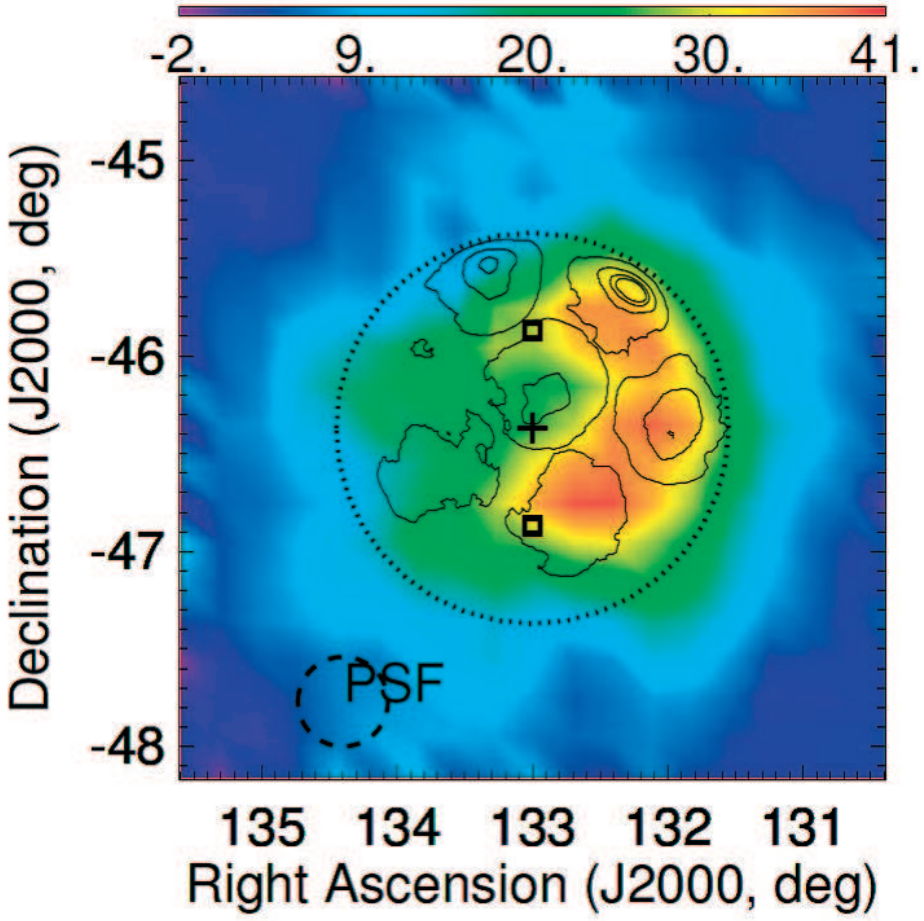

Figure A.6: Morphology of gamma-ray like events by the FD fitting procedure described in the text. The other definitions are the same as in Fig.8.23.

AppendixB

Another TeV Gamma-Ray SNR: RX J1713.7−3946

The supernova remnant RX J1713.7−3946 is first detected in TeV region by the CANGAROO telescope (Muraishi et al. 2000). The CANGAROO group subsequently confirmed the TeV gamma-ray emissions with the new CANGAROO-II telescope (Enomoto et al. 2002a), and concluded that the π^0-decay model is favorable as the emission origin considering the photon flux spectrum. and has proven to be a prominent source of gamma-rays by the HESS group (Aharonian et al. 2004a). It is meaningful to compare the two SNRs, RX J0852.0−4622 and RX J1713.7−3946 in order to study the nature of the particle acceleration in TeV gamma-ray SNRs, moreover, the possibility as an accelerator of the galactic cosmic rays.

This source was first discovered in the *ROSAT* All-Sky Survey (Pfeffermann & Aschenbach 1996). Observations with *ASCA* have revealed intense synchrotron X-ray emission from th entire remnant (Koyama et al. 1997; Slane et al. 1999) without an evidence for thermal X-ray components yet. These features are all common with RX J0852.0−4622. The CO molecular cloud distribution toward RX J1713.7−3946 has been well studied by Fukui et al. (2003). They concluded that the SNR blast waves are interacting with these molecular clouds situated on its western side at a distance of ∼1 kpc. Consequently, the age of the SNR was derived to be ∼1000 years, which is consistent with the estimation from the soft X-ray absorption in the *ASCA* observation (Koyama et al. 1997). RX J1713.7−3946 is considered as followings: it exploded in a low density cavity (∼0.01 cm^{-3}), therefore maintaining an extreme high shock velocity of more than 5000 km s^{-1} (Koyama et al. 1997), still in the free-expansion phase, and its non-decelerated blast wave is colliding with the dense molecular gas in present. Subsequent to Fukui et al. (2003), Moriguch et al. (2005) reported a detailed analysis of the NANTEN CO data. They assumed that the TeV gamma-ray distribution of RX J1713.7−3946 shown by Aharonian et al. (2004a)

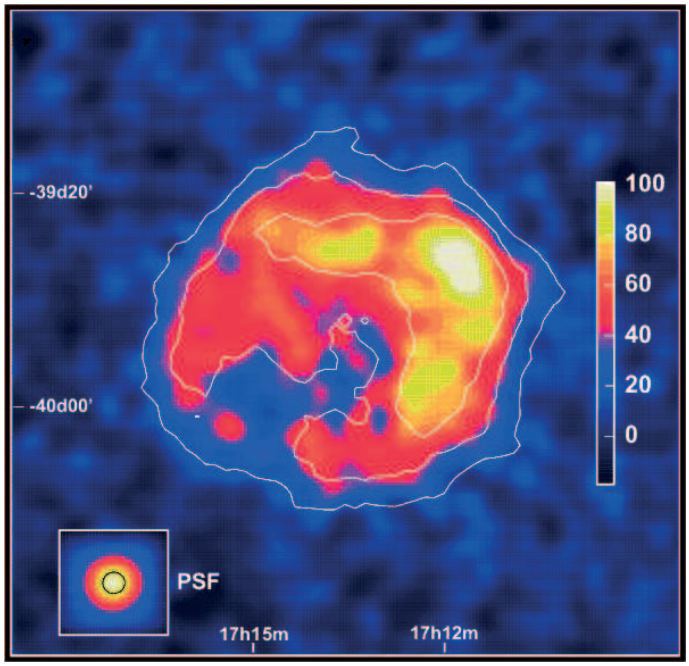

Figure B.1: Gamma-ray image of RX J1713.7−3946. The linear color scale is in units of excess counts. The white contour lines indicate the significance of the different features. Their PSF is shown in the lower left hand corner (Aharonian et al. 2006b).

largely resembles the CO distribution, and they considered that the TeV gamma-ray emission is due to the correlation of the protons and the molecular cloud. They made a rough estimate of the efficiency for the proton acceleration over the entire SNR. The efficiency was estimated to be ~ 0.024.

Recently the HESS collaboration reported the results from a deep observation of RX J1713.0−3946 in 2004 (Aharonian et al. 2006b). They showed the overall morphology of this SNR (Fig.B.1), and it appears very similar to the X-ray image by *ASCA*. The gamma-ray spectrum of the whole SNR was measured from 190 GeV to 40 TeV. The gamma-ray emission mechanism was discussed for two scenarios, the electronic and the hadronic, in conjunction with the consideration of multi-wavelength. First they tried with the synchrotron and IC emission model with some cases of target photons or some magnetic field values, to find out that this model cannot explain the spectrum. The IC gamma-rays make narrow peak, while the TeV gamma-ray emission from RX J1713.0−3946 shows a flat-topped spectrum. Meanwhile, they discussed the π^0 decay model from the point of view of the proton energetic. and concluded that this hadronic scenario is favored. This thought stream

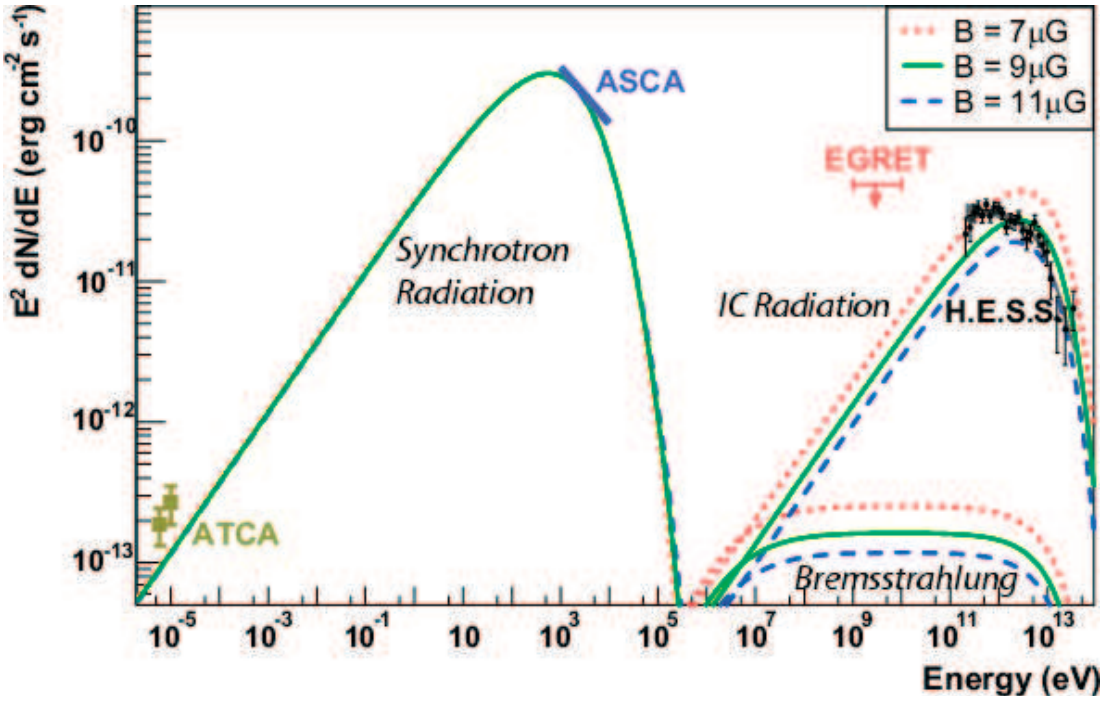

Figure B.2: Broadband spectral energy distribution of RX J1713.7−3946 for the whole SNR (Aharonian et al. 2006b). The synchrotron and IC spectra were modeled assuming a source distance of 1 kpc, an age of 1000 years, a density of 1 cm^{-3}. Shown are three curves for three values of the mean magnetic field as the legend in the figure.

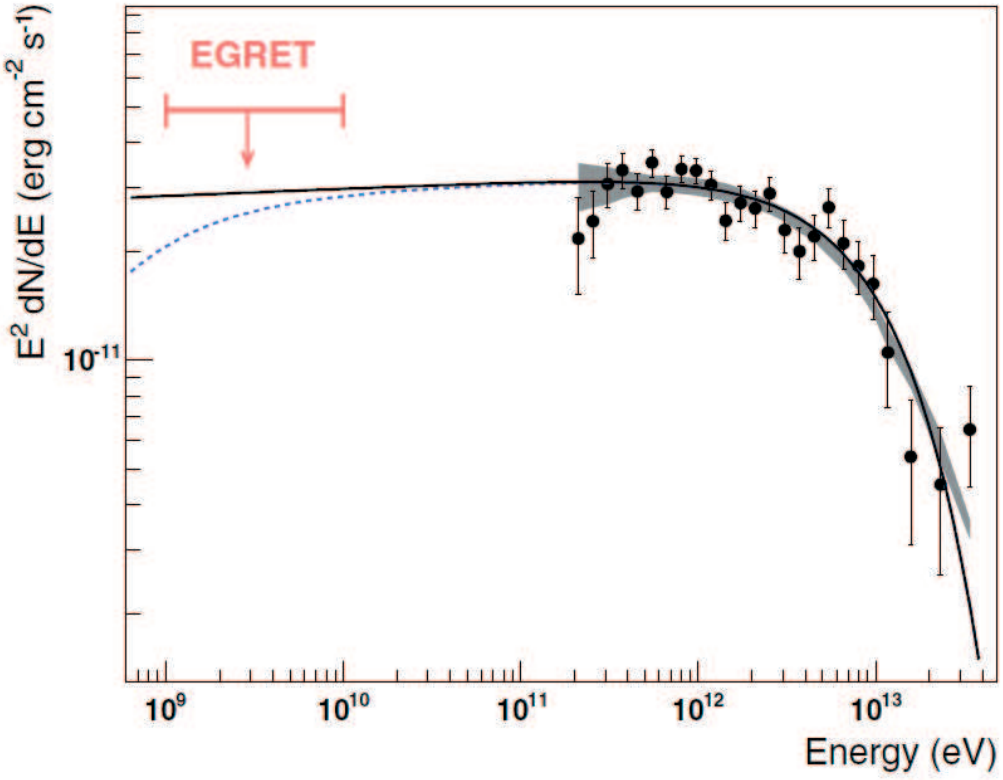

Figure B.3: HESS data points of RX J1713.7−3946 plotted in an energy flux diagram (Aharonian et al. 2006b). The shaded grey band is the systematic error band for their measurement. The black curve is the best fit of a power law with exponential cutoff to the data, extrapolated to lower energies. The dashed blue curves is the same function, but it takes the π^0 kinematics into account. The EGRET upper limit from 1 GeV to 10 GeV is plotted as red arrow.

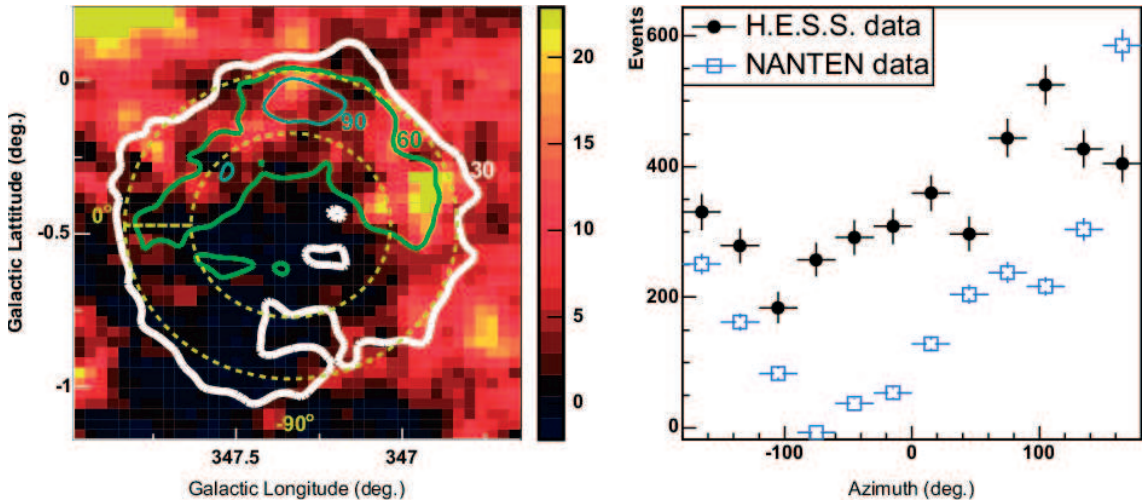

Figure B.4: Left panel: Intensity distribution of CO ($J = 1 - 0$) emission (Fukui et al. 2003) (linear color scale in units of K km s^{-1}, truncated at a value of 23 to highlight important features). Overlaid are colored contours of the HESS gamma-ray excess images. Right panel: Azimuth profile plot integrated in a 0.2°-wide ring covering the shell of RX J1713.7−3946 (dashed yellow circle in the left-hand panel). (Aharonian et al. 2006b).

is almost the same as the discussion in Enomoto et al. (2002a). Thanks to the broader spectrum plot by the HESS group, this conclusion becomes more reliable. As for RX J1713.7−3946, there is a growing acceptance of the hadronic scenario in the world. They fitted their obtained flux with some functions, and plotted in an energy flux diagram (Fig.B.3) for the best fit of a power law with exponential cutoff.

Moreover, Aharonian et al. (2006b) discussed the target gas for the gamma-ray production. They compared the emission intensities of CO and TeV gamma-rays (Fig.B.4). They concluded that the target is not the molecular cloud because of the absence of the exact proportionality between the two measurements for the shell region of RX J1713.7−3946. Although this SNR seems to be beginning to interact with the dense clouds to the west as seen in NANTEN data, they claimed that the bulk of the TeV gamma-rays is not linked to these clouds but must be due to interactions with rather uniform ambient gas. However Fig.B.4 shows a moderate correlation, there still remains the possibility of the gamma-ray emission due to the molecular cloud. Returning to RX J0852.0−4622, we already explained the TeV gamma-ray emission in terms of interactions of accelerated protons with the ambient gas. The emission profile of RX J0852.0−4622 shows a shell-like structure. Then,

the molecular clouds located along the line sight to this SNR are possibly interacting this SNR, and there the TeV gamma-rays might be emitted.

Various physical parameters are compared in Table B.1 for RX J0852.0−4622, RX J1713.7−3946 (Moriguchi et al. 2005) and SN1006. SN1006 is another synchrotron emitting SNR, and its upper limits of TeV gamma-ray flux are reported by the HESS group (Aharonian et al. 2005a). One of the significant features is that the X-ray emission from SN1006 has thermal component. This may indicate that the explosion happened in a higher-density medium, while the other two probably exploded in a cavity. The smaller velocity of the SN1006 shock wave in spite of the comparable age with the other two SNRs also supports this assumption. A smaller velocity provides a smaller maximum energy of acceleration. Then the particle acceleration at the shock wave is less efficient. It is also an important fact that SN1006 is rather far from the galactic plane comparing with the other two SNRs. It means the environment of SN1006 is less dense than the others. Moreover, there is no local molecular cloud. These facts make less possible the same hadronic scenario as RX J1713.7−3946 for SN1006. Additionally, we compared the parameters derived from the TeV gamma-ray results for the two TeV gamma-ray SNRs in Table B.1.

In order to reach a more reliable answer also on the emission mechanism of RX J0852.0−4622, what is necessary? More precise CO observations like that of RX J1713.7−3946 are important. If the collision of the SNR blast wave and molecular gas is established, it offers the distance and the age with great accuracy. Consequently, the parameters such as the maximum energy, the magnetic field, or e/p ratio, are restricted more severely. Of course it can be a strong support for the proton origin of the TeV emission. Nevertheless, deeper TeV gamma-ray measurements seem essential. The gamma-ray spectrum in broader energy band than now observed will give us a clear answer. Additionaly, the launch of GLAST (aiming 50 MeV to 300 MeV) in 2007 will provide us the GeV flux of RX J0852.0−4622, and it will identify the emission mechanisms.

Table B.1: Various physical parameters of the three synchrotron-radiating SNRs. Γ is the best fit value in fitting the TeV gamma-ray flux with a function of $\phi_0 E^{-\Gamma}$, where ϕ is the differential flux normalization, and $E_{\rm tot}$ is the proton total energy in units of ergs under the assumption of a target gas density of 1 cm^{-3}.

	RX J0852.0−4622 (G266.2−1.2)	RX J1713.7−3946 (G347.3−0.5)	SN1006 (G327.6+14.6)
Galactic latitude	−1.2	−0.5	+14.6
Distance	0.2 kpc	1 kpc	1.8 kpc (Green 2001)
Age	680 yr	1600 yr	just 1000 yr
Evolution phase	Free expansion	Free expansion	Sedov
Shock velocity	5000 km s^{-1}	5500 km s^{-1}	3000 km s^{-1}
X-ray emission	Nonthermal	Nonthermal	Thermal+Nonthermal
Molecular cloud	?	Correlating.	None.
Γ	2.7±0.2 (this work)	2.26±0.02	–
$E_{\rm tot}$	2×10^{49} (this work)	6×10^{49}	–

Bibliography

Abe, K. et al. (2001). Measurement of Branching Fractions for $B \to \pi\pi$, $K\pi$, and KK Decays. *Phys. Rev. Lett. 87*, 101801.

Adachi, Y. (2005). Master's thesis. ICRR, University of Tokyo.

Aharonian, F. et al. (2004a). High-energy particle acceleration in the shell of a supernova remnant. *Nature 432*, 75–77.

Aharonian, F. et al. (2004b). The Crab Nebula and Pulsar between 500 GeV and 80 TeV: Observations with the HEGRA Stereoscopic Air Cerenkov Telescopes. *Astrophys. J. 614*, 897–913.

Aharonian, F. et al. (2005). Upper limits to the SN1006 multi-TeV gamma-ray flux from HESS observations. *Astron. Astrophys. 437*, 135–139.

Aharonian, F. et al. (2005). Detection of TeV γ-ray emission from the shell-type supernova remnant RX J0852.0−4622 with HESS. *Astron. Astrophys. Lett. 437*, L7–L10.

Aharonian, F. et al. (2006a). Observations of the Crab nebula with HESS *Astron. Astrophys. 457*, 899–915.

Aharonian, F. et al. (2006b). A detailed spectral and morphological study of the gamma-ray supernova remnant RX J1713.0−3946 with HESS. *Astron. Astrophys. 449*, 223–242.

Allen, C. W. (1973). *Astrophysical quantities*. London: University of London, Athlone Press, —c1973, 3rd ed.

Aschenbach, B. (1998). Discovery of a young supernova remnant. *Nature 396*, 141–142.

Aschenbach, B. et al. (1999). Constraints of age, distance and progenitor of the supernova remnant RX J0852.0-4622/GRO J0852-4642. *Astron. Astrophys. 350*, 997–1006.

Baade, W. et al. (1934). Remarks on Super-Novae and Cosmic Rays. *Phys. Rev. 46*, 76–77.

Bamba, A. et al. (2005a). A Spatial and Spectral Study of Nonthermal Filaments in Historical Supernova Remnant: Observational Results with Chandra. *Astrophys. J. 621*, 793–802.

Bamba, A. et al. (2005b). Chandra Observation of Galactic Supernova Remnant Vela Jr.: A New Sample of Thin Filaments Emitting Synchrotron X-Rays. *Astrophys. J. 632*, 294–301.

Bell, A. R. (1978). The acceleration of cosmic rays in shock fronts. I. *Monthly Notices Roy. Astron. Soc. 182*, 147–156.

Berezhko, E. G., Ksenofontov, L. T., and Völk, H. J. (2003). Confirmation of strong magnetic field amplification and nuclear cosimic ray acceleration in SN1006. *Astron. Astrophys. Lett. 412*, L11–L14.

Berezhko, E. G. and Völk, H. J. (2004). Direct evidence of efficient cosmic ray accleration and magnetic field amplification in Cassiopeia A. *Astron. Astrophys. Lett. 419*, L27–L30.

Blandford, R. D. et al. (1978). Particle acceleration by astrophysical shock. *Astrophys. J. Letters 221*, L29–L32.

Burgess, C. P. et al. (2000). Footprints of the newly discovered Vela supernova in Antarctic ice cores?. *Astropart. Phys. 14*, 1–6.

Cha, A. N. et al. (2000). Spectroscopy and Timee Variability of Absorption Lines in the Direction of the Vela Supernova Remnant. *Astrophys. J. Suppl. 126*, 399–426.

Chen, W. et al. (1999). Progenitor of the New COMPTEL/ROSAT Supernova Remnant in VELA. *Astrophys. J. Letters 514*, L103–L106.

Combi, J. A. et al. (1999). Radio Detection of the Supernova Remnant RX J0852.0-4622. *Astrophys. J. 519*, L177–L180.

Digel, S. et al. (1990). Giant Molecular Clouds in the Outer Arm of the Galaxy. *Astrophys. J. Letters 357*, L29–L33.

Drury, L. O. C. (1983). An introduction to the theory of diffusive shock acceleration of energetic particles in teneous plasmas. *Rep. Prog. Phys. 46*, 973–1027.

Duncan, A. R. and Green, D. A. (2000). The supernova remnant RX J0852.0-4622: radio characteristics and implications for SNR statistics. *Astron. Astrophys. 364*, 732–740.

Enomoto, R. et al. (2002a). The acceleration of cosmic-ray in the supernova remnant RX J1713.7-3946. *Nature 416*, 823–826.

Enomoto, R., Hara, S. et al. (2002b). Design study of CANRAROO-III, stereoscopic imaging atmospheric Cherenkov telescopes for sub-TeV gamma-ray detection. *Astropart. Phys. 16*, 235–244.

Enomoto, R., Watanabe, S. et al. (2006). CANGAROO-III Observations of the Supernova Remnant RX J0852.0−4622. *Astrophys. J. 653*, *in press.*

Esposito, J. A. et al. (1996). EGRET Observations of Gamma-Ray Emission from Supernova Remnants. *Astrophys. J. 461*, 820–827.

Fisher. R. A. (1936). The use of multiple measurements in taxonomic problems. *Annal. of Eugenic 7*, 179–188.

Frank, I. M. (1998). *Vavilov-Cherenkov Radiation.* Nauka, Moscow.

Fukui. Y. (2003). Discovery of Interacting Molecular Gas toward the TeV Gamma-Ray Peak of the SNR G347.3−0.5. *Publ. Astron. Soc. Japan 55*, L61–L64.

Gaisser, T. K. et al. (1998). Gamma-Ray Production in Supernova Remnants. *Astrophys. J. 492*, 219–227.

Gehrels, N. and Williams, E. D. (1993). Temperatures of Enhanced Stability in Hot Thin Plasmas. *Astrophys. J. 418*, L25–L28.

Ginzburg, V. L. et al. (1964). The Origin of Cosmic Rays. Pergamon, London and New York.

Ginzburg, V. L. et al. (1965). The Origin of Cosmic Rays. Pergamon, London and New York.

Görres, J. et al. (1998). Half-Life of 44Ti as a Probe for Supernova Models. *Phys. Rev. Lett. 80*, 2554–2557.

Green, D. A. (2001). A Catalogue of Galactic Supernova Remnants (2001 December version). Cambridge: Mullard Radio Astron: Obs.

Gupta, M. et al. (1989). Cosmic Magnetobremsstrahlung (synchrotron radiation). *Ann. Rev. Astron. Astrophys. 3*, 297–350.

Hartman, R. C. et al. (1999). The Third EGRET Catalogu of High-Energy Gamma-Ray sources. *Astrophys. J. Suppl. 123*, 79–202.

Hayakawa, S. (1956). Supernova Origin of Cosmic Rays. *Prog. Theor. Phys. 15*, 111–121.

Hayashida, N. et al. (1994). Observation of a Very Energetic Cosmic Ray Well Beyond the Predicted 2.7 K Cutoff in the Primary Energy Spectrum. *Phys. Rev. Lett. 73*, 3941–3494.

Heitler, W. (1954). *The Quantum Theory of Radiation*. Oxford, London.

Hess, V. F. (1912). Über Beobachtungen der durchdringenden Strahlung bei sieben Freiballonfahrten. *Physik. Zeitschr. XIII*, 1804–1091.

Hillas, A. M. (1982). *J. Phys. G 8*, 1475–1792.

Iyudin, A. F. et al. (1998). Emission from ^{44}Ti associated with a previously unknown Galactic supernova. *Nature 396*, 142–144.

Iyudin, A. F. et al. (2005). *XMM-Newton* observations of the supernova remnant RX J0852.0-4622/GRO J0852-4642. *Astron. Astrophys. 429*, 225–234.

Jelley, J. V. (1958). *ČerenkovRadiatioin and its Applications*. Pergamon Press.

Katagiri, et al. (2005). Detection of Gamma Rays around 1 TeV from RX J0852.0-4622 by CANGAROO-II. *Astrophys. J. 619*, L163–L166.

Kawachi, et al. (2001). The optical reflector system for the CANGAROO-II imaging atmospheric Cherenkov telescope. *Astropart. Phys. 14*, L261–L269.

Kobayashi, T. et al. (2004). The Most Likely Sources of High-Energy Cosmic-Ray Electrons in Supernova Remnants. *Astrophys. J. 601*, 340–351.

Koyama, K. et al. (1995). Evidence for Shock Acceleration of High-Energy Electrons in the Supernova Remnant SN1006. *Nature 378*, 255–258.

Koyama, K. et al. (1997). Discovery of Non-Thermal X-rays from the Northwest Shell of the New SNR RX J1713.7-3946: The Second SN 1006?. *Publ. Astron. Soc. Japan 49*, L7–L11.

Lewis, D. A. (1990). Optical ccharacteristics of the Whipple Observatory TeV gamma-ray imaging telescope. *Exp. Astron. 1*, 213–226.

Li, T. P. and Ma, Y. Q. (1983). Analysis methods for results in gamma-ray astronomy. *Astrophys. J. 272*, 317–324.

Longair, M. S. (1992). High Energy Astrophysics. Cambridge University Press, Cambridge.

May, J. et al. (1988). A wide latitude CO surveyd of th third galactic quadrant. *Astron. Astrophys. Suppl. Ser. 73*, 51–83.

Moriguchi, Y. et al. (2001). A ^{12}CO(J=1–0) Survey of Molecular Clouds toward the Vela Supernova Remnant with NANTEN. *Publ. Astron. Soc. Japan 53*, 1025–1036.

Moriguchi, Y. et al. (2005). A Detailed Study of Molecular Clouds toward the TeV Gamma-Ray Supernova Remnant G347.3−0.5. *Astrophys. J. 631*, 947–963.

Muraishi, H. et al. (2000). Evidence for TeV gamma-ray emission from the shell type SNR RX J1713.7-3946. *Astron. Astrophys. 354*, L57–L61.

Naito, T., and Takahara, F. (1994). High energy gamma-ray emissionfrom supernova remnants. *J. Phys. G/ 20*, 477–486.

Norman, E. B. et al. (1998). Half-life of ^{4}4Ti. *Phys. Rev. C/ 57*, 2010–2016.

Oda, M. et al. (1989). *Cosmic Ray Astrophysics.* Asakura.

Particle Data Group.
http://www.pdg.lbl.gov
(Courtesy of the COMPASS group, IHEP, Protvino, August 2005)

Pfeffermann, E., and Aschenbach, B. (1996). *ROSAT Observation of a New Supernova Remnant in the Constellation Scorpius MPE Report 263*, 267–268.

Pierre Auger Observatory (1997). *The Pierre Auger Observatory Design Report.* http://www.auger.org/admin/DesignReport/index.html

Reynolds, S. P. (1996). Synchrotron Models for X-Rays from the Supernova Remnant SN 1006. *Astrophys. J. 459*, L13–L16.

Reynolds, S. P. and Stephen (1998). Synchrotron Models for X-Rays from the Supernova Remnant SN 1006. *Astrophys. J. 459*, L13–L16.

Reynoso, E. M. et al. (2006). The interior of the SNR RX J0852.0-4622 (Vela Jr) at radio wavelengths. *Astron. Astrophys. 449*, 243–250.

Rybicki, G. B. and Lightman, A. P. (1979). *Radiative Processes in Astrophysics.* A Wiley-interscience, New York.

Sedov, L. I. (1959). *Similarity and Dimensional Methods in Mechanics.* Academic Press, New York.

Simpson, J. A. (1983). Elemental and Isotropic Composition of the Galactic Cosmic Rays. *Ann. Rev. Nucl. Part. 33*, 323–381.

Slane, P. et al. (2001). RX J0852.0-4622: Another Nonthermal Shell-Type Supernova Remnant (G266.2-1.2). *Astrophys. J. 548*, 814–819.

Slane, P. et al. (1999). Nonthermal X-Ray Emission from the Shell-Type Supernova Remnant (G347.3-0.5). *Astrophys. J. 525*, 357–367.

Tomida, H. (2000). Doctoral thesis. Kyoto University.

Tsunemi, H. et al. (2000). Overabundance of Calcium in the Young SNR RX J0852.0−4622: Evidence of Over-Production of ^{44}Ti. *Publ. Astron. Soc. Japan 52*, 887–893.

Uchiyama, Y. et al. (2003). Fine-structure in the nonthermal X-ray emission of SNR RX J1713.7−3946. *Astron. Astrophys. 400*, 567–574.

Völk, H. J. et al. (2005). Magnetic field amplification in Tycho and other shell-type supernova remnants. *Astron. Astrophys. 433*, 229–240.

Vink, J. and Laming, J. M. (2003). On the Magnetic Fields and Particle acceleration in Cassiopeia A. *Astrophys. J. 584*, 758–769.